X-RAY PHOTOELECTRON SPECTROSCOPIC STUDIES OF METALS, METAL OXIDES AND RELATED SYSTEMS

Thesis submitted to the University of Newcastle upon Tyne
for the degree of Doctor of Philosophy

by

Alan J. Paul, B.Sc.

November 1984

ABSTRACT

X-ray photoelectron spectroscopy (XPS) has been used to investigate the surfaces of some metals, metal oxides and related chemical systems, most of which are of technological importance or relevance. These substances were conductors or non-conductors, and a study was made concerning the correct binding energy referencing in the latter case. In some cases, a variation was found in the C1s binding energy with the surface coverage of adventitious carbon. This study revealed, however, that under suitable conditions this C1s binding energy can be used to obtain reproducible binding energies in insulators.

The surface of borided zirconium has been studied in collaboration with a colleague, with a view to evaluating its use in electrochemical applications. A number of oxides (of both boron and zirconium) have been observed on the substrate surface, and this must inhibit the use of this material for electrochemistry and in cases where the full boride surface properties are required.

Studies of uranium metal and oxide systems were carried out with an emphasis on applications (especially the ammonium uranates) relevant to the nuclear power industry. The heating of uranium metal *in vacuo* has been studied and the presence of unusual species is reported. Some of the results are similar to those obtained by other workers in their studies of both uranium and plutonium. Two uranium species have been detected on the surface of the sample at elevated temperatures. This corresponds to both uranium metal and one of its oxides; the stoichiometry of the latter species is uncertain. Two carbide species were also detected. Some aspects of the ammonium uranate system have been investigated. Problems associated with the use of XPS to analyse this material are discussed. Although conclusions as to the chemical nature of this material are limited, the results do show that XPS has considerable potential for the study of this system.

Finally, the surface segregation of impurities in high purity samples of platinum and palladium has been observed on heating samples *in vacuo* and in oxygen. Such studies are important since these metals are used in many electrochemical and catalytic applications. Silver, gold and carbon were observed to segregate in platinum whereas silver and sulphur segregated in palladium. All species segregated in their elemental form. The core level binding energies of the silver and gold segregants were lower than those measured for the corresponding pure metal state.

ACKNOWLEDGEMENTS

I would like to thank Dr.P.M.A.Sherwood for his help throughout this project and for kindly printing the final manuscript. I gratefully acknowledge the UK Atomic Energy Authority at Dounreay for their cooperation and financial assistance.

My thanks to past and present members of the XPS group for valuable discussions. I sincerely thank Dr.P.H.Middleton for his cooperation in the zirconium work. I am grateful to the Gamet program for many hours of restrained parameters.

I would particularly like to thank the dynamic duo, Mr. Kevin S. Robinson and Mr. Guy R. Wilson for their considerable help in the latter stages of my work.

Finally I would like to thank Dr.H. Yvonne Hall, not only for her many hours of hard work on my behalf, but also for her constant support and encouragement.

CONTENTS

Chapter One

X-Ray Photoelectron Spectroscopy

Chapter Two

Experimental

Chapter Three

Sample Charging, Mounting and Calibration

Chapter Four

Study of the Surface of Borided Zirconium

Chapter Five

Studies of Uranium Oxides and Related Systems

Chapter Six

Surface Segregation of Impurities in Platinum and Palladium

References

CHAPTER ONE

X-RAY PHOTOELECTRON SPECTROSCOPY

1.1 Introduction

Photoelectron spectroscopy is a technique in which samples to be studied are exposed, *in vacuo*, to a flux of nearly monoenergetic electromagnetic radiation, resulting in the emission of electrons. The detection and subsequent analysis of these photoelectrons can provide a wealth of information on the sample under investigation, and consequently this powerful spectroscopic method is being used in many scientific fields.

The technique originates from the photoelectric effect discovered by Hertz (1) in 1887, when he observed that a spark would jump a gap more readily when illuminated with ultra-violet light. Subsequent studies (2,3) identified the process with the emission of electrons and established that the electron current and electron velocity were a function of the intensity and frequency of the incident radiation. These observations were explained in 1905 by Einstein (4) who described the photoelectric effect in terms of absorption of a "quantised package" of light (a photon) and derived the simple energy conservation relationship shown by equation 1.1 in section 1.2.

Despite these early discoveries the evolution of photoelectron spectroscopy was severely hampered by experimental considerations and had to await the development of suitable ultra-high vacuum equipment and high resolution electron energy analysers which did not occur until the late 1950's and early 1960's.

Research in the field then proceeded along two different lines of development:-

1) Ultraviolet Photoelectron Spectroscopy (UPS,5).

Due to the relatively small incident photon energies used in ultraviolet excitation (5-40eV), only valence orbital electrons are normally accessible, although the emission of shallow lying core level electrons has been reported (6). UPS was not used for work described in this thesis.

2) X-Ray Photoelectron Spectroscopy (XPS).

The use of X-ray excitation (photon energy $\gtrsim$ 100eV) permits the ionisation of both core and valence electrons, and much of the pioneering work in this area was done by Siegbahn (7). It should be mentioned that the acronym ESCA (Electron Spectroscopy for Chemical Analysis) is frequently used instead of XPS.

1.2 Some Basic Principles of XPS

The kinetic energies of electrons emitted from a sample via bombardment with radiation of mean photon energy $h\nu$ is given by the Einsteinian relationship:-

$$h\nu = E_{bv}(k) + E_k \qquad (1.1)$$

where

ν = frequency of incident radiation,

$E_{bv}(k)$ = binding energy of the k^{th} level referenced to the vacuum level,

E_k = kinetic energy of emitted photoelectron.

All electron energy levels are accessible provided that the incident photon energy is large enough, and therefore equation (1.1) can be used to calculate binding energies for all the electrons in an isolated atom or molecule. Strictly speaking, equation (1.1) should take account of the recoil energy of the atom or molecule from which the photoelectron was ejected, however this term is normally very small and can generally be neglected.

It is clear that electron emission with a fixed photon energy will yield a number distribution of photoelectrons with kinetic energy. This kinetic energy distribution is the photoelectron spectrum and normally consists of a series of discrete peaks, which is not unexpected since the energy levels occupied by electrons are quantised. Photoemission of electrons into a continuum of final states means that there are no selection rules to restrict the possible transitions. Although every atom in the periodic table has its own unique set of orbital binding energies, the incorporation of atoms into molecules and solids results in significant changes.

The atomic orbitals which participate in chemical bonding lose their atomic character to varying degrees, and XPS can be used to study the resultant molecular or solid state bonding scheme. Photoelectron spectroscopy is a particularly suitable technique for investigating the valence bands of solids since, for each sample, the spectrum is expected in some way to reflect the electronic density-of-states. In XPS, the ejection of electrons into a featureless continuum implies that the valence band spectrum should simply correspond to the occupied density-of-states, modulated by variations in differential photoelectron cross-section (section 1.7).

The core orbitals, which do not participate in bonding, remain essentially atomic in character and their binding energies are sufficiently invariant to identify the specific atoms concerned. There are, however, small but measurable changes in core binding energies which can be correlated with differences in chemical state and environment, and this important aspect will be discussed in section 1.6.

Before going on to consider other aspects of XPS, it should be stated that the technique can be applied to gaseous species (8,9), liquids (10,11) and solids although all samples discussed in this thesis are solid. Thus those special features associated with solid state analysis are presented in this chapter in addition to those aspects which will clearly apply to all states of matter. Furthermore, although XPS has been employed to investigate the valence bands of solids, its major application has in fact been to study core orbital electrons, as was the case for the work reported in this thesis. Thus, this chapter basically discusses core level photoemission although many aspects will clearly apply directly to valence level studies.

1.3 Two Important Processes Accompanying Photoemission

It is important to note that other processes accompany X-ray photoemission (see also section 1.10). The hole produced by the ejection of a core electron in the primary photoemission process (figs 1.1a and 1.1b) normally decays by one of two mechanisms. In both cases the core vacancy is filled by an electron from some sub-shell of lower binding energy. The excess energy created by this transition can be dissipated by emission of a photon, normally in the X-ray region (fig 1.1c), or by emission of an Auger electron (fig 1.1d, ref 12). Auger electron emission is more likely to occur with elements of low atomic number. Auger electrons will therefore be detected in the photoelectron experiment and great care must be taken to differentiate between photoelectron and Auger peaks. Positive identification can be achieved by changing the incident photon energy since Auger electron kinetic energies depend upon differences between energy levels and are therefore independent of the exciting radiation. It should be stressed that the appearance of Auger peaks in photoelectron spectra does not normally present a problem and indeed such peaks can provide useful information in many situations.

1.4 Solid State Studies

The three-step model is often used for the interpretation of photoemission from solids and consists of:-

a) An optical excitation where an electron is excited from an occupied state to a highly antibonding state,

b) transport of the electron through the solid matrix to the surface,

c) escape of the electron into the vacuum.

Those processes which accompany the primary photoemission event are designated "intrinsic" if they occur during step a) and "extrinsic" if they occur during steps b) and c).

Although the incident X-radiation used in XPS experiments can penetrate relatively deeply into solids, the ejected photoelectrons are considerably attenuated by inelastic scattering processes, and can only escape from a very short distance below the surface. As a rough guide, XPS is a study of the top 10-30Å for most inorganic solids, 30-100Å for organic samples and 10-20Å for metals (section 1.7.1). Thus XPS is essentially a surface analysis technique and has been extensively used in this field (13,14).

However XPS can also be used to investigate bulk properties, although this does have its problems and uncertanties in that one must be certain that the surface is indeed representative of the bulk. The possibility of differences in chemical composition between the surface and the bulk must obviously be considered. Surface contamination must also be avoided and this is achieved by analysing the samples under high vacuum conditions (Chapter 2). A more difficult problem to treat concerns the existence of surface electronic states which arise as a result of the environmental asymmetry of atoms at the solid-vacuum interface. Such states can only be observed on ultra-clean surfaces, and although they can be particularly important in UPS (due to lower sampling depths, 15,16), the effect in XPS is normally very small. XPS has however been used to observe a surface atom core level shift for gold, in addition to differences in the valence band (17) and clearly the possibility of such effects must be considered.

1.5 Binding Energy Referencing

Although equation (1.1), in which binding energies are referenced to the vacuum level, is applicable to an isolated atom or molecule, the situation for solids is more complex.

1.5.1 Solid Conductors

Fig 1.2 shows the energy level diagram for an electrically conducting solid in contact with the spectrometer. Thermodynamic equilibrium between the sample and the spectrometer requires that their Fermi levels equalise, and the resultant contact potential is equal to the difference between the sample (Φ_{sa}) and spectrometer (Φ_{sp}) workfunctions ($\Delta\Phi = \Phi_{sa} - \Phi_{sp}$). Hence, photoelectrons passing from the surface of the sample into the spectrometer will experience an accelerating or retarding potential, which adjusts their kinetic energy from E_k to E'_k where:-

$$E'_k = E_k + \Phi_{sa} - \Phi_{sp} \qquad (1.2)$$

It is clear from fig 1.2 that binding energies can easily be referenced to the identical Fermi levels of the sample and spectrometer such that:-

$$h\nu = E_{bf}(k) + E_k' + \Phi_{sp} \qquad (1.3)$$

where $E_{bf}(k)$ = binding energy of the k^{th} level referenced to the Fermi level.

Equation (1.3) shows that the workfunction term is now a constant of the spectrometer, and thus the sample workfunction is not required to determine E_{bf}. Vacuum-referenced binding energies can of course be determined via:-

$$E_{bv}(k) = E_{bf}(k) + \Phi_{sa} \qquad (1.4)$$

The accurate measurement of Φ_{sa} is not only experimentally difficult, but is also subject to considerable uncertainty (18). Hence the Fermi level is the only experimentally convenient reference and is used almost exclusively for core electron binding energies in solids.

1.5.2 Non-Conductors and the Charging Effect

The difficulty of binding energy referencing in poor conductors or insulators arises from the lack of thermodynamic equilibrium between the spectrometer and sample Fermi levels. This problem, which also occurs when a conductor is electrically insulated from the spectrometer, means that binding energies referenced against the spectrometer Fermi edge are not valid as the situation stands. The problem is further complicated by sample charging. Loss of electrons from the surface of a poor conductor or insulator in the photoelectron experiment results in a build-up of positive charge since the rate of photoelectron loss is greater than that of electron return current to the sample. Return current is normally achieved via a background of secondary electrons which are produced by X-rays bombarding the X-ray gun window and internal parts of the instrument, in addition to any direct conduction mechanism operating between the sample and earth.

The competition between the above factors normally results in the sample attaining an equilibrium static positive surface charge which reduces the kinetic energy of the emitted photoelectrons. In order to reference binding energies against the spectrometer Fermi level, sample charging and the lack of Fermi level equilibration must therefore be corrected for. Only the basic aspects of calibration will be outlined here as a more thorough review is given in chapter 3.

Many workers have approached the problem by reduction or removal of the sample charge by, for example, using extremely thin sample films on a conducting substrate, or by flooding the sample surface with low energy electrons to neutralise any positive charge. Removal of the surface charge does not however promote equilibration of the sample and spectrometer Fermi levels. This problem can be overcome via external or internal calibration, which is widely used for samples where the surface charge has not been reduced or removed as described above. Calibration via an external standard is achieved by placing some material, with a known orbital binding energy, on the sample surface. The chosen calibrant must be in good electrical contact with the sample to allow their respective Fermi levels to equilibrate and enable the calibrant to attain the same charge as the sample surface. The use of an internal energy level which is insensitive to chemical change throughout a series of complexes is perhaps the most reliable method of calibration in that the referencing species must truly reflect the static charge of the sample.

Binding energies of non-conductors are therefore effectively referenced against the spectrometer Fermi level by:-

$$E_{bf}(k) = E_{bf}(cal) + E'_k(cal) - E'_k \qquad (1.5)$$

where $E_{bf}(cal)$ = standard orbital binding energy for the calibrant referenced against the spectrometer Fermi level,

$E'_k(cal)$ = kinetic energy of electron ejected from the calibrant core level being used as standard.

1.6 The Chemical Shift and Interpretation of Photoelectron Spectra

As indicated earlier, core electron binding energies are not only dependent upon the element involved, but also upon the charge on the atom concerned and upon its chemical environment. The resultant variation in binding energies for non-equivalent atoms of the same element is the chemical shift effect (7), the magnitude of which is the same for each core level of a particular atom. An example of this effect is given in fig 1.3

which shows the N1s core level region for ammonium nitrate. Two distinct peaks are observed corresponding to the two non-equivalent nitrogen atoms, with the highest binding energy signal corresponding to the nitrogen atom with the highest formal positive charge. On an empirical basis, it would appear that the chemical shift increases with increasing positive charge on the atom concerned since the higher effective nuclear charge would result in a greater attraction of the core electrons for the nucleus. For a specific atom in a series of its compounds, there are a number of cases where this correlation of self-atom charge with core level binding energy is very good (7). However, the situation of an atom incorporated into a molecule or solid is obviously very different to that of an atom which is completely isolated. Thus the potential effect of the surrounding atomic charges (not just those which are nearest neighbours) will, in most cases, have an important bearing on the magnitude of chemical shifts (19,20).

The situation, so far, has only considered actual atomic charges but, in many cases, very simple binding energy predictions can be made on the basis of formal oxidation state. Although it is often true that the experimental binding energy increases with increasing formal oxidation state, there are many cases where this relationship does not hold (21,22). It is much more difficult to empirically predict the binding energy trend in the cases where the formal oxidation state is the same, however the general rule is that the binding energy increases as the electronegativity of the attached atoms or chemical groups increases.

Theoretical calculations have been widely applied to interpret chemical shifts, and have shown the considerable importance of including final state orbital relaxation in the theoretical model. Since energy must be conserved in the photoemission process, it can be seen that the k^{th} orbital binding energy, $E_b(k)$, is equal to the difference in total energy between the initial state (assumed neutral for simplicity) and the final ion state with a vacancy in the k^{th} orbital. Thus $E_b(k)$ will equal the negative of the k^{th} orbital energy if it is assumed that the total wavefunction describing the final ionised state is precisely equal to the initial state wavefunction minus those terms associated with the k^{th} orbital electron. This is Koopmans' frozen orbital approximation (23) in which it is assumed that the photoemission process is so fast that the outgoing photoelectron is unaffected by any rearrangement of the remaining electrons in response to the suddenly created photohole. This simplified form of Koopmans' theorem does not account for the various couplings of spin and orbital angular momenta in the final state (section 1.10).

In reality, electronic relaxation does occur within the time scale of photoelectron ejection and its effect upon the magnitude of an orbital binding energy is quite considerable.The relaxation response is brought about by the removal of the k^{th} active electron which alters the effective potential experienced by the remaining passive electrons. This electron distribution rearranges or relaxes towards and around the k hole with the effect of increasing both the Coulombic and Exchange interaction energy. This screening response therefore increases the total energy of the final state relative to the Koopmans' theorem value. $E_b(k)$ is thus lowered and, in fact, relaxation energy generally lies in the range of 1-10% of the orbital binding energy involved. In free atoms, screening of the photohole can involve inner-shell, intra-shell and outer-shell relaxation with the latter term being the largest contributor (24). In condensed phases the additional effect of extra-atomic relaxation is extremely important (25).

Theoretical calculations which attempt to accurately determine absolute orbital binding energies must, therefore, account for the relaxation energy in addition to correcting for any differences in correlation and relativistic energy between the initial and final states. However, there will always be a major cancellation of relaxation terms in chemical shift calculations where a difference in binding energy is being determined. Correlation and relativistic corrections are unlikely to show significant variation for an element in a series of its compounds, and thus can essentially be ignored in such calculations.

In the case of solid materials such calculations have been mainly of the approximate semi-empirical type. Those methods which are based on Koopmans' theorem have enjoyed only limited success (7, 26-28). As one might expect, at least in principle, calculations which take account of relaxation energy generally give a better agreement with experimental results (26, 29-31).

As a result of orbital relaxation in the final state, photoemission is an inherently many-electron process and not a purely one-electron transition, the latter being implicit in the frozen orbital approach. Furthermore, although photoelectron spectra are often interpreted in terms of the electronic structure of the initial state (i.e. Koopmans' theorem), it should now be realised that each primary feature actually corresponds to a distinct electronic state of the final ionised system. All photoelectron spectra should, therefore, be interpreted on this basis. This can be particularly important in valence studies since spectral interpretation based upon the Koopmans' theorem approach will wrongly predict the order of valence energy levels in cases where there are sufficiently large differences in relaxation energy between the various orbitals.

1.7 Intensity

Information from a photoelectron spectrum is not only obtained by determining peak positions but also peak intensities, since the area under a peak is proportional to the number of corresponding atoms in the sample.

The simplest equation is where the number of photoelectrons with a specific energy, N_o, initially produced from atoms of type A is given by:-

$$N_o = \alpha n F \qquad (1.6)$$

where

α = photoelectron cross section or transition probability,

n = total number of atoms A per unit volume,

F = X-ray flux.

The photoelectron cross section α governs the relative intensity of core level peaks, and is a function of both the initial state orbital and the incident photon energy. This equation is, however, unsuitable for the case of a solid where the photoelectron flux originating from some point x below the surface is attenuated via inelastic scattering. Thus, ignoring any attenuation of the X-radiation as it penetrates into the solid, the number of photoelectrons reaching the surface for an infinitely thick homogeneous sample is:-

$$N_\infty = \int_0^\infty \alpha DF \exp(-x/\lambda).dx = \alpha DF\lambda \qquad (1.7)$$

where

D = density of atoms of type A in the solid,

λ = inelastic mean free path (section 1.7.1),

Thus the measured intensity of photoelectrons by the spectrometer is given by:-

$$I_\infty = k\alpha DF\lambda \qquad (1.8)$$

where

k = instrument response function.

This spectrometer factor is dependent upon the design of the particular instrument used and the type of analysis mode employed (chapter 2).

The measured intensity of photoelectrons emerging from a homogeneous sample film of thickness d is therefore:-

$$I_d = \int_0^d k\alpha DF \exp(-x/\lambda).dx$$

$$= \quad k\alpha DF\lambda\left(1-\exp(-d/\lambda)\right) \qquad (1.9)$$

It must be mentioned that the presence of satellites (section 1.10) complicates the situation by removing intensity from the primary peak, and thus the intensity discussed above applies to both primary peak plus satellites.

Photoelectron intensities are thus dependent on a number of important factors and appropriate expressions have been derived for different types of solid sample (32,33). Most XPS studies do not, however, attempt to use these "ideal" expressions to quantify experimental results. The relative photoelectron peak area ratios of the various chemical species are normally reported since this data is easy to obtain and does provide very useful information.

1.7.1 The Mean Escape Depth

Inelastic scattering in solids occurs mainly via electron-electron mechanisms although scattering via electron-plasmon (section 1.10.5) and electron-phonon processes can be important. The inelastic mean free path λ, which is alternatively known as the mean escape depth or electron attenuation length, represents the depth from which (1-1/e) of the photoelectrons produced there can escape from the solid without suffering any energy loss. λ is not only a property of the material through which the electrons are travelling but is also a function of electron kinetic energy (34-36). The dependence of λ on the latter factor has been shown to follow a universal curve (36) which is shown in fig 1.4 (this is a log-log plot), and it can be seen that surface sensitivity is at a maximum in the 30-100eV kinetic energy range. Finally, it can be shown from equation (1.9) that 95% of the total measured signal derives from a depth equal to 3λ and hence this is a reasonable estimate of the effective sampling depth.

1.7.2 Effect of Angular Variation

Equation (1.9) has not taken account of the dependence of the effective sampling depth upon the angle of the sample surface with respect to the analyser entrance. Fig 1.5 illustrates how the thickness d of the sample studied varies with the angle of emergence of the photoelectrons ϑ, and shows that d actually represents a depth of d sin ϑ below the sample surface.

Thus equation (1.9) can be suitably modified such that:-

$$I_d = k\alpha DF\lambda\left(1-\exp(-d\sin\vartheta/\lambda)\right) \qquad (1.10)$$

The use of angular variation to enhance the surface sensitivity of XPS has been employed both qualitatively and quantitatively to examine the distribution of chemical species in surface layers (37-41). The effects of surface roughness must be considered in any attempt to quantify results (38,42). It is interesting to note that surface sensitivity enhancement depends also upon the angle of X-ray incidence (43). The use of a grazing angle in this case results in X-ray refraction and reflection effects which leads to preferential photoemission from atoms in the immediate surface layers.

1.8 Nature of the X-Radiation

X-rays are normally generated by bombarding a suitable target with high energy electrons. Holes formed in the inner levels of the target atoms are then filled via electronic transitions from higher lying levels resulting in the emission of X-rays. There are normally a number of X-ray lines associated with each target material in addition to a continuous background of Bremsstrahlung radiation.

The choice of X-ray source, which is subject to practical viability, is based upon the ideal requirement for a single, intense, monochromatic X-ray line. In the case of achromatic X-rays the practical limiting factor for photoelectron peak resolution is the intrinsic width of the emitted radiation which is determined, from the Heisenberg uncertainty principle, by the lifetime of the final ion state. The X-ray sources which are most commonly available are given in table 1.1.

Magnesium and aluminium are the most commonly used X-ray source materials in XPS studies, although sodium and silicon have been used to some extent. The X-ray spectrum associated with each of these second row elements is dominated by the very intense, unresolved $K\alpha_{1,2}$ doublet which results from $2p_{3/2} \rightarrow 1s$ and $2p_{1/2} \rightarrow 1s$ transitions in singly ionised atoms. The $K\alpha_{1,2}$ linewidth increases with increasing atomic number because of the larger 2p spin-orbit splitting and decreasing 1s hole lifetime. There are a number of accompanying satellite lines which arise from valence band→1s transitions, and from transitions which occur in multiply ionised atoms. Ultra-soft $M\zeta$ X-rays ($4p_{3/2} \rightarrow 3d_{5/2}$ transition) from yttrium and zirconium have also been used, to a much lesser degree, in XPS studies (44-46).

The monochromatisation of X-rays has been used to achieve narrower excitation sources in addition to eliminating satellite lines and Bremsstrahlung radiation (7,47). Unfortunately this results in a serious loss of incident photon intensity which must be compensated for by using very high intensity X-ray sources and/or special detection equipment (7,47).

1.9 Linewidths and Resolution

The photoelectron peak width, which is usually defined as the full width at half maximum (FWHM), is a convolution of the width of the exciting X-ray line, the inherent width of the core level, and instrumental contributions. The first factor has already been dealt with in section 1.8.

The natural linewidth of an energy level is governed by the uncertainty principle:-

$$\Delta E = \frac{h}{\tau} \qquad (1.11)$$

where

ΔE = linewidth,

τ = final ion state lifetime (secs), h = Planck's constant.

The lifetime of the final state is thus dependent on those processes involved in the decay of the core hole. Hole decay by X-ray fluorescence and Auger electron emission has already been discussed (section 1.3). A third important mechanism, which has a substantial broadening effect on many photoelectron linewidths, is the very fast Coster-Kronig process (48-50). This is a special type of Auger event where one of the holes in the doubly charged final state is located in the same principal shell as was the initial vacancy. Core hole lifetimes are also dependent on the chemical environment of the atom concerned. For example, it has been shown that the probability of a relevant Auger process for hole decay increases with increasing electron density on the atom in question (51). Vibrational broadening is another important effect (52,53) in cases where the involvement of valence electrons in final state relaxation gives rise to significant differences in internuclear separation between the initial and final state. Although important in most polar solids, phonon broadening is expected to be small in the case of metals where relaxation via conduction electrons normally results in little difference between the initial and final state vibrational manifolds. Another factor is the charging effect for non-conductors where photoelectron linewidths are broadened by a small distribution of charge over the sample surface (54).

As was stated earlier, one of the practical difficulties in the development of XPS was the problem of analyser resolution. Resolving power (P) is defined as:-

$$P = \frac{\text{Electron Energy}}{\text{FWHM}} = \frac{E}{\Delta E} \qquad (1.12)$$

Thus, for a constant resolving power, the FWHM will increase as the photoelectron kinetic energy increases. Resolution is not only a function of the particular type of analyser used, but is also dependent on the analyser mode employed (chapter 2).

1.10 Additional Features in the Photoelectron Spectrum

As indicated earlier, a photoelectron spectrum is not simply composed of one peak per energy level for all the elements present in the sample being studied. The presence of chemically shifted photoelectron peaks and Auger peaks has already been discussed. Photoelectrons which have undergone inelastic scattering emerge from the sample with a kinetic energy which is lower than that of the "no-loss" photoelectrons, and give rise to a background of secondary electrons which appear on the higher binding energy side of the primary peak. The use of achromatic X-rays results, as already stated, in the appearance of X-radiation satellite peaks (chapter 2) in addition to a general background to the lower binding energy side of the primary peak, due to Bremsstrahlung radiation. Another less important source of additional structure can arise from excitation via impurity X-ray lines (see chapter 2).

1.10.1 Spin-Orbit Splitting

Spin-orbit splitting of core levels with an angular momentum quantum number $l > 0$ is essentially a final state effect in the photoemission process. Emission of an electron from a closed shell system, to produce a final state that is open shell, gives rise to two final state total energies. This is due to spin-orbit interaction (which averages to zero in a closed shell system) in which the intrinsic spin of the unpaired electron in the core hole state couples to the orbital angular momentum to produce two states characterised by the quantum number $J = L + S$. Thus, depending on the magnitude of the splitting, all p,d and f orbitals will give rise to a doublet in the photoelectron spectrum. The multiplicity of the two j states and thus the relative intensity of the photoelectron peaks is given by $2J+1$.

1.10.2 Multiplet Splitting

This is also known as exchange or electrostatic splitting and occurs in systems where a valence shell(s) is only partially occupied. Ionisation of a core electron will therefore give rise to more than one final state, due to the coupling of the remaining unpaired core electron with the unpaired electrons in the valence shell(s).

An example is the Mn 3s spectrum from MnF_2 (55) in which the Mn^{2+} has 5 unpaired d electrons (all coupled in parallel). The final state for 3s photoemission ($3s^1 3p^6 3d^5$) can be either a ^7S or ^5S state, depending on whether the remaining 3s electron has its spin parallel to (^7S) or antiparallel to (^5S) the d electrons. Thus the 3s photoelectron signal is expected to be a doublet. Actually, in this case, there is more than one peak associated with the final ^5S state due to configuration interaction (section 1.10.3). Multiplet splitting for core levels with $l > 0$ gives rise to more complex structure because of the additional effect of orbital angular momentum coupling (56).

1.10.3 Configuration Interaction Satellites

It is clear that the primary or main photoelectron peak associated with a particular energy level, corresponds to the primary or ground electronic final state generated in the photoemission process. Satellite lines correspond to final states which are excited relative to the primary ion state, and consequently such peaks appear on the higher binding energy side of the primary peak.

Satellite processes are often discussed in terms of the "shake-up" formalism, in which the primary photoemission event is accompanied by a simultaneous transition of a second electron into a higher bound state (i.e. normally a valence level excitation). The excitation of the second electron into an unbound continuum state ("shake-off") does not normally give rise to discrete satellite structure and will not be considered further. Although two-electron transitions are by far the most likely type of "shake-up" to occur, three-electron transitions are weakly probable (57). Satellite intensities are normally much lower than that of the primary peak but can be used in conjunction with peak positions to identify chemical species.

Considerable satellite structure has been observed in a wide variety of chemical systems. Unsaturated organic complexes have shown satellites of appreciable intensity due to $\pi \rightarrow \pi^*$ transitions (58). Very intense satellite lines have been observed for certain transition metal and rare earth compounds which have unfilled 3d or 4f shells respectively (59-62). The satellite intensities and positions have been shown to be strongly dependent on chemical state, and have been interpreted in terms of ligand-to-metal charge transfer processes. For example, the 3d spectra of La_2O_3 and CeO_2 show satellite structures with intensities comparable to the primary peaks, and these satellites are attributed to charge transfer from oxygen to metal (63). Frost (59) has shown that Cu^{2+} ($3d^9$) ions exhibit satellites whereas Cu^+ ($3d^{10}$) ions do not. This is immediately explained on the basis of the closed 3d shell in the Cu^+ state, and illustrates the use of "shake-up" satellites to distinguish between different chemical states (64,65). The interpretation of satellites can be especially complicated in the case of open-shell systems due to the additional effects of multiplet splitting. The "shake-up" approach is a conveniently simple, but rather poor model for the interpretation of satellite processes, which are more correctly described in terms of the configuration interaction formalism (66-71).

Configuration interaction (CI) is the quantum mechanical mixing of different one-electron configurations to account for instantaneous electron correlation in many-electron systems. The process is illustrated for the ground state of Neon which is normally regarded in terms of the single one-electron configuration $1s^2 2s^2 2p^6$. Barr (32) has shown that a more realistic wavefunction Ψ(tot) is achieved by admixing a large number of additional, albeit less important, one-electron basis states such that:-

$$\Psi(\text{tot}) = a1(1s^2 2s^2 2p^6) + a2(1s^2 2s^1 2p^6 3s^1) + a3(1s^2 2s^2 2p^5 3p^1) + a4(1s^2 2s^2 2p^4 4p^2) \text{ ....etc}$$

where the coefficient a1 is almost unity.

Using this approach, satellite processes can be adequately explained by strong configuration interaction in the array of possible final states (FSCI) created by the photoemission process. It will be shown that initial state configuration interaction (ISCI) can actually be of equal importance. The rich satellite structure, accompanying the Neon 1s primary photoemission signal, has been successfully interpreted using the CI model (68) and will be used to illustrate the process.

Fig 1.6 shows the eigenstates for the initial state and the two final states, corresponding to the primary peak and the first satellite. In the "shake-up" formalism, this satellite corresponds to a single 2p → 3p excitation accompanying the primary photoemission event. For simplicity, exchange coupling is ignored and only two one-electron basis states are shown for each eigenstate. The process giving rise to both the primary peak and the first satellite is a one-step, one-electron (i.e considering only the active electron) transition, between the corresponding admixed basis configurations in the initial and final states. If FSCI alone is considered, then the primary peak and the first satellite would arise from paths A and B respectively. The inclusion of ISCI has little effect on the primary peak intensity because path D is extremely weak, but since paths B and C are of equal strength, the calculated satellite intensity is doubled via ISCI. This agrees well with experiment and underlines the importance of ISCI in any attempt to accurately quantify satellite intensities in general. ISCI can also be important in allowing satellite transitions which would otherwise be forbidden (71).

The CI formalism confirms the charge transfer origin of satellites in the transition metal and rare-earth compounds mentioned above, with such processes being attributed to strong FSCI effects.

1.10.4 Core-Line Asymmetry

In solid metals and conductors in general, the form of the density-of-states curve above the Fermi energy provides a continuous range of allowable excitations, analogous to the satellite processes discussed in section 1.10.3. Instead of producing a set of discrete satellite lines, this situation leads to an asymmetric tailing of the primary photoemission peak (72-75). The process is often referred to as "conduction band interaction" and the associated lineshapes of many metal core levels have been well represented by the Doniach-Sunjic function (74). Wertheim (73) has futher demonstrated the particular importance in accounting for core-line asymmetry in any quantitative analysis, and this aspect will be discussed in chapter 4.

1.10.5 Plasmons

Another important energy-loss process, which can occur in solid conductors, is via an extrinsic plasmon excitation in which a quantised mode of collective oscillation of the conduction electron sea is excited by a photoelectron travelling through the solid matrix. Such energy losses correspond to either bulk or surface plasmons, depending on whether the excitation takes place during step 2) or 3) in the three-step model for photoemission (section 1.4). If the characteristic frequencies of the bulk and surface plasmons are given by ω_b and ω_s respectively, then the corresponding single plasmon energy losses are given by $h\omega_b$ and $h\omega_s$. Since photoelectrons can undergo several sequential bulk and/or surface losses, observed plasmon structure normally consists of a series of discrete peaks which, of course, appear to the higher binding energy side of the primary photoemission line (76,77).

So far, only extrinsic plasmons have been considered, because there is still some uncertainty concerning the relative importance of intrinsic plasmon losses in general. The question seems to have been resolved in the case of some simple metals where intrinsic contributions are concluded to be very significant (78).

Table 1.1

Commonly Available X-radiation Sources

Element	Line	Energy(eV)	FWHM(eV)
Na	$K\alpha_{1,2}$	1041.0	0.4
Mg	$K\alpha_{1,2}$	1253.6	0.7
Al	$K\alpha_{1,2}$	1486.6	0.85
Si	$K\alpha_{1,2}$	1739.5	1.0
Ti	$K\alpha_{1}$	4510.0	2.0
Cr	$K\alpha_{1}$	5417.0	2.1
Cu	$K\alpha_{1}$	8048.0	2.6
Y	$M\zeta$	132.3	0.47
Zr	$M\zeta$	151.4	0.77

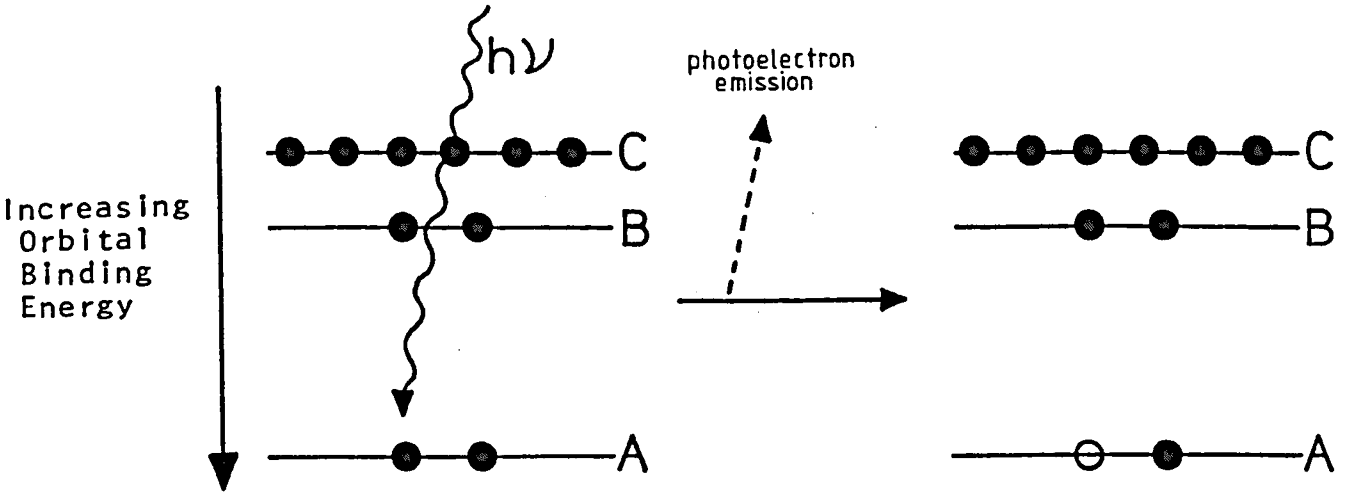

(a) Initial neutral state prior to primary photoemission.

(b) Singly ionised state with primary core vacancy.

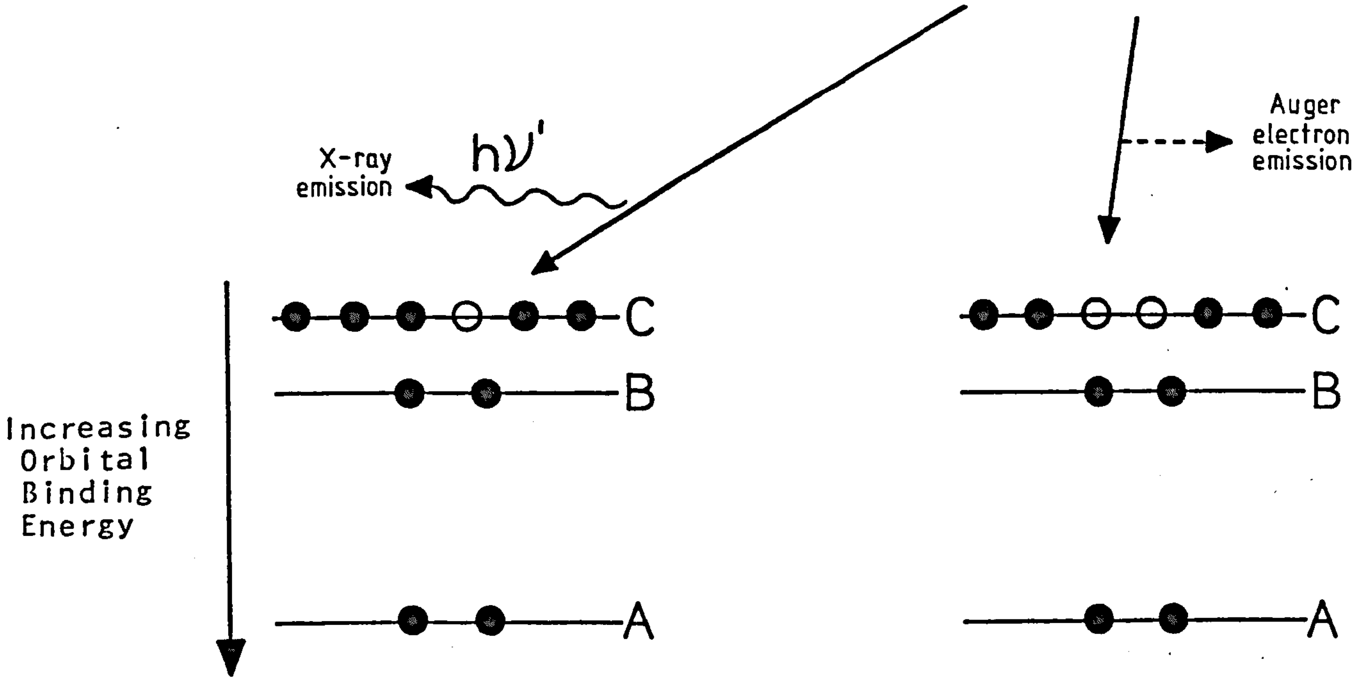

(c) Singly ionised final state after X-ray emission.

(d) Doubly ionised final state after Auger electron emission.

Fig 1.1:- Two important processes accompanying photoelectron emission.

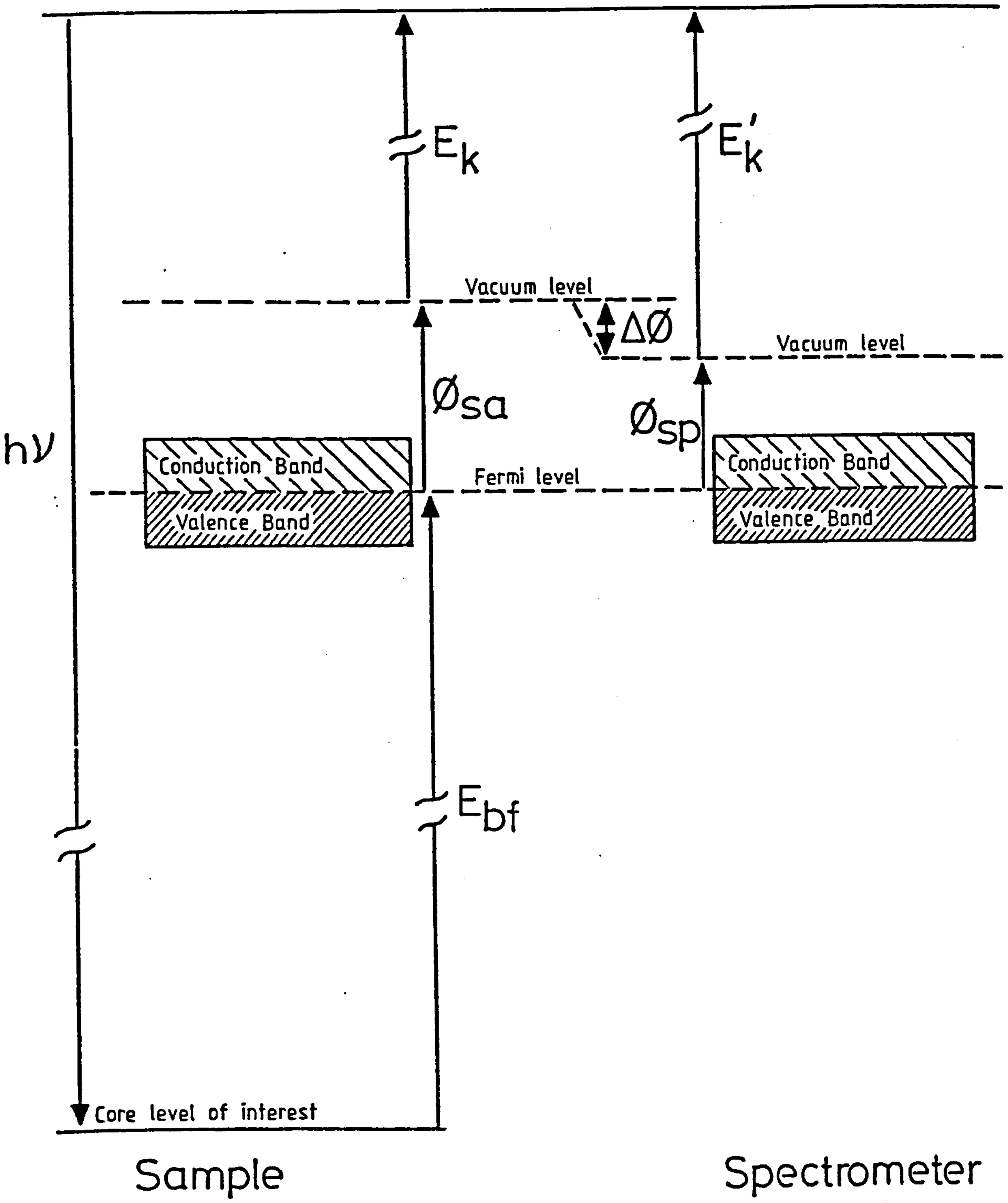

Fig 1.2:- Energy level diagram for an electrically conducting solid in contact with the spectrometer.

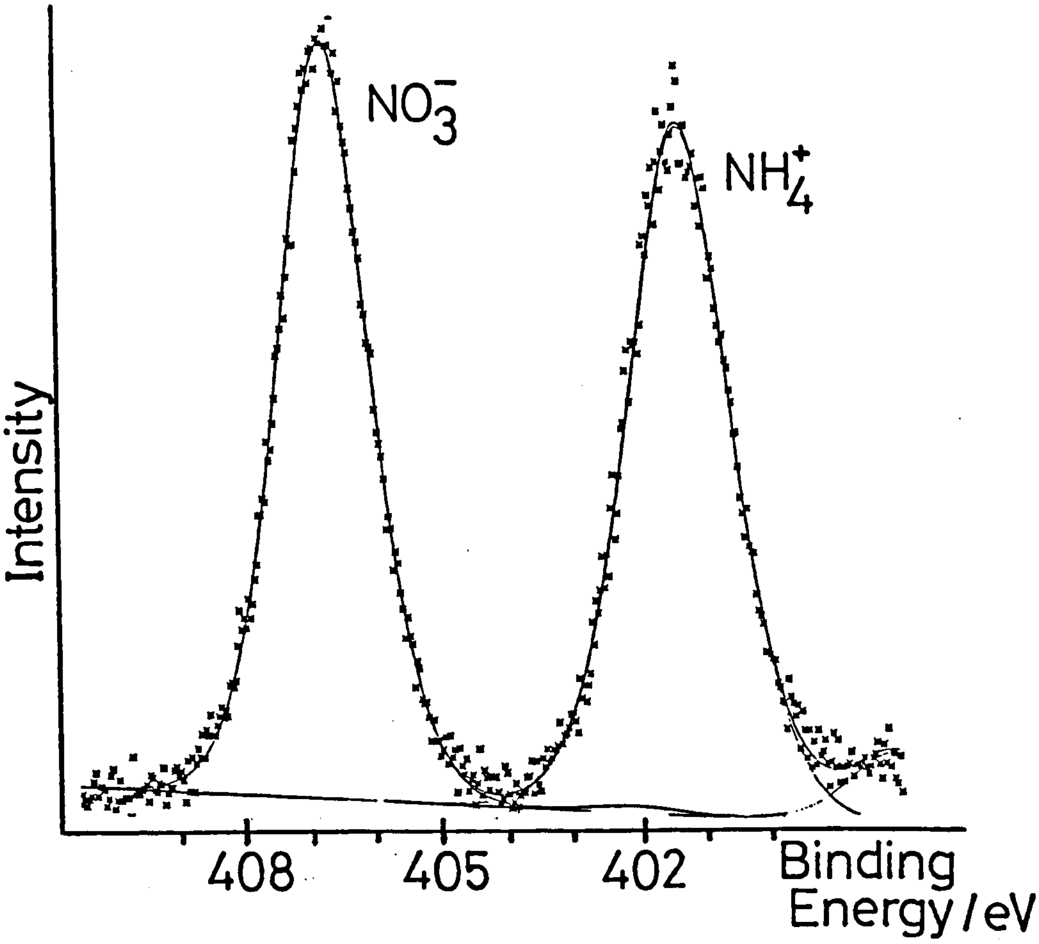

Fig1.3:- The chemical shift effect in the N1s core level region for NH_4NO_3.

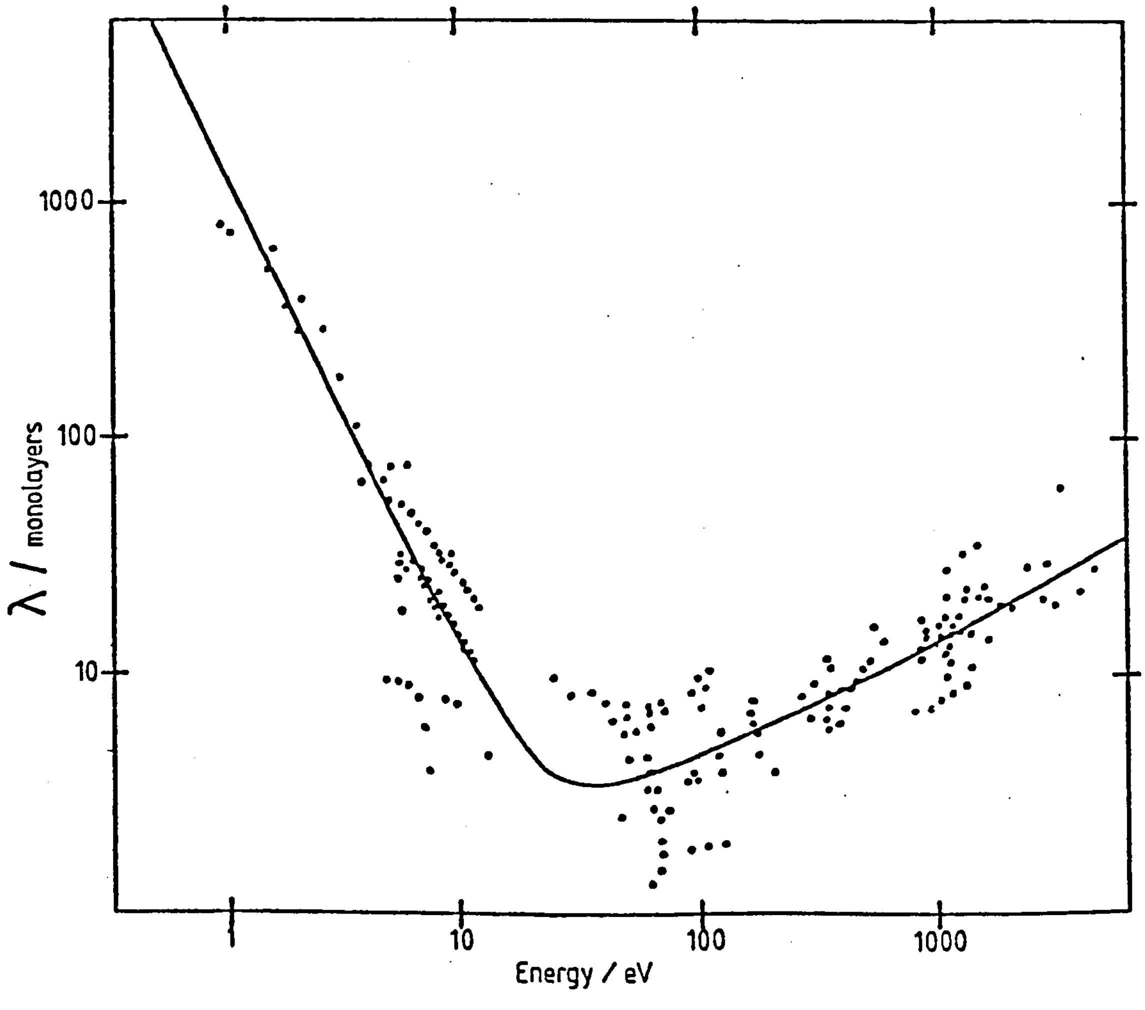

Fig1.4:- The dependence of IMFP upon electron energy.

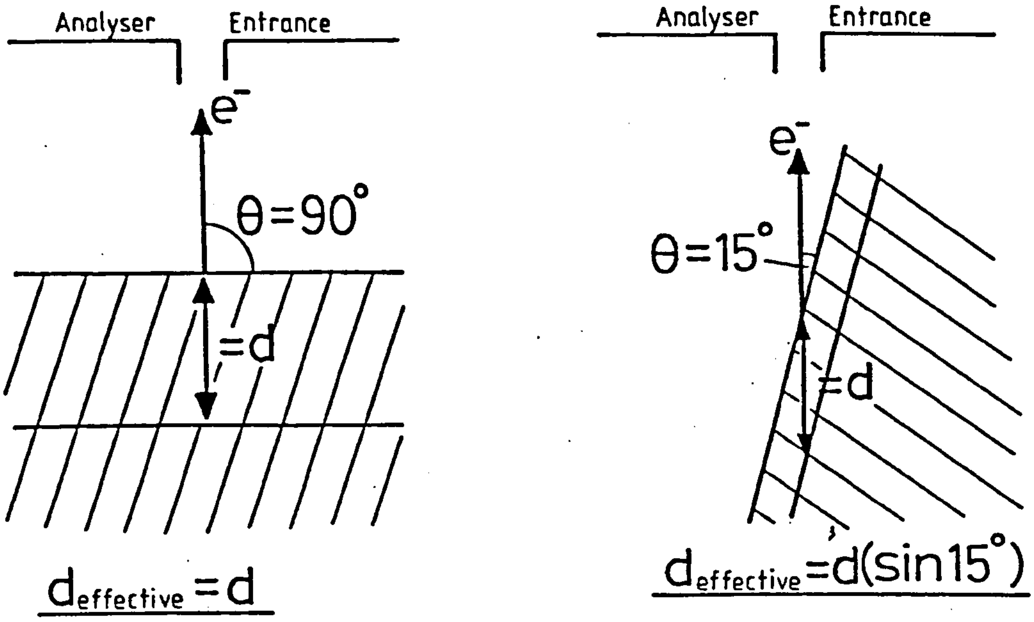

a) bulk sensitive angle.

b) surface sensitive angle.

Fig1.5:- Principle of angular dependence in XPS.

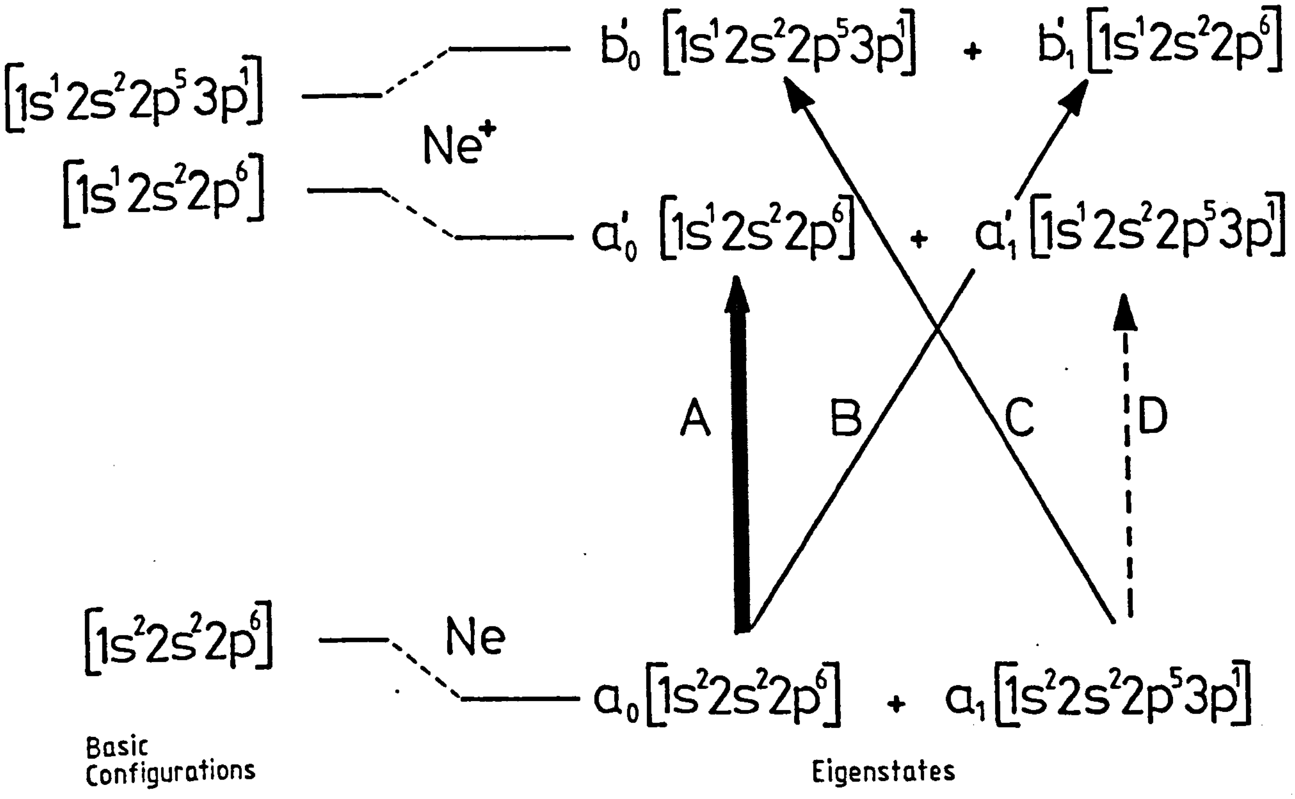

Fig1.6:- Simple model to illustrate the effect of initial and final state configuration interaction in Ne 1s photoemission.

$a_0, a'_0, b'_0 \sim 1$

$a_1, a'_1, b'_1 \sim 0.1$

CHAPTER TWO

EXPERIMENTAL

2.1 The Spectrometer

All XPS spectra were recorded on a Kratos (AEI) ES200B X-ray photoelectron spectrometer. The principle of operation of this instrument is schematically shown in fig 2.1. This diagram illustrates the three basic stages of operation:-

1) Ejection of electrons via a high intensity X-ray source.
2) Electron energy analysis.
3) Electron detection.

2.1.1 The Vacuum System

Before considering each of the above components in more detail, it is necessary to discuss the need for an ultra-high vacuum in the spectrometer. Firstly, this reduces the possibility of photoelectrons being scattered by gas molecules as they are travelling from the sample, through the analyser, to the detector. Such collisions become important at system pressures above 10^{-5} torr. Secondly, the adsorption of gaseous material on the sample surface is considerably reduced. Even at the low pressures used in typical XPS spectrometers, varying degrees of surface contamination are normally present. Those gases which have a high sticking probability (e.g. H_2O, O_2) present much more of a problem than those materials which are relatively inert (e.g. Ar, N_2).

The spectrometer operating pressure, for this work, was approximately 10^{-8} torr. The instrument is equipped with separate oil diffusion pumps on the sample chamber, the analyser, and the X-ray gun chamber. These pumps, each possessing a liquid nitrogen trap, are backed by rotary pumps. The main disadvantage of this system lies in the use of organic fluids in both types of pump which results in hydrocarbon contamination of the sample surface. However, the diffusion pumps are equipped with water and thermoelectrically cooled chevron baffle units to prevent the backstreaming of oil vapour into the system. Molecular sieves, located between the diffusion and rotary pumps, are used to trap oil vapour backstreaming from the rotary pumps. This pumping scheme is advantageous in that it is relatively inexpensive and has the ability to pump a variety of gases efficiently over long periods of time.

2.1.2 The X-ray Source

All XPS spectra were recorded using unmonochromatised Mg $K\alpha_{1,2}$ radiation which results in a series of X-radiation satellites accompanying the primary exciting line. The photon energies and relative intensities of all the important lines are given in table 2.1.

The X-ray gun consists of a water-cooled magnesium-coated copper anode (+12kV) from which X-rays are generated via bombardment with electrons produced from a hot tungsten filament held at ground potential. Most of the spectra were recorded with an X-ray power of 240 watts.

A thin aluminium window separates the X-ray gun from the sample chamber. This prevents bombardment of the sample by electrons from the X-ray gun chamber, in addition to absorbing much of the Bremsstrahlung radiation. Unfortunately, small amounts of Al X-radiation are produced from the window and the various line positions and intensities of such features are given in table 2.1. This did not present much of a problem for the work described in this thesis, although weak peaks due to Al $K\alpha_{1,2}$ radiation, were occasionally observed.

Finally, it is important to note that impurity Cu radiation can be generated by electron bombardment of the copper backing of worn or defective X-ray targets (79). Under the conditions normally used for Mg X-ray generation, Cu $L\alpha$ radiation ($h\nu$ = 929.7eV) is the most intense line and the associated XPS peaks were observed, at one stage, in this work.

2.1.3 The Electron Energy Analyser and Detector

The energy analysis of photoelectrons in the ES200B spectrometer is accomplished using a hemispherical electrostatic dispersive analyser (fig 2.1). For such a system, the resolving power (P) is defined as:-

$$P = \frac{E}{\Delta E} = \frac{2R}{W} \qquad (2.1)$$

where R = mean radius of the hemispherical analyser, W = collector slit width.

This equation shows that the resolving power increases if the radii of the hemispheres are increased. This situation is, however, undesirable since the use of large hemispheres results in a greater analyser volume to be evacuated, in addition to the increased material and machining costs. This problem is generally overcome by using small radius hemispheres and retarding the electrons in the lens system which focuses the image of the source slit onto the analyser entrance.

This is the basis of the Fixed Retardation Ratio (FRR) mode, in which all electrons are retarded to 1/23 of their original energy in the lens system, and spectra are obtained by scanning the voltages applied to the analyser. Thus, for a constant resolving power, ΔE will vary across a spectrum since $E/\Delta E$ is a constant.

The main disadvantage of the FRR mode is the loss of sensitivity at low photoelectron kinetic energies since such electrons have a very low kinetic energy after retardation. This is because the analyser sensitivity increases with increasing electron kinetic energy. This problem can be overcome by using the Fixed Analyser Transmission (FAT) mode in which the lens potential is scanned whilst the analyser voltages are kept constant. All electrons enter the analyser with the same kinetic energy and hence the sensitivity is the same for all the electrons. Furthermore, in this mode, ΔE is a constant across the spectrum. On the other hand the slits can be increased in size to enhance sensitivity in the FRR mode, and still have the same resolution as the narrower slit FAT spectrum at low photoelectron kinetic energies.

The FRR mode was used exclusively for the work described in this thesis since all the photoelectron kinetic energies involved were in the range 700-1250eV. Electrons were detected using an electron multiplier which counts electrons with high efficiency down to very low kinetic energies.

2.2 Sample Mounting and Insertion

The insertion of samples into the spectrometer was achieved using three types of probe. In all cases, samples were mounted such that no part of the sample supporting block was exposed to the X-ray flux.

1) Standard insertion lock probe (SILP, 80).

The use of the SILP allowed samples to be inserted into the spectrometer without letting up the sample chamber to atmospheric pressure. Sample introduction was therefore very rapid and the operating pressure was quickly achieved. The probe tip itself consisted of a small rectangular copper block onto which samples were mounted (*vide infra*). The SILP was capable of resistively heating the sample up to 400°C or cooling to very low temperatures by pumping liquid nitrogen to the sample block.

2) High temperature probe (HTP).

Most of the high temperature work was carried out using the

HTP which allowed samples to be heated to 600°C via a radiating filament process. The HTP was bolted directly onto the sample chamber and it was therefore necessary to let the instrument up to atmospheric pressure in order to change samples. The probe was equipped with a suitable calibrated angular scale to allow accurate angular variation studies to be carried out (section 1.7.2).

3) Fixed angle heatable probe (FAHP).

Similar to the HTP, the FAHP was bolted directly onto the sample chamber but was only capable of resistively heating samples up to 450°C. Unlike the other two probes, the FAHP did not allow angular variation of the sample.

The samples studied in this work, all of which were solid, were either in the form of a thin metallic sheet or a powder. The first type of sample was easily mounted by simply cutting the metal sheets into small strips, of appropriate size, and screwing or clipping them onto the sample probe. A range of methods are generally used to mount powder samples and several of these were investigated with the aim of choosing one which was most suitable for the samples examined in this work.

The following powder techniques were used:-

a) Powders were pressed onto a strip of double-sided sellotape which was directly stuck onto the sample supporting block.

b) Samples were meshed into a metallic gauze which was screwed onto the sample supporting block.

c) Powders were compressed into the form of a disc similar to those used in infra-red spectroscopy. The disc was then cut into the appropriate shape and mounted onto the probe tip via double-sided sellotape or araldite.

d) Powders were directly pressed onto a layer of araldite which was placed on a strip of metal foil interspersed between it and the sample supporting block. The araldite used in methods c) and d) was always mixed with metallic paint to give good electrical conductivity.

e) Powders were pressed into indium foil which was screwed onto the probe tip.

The specific features and problems of all the above methods, with respect to the samples studied in this work, are discussed in detail in chapter 3.

2.3 Ion Etching

In situ cleaning of samples was achieved via Argon ion bombardment of the surface at a gas pressure in the range of 10^{-3} to 10^{-4} torr. This was performed by using an Ion Tech B22 Saddle Field ion source operated at 5kV and 2mA. The etcher incorporated a mechanical scanning facility to enable a uniform etch of the sample surface.

Although ion etching can be used, in conjunction with XPS, for depth profiling, to study the distribution of chemical species in surface layers (41,81,82), its main use in this work, was as a surface cleaning technique. The interaction of an ion beam with a solid surface is often complex and can led to irregular sputtering effects, ion implantation and chemical transformations (83,84).

2.4 Data Acquisition

Spectral data were collected in both analogue and digital form. The digital collection mode has two main advantages over the analogue equivalent. Firstly, there is the effect of repeat scanning to improve signal-to-noise ratios which can be particularly important in the case of very weak signals. The alternative use of high time constants in analogue X-Y recorders can distort peak shapes and/or shift peaks from their true position. Secondly, digital data can be accurately analysed in a variety of ways in contrast to analogue spectra where analysis techniques are limited and very operator dependent. Analogue methods can be particularly inaccurate in the case of complex spectral envelopes. Computers, both main frame and microprocessor, are being increasingly used to analyse digital data and a number of methods were used in this work (section 2.5).

Despite the relative disadvantages of analogue data, such spectra were often recorded on a Hewlett-Packard 7005B X-Y recorder. These spectra were found to be useful as a monitor for any spectral changes which may have been occurring during digital collection. In many experiments, analogue spectra were also employed to quickly scan the various spectral regions prior to the use of the digital mode.

The digital mode consisted of the measurement of the number of electrons, in an energy range ΔE, arriving at the detector in a time T. The variables, T and ΔE, were selected such that most spectra gave approximately 30 points per electron-Volt (eV). An Apple II microcomputer was used to collect the data and allowed a continuous visual display on a TV monitor. The data was then stored on a floppy disc and transferred to the University main frame IBM 370/168 computer. Most of the data analysis was carried out on this computer although, towards the end of this work, some of these analysis techniques became available on a second Apple II microprocessor.

2.5 Data Analysis

Most of the spectra recorded in this work were analysed in considerable detail using a curve fitting program which is described below. Integral background subtraction, spectral smoothing and differentiation techniques were used (85) to some extent.

2.5.1 Curve Fitting

Curve fitting is essentially the process of taking a number of component peaks of chosen shape and varying their associated parameters to obtain the best overall agreement with the experimental data. Non-linear least squares fitting with a

Gaussian-Lorentzian product function incorporating tail parameters was used in this work (86,87). There are 7 parameters associated with each peak:-

1) Centre,
2) Height,
3) Width,
4) Gaussian-Lorentzian mixing ratio (GL),
5) Constant tail (CT),
6) Exponential tail (ET),
7) Constant/Exponential tail mixing ratio (TM).

There are also the linear background slope and intercept parameters for each spectrum. Thus for a spectrum consisting of n peaks, there are a total of 7n+2 parameters. The floating of all these parameters, in any attempted fit, is quite impossible in practice and, in all cases, a significant number of parameters had to be fixed.

The mathematical form of the fitting function is given in the references cited, and fig 2.2 shows the effect of varying the function mix (GL) and tail parameters for a single peak. Fig 2.2a shows the smooth transition from a predominantly Gaussian peak (GL = 0.1) to one which is purely Lorentzian (GL = 1.0). The incorporation of an exponential tail into the fitting function (fig 2.2b) is found to be suitable for representing asymmetric peak profiles which arise from conduction band interaction effects (section 1.10.4). As will be seen in chapter 4, a constant tail (fig 2.2c) was useful in approximating the inelastic background tails associated with photoelectron peaks.

A statistical measure of the quality of a curve fit on a particular spectrum is provided by the chi squared parameter χ^2 (86,87) such that:-

$$\chi^2(\text{calc}) = \sum_{i=1}^{n} \frac{\left(y_i(\text{meas}) - y_i(\text{calc})\right)^2}{y_i(\text{calc})} \qquad (2.2)$$

where y(meas) = experimental count rate,

y(calc) = curve fitted count rate,

n = number of points in the spectrum.

Although this 'goodness of fit' parameter is not really comparable between different spectra, it is meaningful to compare the change in χ^2 ($\Delta\chi^2$) from one fit to another on the same spectrum. This is vitally important in the case of particularly complex spectral envelopes which may result in various combinations of peaks adequately fitting the experimental data. The choice of 'best' or 'most correct' fit must consider both chemical and spectroscopic factors as well as the statistical significance of the fit. In cases where the 'best' single fit is not clearly defined, the implication of a number of different fits can be meaningful.

As previously stated, no attempt is made at Newcastle to monochromatise the X-ray source and the curve fitting program therefore contains the positions and relative intensities of the important satellites.

2.5.1.1 Effect of X-radiation Satellites

Despite their low relative intensities, the radiation satellites exerted a small but significant effect on the curve fitting of some of the principal K$\alpha_{1,2}$ photoelectron peaks. From fig 2.3a, which shows the 3d core level region for silver metal, a number of satellites can be clearly seen lying fairly close to the main Mg K$\alpha_{1,2}$ radiation lines. The curve fitting program assumes that the FWHM's of the primary peak and its associated satellites are equal. It is known, however, that the FWHM's of the satellites are, in fact, greater than that of the main X-ray peak (90). From this work, the Ag3d K$\alpha_{1,2}$ line (fig 2.3b, FWHM = 0.82eV) for silver metal is substantially narrower than the K$\alpha_{3,4}$ lines (fig 2.3c, FWHM = 1.15eV).

The process giving rise to the emission of X-rays has already been outlined in section 1.8. The main Mg K$\alpha_{1,2}$ line arises from transitions which occur within a singly ionised atom. The K$\alpha_{3,4}$ lines, which are the most important satellites in terms of their influence upon the primary peak shape, arise from transitions which occur within a doubly ionised atom. The intrinsic width of these satellites is expected to be greater than the main peak due to the shorter lifetime of the 1s hole state.

The inaccurate assumption, that all the X-ray lines have the same FWHM, meant that two sources of error were introduced into the curve fitting routine. Firstly, the optimisation of spectral peak shapes was significantly affected. For example, in the case of the Ir4f core level region for iridium metal, curve fitting with the satellites included gave an optimal peak shape (GL = 0.94) which was significantly different to that obtained with the satellites removed (GL = 0.78). This will be important in the detection of small spectral differences which may otherwise be overlooked (91). Secondly, problems may arise when the satellites associated with one principal ($K\alpha_{1,2}$) peak lie close to, or overlap with, another principal peak (see chapter 4). For example, in the case of the uranium 4f core region, the $K\alpha_{3,4}$ doublet corresponding to the $U4f_{5/2}$ level lies fairly close to the $U4f_{7/2}$ principal peak. In fact, for all U4f spectra recorded in this work, the error introduced by these satellites was small compared to the problems associated with the presence of a large inelastic background (see chapter 5). Serious problems will, of course, be expected in cases where the relative satellite intensities are greater.

Modifications to the curve fitting program are still in progress since the above factors affect some of the work carried out in this laboratory (91). However, for most of the work reported in this thesis, the radiation satellite errors had little effect on the curve fitting of spectra.

2.5.2 Other Techniques

Integral background removal, using Shirley's algorithm (85,88), was found to be very important for the accurate analysis of many spectra (chapter 4). The method assumes that at any point in the spectrum, the background intensity due to inelastically scattered electrons arises solely from the scattering of electrons at higher kinetic energy, and is therefore proportional to the integrated photoelectron intensity to higher kinetic energy.

Data smoothing, using the method of Proctor (89), proved to be very useful in cases where the spectrum signal-to-noise ratio was poor. The technique is based upon central point smoothing via a sliding least squares fit to a polynomial.

2.6 Infra-Red Studies

A small amount of infra-red work was carried out using two instruments.

1) Perkin-Elmer 598 spectrophotometer. Instrument slit widths of 1.5 cm^{-1} and 3.0 cm^{-1} were used.

2) Perkin-Elmer 125 spectrophotometer. Slit widths (1-3 cm^{-1}) were either set manually or controlled by a selected instrument program.

All samples were analysed as KBr or CsI discs.

Table 2.1

X-rays Produced from Magnesium and Aluminium Targets

	Magnesium			Aluminium		
X-ray Line	Energy	Relative Intensity		Energy	Relative Intensity	
$K\alpha_1$	1253.7	67	100	1486.7	67	100
$K\alpha_2$	1253.4	33		1486.3	33	
$K\alpha'$	1258.2	1.0		1492.3	1.0	
$K\alpha_3$	1262.1	9.2		1496.3	7.8	
$K\alpha_4$	1263.7	5.1		1498.2	3.3	
$K\alpha_5$	1271.0	0.8		1506.5	0.42	
$K\alpha_6$	1274.2	0.5		1510.1	0.28	
$K\beta$	1302	2		1557	2	

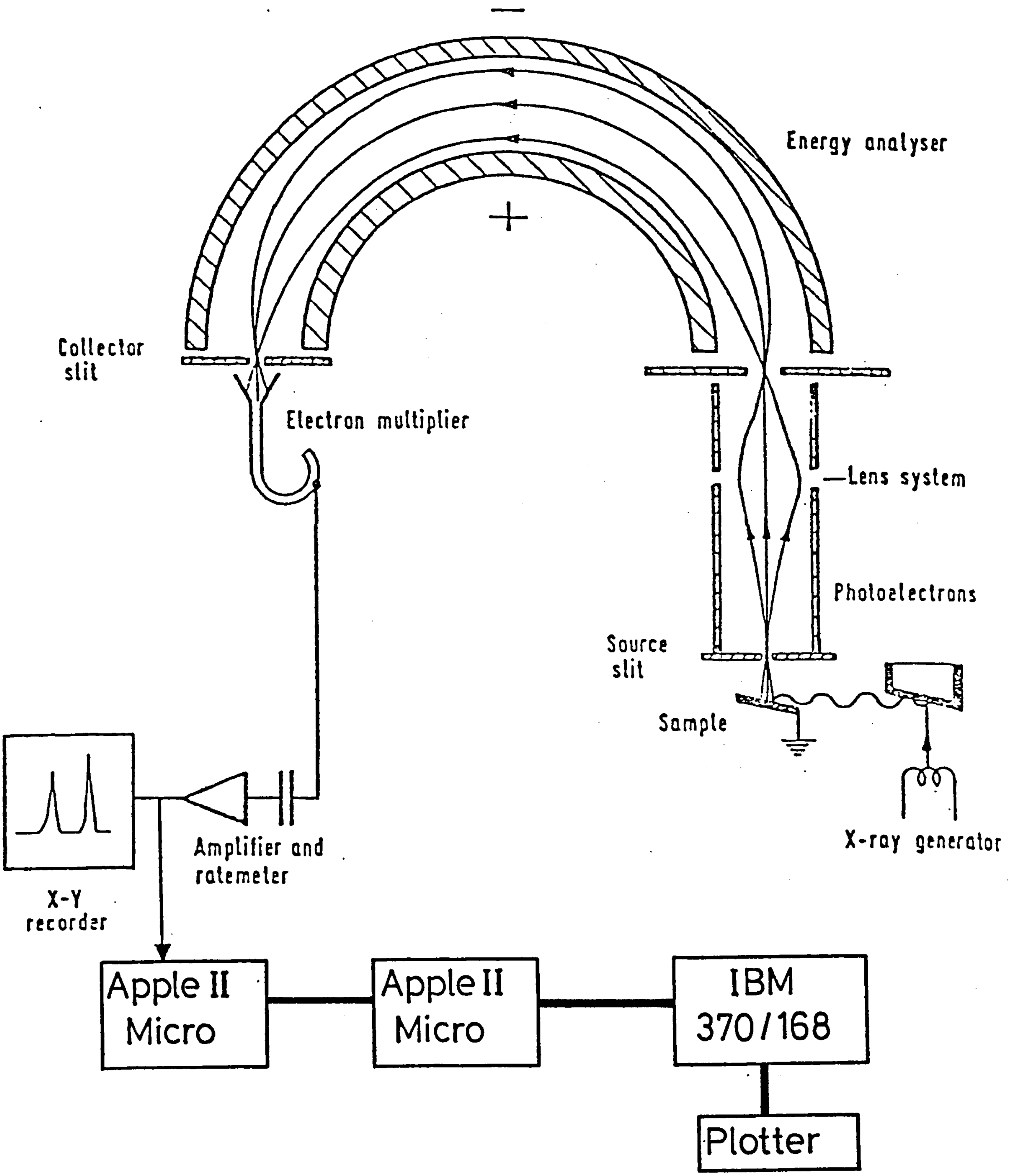

Fig2.1:- ES200B-Principle of Operation.

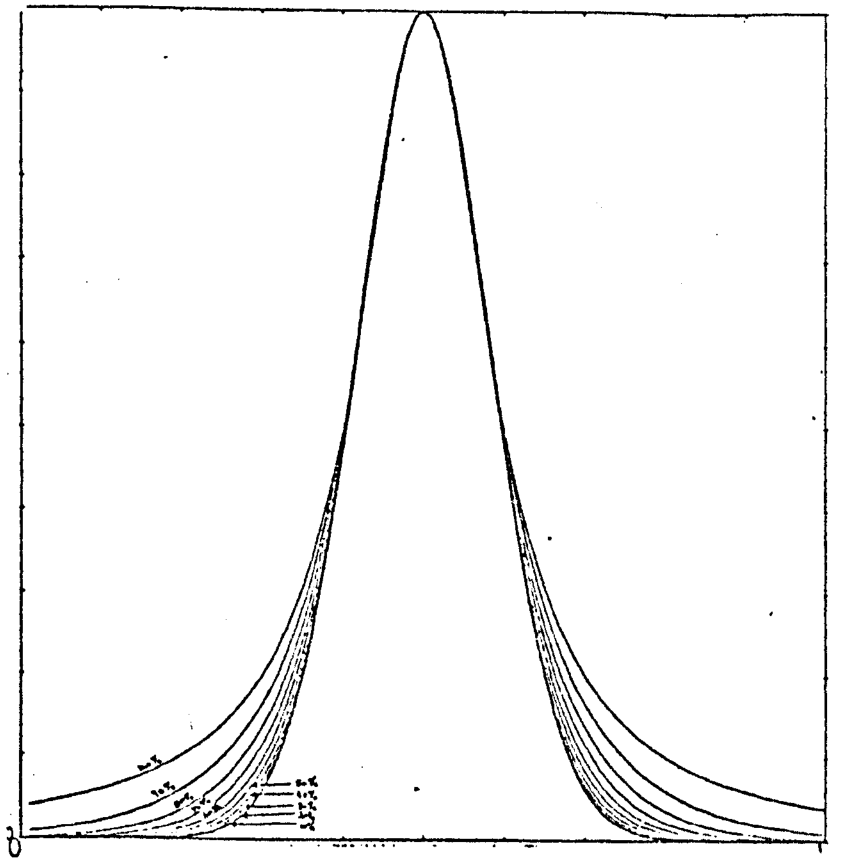

a) Variation of G/L mixing ratio in steps of 10% from 10 to 100% Lorentzian character.

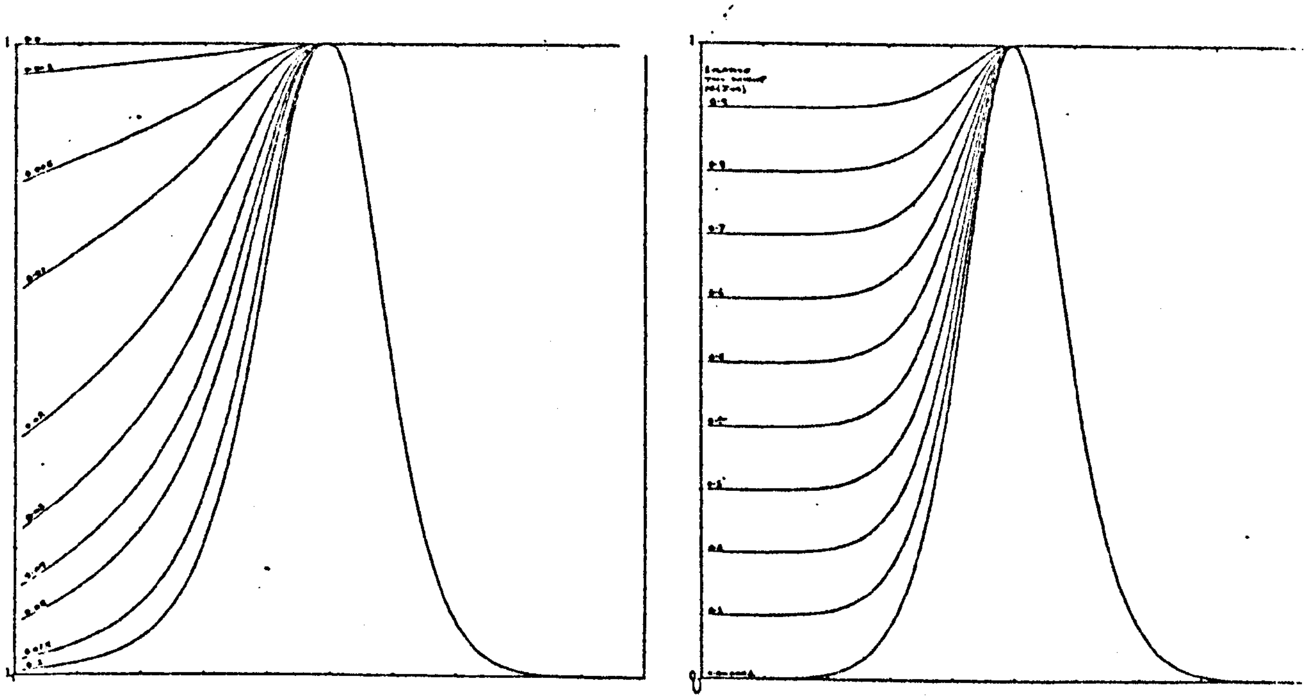

b) Variation of exponential tail.

c) Variation of constant tail.

Fig2.2:- Peak shape variation using a Gaussian/Lorentzian product function with associated tail parameters.

Fig 2.3:- Ag3d Spectrum showing X-Radiation Satellites accompanying the main Mg $K\alpha_{1,2}$ Line.

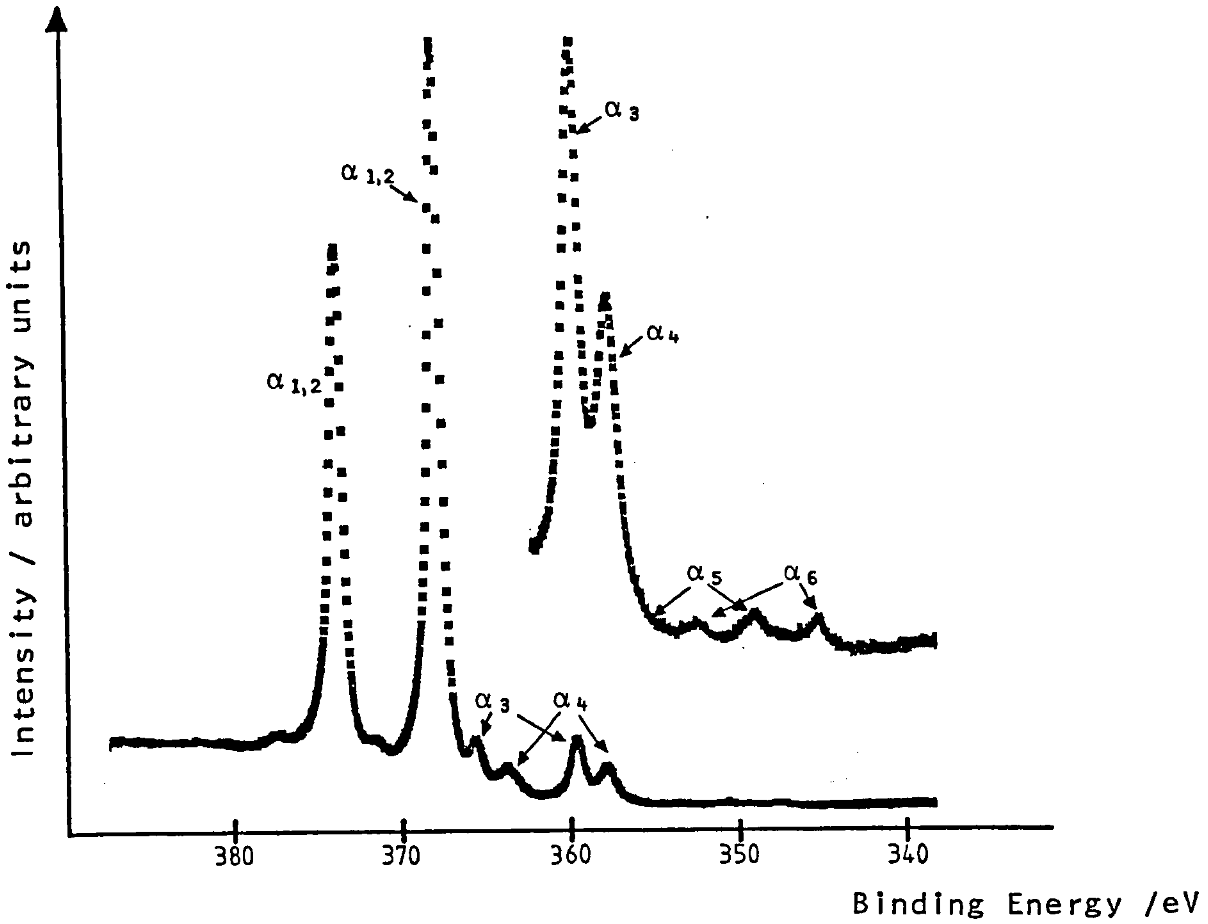

a) Wide Scan of Ag3d Spectrum. Inset shows the $K\alpha_{5,6}$ Satellites more clearly.

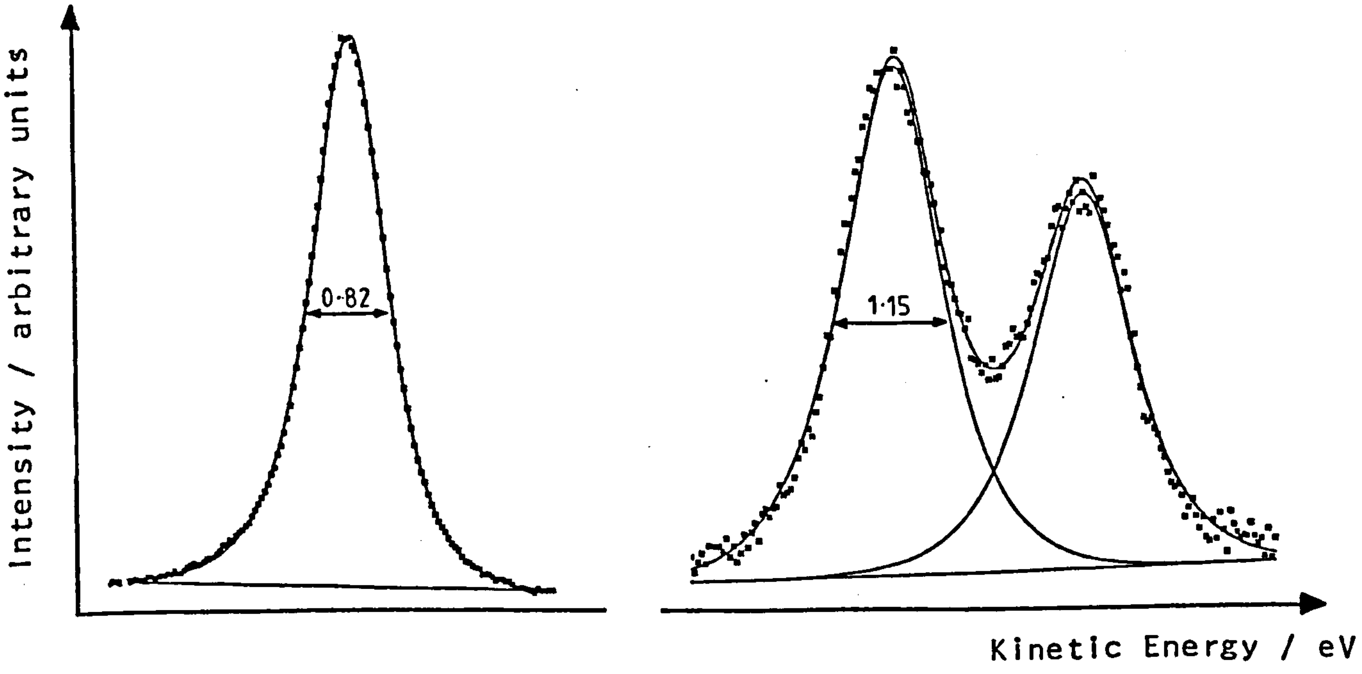

b) $K\alpha_{1,2}$ line for one of the Ag3d Spin-Orbit Components.

c) $K\alpha_{3,4}$ lines for one of the Ag3d Spin-Orbit Components.

CHAPTER THREE

SAMPLE CHARGING, MOUNTING and CALIBRATION

3.1 Sample Charging

As was previously stated (section 1.5.2), the direction and magnitude of non-conductor charging in XPS is dependent upon:-

1) the rate of photoelectron emission from the sample,
2) the secondary electron flux impinging upon the sample,
3) the conduction mechanism operating between the sample and earth.

The relative contributions of each of these competing processes is governed by a number of important experimental factors. Firstly, the resistance between the sample surface and earth must be considered. This depends, not only upon the resistance of the sample material itself, but also upon the additional resistance, if any, arising from the method by which the sample is mounted onto the spectrometer probe. It is important to realise that as the resistance between a sample surface and earth increases, the secondary electron flux plays an increasingly important role in determining the equilibrium value of the static surface charge.

Another factor to consider is the design of the instrument and its component parts. It is not surprising that surface charging is highly dependent upon the type of X-ray gun being used, in addition to the selection of its operational parameters.

These features affect both the rate of photoelectron loss from the sample surface and the number of secondary electrons produced. Surface charging problems are normally accentuated when using a monochromatic X-ray source rather than an achromatic one. This is because there is a significant reduction in the secondary electron flux due to the lower photon intensity and loss of the Bremsstrahlung radiation. Assuming that all other charging dependent variables are the same, reducing the incident X-radiation flux normally results in a reduction of the equilibrium positive charge on the sample surface.

The condition and type of X-ray gun window used also has a major influence on the magnitude of charging effects (92). Sample charging can also be altered simply by rotating the sample surface with respect to the X-ray beam and the analyser entrance slit (section 1.7.2).

Before going on to discuss sample mounting and calibration techniques in XPS, it is necessary to consider the phenomenon of differential charging. In general, non-conductors have a distribution of charge over their surfaces and the resultant effect on photoelectron spectra can be quite varied. A small charge distribution normally manifests itself in the broadening of photoelectron peak linewidths (93,94). More significant charge variations result in peak tailing (94) and in extreme cases, multiple peaks can be observed (95). Differential charging is not only a function of the properties of the sample material itself (95,96), but can also depend upon the method by which samples are mounted onto the spectrometer probe as discussed below (section 3.2). Furthermore, as was observed in this work, the application of a potential bias to powder samples normally results in the enhancement of differential charging effects.

3.2 Sample Mounting

It is important to briefly discuss the problems associated with the various methods of mounting powder samples on to the spectrometer probe. Several different powder materials, such as KCl, U_3O_8 and UO_3, were studied using a variety of techniques (see Chapter 2) with the aim of selecting the most appropriate one for the work discussed in this thesis.

Differential charging, on powder samples, was always expected to be present to some degree (i.e. peak broadening). This is because the charge will vary over the surface of the sample particles themselves irrespective of the mounting method used. This charge distribution is not only a function of the particle size but will depend significantly upon the particle shape (96). Indeed, even those samples which are composed of very small particles are expected to show some degree of surface charge variation since the particles are, of course, very large on an atomic scale.

The spreading of powder on to double-sided sellotape was found to be the most effective sample mounting technique. Charge correction factors were never particularly high since the sellotape itself was not highly insulating. Multiple peaks, due to serious differential charging, were never observed and only on very rare occasions did peak tailing occur. The relative advantages of this method meant that it was used for all powder samples studied in this work. It should be noted that the use of a highly insulating, poorly adhesive, tape in the early stages of this project was unsatisfactory since the C1s region was dominated by the a peak corresponding to the sellotape carbon. Erroneous charging corrections were, therefore, obtained since this species was not in electrical equilibrium with the sample surface.

The pressing of powder into indium metal was found to be a reasonably good technique although serious differential charging did occur on several occasions. This technique was used for the sample biasing experiments discussed in section 3.4. The meshing of powder into a metallic gauze gave results similar to those obtained for the indium experiments. This method was, by necessity, used in the uranate heating experiments discussed in chapter 5. The spreading of powder on to a conducting araldite mixture was quite unsuitable since spectral peaks (e.g. O1s, C1s) due to araldite were invariably observed. Finally, the method of compacting material into the form of a disc proved to be unsuccessful especially in the case of UO_3 samples. An equilibrium surface charge was only achieved after several hours in the X-ray beam and charging corrections for the UO_3 samples were enormously high. In view of the similarities in the chemical and physical nature of UO_3 to the ammonium uranates, it was decided to abandon this mounting technique.

3.3 Calibration Techniques

This section briefly reviews the techniques which are commonly used to calibrate photoelectron spectra obtained from non-conducting materials. Although the study of such techniques was not the aim of this work, it was necessary to find a method which was suitable for the calibration of spectra recorded for the non-conducting uranium complexes discussed in chapter 5.

3.3.1 Internal Standards

Of all the calibration methods currently being used, internal standardisation is perhaps the most reliable. As previously stated, the method uses an internal energy level which is insensitive to chemical change throughout a series of chemically related systems (97-99). This method is particularly attractive in that the standard material must reflect the static charge of the system. This approach is, however, limited in its application since the referencing species must be common to all the samples studied and, more importantly, the internal energy level being used as the standard must be truly invariant throughout the particular series of complexes under investigation.

3.3.2 Physically Admixed Calibrants

The possibility of external calibration, using an internal energy level of an admixed standard compound, has been investigated by a number of workers. In the case of powdered samples, standards such as graphite (100,101), molybdenum trioxide (102), triplumbic tetroxide (103) and gold (104) have been used. Although consistent results have been obtained for some materials (100,102,103), this method has been shown to be unreliable for others (101,104,105). The principal difficulty with this technique seems to lie in the production of sufficiently intimate mixtures such that electrical equilibrium between the sample and the standard is attained. Ideally, mixing on an atomic or molecular scale is required but unfortunately this condition can only be satisfied for a very limited range of materials (106).

3.3.3 Surface Deposition Techniques

The deposition of a standard material on to a sample surface is a widely used method of calibration. Noble metals, because of their relative inertness and ease of evaporation, have been extensively employed in this area (107-109). The use of gold has received most attention and several studies have confirmed that, in many cases, this material is a very effective calibrant. In certain experiments, sample biasing has been used to confirm that the gold and the sample are in true electrical equilibrium (104,107). However, it has been shown that the amount of gold deposited on to the sample surface can be a critical factor in accurate calibration (108,110). Enhanced surface charging can ensue (108) and the electrical equilibrium between the gold and the sample can change significantly with variation in gold coverage, resulting in erroneous charging corrections (108,110). Furthermore, there have been several reports on the reaction of evaporated gold with certain samples (111,112) and clearly the assumption of calibrant inertness may be invalid.

A number of other standards have been used in the surface deposition approach including organic materials (106) and implanted argon atoms (113).

3.3.4 Adventitious Surface Layers

The use of adventitious carbon, which is present on nearly all sample surfaces, is the most convenient and commonly applied method of calibration. This species has been found to be effective for binding energy referencing in a wide range of non-conducting materials (114-116). The suitability of this calibrant has been tested via biasing experiments on non-conducting samples such as NaCl (101) and MoO_3 (104). These studies demonstrated that the carbon species was in electrical equilibrium with the particular sample in question and that it followed the static surface charge within acceptable experimental limits (within ~0.1eV).

There are, however, a number of problems associated with the use of this referencing material (117). The chemical state of the carbon in the contamination layer is obviously very important. Siegbahn (7) first reported the presence of a carbon contamination layer on sample surfaces, and concluded that this layer originated from vacuum pump oil since the amount of carbon increased with the time that the samples were in the spectrometer. Subsequently, it has generally been assumed that the C1s electrons, used as reference, are ejected from carbon atoms in adsorbed saturated hydrocarbon components, or from carbon atoms which exist in a very similar chemical environment. The principal disadvantage of the technique is the uncertainty in the binding energy for the carbon 1s electrons, with 284.6eV and

285.0eV being the most commonly used values. A number of studies have also shown that the C1s binding energy is affected by:-

a) the thickness of the contamination layer (118,119),

b) the chemical and physical nature of the sample under investigation (101,117,119),

and c) the preparation and treatment of the sample surface (101,117,120).

3.3.5 Suppression of Sample Charge

So far, there has been no mention of techniques which reduce or remove the sample charge. Charge suppression can be accomplished either by depositing a sufficiently thin sample film on to a conducting backing material (121), or by employing a low-energy electron flood gun (122-124). The use of a flood gun can be particularly important in the case of instruments equipped with monochromatic X-ray sources since a steady-state static surface charge is seldom attained, and charging shifts are usually very large. Although the designs of flood guns presently in use allow accurate calibration measurements to be made on smooth sample surfaces, the technique is not yet sufficiently accurate for the type of powdered materials which are often studied (125).

3.3.6 Concluding Remarks

Unfortunately there is no single calibration technique available which can be regarded as universally acceptable. In order to decide upon the most appropriate method, it is useful to consider work published in the literature which assesses charge correction methods, using different spectrometers, for a number of non-conducting samples (116,126,127).

Madey (126) has reported the results of an ASTM-sponsored round-robin study of three insulators using twelve spectrometers (seven different types of construction). Charge referencing by gold deposition and compensation via electron flooding gave results inconsistent with each other and with the adventitious carbon referenced values. Although the study showed that the best results were obtained using carbon as a calibrant, it was concluded that a more consistent referencing method was needed. Nefedov (127) has used two different spectrometers to measure core binding energies for sixteen non-conducting solids and concluded that adventitious carbon was a suitable calibrant. The study also compared carbon with deposited gold as a reference and showed that both methods of charge correction gave the same results provided that the quantity of deposited gold was minimised. In a very recent round-robin study (116), spectra from six non-conducting materials were obtained using nine spectrometers (seven different constructions). The study showed that calibration using the C1s line provides, in most cases, a good method to account for sample charging.

3.4 Calibration and Charging in this Work

Despite its uncertainties, the use of adventitious carbon appears to be the most generally applicable calibrant as demonstrated by a number of studies (section 3.3.6). However, it is clear, at least in principle, that any attempt to use this calibrant must be validated by experiments which demonstrate that this species is contiguous to the samples being studied.

The remainder of this chapter therefore discusses the experiments carried out in order to test the suitability of adventitious carbon as a calibrant. The viability of calibration via an admixed standard was also briefly investigated.

3.4.1 Curve Fitting

Apart from the Φ_{sp} measurement reported in section 3.4.3, all kinetic energies were obtained via the curve fitting program in order to ensure a high degree of accuracy. The errors in these measurements (±2 x standard deviation) are clearly shown where necessary. Starred values refer (±2 x standard deviation) to binding energies averaged over a number of different spectra which should be distinguished from the other values that refer to the accuracies of fitting single spectra.

3.4.2 Carbon Is Line Shape

It is important to consider the Cls line shape since the use of adventitious carbon as a calibrant is subject to uncertainty in cases where the Cls peak is very broad or asymmetric (126). The problem is accentuated if the Cls region consists of a number of closely overlapping peaks. For most samples studied in this work, both conductors and insulators, the Cls region was dominated by a single peak. Two very weak signals were often observed on the higher binding energy side of the main peak possibly corresponding to CO/CO_2 adsorbed on to the sample surfaces. For all metal surfaces studied, the FWHM of the main C1s peak was typically 1.7-1.9 eV. The absence of multiple peaks in the C1s region does not, of course, include those cases where differential charging effects were particularly serious (section 3.3.2).

3.4.3 Adventitious Carbon on Metal Surfaces

In order to use adventitious carbon as a calibrant, it was clearly necessary to measure the C1s binding energy against more reliable standards. High purity samples of gold , silver and palladium were thought to be ideal for this measurement since each metal gives rise to sharp, intense lines suitable for calibration purposes i.e. Au4f, Ag3d and Pd3d. There are, however, a spread of literature values for each standard as shown in table 3.1. For the purposes of accuracy, the binding energies of these standard lines were measured directly in the instrument at Newcastle. Argon ion etching was employed to produce extremely clean metal surfaces and the spectrometer workfunction was determined from the palladium valence band (fig 3.1a). The procedure described by Bird (128) and Powell (129) was used to determine the precise position of the Fermi edge which in turn is used as the zero point of the binding energy scale. In this method, the Fermi cutoff corresponds to the half-height position where the height is defined as the difference in intensity between the valence band maximum and the background level on the low binding energy side of the band edge. The measurement of this position was facilitated by the use of an expanded plot (fig 3.1b) and by the use of derivative and smoothing techniques (figs 3.1c, d). These procedures allowed the spectrometer workfunction to be evaluated with great accuracy and enabled the determination of standard metal binding energies to ±0.02 or ±0.03eV. The binding energies obtained for the gold ($4f_{7/2}$ = 83.92eV), silver ($3d_{5/2}$ = 367.90eV) and palladium ($3d_{5/2}$ = 335.18eV) samples are in excellent agreement with values reported in the literature (101,128-135).

A number of papers in the literature have reported the C1s binding energy for adventitious carbon adsorbed on to metal surfaces (117). Values (eV) such as 285.2, 285.0, 284.8 and 284.6 have been obtained. Unfortunately, the referencing of adventitious carbon against a metal standard is more complex than might be imagined. It has been shown that the thickness of the contamination layer has a major influence on the C1s binding energy (118,119). For a palladium sample, Kohiki (119) has observed that the C1s binding energy increases with increasing carbon surface coverage. The C1s binding energy was 284.3eV at lower coverages (0.3 monolayers) and 284.9eV at higher coverages (1-1.5 monolayers). Jaegle (120) investigated a number of metallic samples and showed that externally contaminated surfaces gave a C1s binding energy of 285.0eV. However, significantly lower values were found on freshly ion bombarded surfaces (e.g. 283.6eV on Au, 283.1eV on Cr).

In this work, experiments carried out on the Au, Ag and Pd samples also showed an increase in the C1s binding energy with increasing carbon coverage. The results are illustrated by fig 3.2 which shows the variation in the C1s binding energy with the amount of carbon on gold; the latter quantity is expressed in terms of the C1s/Au$4f_{7/2}$ peak area ratio (Ra). In this experiment, an externally contaminated piece of gold was argon ion etched for 5 minutes to give a reasonable gold signal (Ra = 2.1). The sample was further etched for various lengths of time to give a minimum Ra of 0.02. Accordingly, the C1s binding energy decreased from a maximum of 284.97eV to a minimum of 284.15eV (i.e. -0.82eV). Biasing was used to show that the carbon overlayer for the Ra = 2.1 sample was in electrical equilibrium with the gold substrate. Furthermore, for a heavily etched gold sample, the C1s binding energy was observed to increase with the time the sample was in the instrument due to the gradual *in situ* adsorption of carbon. The minimum C1s binding energy observed for the Ag and Pd samples was 284.15eV and 284.26eV respectively.

Kohiki (119) and Jaegle (120) have attributed the above behaviour to the variation in the extra-atomic relaxation energy (EARE) of the carbon atoms in the adsorbed film. For adsorbate species in general, extra-atomic relaxation is expected to be very significant in the case of metallic substrates. The observed increase in the C1s binding energy with carbon coverage is due to the corresponding reduction in the EARE given by the substrate. Increasing the carbon coverage means that carbon hole states are situated in an increasingly carbon-like environment with a resultant decrease in the EARE.

Clearly the simple assumption of measuring the adventitious carbon 1s binding energy against metallic standards is not a valid one. However, the object of these experiments was to establish the C1s binding energy in order to effectively measure binding energies for the non-conducting complexes discussed in chapter 5. Being insulators, such systems should contribute very little EARE to the carbon atoms in the adventitious layer (119). The implication of the above results is that a C1s binding energy of 285.0eV is much more suitable than other commonly used values such as 284.6eV.

It is necessary to briefly mention the effect of heat treatment on the adventitious C1s binding energy since the work discussed in chapter 5 involved the heating of a uranium metal/oxide sample up to 600°C, and some ammonium uranates up to 275°C. There seems to be some uncertainty in the literature in this area. Some workers have observed a decrease in the C1s binding energy corresponding to the formation of a graphitic type carbon (101), whereas others have found carbon to be a suitable calibrant at elevated temperatures (136). The results of a simple experiment on a gold sample (Ra = 0.06) are shown in table 3.2. The C1s binding energy decreased through the temperature range from 284.54eV at ambient to reach a minimum value of 284.16eV at 600°C. The decrease in binding energy is not due to a reduction in the amount of adsorbed carbon on the surface since the Ra value was essentially the same throughout the experiment. The most likely explanation seems to be a change in the chemical nature of the adventitious layer.

3.4.4 Calibration and Charging of Uranium Samples

In order to validate binding energies obtained for the non-conducting samples discussed in chapter 5, it was considered important to reference the adventitious carbon against some standard insulators. Furthermore, it was clearly vital to test the assumption of electrical equilibrium between the carbon overlayer and the substrate.

3.4.4.1 Al_2O_3/KCl Studies

It is not possible to quote a Cls binding energy for the adventitious layer adsorbed onto these materials since there was no independent reliable method of measuring the Al2p (Al_2O_3) and $K2p_{3/2}$ (KCl) core binding energies to be used as standard. It is useful, however, to select an arbitrary value for the Cls line and use this to obtain binding energies for the standard insulators. This procedure then allows easy comparison of binding energies between workers since any absolute difference in the adventitious Cls binding energy should be observed as a difference in the carbon-referenced core binding energy of the particular standard material. Of course, this situation requires that the calibrant and substrate are in electrical equilibrium.

As indicated above, a Cls binding energy of 285.0eV was selected and the Al2p (Al_2O_3) and $K2p_{3/2}$ (KCl) core levels were referenced against this value. For Al_2O_3 (99.99%), the Al2p binding energy of 74.33(±0.04*,±0.04) eV was obtained from two measurements with Cls/Al2p peak area ratio's of 0.74 and 0.93. This is in good agreement with carbon (ls = 285.0eV) and gold ($Au4f_{7/2}$ = 83.8eV) referenced values published in the literature (116,126,127). Difficulties in etching the powdered samples on sellotape meant that no conclusions could be made on any possible variation in the Cls binding energy with carbon surface coverage. Shohiki (119) has studied an Al_2O_3 wafer and showed that extra-atomic relaxation effects are only important at very low carbon coverages. It was also demonstrated that above ≈0.7 monolayer coverage, the C1s binding energy almost reached a constant value. The level of contamination for these samples implies that the EARE contribution to the C1s binding energy was small. Some aluminium oxide powder was pressed into indium in order to carry out sample biasing work. Of course, the highly insulating nature of Al_2O_3 meant that the spectral peaks shifted in kinetic energy by an amount substantially less than the applied bias. Although differential charging effects were quite considerable, the results suggested that the adventitious layer and the oxide substrate were in good electrical contact.

One of the difficulties in using KCl as a reference material stems from the formation of colour centres which arise from the exposure of the material to the X-ray beam. This gives KCl samples an increased degree of electrical conductivity which is expected to enhance any EARE contribution to the carbon overlayer. Using carbon as a reference (1s = 285.0eV), a sample (>99.8%) with a C1s/K2$p_{3/2}$ peak area ratio (Rb) of 4.83 gave a K2$p_{3/2}$ binding energy of 293.1(±0.05) eV. This is in good agreement with published values (116). The EARE contribution is expected to be negligible in view of the thickness of the carbon overlayer. Sample biasing, up to +25V, indicated that the carbon overlayer and the KCl substrate were in good electrical equilibrium since the C1s-K2$p_{3/2}$ binding energy separation showed a maximum deviation of 0.12(±0.03) eV relative to an unbiased sample. The significant conductivity of KCl in the X-ray beam is clearly demonstrated by the shift in peak positions with the applied bias. For example, the application of a +25V bias resulted in all peaks being shifted by approximately +22eV relative to an unbiased sample.

The physical nature of the KCl sample permitted the material to be suitably compacted on to the sellotape or indium backing allowing meaningful argon ion etching to be carried out. A significant EARE contribution to the carbon overlayer is confirmed since the reduction of Rb from 4.83 to 0.19 resulted in a reduction of the C1s binding energy by 0.32eV.

3.4.4.2 U_3O_8/UO_3 Studies

The detailed analysis of spectra obtained from these materials are given in chapter 5 and this section merely reports the results which relate to the theme of this chapter. The comparison of binding energies with literature values is also given in chapter 5.

Only a small amount of work was carried out on the standard oxide U_3O_8 (supplied by BDH). Carbon surface coverages (Rc = C1s/U4f$_{7/2}$ peak area ratio) were always fairly low ranging from 0.16 to 0.34. This material was extensively used in the sample mounting experiments and the observed U4f$_{7/2}$ binding energy was reproducible despite the different binding energy correction factors. By using the adventitious C1s line as reference (285.0eV), a U4f$_{7/2}$ binding energy of 380.66(±0.14*,±0.04) eV was obtained. Unfortunately, the small range of Rc values for all samples of U_3O_8 means that no comment can be made concerning the significance of the EARE contribution to the adventitious C1s binding energy.

The study of UO_3 (supplied by BDH) was particularly appropriate since this material is closely related to the ammonium uranate complexes discussed in chapter 5. Surface carbon levels were lower than those obtained for U_3O_8, with Rd (= C1s/U4f$_{7/2}$ peak area ratio) ranging from 0.10 to 0.14. The U4f$_{7/2}$ binding energy obtained via different sample mounting techniques was 381.69(0.19*,0.04) eV. It is important to realise that the binding energy correction factors varied from 8.5 to 14.5eV. The good degree of reproducibility in the U4f$_{7/2}$ binding energy indicates the suitability of adventitious carbon as a calibrant for this material. This is emphasised by sample biasing experiments, up to +25V, which showed a maximum deviation in the U4f$_{7/2}$-C1s binding energy separation of 0.11(±0.04) eV. The highly insulating nature of UO_3 meant that that the effective sample bias was considerably lower than the applied value. Thus, for example, an applied bias of +25V resulted in a +7.4eV shift in the spectral peak positions relative to an unbiased sample.

The consistently low Rd values means that little can be said about the possible EARE effect on the adventitious C1s binding energy. A UO_3 disc was mounted onto sellotape in order to allow meaningful argon ion etching to be carried out. Attempts to reduce the adventitious layer via this process were accompanied by simultaneous reduction of the UO_3 sample.

3.4.4.3 Calibration via an Admixed Standard

The possibility of calibration via an admixed standard was briefly investigated in this work. Very fine gold powder was chosen for this purpose since the extremely small particle size suggested that a sufficiently intimate sample-gold mixture could be obtained. A number of experiments, carried out on KCl-Au and UO_3-Au mixtures, gave results which were inconsistent. In most cases, there was a poor correlation between the gold ($Au_{7/2}$ = 84.0eV) and carbon (1s = 285.0eV) referenced values. The amount and distribution of intermixed gold was clearly an important factor in this respect. The intermixing of samples with large amounts of gold often resulted in the appearance of multiple peaks due to serious differential charging. Sample biasing experiments also demonstrated that the gold powder and the sample material were often in poor electrical contact. The overall set of experiments clearly indicated that this technique was quite unsuitable for calibration purposes.

3.4.5 Conclusions

Is is quite clear from the literature, that there are a number of difficulties associated with all methods of calibration. The problems of valid binding energy referencing in non-conductors are particularly serious due to the effect of sample charging. This chapter has tried to demonstrate that adventitious carbon may, in certain cases, be used to obtain reproducible binding energies for non-conducting complexes (see chapter 5). The problem caused by the uncertainty in the C1s binding energy has been overcome by effectively referencing this species against more reliable standards. The assumption of electrical equilibrium between the calibrant and the substrate has been validated via sample mounting and biasing experiments. The range of carbon coverages observed in this work means that little can be said concerning the extent of EARE effects on non-conductors. Previous work has already indicated that EARE effects are expected to be small on insulators (119).

Finally, the use of admixed gold powder was found to be unsuitable for the calibration of powder samples studied in this work.

Table 3.1

Measured Binding Energies (eV) Compared with Literature Values.

		Metal Binding Energies (eV)		
Ref	Instrument	Au $4f_{7/2}$	Ag $3d_{5/2}$	Pd $3d_{5/2}$
130	AEI ES100	84.0	368.2	335.2
101	Magnetic	83.8±0.2	368.2±0.2	335.2±0.2
131	AEI ES200	84.07	368.23	335.20
132	AEI ES200	84.0	-	335.2
133	Varian IEE-15	83.8	367.9	-
129	E-42 Survey	84.0	-	-
128	AEI ES200B	83.98±0.02	368.21±0.03	335.2±0.03
134	VG ESCA3 Mk 1	83.7	367.9	335.3
135	HP 5950A	84.0	368.2	-
This Work	AEI ES200B	83.92±0.02	367.90±0.02	335.18±0.03

Table 3.2

The effect of temperature on the C1s line for adventitious carbon on an argon ion etched gold surface.

	Binding Energy Differences (eV)	
Temp (°C)	(C1s-Au$4f_{7/2}$)	(C1s(amb)-C1s(T))
Ambient	200.62±0.02	-
200	200.65±0.02	0.03±0.04
400	200.31±0.02	0.31±0.04
600	200.24±0.02	0.38±0.04

where C1s(T) = binding energy of adventitious carbon at an elevated temperature.

Fig 3.1:- Valence Band for Palladium

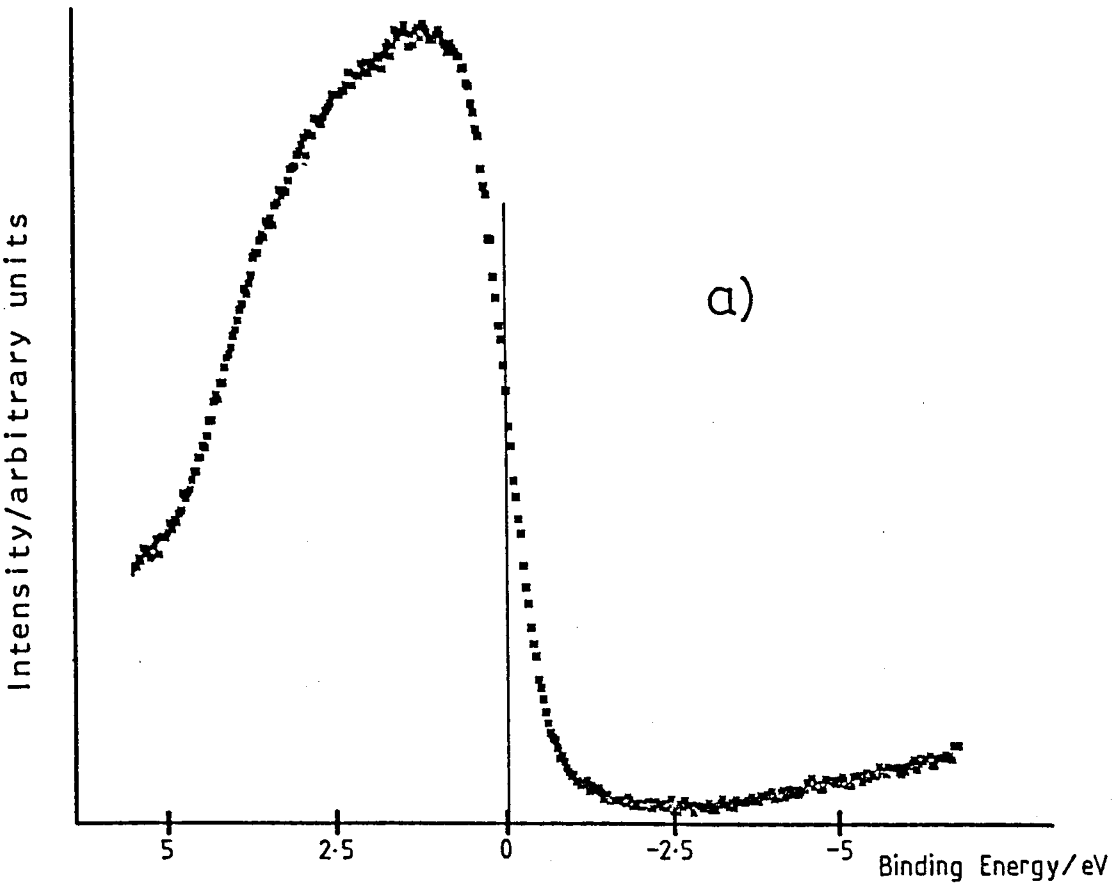

a) Original Data

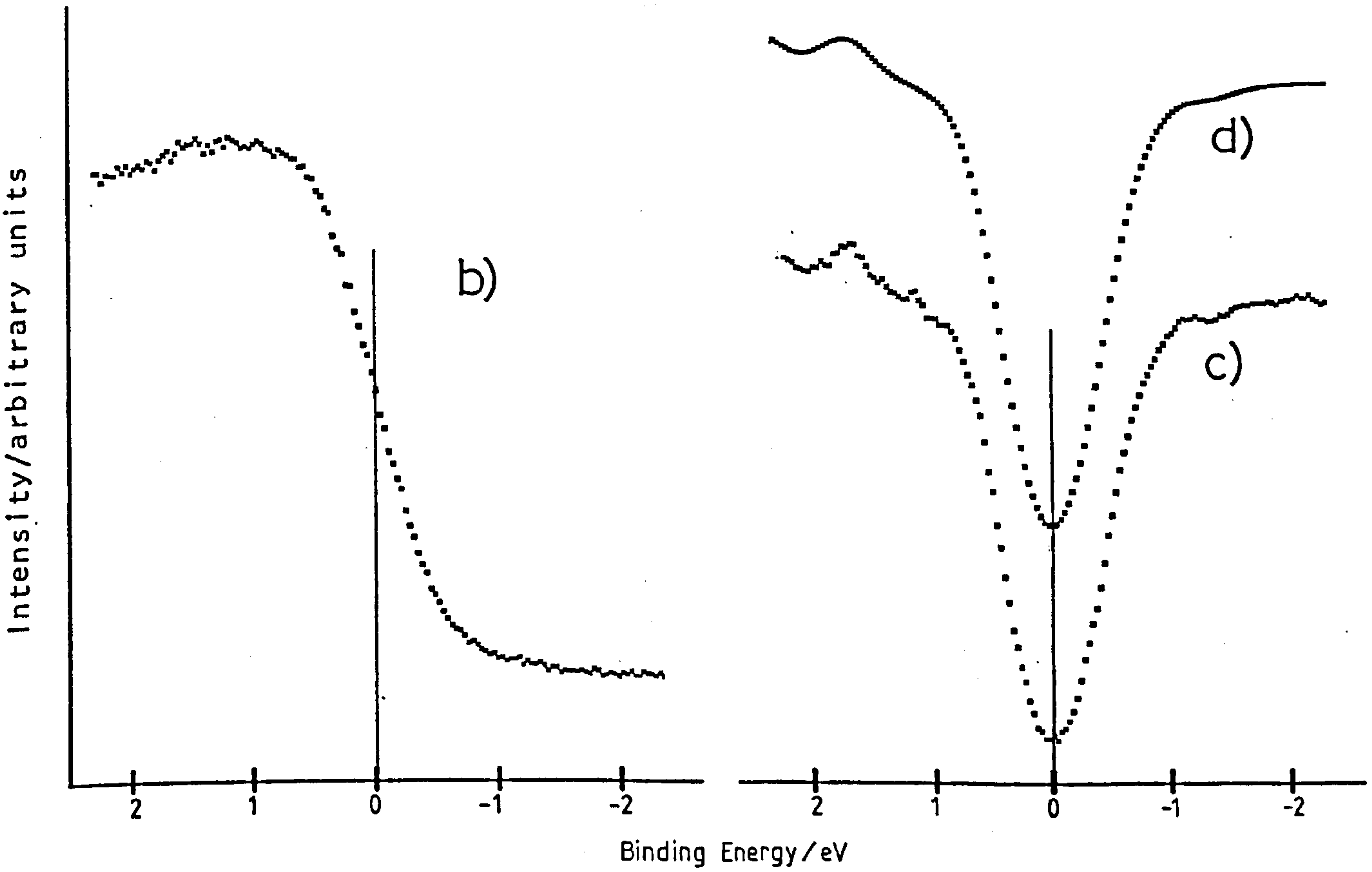

b) Expanded Plot

c) First Derivative of b).

d) Smoothed First Derivative of b).

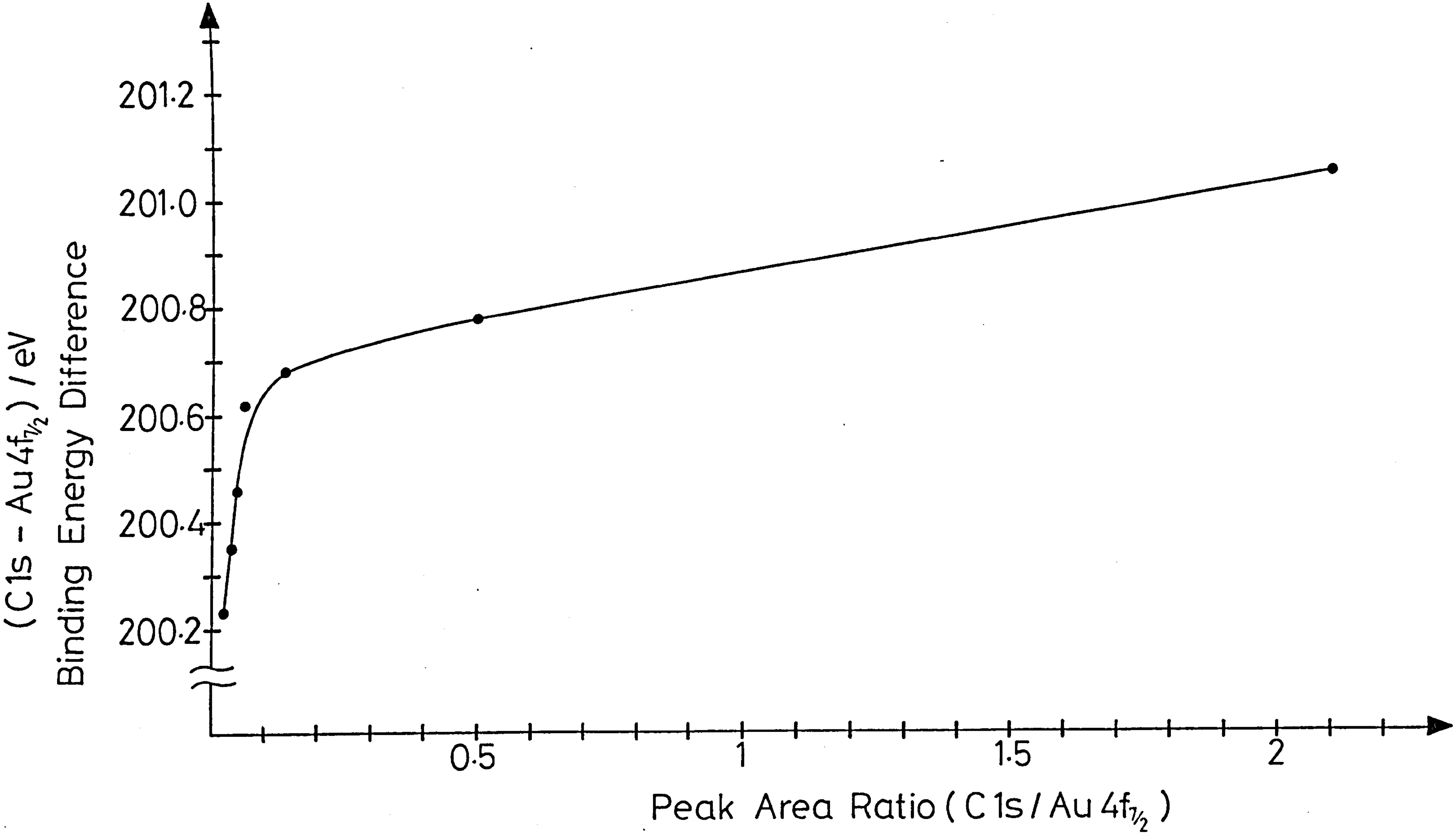

Fig 3.2:- The Change in C 1s Binding Energy with the Amount of Adventitious Carbon Adsorbed onto a Gold Surface.

CHAPTER FOUR

STUDY OF THE SURFACE OF BORIDED ZIRCONIUM

4.1 Introduction

There has been considerable interest in the metal borides and related carbides and nitrides over the past thirty years (137). They are all characterised by high melting points, hardness and chemical durability while the metal borides have the added property of being electrical conductors. The uses of borides fall roughly into six areas, as refractories (137), as catalysts in the hydrogenation of unsaturated hydrocarbons (138), as thermionic emitters (139), in case hardening of metals (140), as cutting tools and abrasives (137), and as cathodes in the electrolytic production of aluminium (141). The electrical conductivity is particularly high in the transition metal borides such as ZrB_2 and LaB_6. ZrB_2 has a resistivity of 7-10 μΩ cm (137) compared with the value of 1.7 for copper (142). The electrical conductivity has only been exploited in industrial electrodes and thermionic emitters. This study arose from the work of Dr.P.H.Middleton in his attempt to use ZrB_2 as a novel cathode material in electrochemistry. This boride was chosen because it forms a stable dodecaboride and diboride (137), and the high boron content was thought to make for interesting electrochemical behaviour. The great hardness of the boride makes shaping of the material very difficult, requiring diamond tipped tools or spark erosion. Dr. Middleton thus decided to prepare the material to the required shape by using the boriding (boronising) process. The use of ZrB_2, prepared in this way, as an electrode material requires an uncontaminated boride surface at the electrode/electrolyte interface.

There are a few XPS and related studies of zirconium boride reported in the literature (143-146). Studies of borides in general have shown the importance of surface oxidation of air exposed samples (143,147-152).

This chapter describes an X-ray photoelectron spectroscopic study of borided zirconium which was carried out as a joint project with Dr P.H.Middleton. The chapter will discuss the aspects of the work which involved the author of this thesis. Other aspects of the work have been discussed eleswhere (153). The project involved depth profiling and angle dependent studies to investigate the surface of borided zirconium. The author's contribution to the work involved the curve fitting and detailed analysis of all the results in addition to the experiments on the metal, oxide and conventionally prepared boride systems.

4.2 Experimental

Boron powder (95%, 325 mesh) supplied by Alpha Chemicals Ltd and zirconium sheet (99.9%, 1mm thick) supplied by Goodfellow Metals Ltd were used. Zirconium boride was prepared by Dr P.H.Middleton using the boriding process (140,154). This method uses the diffusion of boron atoms into the metal lattice at high temperatures, but significantly below the melting points of either component or boride. The metal plate used was cut out as 2cm x 0.5cm and placed in a layer of boron powder in a silica crucible. The composite was then compacted and placed in a Metals

Research Vacseal VS2 furnace, evacuated to 10^{-4} torr, flushed with high purity argon at atmospheric pressure, and heated to 1250°C for 24 hours while maintaining a steady flow of argon to remove any volatile matter. The furnace was then cooled to ambient temperature over a period of 12 hours. The extracted borided sample was analysed after the removal of residual boron particles by light abrading with a 'selvyt' cloth. A sample of conventionally prepared boride (ZrB_2) was also studied. The boride samples were directly attached to a metal block in such a way that no part of the metal block was exposed to X-rays in the XPS studies.

Zirconium foil was mounted on the HTP probe and heated up to a maximum temperature of 600°C. Angle dependent studies are achieved by varying the effective depth of the sample studied (d) with the angle of emergence of the photoelectrons (ϑ) such that d represents a depth $d\sin\vartheta$ below the sample surface (section 1.7.2). Hence, $\vartheta = 90^{o}$ corresponds to a bulk sensitive angle, and $\vartheta = 5^{o}$ is a surface sensitive one. Boron powder samples were studied as powder mounted on double-sided sellotape.

4.3 Results and Discussion

It was important to record spectra from both boron and zirconium samples in addition to the study of the borides. These samples provided useful information about the various oxides that can be found on the surface of these materials.

The binding energies of all species encountered in this study are summarised in table 4.1.

4.3.1 Zirconium Foil Studies

Initial studies on zirconium revealed the presence of a tenacious oxide layer (ZrO_2), as expected (155). Argon ion etching failed to remove this layer and the resultant Zr3d spectrum (fig 4.1a) shows mainly oxide although small metal peaks are clearly discernable.

Using residual carbon as a calibrant (1s = 284.6eV) gave an $Zr3d_{5/2}$ binding energy of 182.00eV with a 3d spin-orbit separation of 2.41eV. It was decided to use this level as an internal calibrant for the boride studies. The O1s region for the ZrO_2 layer showed three peaks at 532.2, 531.0 and 529.4 eV corresponding to adsorbed oxygen and/or water, hydroxide and oxide respectively.

Attempts to remove the oxide layer via chemical polishing were unsuccessful (see section 4.4). Scraping the foil surface produced large metal peaks in the Zr3d region, almost equal in intensity to those of the oxide. The metal 3d levels were shifted 4.25eV relative to those of ZrO_2 giving a binding energy of 177.75eV for the $3d_{5/2}$ peak.

The oxide overlayer was completely removed by heating in vacuo to 600°C (156) and recording the spectrum at this temperature (fig 4.1b). The oxide layer is removed at high temperature by the diffusion of oxygen from the oxide film into the bulk of the metal. The O1s spectrum showed two peaks at 531.5 and 529.5 eV. The lower binding energy species does not correspond to oxide since the associated Zr3d levels would have been easily observable. The oxygen peaks are thought to correspond to both subsurface and chemisorbed oxygen (157-161).

The distinct asymmetry of the metal 3d peaks is quite apparent and an exponential tail was included in the Gaussian/Lorentzian fitting function to account for this. The asymmetric lineshape is not considered to arise from chemically shifted Zr3d intensity (due to the presence of subsurface and chemisorbed oxygen) since many studies have observed such asymmetry to be associated with conducting species (72-75,162-165).

Wertheim (73) has shown the importance of including asymmetry effects in quantitative analysis. There is, however, some doubt concerning the ability to distinguish between asymmetric broadening and inelastic background intensity (73). From fig 4.1b, it would appear that there is a considerable inelastic tail associated with the metal 3d core levels. The use of a program calculated linear background over-estimates the 'true' intensity of the Zr3d levels and this effect is observed as an enhancement of the associated asymmetric tails. Inelastic background removal has been employed by a number of workers (88,166-169) and fig 4.1c shows the effect of background removal (85) on the metal Zr3d spectrum. The iterative form of Shirley's algorithm was used to remove the background (85). With reference to fig 4.2, the value of the background at a point x in a spectral array of k equally spaced points is

$$B(x) = \frac{(a - b)\,Q}{(P + Q)} + b \qquad (4.1)$$

where a is the average start point, b the average end point, (P+Q) the total background subtracted (BS) peak area, and Q the (BS) peak area from point x to point k. The (BS) areas are calculated initially by choosing a linear constant background of magnitude b, line B1 in fig 4.2. Substitution in eqn 4.1 leads to the background B2 which is then used to calculate new (BS) areas resulting in the background B3. The process is repeated until (P+Q) remains essentially unchanged on successive iterations.

It is a prerequisite of this technique that the extreme ends of the spectral region are a true representation of the background alone. The magnitude of the calculated asymmetric tail at the high binding energy of fig 4.1b is extremely small and will have little adverse effect on the background subtraction method. It is clear from fig 4.1c that the overall line shape is still well fitted by the use of an exponential tail in the fitting function. There is, however, less asymmetry and therefore less intensity associated with the metal 3d levels. Indeed, if the $Zr3d_{5/2}$ peak area from the original spectrum (fig 4.1b) is taken as 100%, then the background subtracted $Zr3d_{5/2}$ peak area is 89.7%. Background removal is therefore important in quantitative analysis although the danger of removing true signal intensity is always present.

In the case of the zirconium boride spectra (*vide infra*), both inelastic background and peak asymmetry effects were significant. It was, therefore, important to compare the effect of a linear and non-linear background on quantitative analysis. It will be seen that fundamental difficulties arose when using the background subtraction method due to the considerable complexity of the boride spectra.

4.3.2 Boron Powder Study

Boron powder gave a B1s spectrum (fig 4.3a) which showed three peaks at 192.2, 188.5 and 186.8 eV corresponding to B_2O_3, elemental boron, and boron carbide. It should be noted that these binding energies are referenced against a residual C1s binding energy of 284.6eV rather than 285.0eV. The oxide and carbide peaks were substantially reduced after a 10 minute etch indicating that they represented a considerable surface impurity on the boron particles. The O1s spectrum showed two peaks at 532.0 and 531.0eV corresponding to adsorbed oxygen and/or water, and B_2O_3.

There is a range of B_2O_3 B1s binding energies given in the literature (191.5 - 193.5 eV) using various calibrants (170-172). The value observed in this work is close to that of Wheeler (171). The carbide B1s value shows a separation of 1.7eV from elemental boron and is thought to correspond to B_4C. This is supported by the presence of a carbide peak at 286.3eV in the C1s region (173).

4.3.3 Conventionally Prepared Boride Study

The B1s/Zr3d spectrum of the conventionally prepared boride

(ZrB_2) sample is shown in fig 4.3b. The spectrum shows peaks due to boride ($Zr3d_{5/2}$ = 177.80eV, B1s = 186.4eV), ZrO_2 ($Zr3d_{5/2}$ = 182.00eV) and B_{ox} (oxidised boron, B1s = 191.7eV). The oxidised boron (B_{ox}), the stoichiometry of which is unknown, has been observed at similar B1s binding energies on many other metal borides (143,152,171). The O1s region showed peaks at 531.3 and 529.4 eV which are assigned to adsorbed oxygen and ZrO_2. There will be a small amount of oxygen intensity associated with B_{ox} which would be expected to lie under the 531.5eV peak. The boride peaks were fitted using an exponential tail due to conduction band interaction, as expected for conducting species. In addition to the main peaks described above, the spectrum showed oxide satellite peaks at 14-15 eV to the higher binding energy side of the ZrO_2 3d peaks. Rao (174) suggests a plasmon excitation process as a possible origin for these peaks.

Extensive argon ion etching (several hours) was employed in an attempt to reduce the zirconium oxide/boride peak area ratio, without success.

4.3.4 Study of Borided Sample

The sample of borided zirconium was analysed by depth profiling and recording spectra at different sample angles. Spectra were recorded at a bulk sensitive angle ($\vartheta = 90^\circ$) for all etch times, and at angles of $\vartheta = 5^\circ, 45^\circ$ for etch times of 45 and 165 minutes. All spectra discussed in this section were fitted using the linear background approximation. The alternative approach of using integral background removal is considered in section 4.3.5.

The considerable number of peaks in the Zr3d/B1s spectra made it quite impossible to float all the parameters in the curve fitting procedure. As previously indicated (chapter 2), the floating of all parameters in any spectrum is quite impossible in all but the most simple cases. The considerable complexity of the boride spectra made it necessary to manually vary an unusually large number of parameters in order to achieve the best set of fits.

Fig 4.4 shows the change in the Zr3d/B1s spectra at $\vartheta = 90^{\circ}$ for all etch times. Two sets of Zr3d doublets were clearly observed with $3d_{5/2}$ binding energies of 182.00 and 177.86 eV due to ZrO_2 and ZrB_x respectively. Careful fitting showed that there was considerable asymmetry associated with the boride Zr3d levels, as expected. Joyner and Hercules have observed considerable asymmetry effects in the 2p spectra of Fe, Fe_2B and FeB (147).

A linear background method was adopted ignoring any satellite structure from the oxide Zr3d peaks. A small amount of intensity would be expected for the satellites above the rising linear background, since the oxide $Zr3d_{5/2}$ satellite peak occurs at a binding energy of 196-197.0eV. It was not possible, however, to confidently determine the amount of satellite intensity above the background although its effect on calculated intensity ratios would be small.

The spectra showed B1s peaks at 194.8, 191.8 and 186.5

eV. The two latter peaks are assigned to 'oxidised boron' (B_{ox}) and ZrB_x. It is important to note that the boride B1s peak appeared to possess significant asymmetry since this peak was best fitted with the use of an exponential tail.

Recently, Alyeshin has used XPS to study the surface of borided iron powder (152). The preparative conditions for this sample (i.e. 1100°C, Ar atmosphere, etc.) were quite similar to those used for zirconium in this work. A boron species with a B1s binding energy of 194.8eV was observed by Alyeshin, corresponding to "the formation of a new surface anomalous combination of boron with oxygen (B_xO_y)". There were, however, no suggestions as to the exact stoichiometry of this new boron oxide species.

Zintl (175) has reported that high temperature reactions of boron with alumina (1300°C) and zirconium dioxide (1800°C) produced a volatile suboxide of boron. By condensing the evolved vapour, a bright brown transparent and amorphous sublimate was obtained with an empirical formula BO. This is the most commonly known boron suboxide (176), although a wide variety of such species has been reported:- e.g. B_7O, B_3O, B_4O_3, B_4O_5. The production of BO (empirical formula) by the high temperature reactions of some metal oxides with elemental boron has been well established (176-178).

The zirconium sample used in the boride preparation would have, of course, possessed a film of ZrO_2 on the surface. The reaction with boron at 1250°C would be expected to produce BO (empirical formula). It is reasonable, therefore, to assign the boron peak with the highest B1s binding energy (194.8eV, fig 4.4) to this species. Most of the boron monoxide observed on the surface of the borided sample probably corresponds to unvolatilised material, although significant re-adsorption of evolved vapour would not be suprising.

The O1s regions for all etch times (ϑ = 90°) are very similar in that they show three peaks and the 10 minute and 105 minute etch spectra are shown as examples (figs 4.5a and 4.5b). The binding energies at 533.6, 532.1 and 529.5 eV (figs 4.5a and 4.5b) correspond to subsurface oxygen, a mixture of surface boron oxides and adsorbed species (*vide infra*), and ZrO_2. Clearly the highest binding energy species dominates the spectrum. Angle dependent results for the 165 minute etched sample (figs 4.5c to 4.5e) show considerable changes in relative peak intensities. The highest binding energy species is mainly located in the bulk and is therefore assigned to dissolved oxygen. The presence of this peak is accounted for by the collapse of the oxide film at high temperature in addition to oxygen impurities originating from the argon atmosphere during the boride preparation. The considerable dissolution of oxygen in zirconium at elevated temperatures has been well reported (156, 179-181). The other oxygen peaks appear to arise from surface species located close to the surface, as expected for the surface oxides of boron and zirconium.

The O1s spectra, discussed above, are more complicated than might, at first, be imagined. From a large number of fitting attempts, it was clear that the spectral envelopes were best described by three peaks. This does not imply, however, that there are simply three types of oxygen species on the sample surface. Indeed, there are at least four oxygen species corresponding to dissolved oxygen, BO, B_{ox}, and ZrO_2. Furthermore, it is reasonable to expect some additional signal due to adsorbed species (e.g. O_2, H_2O) since spectra were often collected over periods of many hours. The slightly crude, but necessary, use of three peaks in the curve fitting procedure means that oxygen species of similar 1s binding energy are being described by a single peak. The O1s peak at 532.1eV most likely corresponds to a number of species since both boron oxides (BO, B_{ox}) and adsorbed species (O_2, H_2O) are expected to lie in, or close to, this binding energy region.

Angular variation studies for the Zr3d/B1s region are shown in fig 4.6 and clearly show BO and B_{ox} to lie on the surface. It would appear that B_{ox} is caused by surface oxidation of BO possibly caused by the etching process, although it would not be unreasonable to expect other oxides of boron to be formed in the sample preparation. The large increase in the relative B_{ox}/BO intensity ratio (fig 4.6e) clearly shows that the 'oxidised boron' (B_{ox}) species is located mainly on the immediate sample surface. The smoothed overlay of this spectrum shows the changes in relative peak intensities more clearly. The presence of a small peak at the highest binding energy side of the most surface sensitive spectra (figs4.6c and 4.6e) may correspond to some other boron suboxide.

Fig 4.7 is a graph of the change in relative intensities with etch times for spectra recorded at $\vartheta = 90^\circ$. Fig 4.8 shows the variation of individual peak areas with respect to the total area in the angle variation studies for each species in the spectrum after 45 and 165 minutes. The variations in relative intensities with both etch time and angle, lead to an approximate representation of the surface as shown in fig 4.9. The results clearly show the boron oxides located on the immediate surface although some BO concentration is found as one penetrates the layers. There would appear to be considerable mixing of the zirconium oxide and boride layers as was found for the conventionally prepared boride where in fact the oxide dominated. However the boride/oxide ratio increases with both etch time and ϑ and shows a greater proportion of boride with increasing distance into the sample.

The peak intensities can be used to give information which can assist in the identification of compound stoichiometry. Thus, if the familiar photoelectron intensity expression (182, section 1.7) is used:

$$I = \frac{F\alpha Dk}{\sigma}.\left(1 - \exp(-\sigma x)\right) \qquad (4.2)$$

where

I = intensity of emitted photoelectron,

F = X-ray flux,

α = photoionisation cross section,

D = density of a given atom in the material,

k = spectrometer constant,

σ = reciprocal of the mean escape depth (λ) of photoelectrons of a given kinetic energy.

Thus, the equation for the determination of the zirconium boride (ZrB_x) stoichiometry is:

$$\frac{I(B1s)}{I(Zr3d_{5/2})} = \frac{\alpha(B).D(B).\sigma(Zr).[1 - \exp(-\sigma(B).x)]}{\alpha(Zr).D(Zr).\sigma(B).[1 - \exp(-\sigma(Zr).x)]} \qquad (4.3)$$

Since B1s and Zr3d electrons appear at essentially the same kinetic energy, $\sigma(B1s)$ will be approximately equal to $\sigma(Zr3d_{5/2})$ and hence equation (4.3) simplifies to:

$$\frac{I(B1s)}{I(Zr3d_{5/2})} = \frac{\alpha(B).D(B)}{\alpha(Zr).D(Zr)} \qquad (4.4)$$

This approximate expression can be used to determine boride stoichiometries using cross section information provided by Scofield (183). They range from x = 3.5 to 4.0 for the borided sample in most cases as compared with x = 2.4 for the conventionally prepared boride, but these figures may be distorted by differential sputtering effects.

The chemical shifts observed, in this work, for the boride metal core levels are clearly very small. Small chemical shifts are, however, not unusual in the case of some metal borides (147). Dr Sherwood has used a CNDO relaxation-potential model calculation (184) to theoretically predict the chemical shift for zirconium diboride (ZrB_2). Although the calculation gives a slightly negative chemical shift with respect to the metal (-0.06eV), it is close to the slightly positive chemical shifts observed in this work (+0.05, +0.11 eV).

4.3.5 Curve Fitting and the Inelastic Background

The use of a linear background, in the curve fitting of the Zr3d/B1s spectra, meant that a significant difference was expected between the calculated absolute intensities and the 'true' values. This is mainly due to the inherent deficiencies of the linear background in terms of its ability to approximate the 'true' background profile. Furthermore, additional errors were introduced by ignoring both the satellite structure associated with the oxide Zr3d peaks, and the weak 'boron suboxide' feature lying on the high binding energy side of the boron monoxide B1s peak. The latter approximation was, of course, only used at sample angles of ϑ = 45° and 90°.

It was thought that integral background removal would be useful in helping to assess the possible errors associated with the relative peak intensity ratios which were obtained from the curve fits using a linear background. However, a major problem was immediately apparent since the spectral start and end points, in all cases (see fig 4.4), were not truly representative of the background intensity alone. Although this problem could be overcome by estimating the 'true' background intensity at these points prior to background subtraction, analysis of the metal/oxide spectra (section 4.3.1) revealed a fundamentally more serious problem associated with the use of the background removal algorithm.

From fig 4.1, it would appear that the metal 3d spectral peaks have a larger associated inelastic tail than that of the oxide. This is confirmed by the use of a constant tail in the fitting function and setting the background slope to zero (fig 4.10). Thus, the inelastic tail associated with each species, is incorporated into the fundamental Gaussian-Lorentzian peak shape. It can be clearly seen that the constant tail associated with the metal Zr3d levels (fig 4.10a) is greater than that of the oxide (fig 4.10b).

Due to differences in associated inelastic tail, one cannot use inelastic background subtraction to effectively analyse zirconium metal/oxide mixtures. The background subtraction method cannot discriminate between varying inelastic contributions for different species in the case of closely overlapping peaks. The background routine depends solely on the variation of the total peak envelope area within a spectrum and, therefore, the application of this method to analyse zirconium metal/oxide spectra is invalid.

This would seem to be confirmed in the case of spectra containing large proportions of metal 3d signal. The use of standard metal and oxide peak parameters to fit background subtracted metal/oxide spectra was clearly unsuitable.

Complications, similar to those above, would also be expected in the case of the boride Zr3d/B1s spectra. From fig 4.4, it is clear that the linear background slope increases with increasing boride Zr3d intensity. This observation is due to the enhanced inelastic background intensity associated with the boride Zr3d levels (i.e relative to the oxide 3d levels). Inelastic tails associated with other peaks in the Zr3d/B1s region must also be considered. Clearly, the use of integral background subtraction is quite unsuitable for these spectra.

For a spectrum containing peaks with different inelastic tails, it is feasible, at least in principle, to use individual peak constant tails to account for this effect. Indeed, from fig 4.10, it is clear that the use of a constant tail in the fitting function gives a good approximation to the associated inelastic background. Furthermore, the correlation between the pure metal Zr3d$_{5/2}$ peak area in fig 4.10a (87.4±0.5%) and fig 4.1c (i.e. background subtracted, 89.7%) is fairly good. These metal Zr3d$_{5/2}$ peak areas are relative to the value which was calculated for the original spectrum (fig 4.1b, 100%). The peak area calculation in the curve fitting program does not, of course, include the constant tail component of the fitting function.

Constant tails have been used by a number of other workers (185-187) to approximate inelastic backgrounds. Recently, Robinson (187) used this technique to analyse Ti2p spectra containing mixtures of $TiO_2/TiO_xN_y/TiN$. The differing inelastic tails associated with each peak meant that constant tails were used in the curve fitting analysis.

A number of curve fits were carried out on the Zr3d/B1s spectra using constant tails. Both absolute and relative peak intensities were highly inconsistent. The number of parameters to be manually varied was excessive and the parameter optimisation times were prohibitively long. The considerable complexity of the spectra meant that the use of constant tails was of little practical value in this work.

4.4 Chemical Polishing of Zirconium

As briefly stated in section 4.3.1, chemical polishing was employed in an attempt to remove the tenacious oxide layer (ZrO_2) present on the surface of zirconium foil. The well known cleaning method (*vide infra*), used in this work, is reported to be suitable for titanium and hafnium in addition to zirconium (188,189).

The experimental procedure consists of (188):-

1) Swabbing the sample with a solution of nitric acid (45ml), hydrofluoric acid (8-10ml) and water (45ml). After a few seconds, a brownish-yellow vapour is evolved on the sample surface. Indeed, this reaction was observed in this work.

2) Continued swabbing for 5-10 secs.

3) Thoroughly rinsing the sample in running water.

The method is based upon the formation of a complex metal flouride which dissolves into solution to ideally leave a clean metal surface. Of course, the extreme affinity of zirconium for oxygen implies that oxide formation is likely to take place immediately after the cleaning procedure.

Cleaning treatments were performed both in air and under nitrogen in this work and samples were inserted into the spectrometer as quickly as possible. Zirconium samples were normally argon ion etched prior to chemical polishing. This resulted in the attainment of an oxide covered surface with Zr3d spectra similar to that shown in fig 4.1a. Use of the above cleaning procedure transformed an essentially dull surface into one which was metallic-like in appearance. However, the XPS measurements clearly demonstrated that the surface did not correspond to clean metal.

Typical spectra, obtained for the "chemically cleaned" samples are shown in fig 4.11. The Zr3d spectrum was composed of three doublets (fig 4.11a), with the lowest binding energy species corresponding to zirconium metal. The increased intensity of the metal peaks (i.e. compared to an argon ion etched Zr surface) was noticeable for all treated samples. If the metal $3d_{5/2}$ peak is used for calibration purposes (177.75eV), then binding energies of 183.4 and 185.8 eV were obtained for the two other zirconium $3d_{5/2}$ peaks. This corresponds to chemical shifts (w.r.t metal) of +5.7 and +8.1 eV respectively, which compares with a value of +4.25eV for ZrO_2. The O1s region (fig 4.11b) shows three peaks with the lowest binding energy species appearing at 530.6eV. This would seem to correspond to oxide although its binding energy is considerably higher than that obtained for ZrO_2 (529.4eV). Furthermore, the F1s region (fig 4.11c) showed a single peak at 685.3eV, indicating the presence of a fluoride species. Two very weak N1s signals were also observed (400.3 and 398.8eV) although their assignment is uncertain.

It is clear from this work that the above cleaning technique is totally unsuitable for the chemical polishing of zirconium metal. The treatment appears to have produced a layer of zirconium oxyfluoride on the sample surface which gives rise to the $Zr3d_{5/2}$ peak at 183.4eV, discussed above. The other peak (185.8eV) corresponds either to a higher zirconium oxyfluoride (or fluoride), or to a satellite associated with the principal oxyfluoride species. It should be noted that chemical polishing of a scraped zirconium surface produced spectra which were quite similar to those discussed above.

Previous work in this laboratory (91,190) has already shown that certain commonly used metal cleaning techniques are quite unsuitable for the production of clean metal surfaces. Thus it is clear, from this and other work, that great care must be taken in attempts to obtain clean metal surfaces via chemical polishing methods.

4.5 Conclusions

The presence of surface oxidation on fabricated borides is clearly demonstrated in this work. This oxide formation must restrict the application of such borides when the surface must reflect the full boride properties, as in electrochemical applications.

Sophisticated curve fitting has been employed to analyse highly complex spectra. Some problems associated with inelastic background effects have been highlighted. The widely used integral background removal technique should not be used in the analysis of closely overlapping peaks if some or all of the individual peaks have significantly different associated inelastic tails.

Table 4.1

Binding Energies of Compounds Studied

Boron Powder

Core Level	Binding Energy(eV)	FWHM(eV)	Assigned Species
B1s	192.16(0.04)	1.82(0.10)	B_2O_3
B1s	188.50(0.03)	1.71(0.03)	B
B1s	186.84(0.03)	1.49(0.03)	B_4C
O1s	531.98(0.06)	2.03(0.04)	$O/O_2/H_2O_{ads}$
O1s	530.95(0.20)	2.20(0.11)	B_2O_3
C1s	286.35(0.04)	1.62(0.02)	B_4C

Zirconium Metal/Oxide

Treatment	Core Level	Binding Energy(eV)	FWHM(eV)	Assigned Species
Etched	$Zr3d_{5/2}$	182.00(0.01)	1.46(0.01)	ZrO_2
	O1s	532.16(0.09)	1.57(0.03)	$O/O_2/H_2O_{ads}$
	O1s	531.00(0.09)	1.57(0.03)	-OH
	O1s	529.39(0.03)	1.57(0.03)	ZrO_2
Scraped	$Zr3d_{5/2}$	182.00(0.01)	1.46(fixed)	ZrO_2
	Zr3dU5/2	177.75(0.02)	1.15(fixed)	Zr
600°C	$Zr3d_{5/2}$	177.75(0.01)	1.15(0.01)	Zr
	O1s	531.51(0.19)	1.83(0.16)	O_{ads}
	O1s	529.38(0.07)	1.83(0.16)	O_{sub}

Table 4.1 (continued)

Conventional Zirconium Boride

Core Level	Binding Energy(eV)	FWHM(eV)	Assigned Species
$Zr3d_{5/2}$	182.00(0.01)	1.52(0.03)	ZrO_2
$Zr3d_{5/2}$	177.80(0.05)	1.42(0.06)	ZrB_x
B1s	191.74(0.11)	2.08(0.10)	B_{ox}
B1s	186.37(0.08)	1.60(0.13)	ZrB_x
O1s	531.26(0.21)	2.37(0.35)	$O_2/O/B_{ox}$
	529.45(0.46)	2.37(0.35)	ZrO_2

Borided Zirconium

Core Level	Binding Energy(eV)	FWHM(eV)	Assigned Species
$Zr3d_{5/2}$	182.00(0.02)	1.65(0.12)	ZrO_2
$Zr3d_{5/2}$	177.86(0.12)* (0.04)	1.19(0.11)	ZrB_x
B1s	194.79(0.56)* (0.08)	2.92(0.52)	BO
B1s	191.82(0.16)* (0.09)	2.43(0.36)	B_{ox}
B1s	186.48(0.10)* (0.08)	1.48(0.22)	ZrB_x
O1s	533.65(0.10)* (0.06)	2.55(0.09)	O_{sub}
O1s	532.14(0.33)* (0.09)	2.55(0.09)	$BO/B_{ox}/O/O_2/H_2O$
O1s	529.46(0.31)* (0.10)	2.55(0.09)	ZrO_2

Note:

ads=adsorbed species, sub=subsurface species. A greater degree of accuracy is attained when the calibrant and measured peak are within the same spectrum. The errors (±2 x standard deviation) are shown in parentheses. Starred values show (±2 x standard deviation) of binding energies averaged over a number of different spectra, which should be distinguished from the other values that refer to the accuracies of fitting single spectra.

Fig 4.1:- Zr3d Region for Metal Foil

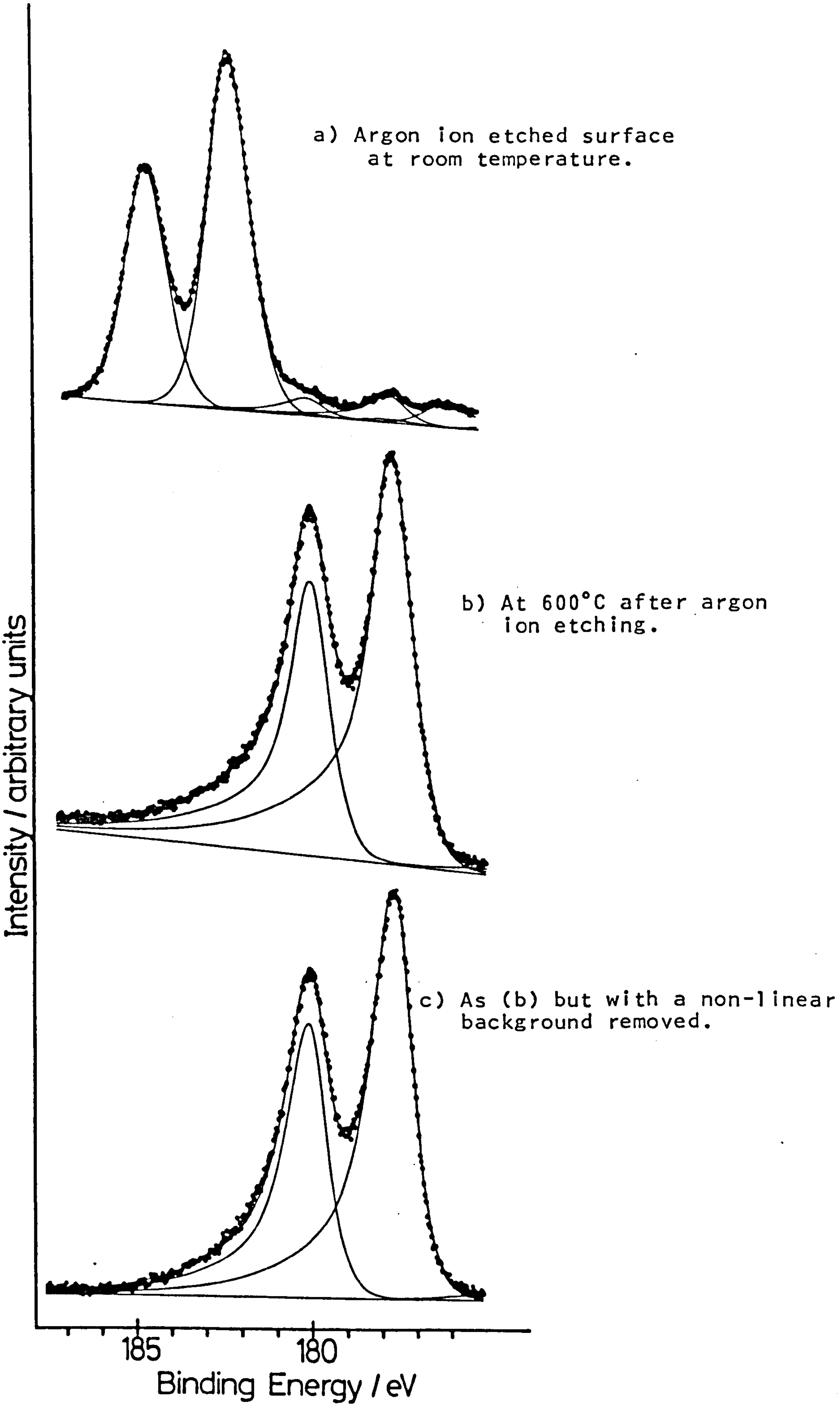

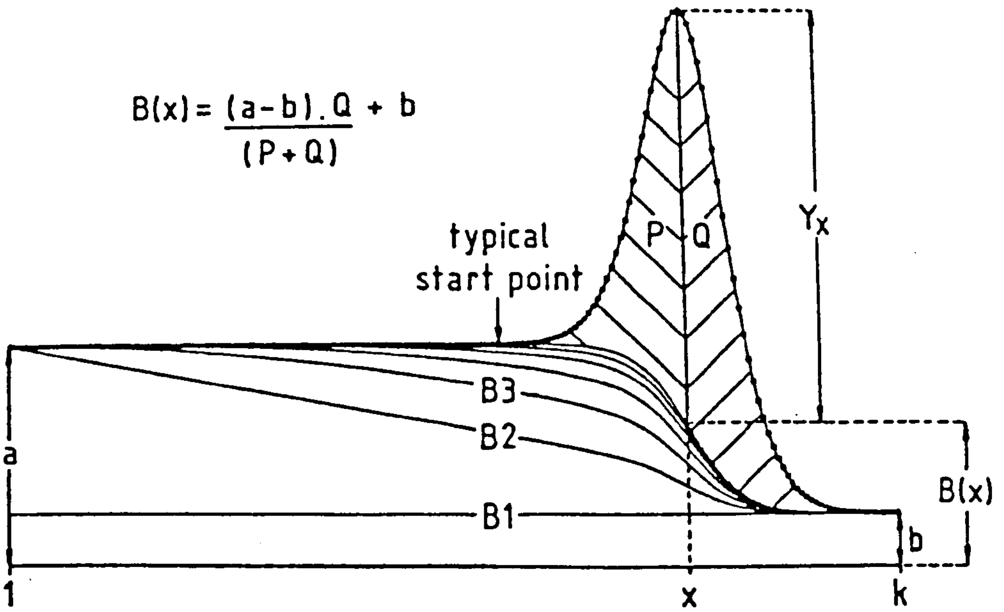

Fig 4.2:- Inelastic Background Determination. B(x) is the background at point x in the spectrum which contains k equally spaced points. (Reprinted from: A.Proctor and P.M.A.Sherwood, Anal.Chem, Vol 54, P13, 1982.)

Fig 4.3:- Spectra of Reference Compounds

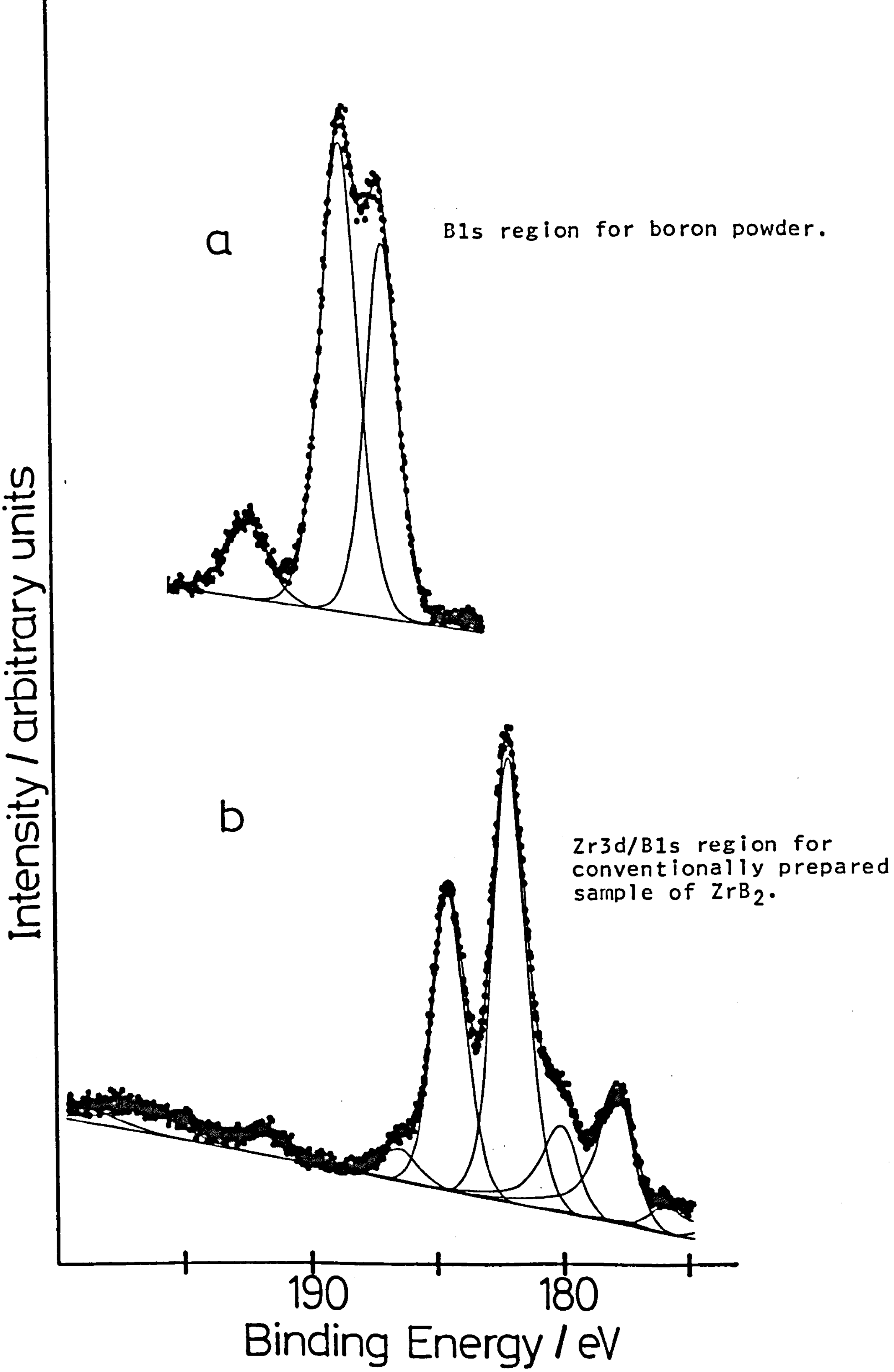

B1s region for boron powder.

Zr3d/B1s region for conventionally prepared sample of ZrB_2.

Fig 4.4:- Variation of Zr3d/B1s region for borided zirconium.
Spectra were recorded at θ=90° after etch times of:

a) 10 mins, b) 45 mins, c) 105 mins,

d) 165 mins.

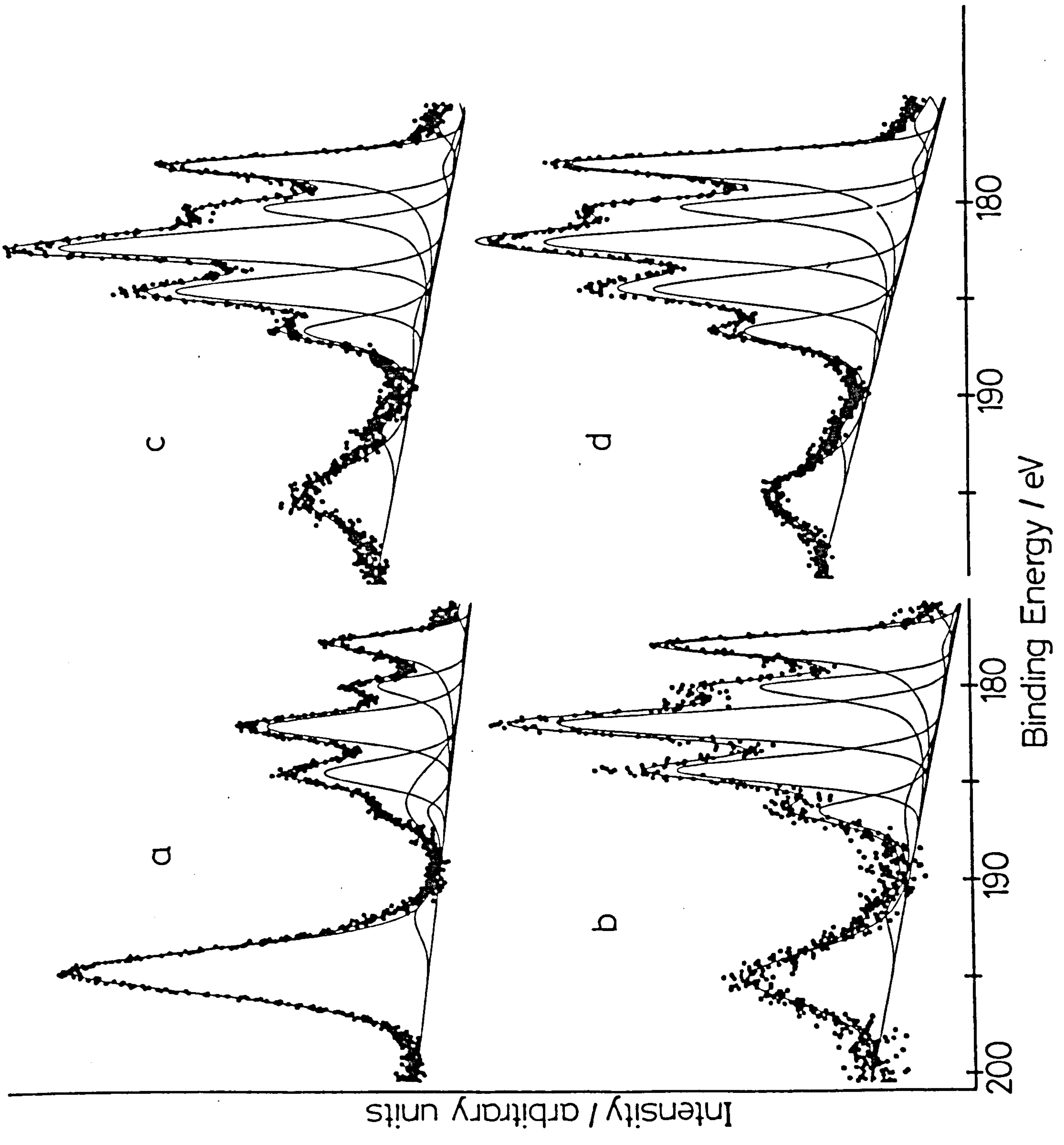

Fig 4.5:- Selection of O1s spectra for borided zirconium. Etch times and angles are as follows:

a) 10 mins and θ=90°,
b) 105 mins and θ=90°,
c) 165 mins and θ=90°,
d) 165 mins and θ=45°,
e) 165 mins and θ=5°.

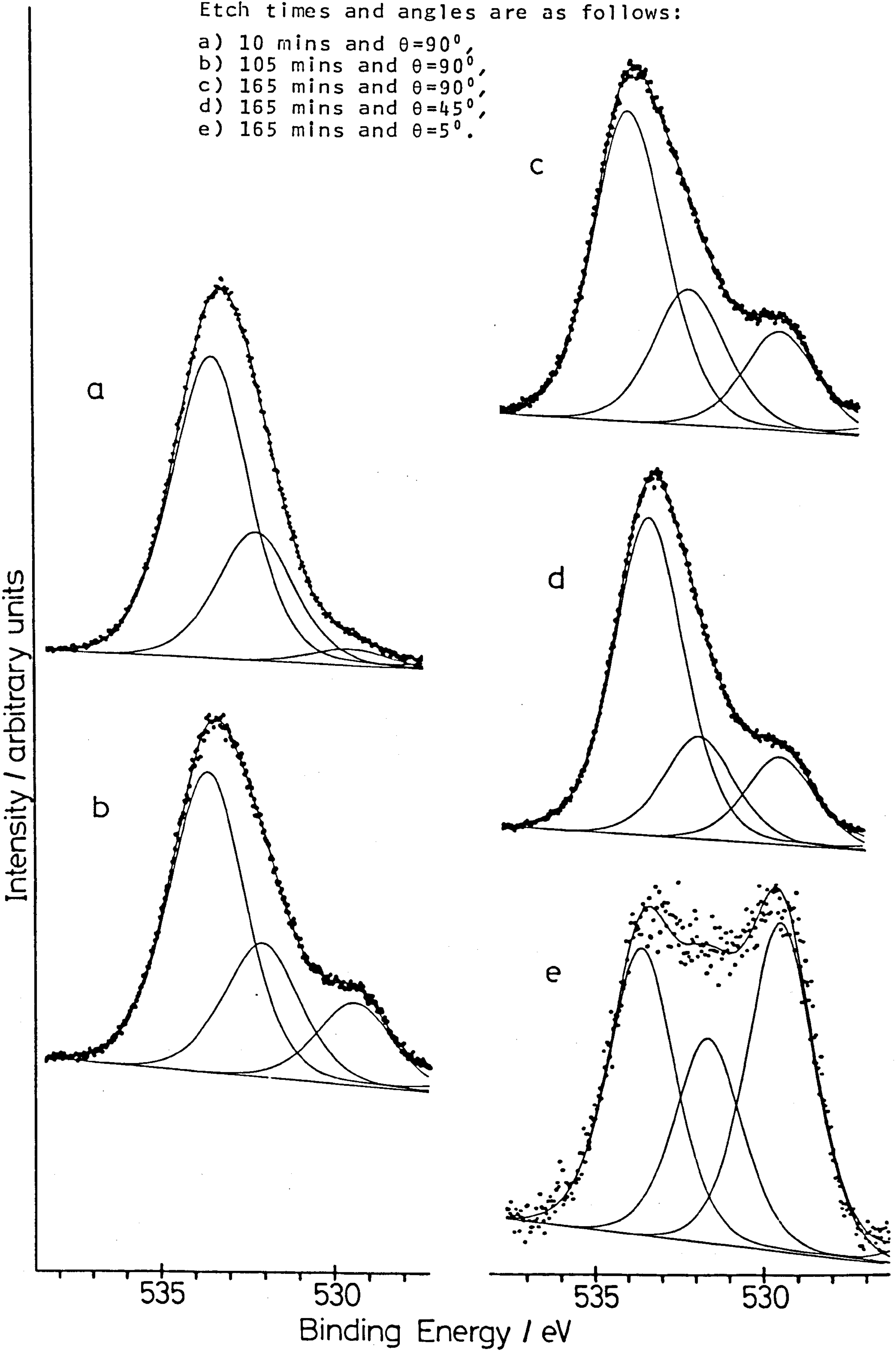

Fig 4.6:- Angular variation in the Zr3d/B1s region for borided zirconium. Etch times and angles are as follows:

a) 45 mins, θ=90°, b) 45 mins, θ=45°, c) 45 mins, θ=5°, d) 165 mins, θ=90°, e) 165 mins, θ=5°.

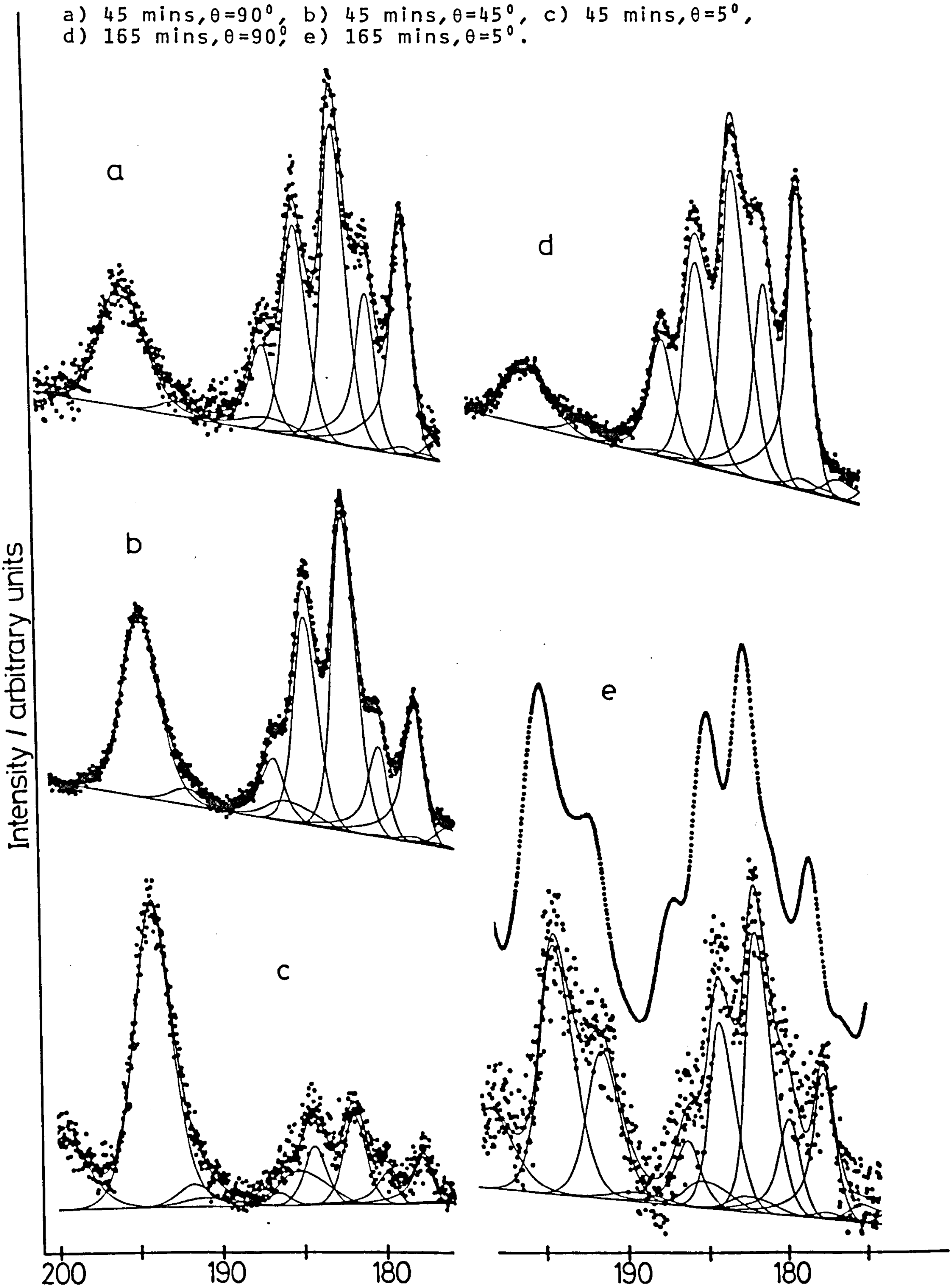

Fig 4.7:- Graph showing the variation of individual peak areas with respect to the total area for each species in the Zr3d/B1s region versus etch time (θ=90°).

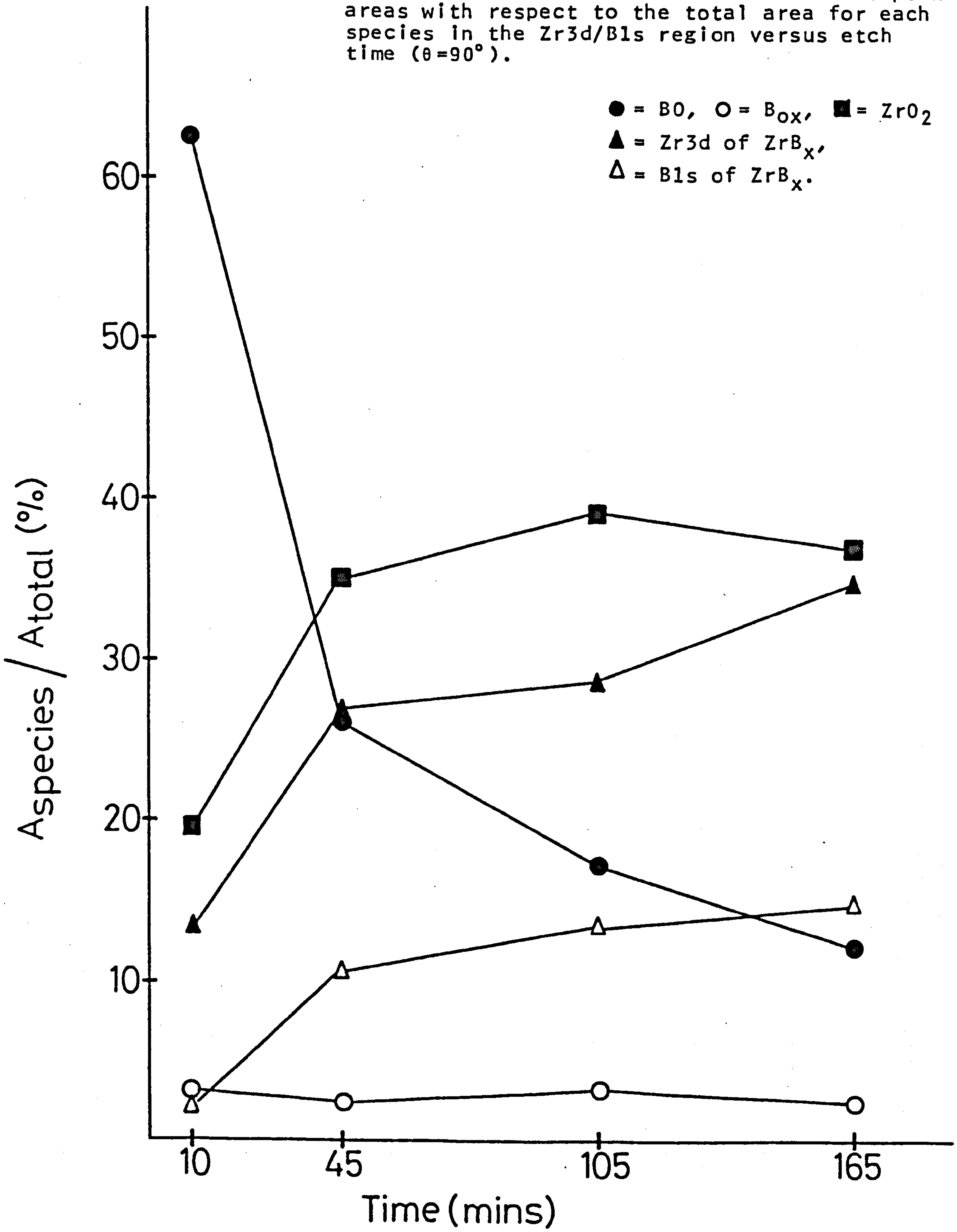

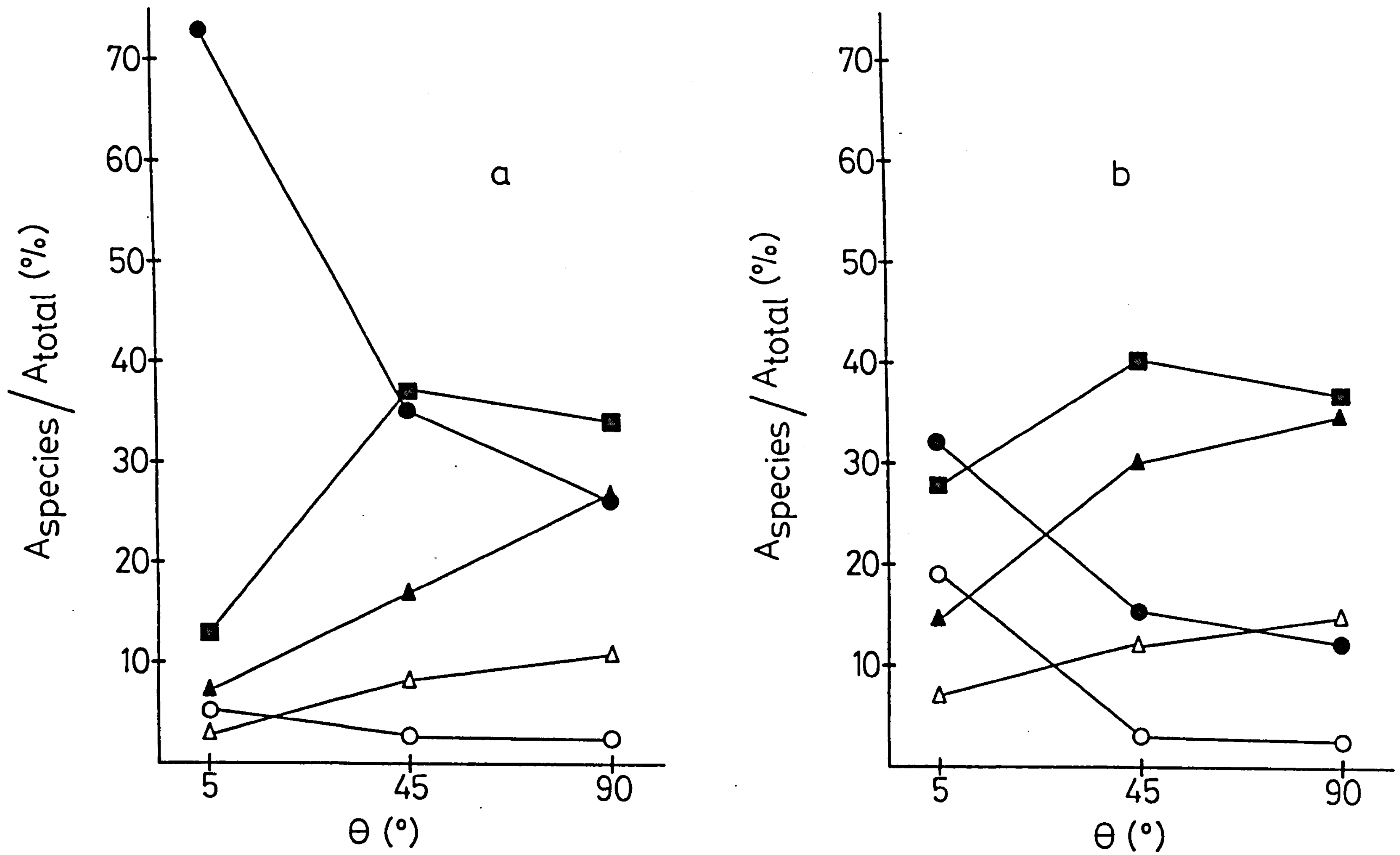

Fig 4.8:- Angular variation of individual peak area with respect to the total area for each species in the Zr3d/B1s region after etch times of a) 45 mins and b) 165 mins. Symbols as in fig 4.7.

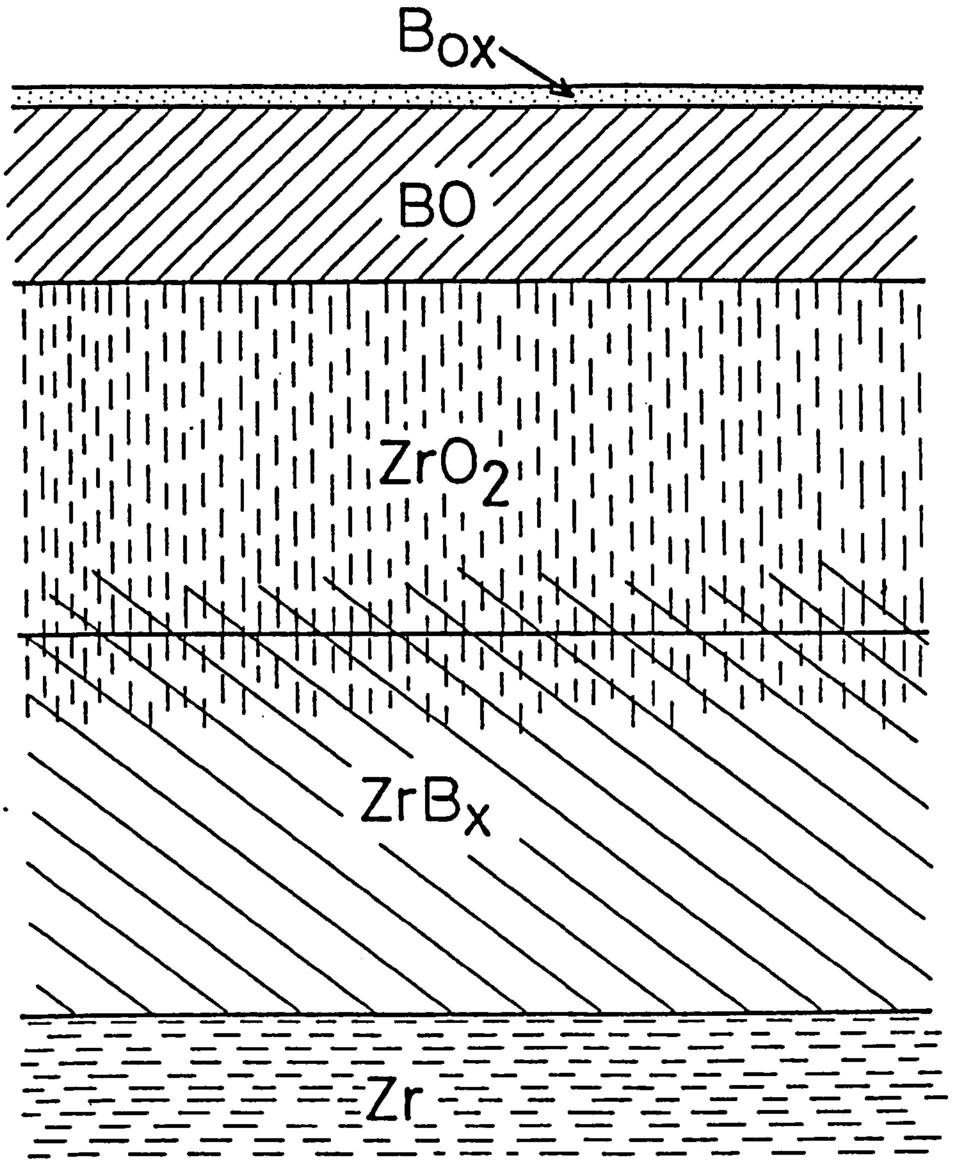

Fig 4.9:- Schematic representation of the surface structure of borided zirconium.

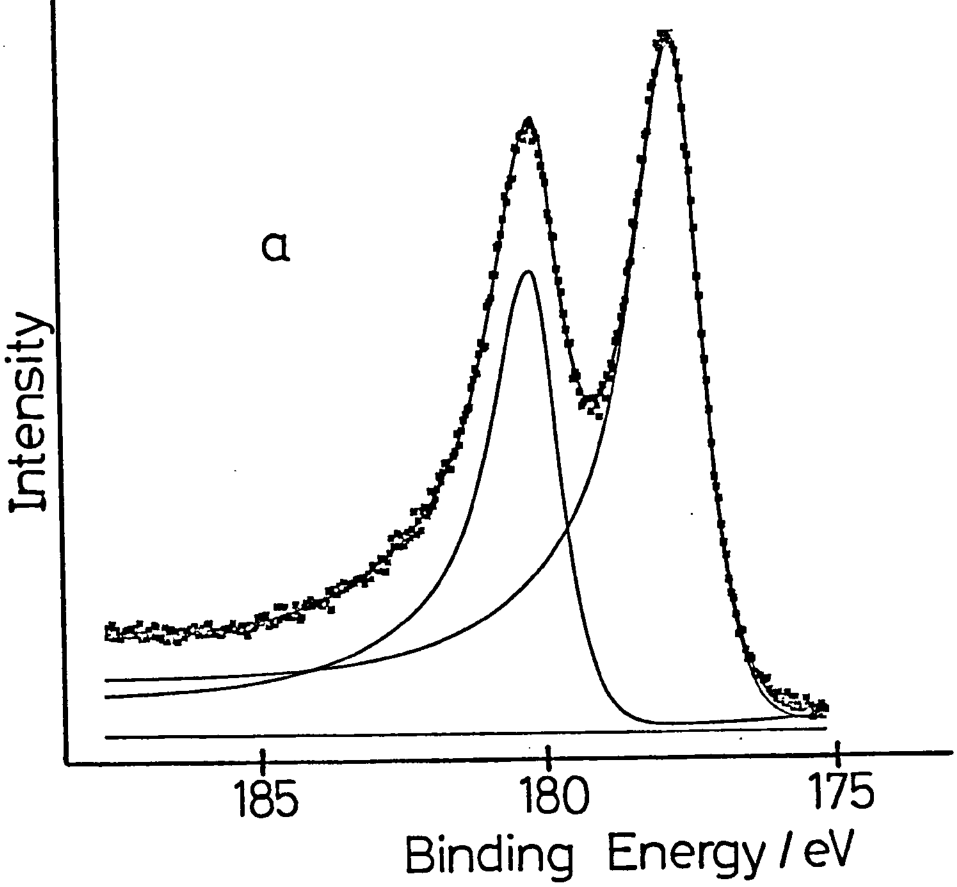

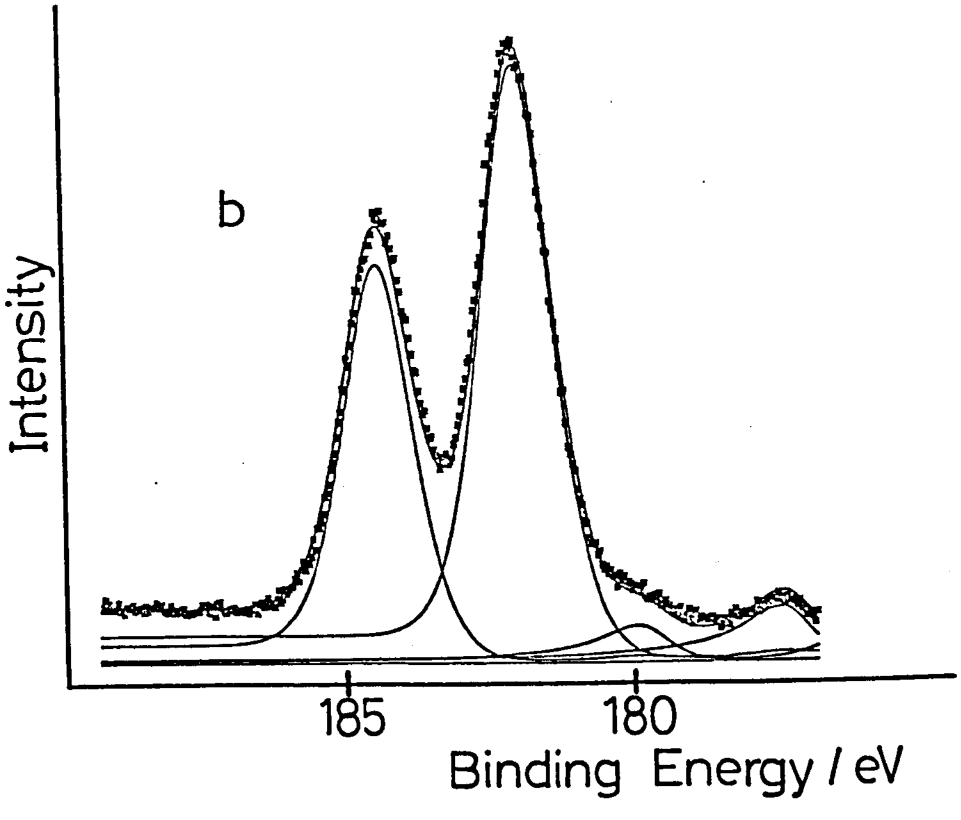

Fig 4.10:- Use of constant tails in the curve fitting of zirconium 3d spectra:

a) Pure Zr metal, b) Mainly oxide (ZrO2).

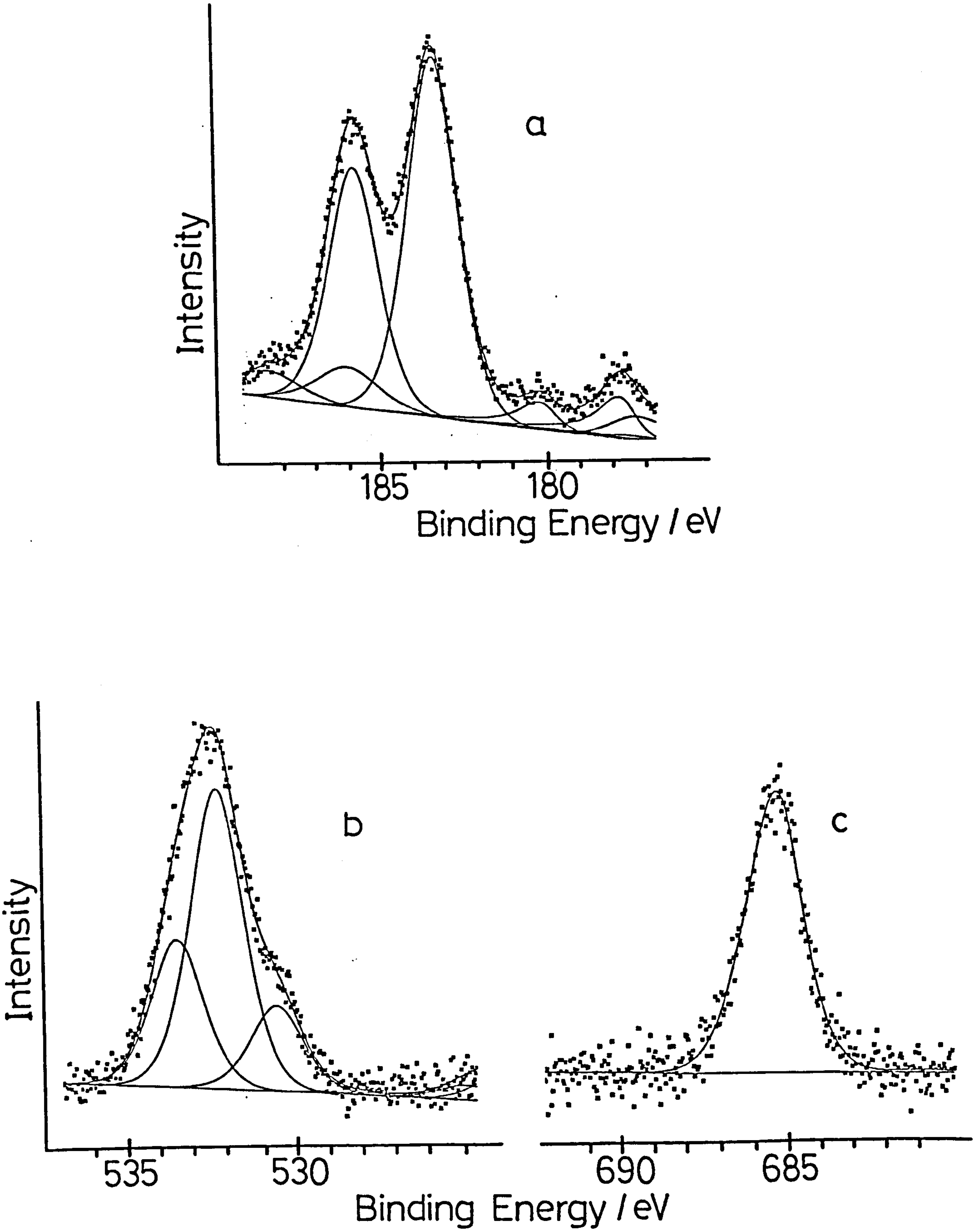

Fig 4.11:- Spectra recorded for zirconium foil after chemically cleaning with $HF/HNO_3/H_2O$. Spectral regions are:-
a) Zr3d, b) O1s, c) F1s.

CHAPTER FIVE

STUDIES OF URANIUM OXIDES AND RELATED SYSTEMS

5.1 Introduction

The work described in this chapter can essentially be divided into two parts. Firstly, the effect of heating uranium foil *in vacuo* has been investigated. The original aim of this particular study was to record spectra characteristic of the pure uranium metal in order to allow the direct measurement of the metal U4f core binding energies. The interesting and unusual results obtained in these experiments are discussed in comparison with work published in the literature. Secondly, a study was carried out on a class of compounds known as the ammonium uranates. Problems associated with their analysis by XPS are discussed in addition to some conclusions as to their chemical nature.

5.2 Data Analysis

The problems due to the inelastic background, associated with many uranium 4f spectra, were much more severe than the corresponding effects in the zirconium work (see Chapter 4). This is demonstrated by fig 5.1 which shows the U4f spectra recorded for one of the uranium oxides (fig 5.1a, see section 5.3.4) and one of the ammonium uranates (fig 5.1b). It is clear that the validity of the linear background approximation, in any curve fitting analysis, is questionable. Thus, the integral backround subtraction technique (85) was extensively used in this work. It must be stated, however, that the background subtraction method could not be applied to spectra in cases where:-

a) The spectral start and end points were not wholly, or indeed approximately, representative of the background alone.

b) The background profile on the high binding energy side of the principal photoelectron peaks was not approximately constant.

In order to satisfy condition a), many U4f spectra were recorded over an unusually large kinetic energy range.

Curve fitting was extensively employed to analyse spectra. However, as will be discussed in the text, there were many cases where the use of this technique was unsuccessful. Binding energy and FWHM errors (±2 x standard deviation), obtained from the curve fitting analysis, are quoted in parenthesis.

5.3 Studies Of Uranium Oxides

5.3.1 Introduction

Uranium metal has a considerable affinity for oxygen and water and readily forms oxide films (191,192). In the uranium atom, the 5f, 6d and 7s atomic energy levels are involved in chemical bonding giving rise to a large range of potential oxidation states. The uranium atom has an electronic configuration of $5f^3 6d^1 7s^2$ and this allows for a range of formal oxidation states from VI (corresponding to the involvement of all the valence electrons in chemical bonding) to III in the solid and solution states, and to II in the solid state only.

The uranium-oxygen system is an extremely complex binary system and many aspects of its chemistry are poorly understood (191,192). This is not only due to the existence of a large number of oxide phases but also to the fact that deviations from simple stoichiometry are more the rule than the exception. Many workers have examined the phase diagram of the uranium-oxygen system and the existence of at least four thermodynamically stable oxide phases (i.e. UO_2, U_4O_9, U_3O_8, UO_3) has been well established. In addition to these, several metastable phases such as U_3O_7, U_2O_5 and UO have been reported. Each of these oxide phases, both stable and metastable, can exhibit a wide variation in stoichiometry giving rise to the existence of a large number of non-stoichiometric phases. A full discussion of the chemistry of the oxides of uranium is beyond the scope of this thesis but excellent reviews by Cordfunke (191) and Colmenares (192) provide more details.

In this work, the examination of some oxide phases was particularly important since results could then be compared with those obtained for the ammonium uranates. The uranate complexes are "merely" ion exchange modifications of the oxide $UO_3.2H_2O$.

5.3.2 U_3O_8 Results

As previously stated (section 3.4.4.2), the use of adventitious carbon as a calibrant (1s = 285.0eV) gave a U_3O_8 $U4f_{7/2}$ binding energy of 380.66 (±0.14*, ±0.04eV). For this material, there are a range of U4f binding energies reported in the literature (380.6 - 381.5 eV), using various calibrants (193-195, and references therein). Most values, in fact, lie in the range 380.6 - 381.1 eV which is in reasonable agreement with that obtained in this work. These values, however, only refer to the observation of a single spin-orbit doublet in the U4f region, as was the case in this work (fig 5.2a). Other workers (196-198) have recorded better resolution spectra revealing the presence of two spin-orbit doublets corresponding to the presence of two types of uranium atom which exist in the formally mixed valence U_3O_8 material (i.e. $2UO_3.UO_2$).

Fig 5.2a shows the background subtracted U4f spectrum for U_3O_8. There were problems with the background subtraction procedure for this spectrum (i.e. condition b) was not fully satisfied, *vide supra*). However, from the analysis it was concluded that only one satellite (see also section 5.3.4) was associated with each principal U4f component. All peak centres could be measured with high accuracy to give a satellite energy loss value of 7.92 (±0.03) eV. This value is in good agreement with that obtained by other workers (195,197).

Using carbon as a calibrant (1s = 285.0eV), the oxide O1s binding energy was measured at 530.29 (±0.03) eV with a FWHM of

1.60 (±0.04) eV. It should be noted that, in the same experiment (using double-sided sellotape), the U4f FWHM was 2.38 (±0.04) eV. The presence of other oxygen components in the O1s region (O1s = 533.39, 531.80eV) indicated the existence of adsorbed and/or 'bulk' stored water, and oxygen associated with the sample.

5.3.3 UO_3 Results

The use of adventitious carbon as a calibrant (1s = 285.0eV) gave a UO_3 $U4f_{7/2}$ binding energy of 381.69 (±0.19*, ±0.04) eV. This is in good agreement with most values reported in the literature (381.5 - 381.9eV, refs 193-195,198,199). The U4f spectrum (fig 5.2b) did not show easily observable satellite structure as was the case for U_3O_8 (fig 5.2a). In fact, the background subtracted spectrum (i.e fig 5.2b) was well fitted to a single doublet. Inconclusive evidence for the presence of a satellite feature is given by the smoothed portion of fig 5.2b where a very weak feature is barely discernable lying approximately 4eV to the higher binding energy side of the $U4f_{5/2}$ component. Verbist (193) has published a particularly high quality spectrum for UO_3 showing the presence of a weak satellite peak lying approximately 3.8eV to the higher binding energy side of each principal 4f spin-orbit component.

In this work, it is important to note that attempts to obtain spectra with higher quality statistics were hindered by sample decomposition. The reduction of the sample was clearly observed in cases where spectra were recorded over extended time periods. The measured $U4f_{7/2}$ binding energy for such samples was considerably lower than that which was measured for samples analysed in a short timescale. Furthermore, in the former cases, a strong satellite was observed in the U4f spectra lying approximately 6.8eV to the higher binding energy side of the main U4f components. Sample discolouration was clearly noticeable after the material had been standing *in vacuo* for a considerable length of time (under X-ray bombardment). Allen (197) has also reported a similar decomposition process associated with other uranium oxides due to long term exposure to a vacuum. Further conclusive evidence was provided by the UO_3 valence band spectrum which is discussed in section 5.4.2.6.

The oxide O1s binding energy was measured at 530.13 (±0.08) eV with a FWHM of 2.07 (±0.06) eV. It should be noted that, in the same experiment (using double-sided sellotape), the U4f FWHM was 2.29 (0.04) eV. The O1s spectrum was similar to that obtained for U_3O_8 with other O1s components clearly visible (O1s = 533.23, 531.26eV). Previous workers have shown that hydration of UO_3 does not cause any change in the U4f binding energy (198, and references therein).

5.3.4 *In Vacuo* Heating Study

5.3.4.1 Experimental

Uranium metal sheet (>99.8%), supplied by Koch-Light Laboratories Ltd, was used in the experiments discussed in this section. A sample, cut from the sheet, was mounted onto the HTP probe in such a way that no signal could be attributed to the probe tip. The sample was chemically cleaned using nitric acid followed by water (triply distilled) and ethanol washing (193,200), before insertion into the spectrometer.

The spectrometer workfunction, which was measured at the time these experiments were carried out, was used for primary calibration purposes. Adventitious carbon (1s = 285.0eV) was used as a secondary calibrant. It should, however, be remembered that the C1s binding energy is not only a function of surface coverage (especially for conducting substrates), but also varies with substrate temperature (see chapter 3). Most binding energy values, quoted in the next section, were obtained by using the spectrometer workfunction for calibration. Values obtained by using adventitious carbon as a reference are clearly indicated in the text.

It is important to note that sample biasing was used to demonstrate that the surface uranium oxide layer, discussed in the next section, was a good conductor. Indeed, sample charging effects were not expected to be present (191,195,197).

5.3.4.2 Ambient Temperature Work

The considerable affinity of pure uranium for oxygen (191) means that surface studies of the clean metal are very difficult even at the typical instrument pressures used in XPS. The chemical cleaning method, discussed above, was not expected to generate a clean metal surface (193,200). This pretreatment was, however, successful in removing the thick, black oxide overlayer which was initially present on the uranium sheet. The resultant sample surface was bright and metallic-like in appearance. Once inserted into the spectrometer, the sample was argon ion etched for approximately 15 minutes to remove surface contaminants present after chemical cleaning.

The spectra recorded at this stage of the experiment were characteristic of a uranium oxide species on the substrate surface. No signal, corresponding to pure metal, was evident. Extensive argon ion etching was employed in an attempt to remove the oxide overlayer, without success. All uranium 4f spectra were similar to that obtained above, indicating the presence of a single oxide species. Fig 5.3a shows a wide scan, high quality U4f spectrum recorded at this stage of the work. The presence of a single uranium oxide species was confirmed, not only from the curve fitting of this spectrum, but also by recording a spectrum at a highly surface sensitive angle (see section 1.7.2). Surface oxidation did not occur during spectral collection.

As discussed earlier, curve fitting was complicated by the effect of the integral spectral background, which was therefore removed. The U4f spectrum, shown in fig 5.3a, is well fitted to 3 doublets (fig 5.4a). An exponential tail was included in the Gaussian-Lorentzian product function used to fit the principal U4f peaks. This was to account for conduction band interaction effects which were expected to be present (see section 1.10.4). Indeed, it was clear from the curve fitting analysis that the quality of the curve fit was significantly improved by the use of an exponential tail compared to the fit which was obtained when the exponential tail contribution was ignored.

The principal $U4f_{7/2}$ binding energy was measured at 379.54 (±0.01) eV with a peak FWHM of 1.96 (±0.01) eV. The carbon referenced binding energy (1s = 285.0eV) was in fair agreement with this value (i.e $U4f_{7/2}$ = 379.77±0.02 eV). This implies that a lower adventitious C1s binding energy (e.g 284.8eV) is more suitable for calibration purposes which is probably due to the substrate EARE effect (see chapter 3). Two satellite features, with energy loss values of 7.14 (±0.04) eV and 15.17 (±0.22) eV are clearly observed in the U4f spectrum (fig 5.4a). The oxygen 1s region (fig 5.4b) revealed the presence of three peaks (FWHM = 1.35±0.03 eV) at 532.60 (±0.11), 531.29 (±0.08) and 529.93 (±0.01) eV. The valence band spectrum was also recorded (fig 5.3b) since previous work has already shown that this region is very useful for identification of uranium oxide species (193,200-203).

The surface treatments, used in this work, are thought to have produced a non-stoichiometric oxide film which is closely related to uranium dioxide (UO_2). Previous work (193) has shown that chemical cleaning alone, using the procedure described above, produces a UO_2 surface film on uranium foil. A large amount of XPS work has been carried out on UO_2 (193-207) and the problems of non-stoichiometry have been highlighted (195,197,198,204). It is probable that the latter phenomenon accounts for the wide range of UO_2 U4f binding energies reported in the literature. Most values lie in the range 379.6-380.5 eV (193-196,199,201,204,205), using various calibrants. The most reliable values for stoichiometric UO_2 (i.e. $UO_{2.0}$) are 380.0-380.3 eV, refs 194,195,204). The tentative implication, based on the $U4f_{7/2}$ binding energy alone, is that the surface uranium oxide phase produced in this work corresponds to a species with an O/U molar ratio less than 2 (i.e UO_{2-x}). It is important to immediately point out that the value of x may be very small despite the apparently large difference in $U4f_{7/2}$ binding energy compared to the UO_2 literature values (0.5-0.8 eV). Other workers have shown that very small changes in oxide stoichiometry can have a relatively large effect on the U4f binding energies (195,204). Thus, Allen (204) has shown that the $U4f_{7/2}$ binding energy shift between $UO_{2.001}$ and $UO_{2.1}$ is 0.6eV. However, the general problems of binding energy calibration, make conclusions based upon the U4f binding energy alone, somewhat uncertain. More substantial evidence is given by the uranium metal - uranium oxide binding energy shift and this will be discussed later in the text.

Further information, as to the nature of the uranium oxide phase, is given by the satellite structure in the U4f region (fig 5.4a), and the valence band spectrum (fig 5.3b). The principal satellite, observed in the U4f spectra of UO_2 and its range of closely related non-stoichiometric oxide phases, is thought to correspond to a shake-up transition involving predominantly O2p and U5f molecular orbitals (206,207).

Allen (204) has shown that the satellite position is particularly sensitive to the value of x in UO_{2+x} phases. This satellite feature can therefore be used as a monitor of surface composition. It is well known that the satellite energy loss value in stoichiometric UO_2 is 6.8±0.1 eV (195,201,204,206). The value measured in this work was 7.14eV which indicates that the surface oxide phase, produced in this experiment, is not stoichiometric UO_2. Furthermore, for stoichiometric UO_2, Allen (204) has shown that the second satellite peak (see inset of fig 5.3a), lies 16.1eV to the higher binding energy side of the principal U4f peaks. Allen (204) has demonstrated that this feature is also sensitive to oxide composition. The much lower energy loss value (15.17eV), measured for this feature in this work, is again indicative of the formation of a non-stoichiometric oxide phase.

The valence band spectrum (fig 5.3b) is very similar to that published in the literature by a number of other workers for UO_2 (193,200,202,203,206). This indicates that the oxide phase, produced in this work, is closely related to UO_2. It has been shown that the uranium ion (U^{4+}), present in UO_2, has a $5f^2$ configuration (202, and references therein) and that the two 5f electrons occupy states immediately below the band gap, but well separated from the mainly O2p bonding band. Lam (202) has investigated the transfer of 5f electron density into the mainly O2p bonding band as a function of oxygen content for the UO_{2+x} system. The study clearly shows that as x is reduced from 0.67 to 0.0 (i.e $U_3O_8 \rightarrow UO_2$), the U5f/O2p peak height ratio increased. It was thought that the U5f/O2p peak height ratio, obtained in this work, could be used to help in the assignment of the uranium oxide phase produced in this experiment. However, examination of UO_2 valence band spectra published in the literature (193,200,202,203,206) revealed large discrepancies in this quantity. Different levels of surface contamination probably accounts for some of the differences. However, it is also probable that some of the spectra, published in the literature, do not correspond to stoichiometric UO_2. Thus, the U5f/O2p peak height ratio could not be used to help in the identification of the uranium oxide phase produced in this work.

As previously stated, the O1s spectrum corresponding to this surface uranium oxide was composed of three peaks (fig 5.4b). This spectrum is actually very similar to that obtained by other workers for an oxidised uranium surface (209). The lowest binding energy component (529.93eV) clearly dominates the spectrum and is obviously assigned to oxide species. The highest binding energy peak (532.60eV) is assigned to water whilst the intermediate O1s component is believed to be due to a mixture of hydroxide (209) and chemisorbed oxygen (210).

5.3.4.3 Elevated Temperature Work

The work discussed in this section will be closely compared with a similar study carried out by Allen and Tucker (205). These workers used a different chemical precleaning treatment on their uranium foil in addition to heating the sample to a higher maximum temperature (i.e 800°C).

Allen and Tucker (205) have previously shown that the heating of a uranium sample possessing a thin oxide overlayer (in 10^{-8} Nm^{-2}) results in the diffusion of metal atoms from the bulk to the surface of the material. The study showed that even at high temperature (800°C), the diffusion process (which competes with surface oxidation) was not sufficiently rapid enough to generate a pure metal surface. However, at 800 °C, the experimental data indicated that the substrate surface consisted of approximately 90% metal.

In this work, the uranium sample discussed above was heated 200°C, 400°C and 600°C *in vacuo* and spectra recorded at each temperature. Data were collected almost immediately and after approximately 1-2 hrs upon reaching each temperature. After the first run, the sample was cooled, re-etched and re-heated. The second, third and fourth runs were fairly short and involved sample heating to either 400°C and/or 600°C.

5.3.4.3.1 The Uranium 4f Region

Sample heating to 200°C produced essentially no change in the U4f spectrum (fig 5.5a) compared to that which was recorded at ambient temperature. This is in complete contrast to the spectrum recorded at 400°C where a dramatic change in the U4f region was observed (fig 5.5b). Although uranium oxide peaks are still evident, the spectrum is clearly dominated by a new set of U4f peaks which correspond to uranium metal (*vide infra*). The uranium metal/oxide ratio did not increase with time implying that an equilibrium situation (i.e. metal diffusion vs surface oxidation) was achieved very quickly. Heating to 600°C significantly increased the metal/oxide ratio although some oxide intensity is discernable (fig 5.5c). Results again showed that the metal/oxide equilibrium surface concentration was achieved very quickly.

It is clear, from figs 5.5b and 5.5c, that the spectral background associated with the U4f metal peaks is much larger than the background associated with the corresponding peaks for the uranium oxide (fig 5.5a). This severely complicated the application of data analysis methods to these spectra. It was thought that curve fitting would be extremely useful in analysing such spectra since, indeed, there may have been more than two uranium species present (*vide infra*). Such analysis, however, could only be carried out on background subtracted spectra. As already discussed in section 4.3.5, the background subtraction technique cannot discriminate between varying background contributions for different species in cases where the corresponding peaks are closely overlapped. Despite a large number of attempts, it was clear that curve fitting was of little use in analysing these spectra. This failure is attributed to the errors introduced by the use of background subtraction routine in addition to the considerable complexity of the spectra.

Despite the problems with the data analysis, the $U4f_{7/2}$ binding energy for uranium metal could be measured reasonably accurately to give a value of 377.60 (±0.08eV). This compares fairly well with most values reported in the literature which range from 377.1 - 378.0 eV (194,195,199,201,204,209). Thus, the difference in the U4f binding energy between U metal and the uranium oxide overlayer observed at ambient temperature (and also 200 C) is 1.94 (±0.09) eV. Indeed, this binding energy difference was also determined by direct measurement of the metal - metal oxide U4f peak centre separation in each spectrum. It is well established that the $U4f_{7/2}$ binding energy difference between U and UO_2 is 3.0±0.1 eV (193-195,201,204). This confirms that the uranium oxide species observed in this work is not stoichiometric UO_2.

It was important to be able to accurately measure the uranium oxide U4f binding energy at 400°C and 600°C since it was possible that the oxide stoichiometry had changed due to the heat treatment. This measurement was facilitated in two ways. Firstly, the oxide U4f$_{7/2}$ peak centre was measured from a spectrum which had been recorded at a surface sensitive angle (fig 5.5d). The greater proportion of oxide U4f signal in the spectrum meant that the U4f$_{7/2}$ peak position for this species could be determined with good accuracy. Secondly, a portion of each spectrum (containing the U4f$_{7/2}$ signals) was considerably expanded (fig 5.6). The results confirm that the oxide species observed at 400°C and 600°C is identical to that which was observed at ambient temperature.

The changes in the uranium 4f region bear some similarity to those observed by Allen and Tucker (205). One major difference lies in the nature of the oxide overlayer. The oxide species observed by Allen and Tucker (205) corresponds to UO_2. Nevertheless, their U4f spectrum indicates only two uranium species with the metal/oxide signal intensity ratio increasing with increasing temperature. However, these workers claimed that a third species, uranium monoxide (UO), was also formed on the uranium substrate surface at very high temperature (800°C). This was basically concluded from other spectral regions since there was certainly no indication of such a species in the U4f spectra. It is important to note that a U4f$_{7/2}$ binding energy for UO has not been reported in the literature. As previously stated, only two species are thought to be present in this work. This is of course not completely certain since curve fitting could not be applied to analyse the spectra.

Cooling the uranium sample to ambient temperature, re-etching the sample surface, and reheating to 400°C and/or 600 °C produced results which were similar to those discussed above, although the metal/oxide signal intensity ratios were different. Subsequent runs also produced different amounts of metal and oxide. This behaviour is unexplained.

5.3.4.3.2 The Carbon 1s Region

The C1s spectra, recorded in this work, were both interesting and somewhat unusual (fig 5.7). At 200°C, the region was dominated by a single peak which is assigned to adventitious carbon (fig 5.7a). The binding energy of this species (using the spectrometer workfunction) was 285.27 (±0.02) eV. Heating to 400°C produced a number of changes in this region (fig 5.7b). The adventitious carbon peak shifted in binding energy to 284.35 (±0.02) eV which is consistent with a change in the chemical nature of the adventitious layer (see chapter 3). Two components, at C1s binding energies of 285.89 (±0.08) and 287.61 (±0.13) eV, were also observed corresponding to CO and possibly CO_2, adsorbed onto the sample surface. The most interesting species, however, were observed at binding energies of 282.47 (±0.03) and 281.52 (±0.02) eV. These peaks are shifted -1.88 and -2.83 eV with respect to the adventitious C1s binding energy and are assigned to carbide species. It can be seen that the amount of carbide (both species) further increases at 600°C (fig 5.7c).

The binding energy shift of both carbide species w.r.t the adventitious carbon line is well within the range determined by Ramqvist (211,212) for other metal carbides. Allen and Tucker (205) have also observed carbide formation on the surface of uranium foil at high temperature. However, as can be seen from fig 5.9, a single species (-3.1eV w.r.t adventitious C1s line) was only observed at 800°C. This is obviously very different to the results obtained in this work.. The observation of carbide formation in the work of Allen and Tucker (205) lent support to their claim that UO was produced on the sample surface at very high temperature. There is some evidence to suggest that that the uranium monoxide (UO) phase can only exist in the presence of impurities such as carbon or nitrogen (191,213). This, however, is disputed by other workers (214).

A surface sensitive C1s spectra was recorded at 400°C (fig 5.7d), which can be directly compared with the corresponding "bulk" sensitive spectrum shown in fig 5.5b. It is clear that the carbide species lie further towards the bulk than the adventitious carbon layer, as expected. It is interesting to note, however, that the highest binding energy carbide species lies closer to the immediate sample surface as indicated by the change in the relative carbide C1s peak intensities with angle. This was confirmed by comparing other sets of C1s spectra. However, the actual distribution of each carbide species within the surface layers is unknown.

Finally, it is important to note that the FWHM's of the carbide species was fairly small (0.84±0.04 eV). This is more clearly demonstrated by a C1s spectrum which was dominated by the carbide signals (fig 5.7e). The small FWHM's are probably due to a lack of phonon broadening in the final C1s ion state due to the location of the carbide ions within the conducting uranium surface layers.

5.3.4.3.3 The Oxygen 1s Region

The O1s region, recorded at 200°C (fig 5.8a), was fairly similar to that which was observed at ambient temperature with three components being observed corresponding to water, hydroxide/chemisorbed oxygen, and oxide (*vide supra*). Heating to 400°C resulted in a massive loss of O1s intensity which corresponds to the appearance of large amounts of uranium metal (fig 5.8b). Further heating to 600°C resulted in a further reduction in the O1s signal intensity (fig 5.8c) corresponding to increased amounts of uranium metal diffusing to the sample surface.

The O1s spectra, recorded in this work, are quite different to those published by Allen and Tucker in their study (205). At elevated temperatures, these workers observed the appearance of two new O1s components (526.2 and 535.7 eV, see fig 5.9) which were well separated from the UO_2 O1s signal (530.7eV). These new peaks were assigned to UO and CO respectively. As can be seen from fig 5.9, the intensity of these peaks increases with increasing temperature. This region, therefore, constitutes the principal evidence for the existence of uranium monoxide on the surface of the uranium foil studied by these workers. Based on this evidence alone, it would seem that UO was certainly not produced in this work. However, as will be discussed in the next section, this conclusion may not be true.

5.3.4.4 Concluding Remarks

In this work, the heating of uranium foil in vacuo (400-600 °C) has produced a mixture of metal and oxide (of unknown stoichiometry) with considerable amounts of carbide present. Two carbide species are clearly in evidence although their distribution in the surface layers is uncertain. It is important to immediately point out that in a similar study of plutonium (heated in vacuo to 500°C), Larson and Haschke (215) have also observed carbide formation in addition to a mixture of metal and oxides. Indeed the existence of an oxycarbide phase (PuO_xC_y) was concluded.

The work, described in this thesis, is similar to that of Allen and Tucker (205) in several respects but differs significantly in others (*vide supra*). The major difference seems to concern the possible existence of uranium monoxide. In this work, there is no evidence for the existence of such a species although this is by no means conclusive due to the inability to accurately analyse the metal/oxide spectra. Allen and Tucker have claimed that UO is present on their uranium sample at 800°C, as concluded from the C1s and O1s spectral regions. The presence of carbide at high temperature lends support to this claim since, as previously stated, other workers have suggested that UO can only exist in the presence of impurities (191,213). This chemical model, for UO stabilisation, is rejected by Ellis (214) who claims that UO is a stable surface species at elevated temperatures, in the absence of impurities. Indeed, in this work, Ellis used Auger spectroscopy to observe a signal which was assigned to UO for a uranium sample heated to 700°C after various heat treatments in low amounts of oxygen. The stability of this phase was claimed to be dependent on the near-surface oxygen concentration and temperature. Carbide species were not observed and it was concluded that this species is not neccessary for the formation of uranium monoxide.

The effects of temperature on uranium and its oxides is a very important subject in view of the considerable use of uranium fuel rods in the nuclear power industry. The processes which occur at elevated temperatures are poorly understood. The differences between this study, the study of Allen and Tucker (205), and that of Ellis (214) testify to the complexity of the uranium-oxygen system and clearly much more work needs to be carried out in this area. In particular, the role of carbide species in the uranium oxide system needs to be clarified. Furthermore, work is required to establish the conditions neccessary for uranium monoxide formation.

Finally, it must be stated that the author of this thesis rejects the evidence presented by Allen and Tucker (205) for the presence of uranium monoxide on their uranium sample at 800°C. It is more likely that the peaks, evident in the O1s region at 526.2 and 535.7 eV, correspond to antimony impurity (i.e. Sb3d levels) which is observed due to its surface segregation *in vacuo* (see chapter 6). This conclusion is based upon the binding energy of both components in addition the the peak separation which is in excellent agreement with published values for the Sb3d spin-orbit splitting. The surface segregation of antimony in gold has been reported (258).

5.4 The Ammonium Uranate System

There is considerable interest in the ammonium uranate system in the nuclear power industry. Ammonium uranate (ADU) is precipitated when ammonia is added to a uranium (VI) solution. This reaction is employed for the removal of uranium from waste effluent from nuclear fuel reprocessing. Unfortunately, the volume of uranate precipitant varies considerably with the slightest change in conditions causing considerable technical difficulties. Part of the problem stems from the general uncertainty as to the exact chemical nature of the ammonium uranate system.

Most of the work reported in the literature has studied ammonium uranate compounds prepared by the reaction of ammonia with uranium trioxide dihydrate (216-218) or uranyl nitrate (217-223). Studies have shown that the chemical nature of the ammonium uranates is critically dependent upon a number of experimental factors (217,222,224) e.g. pH, temperature, reaction time, solution concentration etc. The problem is complicated by poorly characterised transformations and ion-exchange reactions which occur in both the solution and solid phases (219,225). Furthermore, the nature of the ammonia coordination within the uranate complexes is uncertain. It can, however, be said that the original name of ammonium diuranate (ADU) and formula of $(NH_4)_2U_2O_7$ are incorrect. No compound, even at high ammonia concentrations, can be identified as having a N/U molar ratio approaching unity.

Conclusions, as to the chemical nature of the ammonium uranate system, have been based upon infrared spectroscopy, chemical analysis and X-ray diffraction. No photoelectron work has been reported to date. Several chemical structures exist for these compounds. Cordefunke (216) has proposed a multiphase hypothesis and states that only four distinct phases can occur with the compositions:-

$UO_3.2H_2O$
$3UO_3.NH_3.5H_2O$
$2UO_3.NH_3.3H_2O$
$3UO_3.2NH_3.4H_2O$

Thus, in the uranates, ammonia (NH_3) coordination is postulated. Deane (226) has also concluded that ammonia is present as coordinated NH_3 molecules but suggested a different structure to that presented above (216) i.e. $UO_2(OH)_2.xNH_3.H_2O$. Hermans (217) has also postulated NH_3 coordination with chemical structures similar to those of Cordefunke (216). Debets and Loopstra (227) have suggested that ammonia is combined as the NH_4^- ion, but did not present direct experimental evidence for this.

The structural model proposed by Stuart (218,228) is in complete disagreement with the above view. A continuous-phase system is thought to exist with the general formula:-

$$UO_2(OH)_{2-x}.(ONH_4)_x.yH_2O$$

Thus, in this model, ammonium ions are coordinated within the uranate structure. The presence of coordinated ammonium ions is supported by other workers (219,221). Quy-Dao (219) has proposed that the ammonium uranate formula is of the form:-

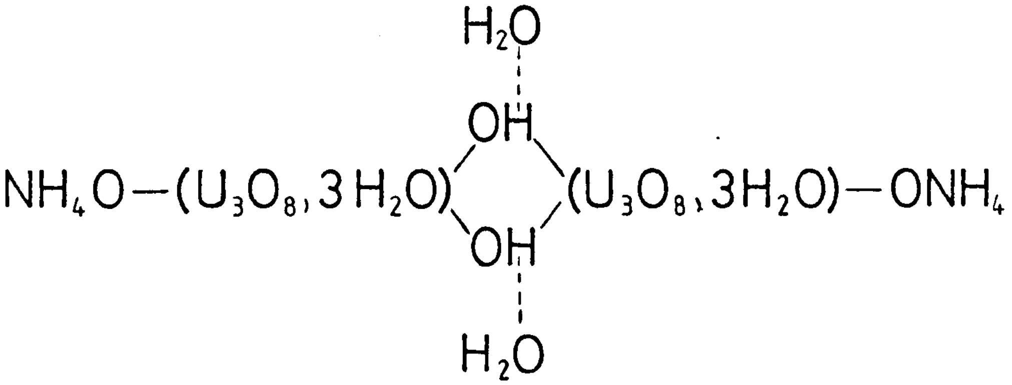

Finally, Urbanek (223) has postulated that both NH_3 and NH_4^+ species are present under the appropriate reaction conditions.

As previously stated, the complex ion-exchange processes, which occur in both the solution and solid phases, are poorly characterised. Numerous workers (216,217,219,220, and references therein) have studied the reaction between uranyl nitrate and ammonia, and have interpreted their results in terms of complex ion formation. In aqueous solution, all uranyl ions are hydrolysed and a large proportion also associate with other coordinating groups to form a range of polymeric species. A wide variety of such species have been reported and many results are conflicting to say the least. Species such as $UO_2(OH)^+$, $U_2O_5^{2+}$, $(UO_2)_2(OH)_2^{2+}$, $U_3O_8^{2+}$, $(UO_2)_3(OH)_5^+$, $U_4O_8(OH)_6^{2+}$, $U_3O_8(OH)^+$ and $UO_2\left((OH)_2UO_2\right)_n^{2+}$ are said to exist (220, and references therein). The nature and the amount of such species is critically dependent upon reaction conditions i.e pH, solution concentration, reaction time, temperature etc. The incorporation of ammonium and/or ammonia species into such structures adds to the complexity of the system.

It is thus apparent that the precise chemical nature of the ammonium uranates is quite uncertain. The following sections describe some initial experiments carried out using XPS to study this chemical system.

5.4.1 Experimental

Some ammonium uranate compounds were prepared in the laboratory by the direct titration of uranyl nitrate solution (0.20M) with ammonia (20.55M), at a solution temperature of 40±2°C. The pH curve for this reaction is shown in fig 5.10 and is very similar to that obtained by Cordefunke (216). Uranate precipitation was observed to begin at a pH of approximately 3.5 and appeared to be complete at around pH 4. Samples were prepared by titrating to the correct pH, equilibrating the solution at 40°C for approximately three hours, and quickly filtering off the yellow solid in air. Each sample was obtained by carrying out a different titration run. The filtered samples were washed with ethanol to remove adsorbed ions (223,224,229), particularly nitrate which is known to be strongly retained on and/or within ammonium uranate samples (216,224). Samples were then partially dried at 40-45°C (principally to remove residual ethanol) and stored over P_2O_5 in a dessicator.

Seven samples were synthesised using the above procedure and the preparative conditions are tabulated in table 5.1. It should be noted that an initial and final solution pH is quoted for each sample. The observed decrease in solution pH with sample equilibration time has been noted by other workers (216). This behaviour is attributed to the complex solution and solid ion-exchange processes described above (216, and references therein). It should be noted that the samples will be identified in the following text by their corresponding final pH solution values.

Two ammonium uranate samples were also supplied by Dounreay. These compounds were also prepared by the reaction of uranyl nitrate with ammonia. The sample equilibration times (at room temperature) were, however, much longer than those used for the above preparations. Thus ADU1 (final solution pH = 8.0) had been equilibrated for several months whereas ADU2 (final solution pH = 7.0) had been equilibrated for over a year. Both samples were filtered off, washed and dried in a manner similar to that described above. It should be noted that for all samples discussed in this section, unwashed sample portions were collected and, in some cases, XPS and IR spectra recorded. A significant nitrate signal was observed in all cases , even for samples synthesised at high pH's.

All samples were mounted on double sided sellotape with the exception of those used in the thermal decomposition experiments (see section 5.4.2.7). The latter samples were mounted on a grid of fine mesh (approx 0.5mm mesh size) since double sided sellotape was unsuitable for elevated temperature work. All samples were freshly ground in a small mortar prior to their insertion into the spectrometer. All binding energies discussed in this section are referenced against the C1s line (285.0eV) corresponding to adventitious carbon. The suitability of this calibrant, for the ammonium uranates, has already been validated in chapter 3.

Much of the initial work concentrated on the collection of data at ambient temperature. However, it was realised that slow sample decomposition was occuring *in vacuo* under X-ray bombardment. Changes in all spectral regions were clearly evident for samples analysed over very long time periods. Sample discolouration was also noticeable. Thus it was neccessary to cool samples to a low temperature (77K) *in situ*. This was achieved by simply pumping liquid nitrogen to the sample support block. This cooling procedure consisted of a) letting up the sample chamber to argon gas, b) insertion of the sample under investigation, and c) pumping liquid nitrogen to the sample block while simultaneously pumping down the chamber.

5.4.2 Results and Discussion

5.4.2.1 Reference Compounds

The XPS spectra for some uranyl salts were analysed for comparison with the ammonium uranate spectra. These compounds complemented the spectra of the uranium oxide system discussed earlier.

Table 5.2 contains the $U4f_{7/2}$ binding energies for uranyl nitrate, sulphate, formate and oxalate, in addition to the satellite energy loss values. The latter two compounds were analysed at 77K. The U4f spectra for the latter three compounds are shown in fig 5.11. No satellite was observed to be associated with the U4f peaks for uranyl nitrate. In fact, in this sample, a small amount of decomposition was evident, indicated by the presence of a small shoulder on the nitrate U4f peaks. Furthermore, a very weak satellite was observed lying approximately 9 eV to the higher binding energy side of the principal nitrate U4f peaks. It has already been shown that satellite features are very sensitive for monitoring changes in chemical state and environment (*vide supra*). This is illustrated by the significant differences in the satellite feature (both peak position and intensity) associated with the principal U4f peaks for each of these materials.

It should be noted that table 5.2 contains the N1s binding energies for some ammonium salts (recorded at 77K) for comparison with the N1s region of the ammonium uranates (*vide infra*).

5.4.2.2 Infrared Spectra of the Uranates

Infrared spectra, recorded for all washed uranate samples, were very similar in most respects. A typical example is given in fig 5.12a which shows part of the spectrum recorded for the pH 10.3 sample (700-2000cm^{-1}). Table 5.3 lists the important band assignments for this spectrum. Thus, the presence of the groups UO^{2+}, -OH, H_2O and NH_4^+ are clearly indicated. The latter assignment is in agreement with some other workers (219,221,228) and is based on the fact that ammonium salts are well known to exhibit a strong band in this region. However, Deane (226) has assigned this band to coordinated ammonia. This typifies the uncertain chemical nature of the ammonium uranates. It is interesting to compare the above spectrum with that obtained for the corresponding unwashed sample (fig 5.12b). The strong, sharp signal due to nitrate (1383cm^{-1}) is clearly observed.

Stuart and Whately (218) have prepared a set of ammonium uranates by the reaction of uranium trioxide dihydrate or uranyl nitrate with ammonia and observed interesting behaviour associated with the principal UO^{2+} (U-Ostr) band at approximately 900cm^{-1}. These workers observed a decrease in this U-Ostr band stretching frequency as the uranate N/U molar ratio increased (i.e. as the solution pH increased). A similar observation is made in this work. A maximum shift of 20cm^{-1} is observed between the pH 4.2 (910cm^{-1}) and pH 11.2 (890cm^{-1}) samples. This, therefore, indicates that the uranyl U-O bond distance increases with increasing pH, for the samples prepared by the author (218, and references therein). Finally, it should be noted that the ADU2 sample had the highest principal U-Ostr band stretching frequency out of all the samples analysed (922cm^{-1}).

5.4.2.3 The Uranium 4f Region of the Uranates

XPS spectra were recorded for the following samples:- pH's 5.6, 8.0, 10.3, 10.5, 11.2 and both samples supplied by Dounreay. Some wide scan U4f spectra were recorded in order to allow the use of the background subtraction technique for curve fitting purposes. The use of a wide scan also meant that the N1s signals due to ammonium/ammonia and nitrate could be observed in conjunction with the U4f signals. It is clear from fig 5.13, that the amount of nitrogen species associated with the pH 10.3 (fig 5.13a) and ADU2 (fig 5.13b) samples is extremely small. All samples were, in fact, characterised by extremely weak nitrogen signals (see section 5.4.2.4) This was also true for unwashed uranate samples.

Table 5.4 displays the $U4f_{7/2}$ binding energies calculated for each sample. The table shows that the lower pH samples (i.e. 5.6, 8.0), prepared by the author, have $U4f_{7/2}$ peak binding energies which are lower than the corresponding values for the higher pH samples. Although spectra were only recorded for a few samples, these binding energy differences are thought to be genuine in view of the preliminary work carried out on the suitability of adventitious carbon as a calibrant (see chapter 3). There seems to be some correlation between the U4f binding energy and the uranyl ion U-Ostr stretching frequency discussed in the previous section. Thus, as the pH increases, the U-Ostr band stretching frequency decreases whilst the $U4f_{7/2}$ binding energy increases. This therefore implies that the U4f binding energy increases with increasing uranyl ion U-O bond distance (see previous section).

No correlation between the satellite energy loss and sample pH is evident. The satellite was observed at $\sim 7{\cdot}2$ eV in all cases. The intensity of the satellite features in all spectra were weaker than the corresponding features in uranyl sulphate and uranyl formate. It is interesting to note that the ADU2 sample had a $U4f_{7/2}$ binding energy which was similar to those obtained for the low pH samples prepared with short solution equilibration times (*vide infra*).

5.4.2.4 The N1s Region of the Uranates

As stated above, the nitrogen 1s signals for all samples were extremely weak. This is clearly demonstrated by fig 5.14 which shows the N1s/U4f$_{5/2}$ satellite region for the pH 5.6 (fig 5.14a), pH10.3 (fig 5.14b) and ADU2 (fig 5.14c) samples.The infrared spectrum seems to indicate the presence of ammonium ions in all uranate samples. It is therefore reasonable to assign this N1s signal to ammonium species. The N1s binding energy for this species was 402·4 ± 0·15 eV. It is not possible to assign this species on the basis of its XPS binding energies alone in view of the considerable variation in N1s binding energy for a series of ammonium salts (see table 5.2).

5.4.2.5 The O1s Region of the Uranates

O1s spectra, recorded for all samples, were composed of three components (fig 5.15). The lowest binding energy species (~530 - 530·5 eV) corresponds to oxide type oxygen. The other species are assigned to be hydroxide (~531- 532 eV) and water (~533 eV). It can be seen from the spectra (fig 5.15) that there is no discernable trend in terms of relative peak intensity ratios. The variation in the O1s region may be explained by the existence of a variety of oxygen species. Thus, for example, one might expect that coordinated water would have a different binding energy to water which is simply trapped or adsorbed. The different forms of hydroxide (i.e. bridged or unbridged) may also give rise to different O1s binding energies. The magnitude of such effects is not known but the O1s spectra recorded in this work testify to the complexity of the system.

5.4.2.6 Valence Band Spectra

The valence band spectra of some of the uranates were studied at liquid nitrogen and ambient temperature. Fig 5.16 shows the valence band region for ADU2 (fig 5.16a), and laboratory prepared samples at pH 10.3 (fig 5.16c) and pH 5.6 (fig 5.16b). The latter sample was studied at liquid nitrogen temperatures. These spectra can be compared with the valence band regions recorded for UO_3 and uranyl nitrate at ambient temperature (Fig 5.17). The uranates and the oxide all show a U5f band which is not expected since they formally contain uranium in the VI valence state, and therefore should have zero occupation of the U5f non-bonding band. This situation is observed in the spectrum of uranyl nitrate. The presence of the U5f band would therefore appear to be due to sample decomposition. Although decomposition is expected at ambient temperature, it is surprising to observe this process at liquid nitrogen temperature (pH 5.6 sample). It should be pointed out, however, that sample decomposition at 77K is much less serious than the corresponding effect at ambient temperature. It should also be noted that the data collection time for the valence band shown in fig 5.16b was considerably longer than the corresponding time taken for the core levels. Thus, sample decomposition effects are expected to be small in all core level spectra. It is difficult to conclude by what mechanism the decomposition process takes place. One possibility is that highly localised surface heating is taking place. Direct X-ray decomposition is also possible.

5.4.2.7 Thermal Decomposition studies of the Uranates

All the above studies of the uranates were carried out at liquid nitrogen temperature. Above this temperature the samples decompose, slowly at ambient temperatures, and more rapidly at elevated temperatures. The pH 5·6 and 10·3 samples were studied at ambient temperature , and a range of temperatures from 105°C to 275°C where the samples were heated *in vacuo* in the XPS machine.

These studies showed spectral changes which it was hoped would throw more light on the spectral features at liquid nitrogen temperatures. As explained above these experiments had to be carried out with samples mounted on a grid, and this led to problems due to differential sample charging which complicated the interpretation of the results. Thus fig 5.18 illustrates differential sample charging in the U4f region of the pH 10.3 sample by comparison of the spectrum at ambient temperature (fig 5.18a) and that at 275°C (fig 5.18b). It can be seen that the sample charging falls off as the temperature is raised due to the conversion of the uranate into a reasonably conducting oxide species due to the thermal decomposition process.

Significant changes were seen in the U4f and O1s regions for both samples after heating to a range of temperatures. The most striking features of the results are:

(a) For both samples, heating to 105°C caused a very significant decrease in the 'hydroxide'/'oxide' O1s peak area ratio. Such an observation perhaps impies that there are two general types of hydroxide species present in the uranate lattice, one of which is less strongly bound within the sample. It must also be noted that the 'hydroxide' peak is still present in the spectrum after heating up to 275°C. This signal is unlikely to correspond to hydroxyl species (*vide supra*) and probably corresponds to oxidic type species. This latter peak is observed in conjunction with the other dominant oxide peak which is observed at lower binding energy.

(b) On heating the samples from ambient temperature to 275 °C, it was clear that the reduction in the pH 5.6 sample U4f binding energy was less than that which was observed for the pH 10.3 sample. This would suggest that the former sample is more oxide-like in its chemical nature.

(c) Small amounts of nitrate can be seen even after heating to high temperatures. This supports the observation in the literature that nitrate ions are strongly retained on ammonium uranate samples.

(d) There was no sign of a N1s signal corresponding to the presence of ammonium ions on any of the samples after heating above 105°C. This clearly suggests ready decomposition of the ammonium ions as might be expected.

As previously discussed the nature of the nitrogen coordination in these compounds is still unresolved, thus it is not known whether the nitrogen is in the form of NH_4^+ or NH_3. The infra-red spectrum before thermal decomposition shows a band characteristic of ammonium coordination (see fig 5.19). The infra-red spectrum after thermal decompostion clearly showed a massive loss in ammonium intensity and the appearence of a new band at 1240 cm^{-1} (Fig 5.19). This latter band is assigned to ammonia formation which will arise from decomposition of the ammonium ions. The observation of this new band clearly favours the idea that the nitrogen species incorporated into the original uranate samples is in the form of ammonium. The complete loss of hydroxyl groups was also evident, consistent with the formation of a more oxide type species.

5.5 Conclusions

The effect of *in vacuo* heating of uranium has been studied. The treatment has produced a mixture of uranium metal and oxide on the sample surface in addition to the formation of two carbide species. This study has been compared with those of other workers and further indicates that a better understanding of the uranium metal/oxide system, at elevated temperatures, is required.

The ammonium uranate system has been studied. Problems associated with the analysis of these samples have been mentioned. Indeed, it is clear that future work must carefully monitor such effects. Most samples were prepared using short solution equilibration times which seems to have resulted in the incorporation of only small amounts of ammonium ion into the uranate samples. The small amounts of ammonium species observed for the Dounreay samples is thought to be due to the relatively low solution pH's and low solution temperature. It is therefore suggested that more conclusive characterisation of the nitrogen species would be better achieved via longer term,high temperature equilibration (e.g >40°C) of high pH samples. For samples prepared by the author, there would appear to be some correlation of U4f binding energy with sample pH, and with the principal U-Ostr band stretching frequency for the uranyl ion. This correlation may be of considerable use in future work on this chemical system. It is clear that the samples prepared by the author and those supplied by Dounreay are very similar in their chemical nature.

Table 5.1

Preparation of the Ammonium Uranates

Initial Solution pH	Final Solution pH	Molarity and Volume of Uranyl Nitrate used	Molarity and Volume of Ammonia used
4.5	4.2	0.20M/200ml	20.55M/6.6ml
6.1	5.6	0.20M/200ml	20.55M/6.8ml
8.5	8.0	0.20M/200ml	20.55M/9.2ml
10.9	10.3	0.20M/200ml	20.55M/167ml
11.0	10.5	0.20M/100ml	20.55M/160ml
11.3	11.1	0.20M/50ml	20.55M/125ml
11.4	11.2	0.20M/50ml	20.55M/250ml

Table 5.2

Spectral Data Obtained for some Reference Compounds

Compound	$U4f_{7/2}$ Binding Energy(eV)	Satellite Loss(eV)
Uranyl Oxalate	381.93 + 0.07	5.62 + 0.07
Uranyl Formate	380.81 + 0.04	5.80 + 0.14
Uranyl Sulphate	381.92 + 0.03	5.60 + 0.10
Uranyl Nitrate	382.45 + 0.05	-

Compound	N1s Binding Energy (eV)
Ammonium Nitrate	401.97 + 0.07
Ammonium Sulphate	402.24 + 0.02
Ammonium Carbonate	401.00 + 0.04
Ammonium Chloride	401.48 + 0.02

Band Assignments for Infrared spectrum of pH 10.3 (washed)

Table 5.3

Absorption(cm^{-1})	Absorbing Group	Type of Vibration	Intensity
3440	H_2O	$O\text{-}H_{str}$	strong, broad
3180	NH_4^+	$N\text{-}H_{str}$	strong, broad
1625	H_2O	$O\text{-}H_{def}$	medium, broad
1405	NH_4^+	$N\text{-}H_{def}$	strong, medium sharp
995	-OH	$O\text{-}H_{def}$	weak, broad
895	UO_2	$U\text{-}O_{str}$	strong, medium-sharp
470	U-O	-	medium, broad
370	U-O	-	medium, broad

Table 5.4

Uranium $4f_{7/2}$ core binding energies for the Ammonium Uranates

Sample	$U4f_{7/2}$ binding energy / eV
pH 5.6	381.40 ± 0.06
pH 8.0	381.67 ± 0.05
pH 10.3	381.83 ± 0.08
pH 10.5	382.20 ± 0.07
pH 11.2	382.02 ± 0.08
ADU1	381.78 ± 0.06
ADU2	381.54 ± 0.05

Errors (± 2 x standard deviation) associated with each curve fitting analysis are given.

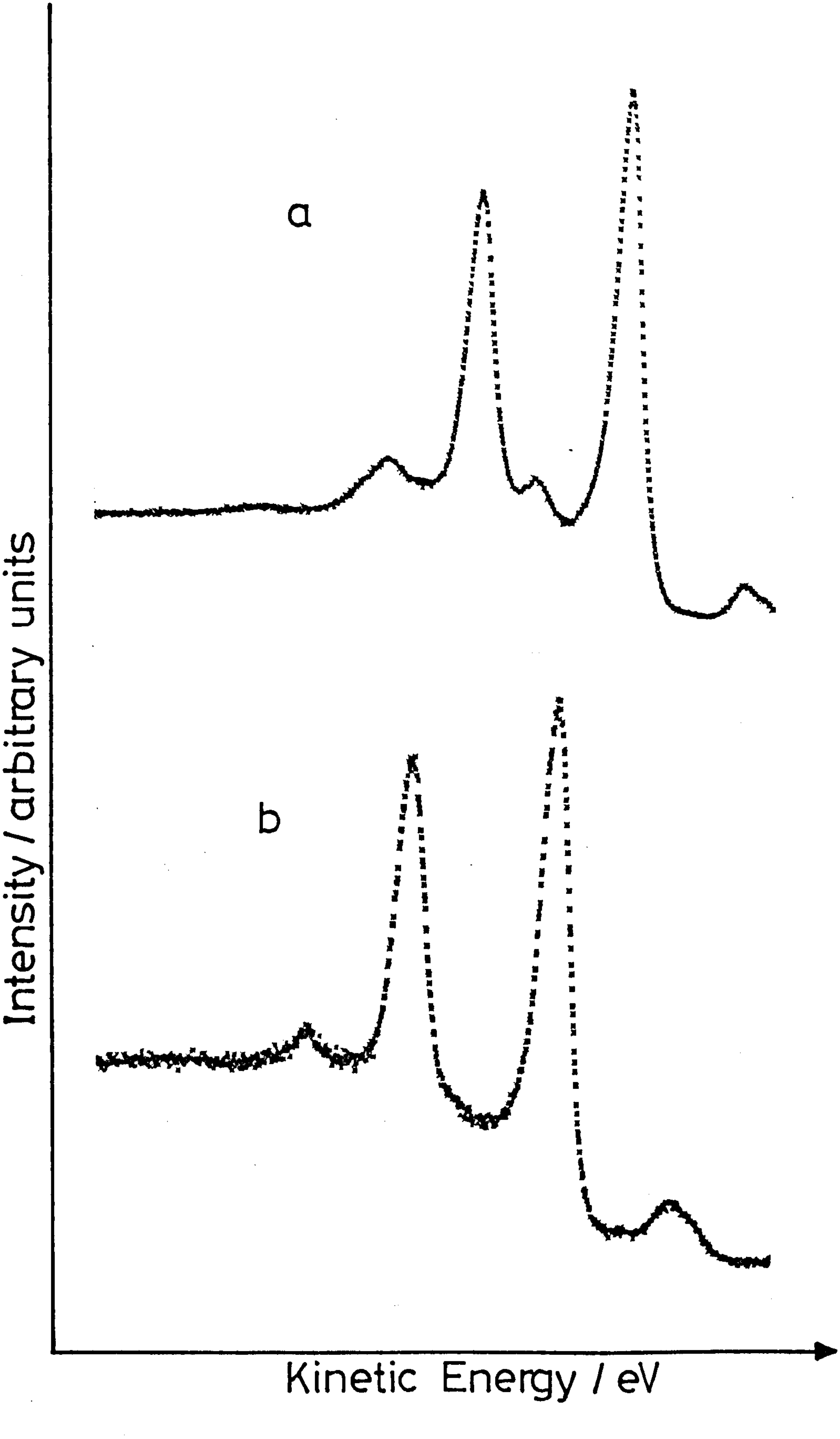

Fig 5.1:- Wide scan uranium 4f spectra for
a) Uranium Oxide (see section 5.3.4),
b) Ammonium Uranate (pH = 10.3).

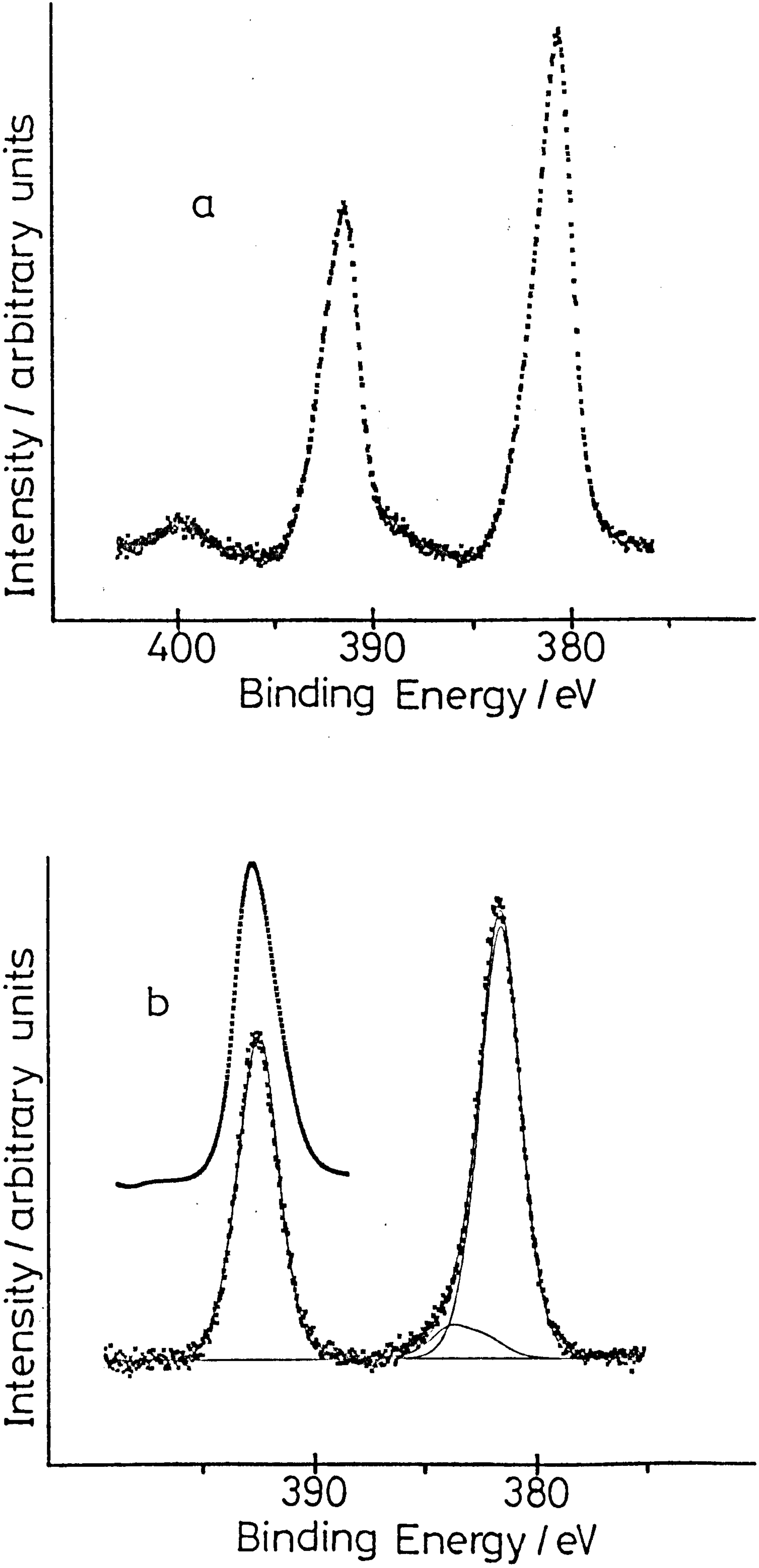

Fig 5.2:- Background subtracted U4f spectra recorded for a) U_3O_8, b) UO_3.

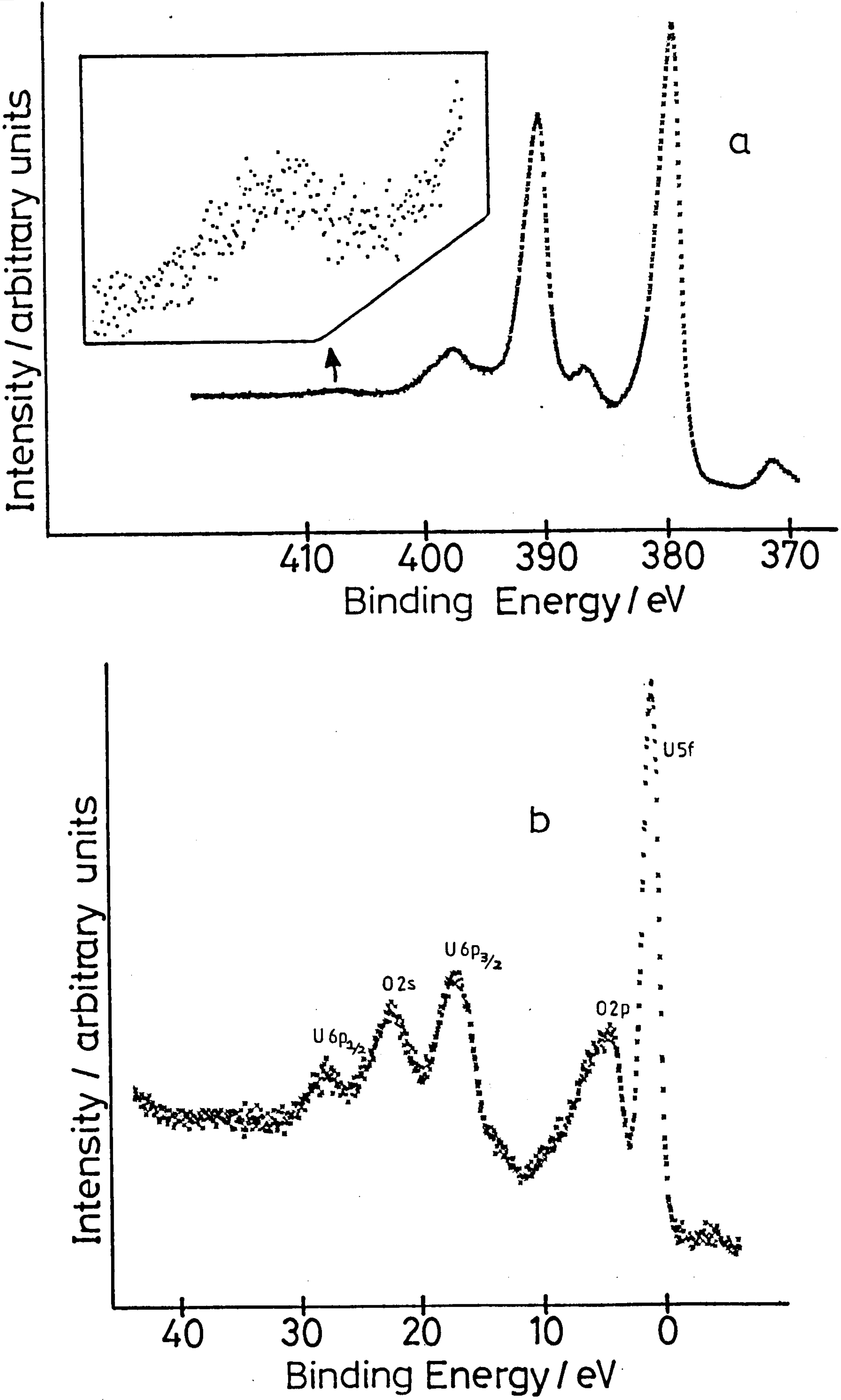

Fig 5.3:- Spectral regions recorded for uranium oxide (see text, section 5.3.4) at ambient temperature

a) U4f, b) Valence band.

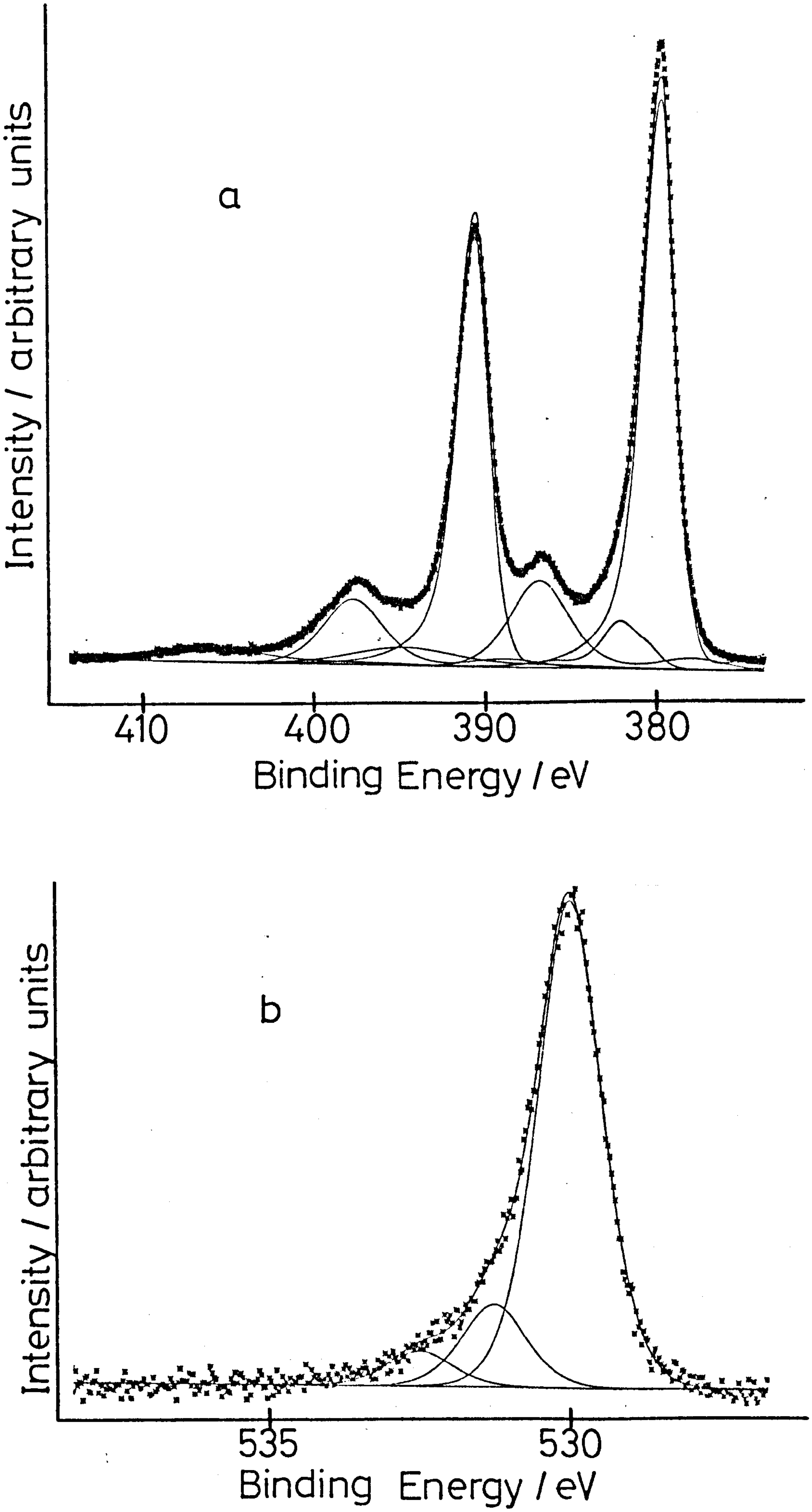

Fig 5.4:- Spectral regions recorded for uranium oxide (see text, section 5.3.4) at ambient temperature

a) U4f (background subtracted)

b) O1s

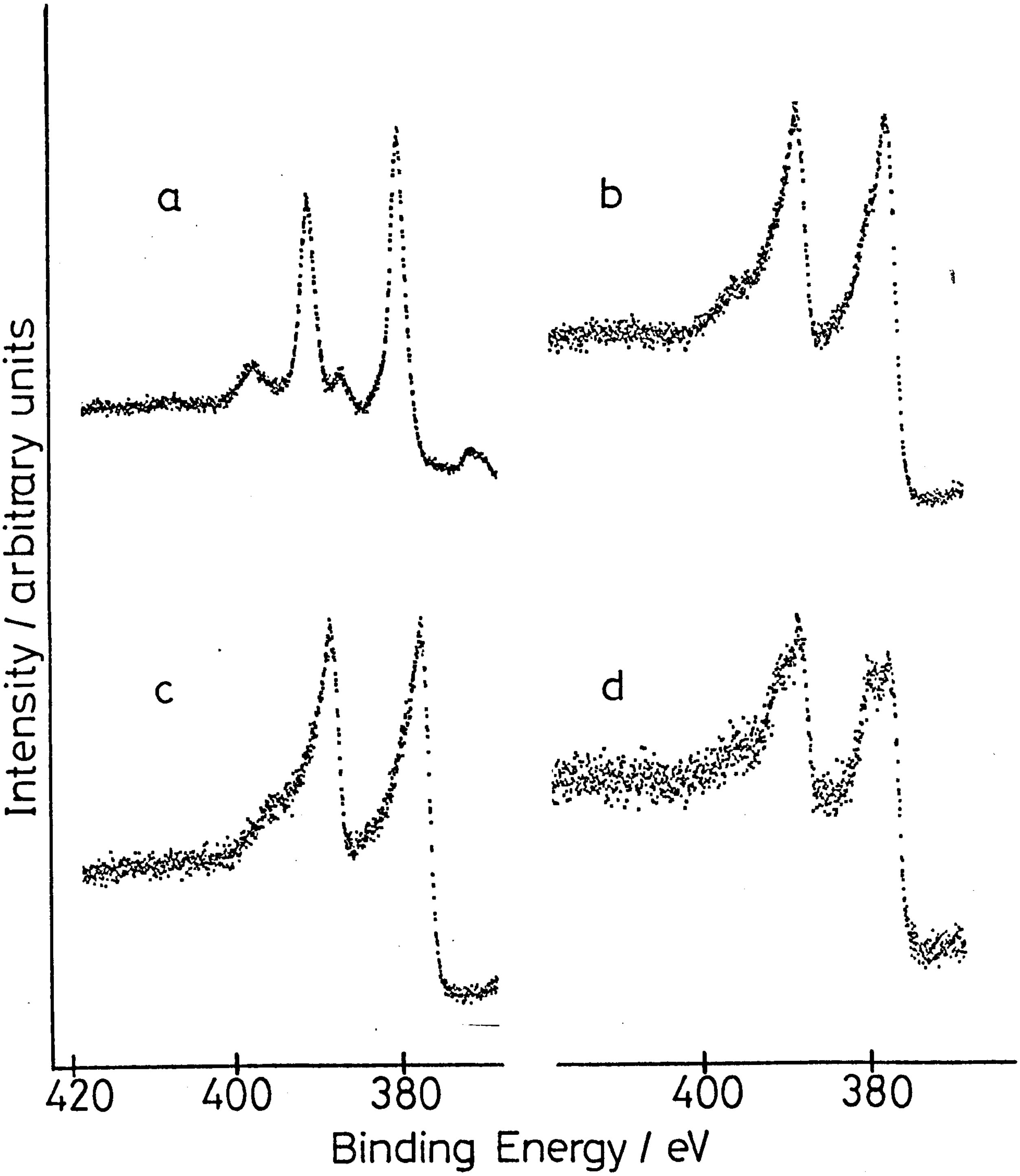

Fig 5.5:- Wide scan U4f spectra recorded for uranium foil heated in vacuo at

a) 200°C, b) 400°C, c) 600°C,

d) 400°C (at a surface sensitive angle).

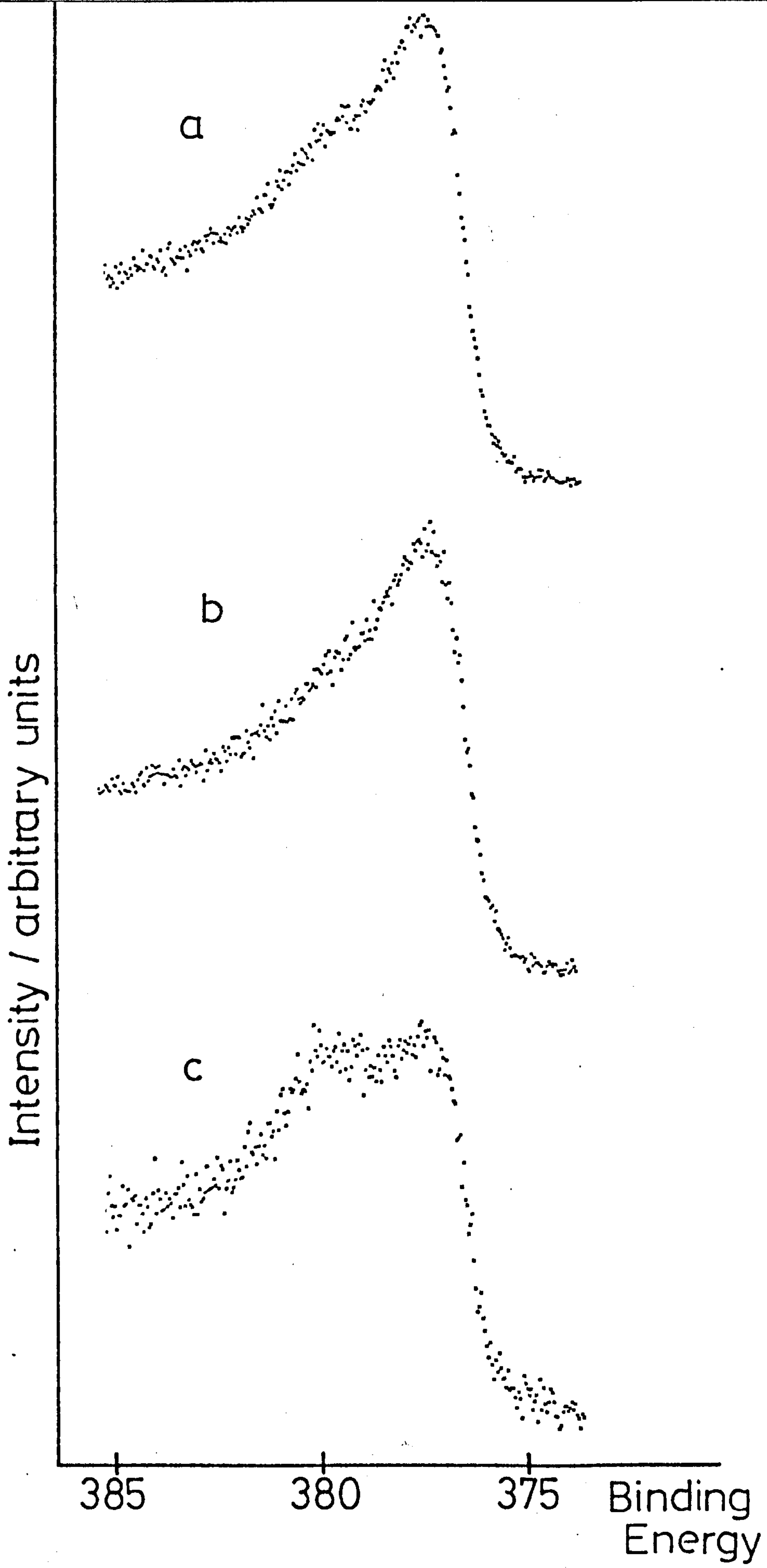

Fig 5.6:- Expanded U4f spectra recorded for uranium foil heated in vacuo. Only principal U4f$_{7/2}$ component is shown for each species (i.e. metal and oxide). Recorded at

a) 400°C, b) 600°C,

c) 400°C (at a surface sensitive angle).

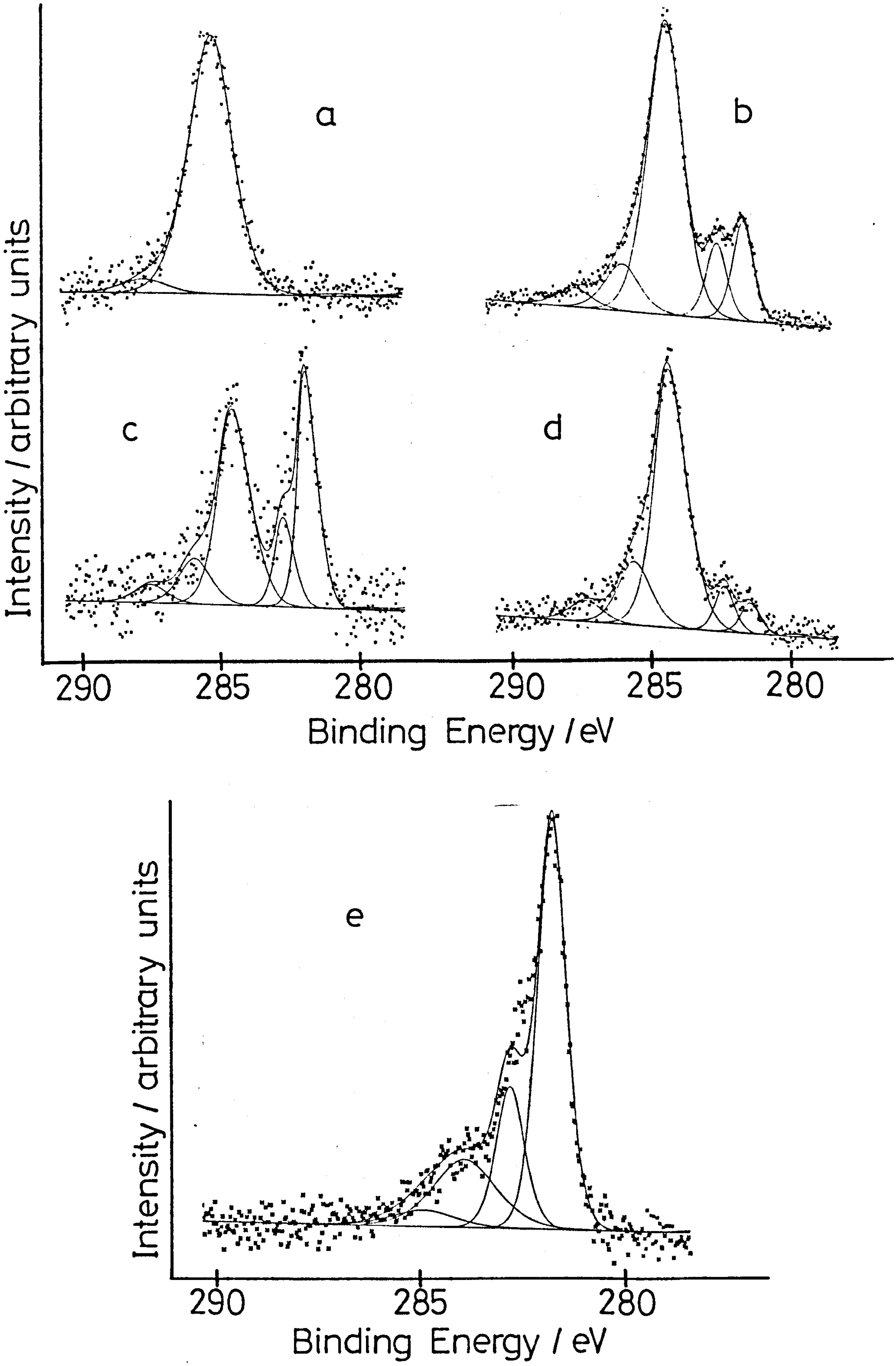

Fig 5.7:- C1s spectra recorded for uranium foil heated in vacuo at
a) 200°C, b) 400°C, c) 600°C
d) 400°C (at a surface sensitive angle)
e) 600°C (third heating cycle).

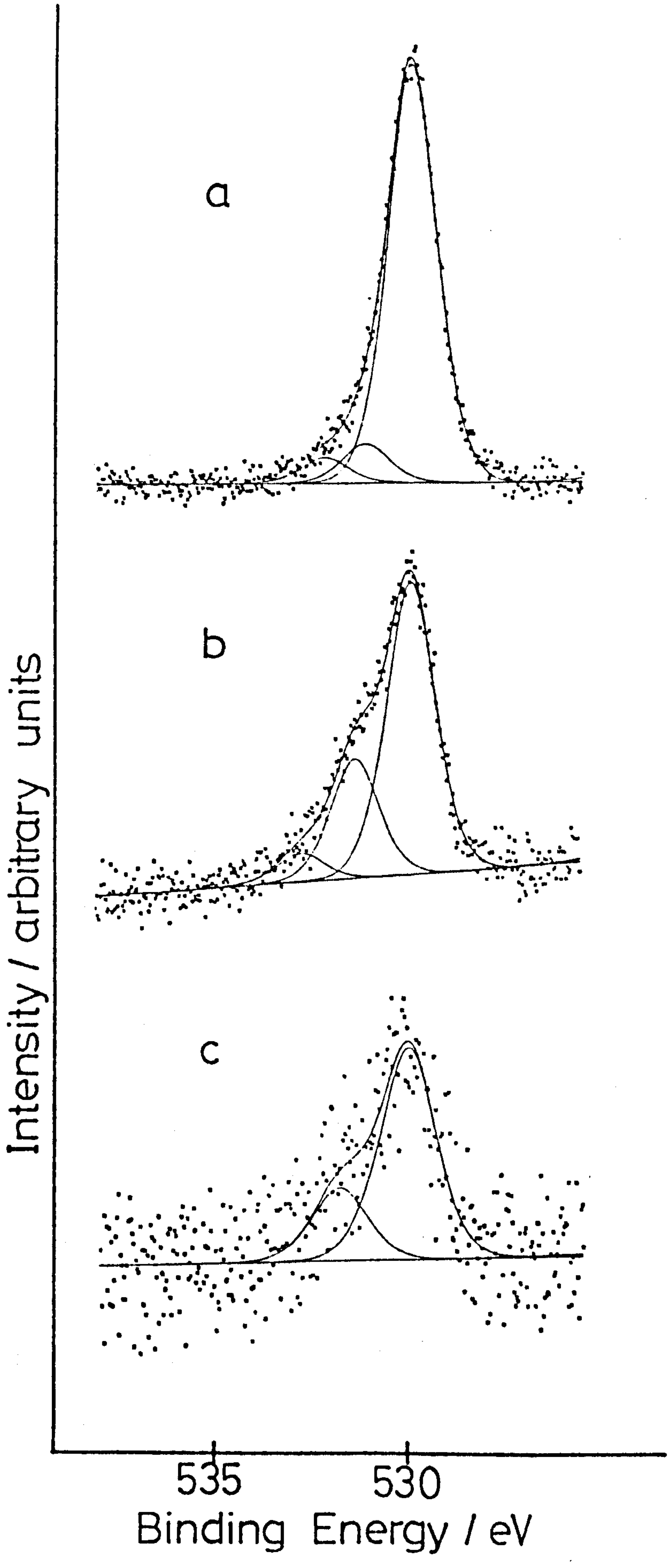

Fig 5.8:- O1s spectra recorded for uranium foil heated in vacuo at

a) 200°C, b) 400°C, c) 600°C.

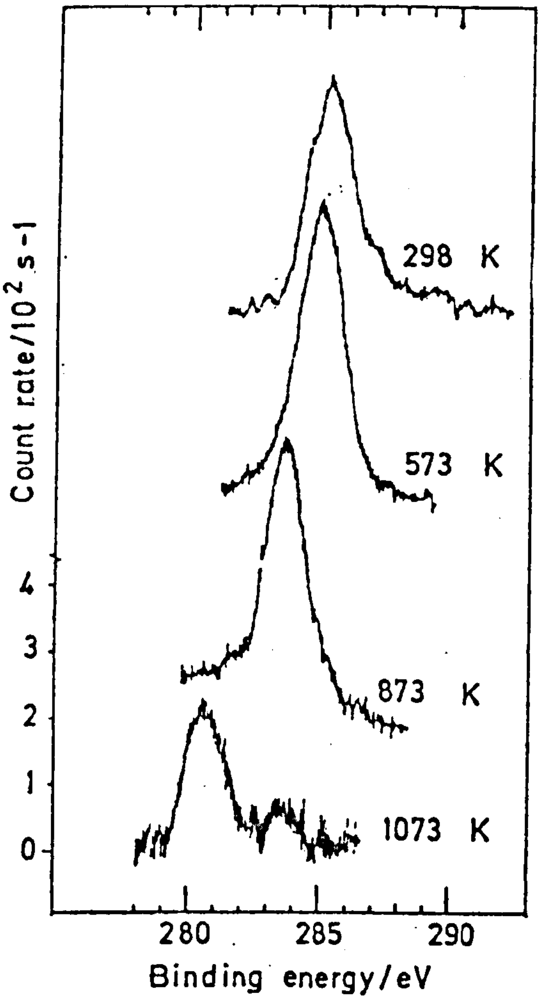

Effect of temperature upon the C$1s_{1/2}$ peak

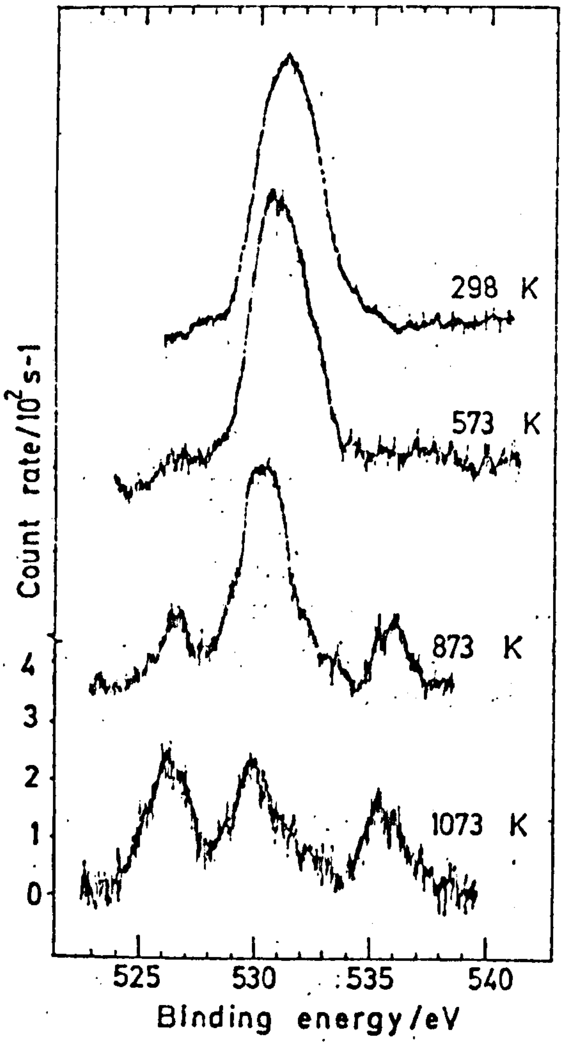

Oxygen $1s_{1/2}$ peaks recorded from uranium surface at denoted temperatures

Fig 5.9:- Change in the O1s and C1s regions for a piece of uranium foil heated in vacuo at various temperatures (reprinted from ref 205).

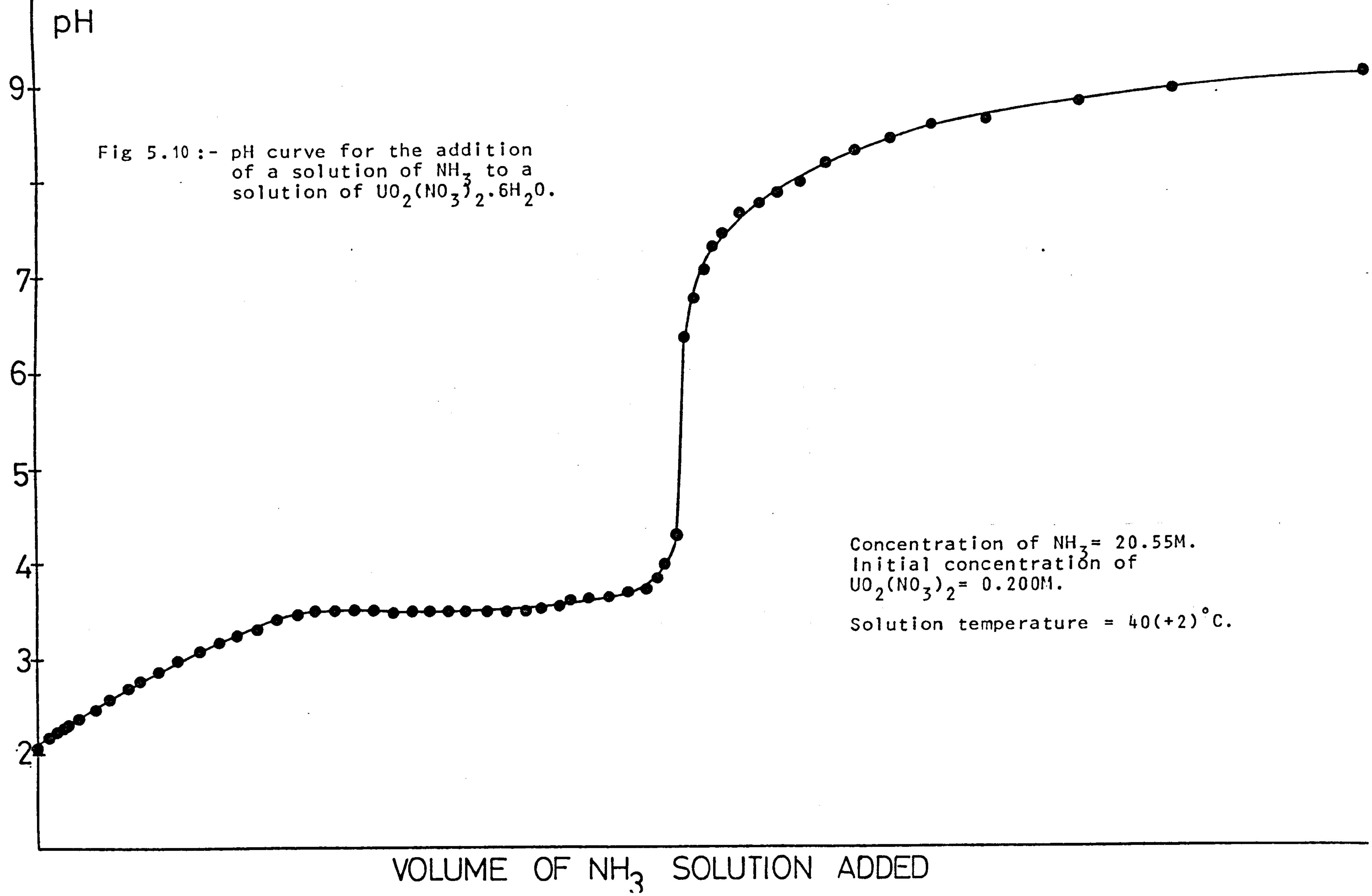

Fig 5.10 :- pH curve for the addition of a solution of NH_3 to a solution of $UO_2(NO_3)_2.6H_2O$.

Concentration of NH_3= 20.55M.
Initial concentration of $UO_2(NO_3)_2$= 0.200M.

Solution temperature = 40(+2)°C.

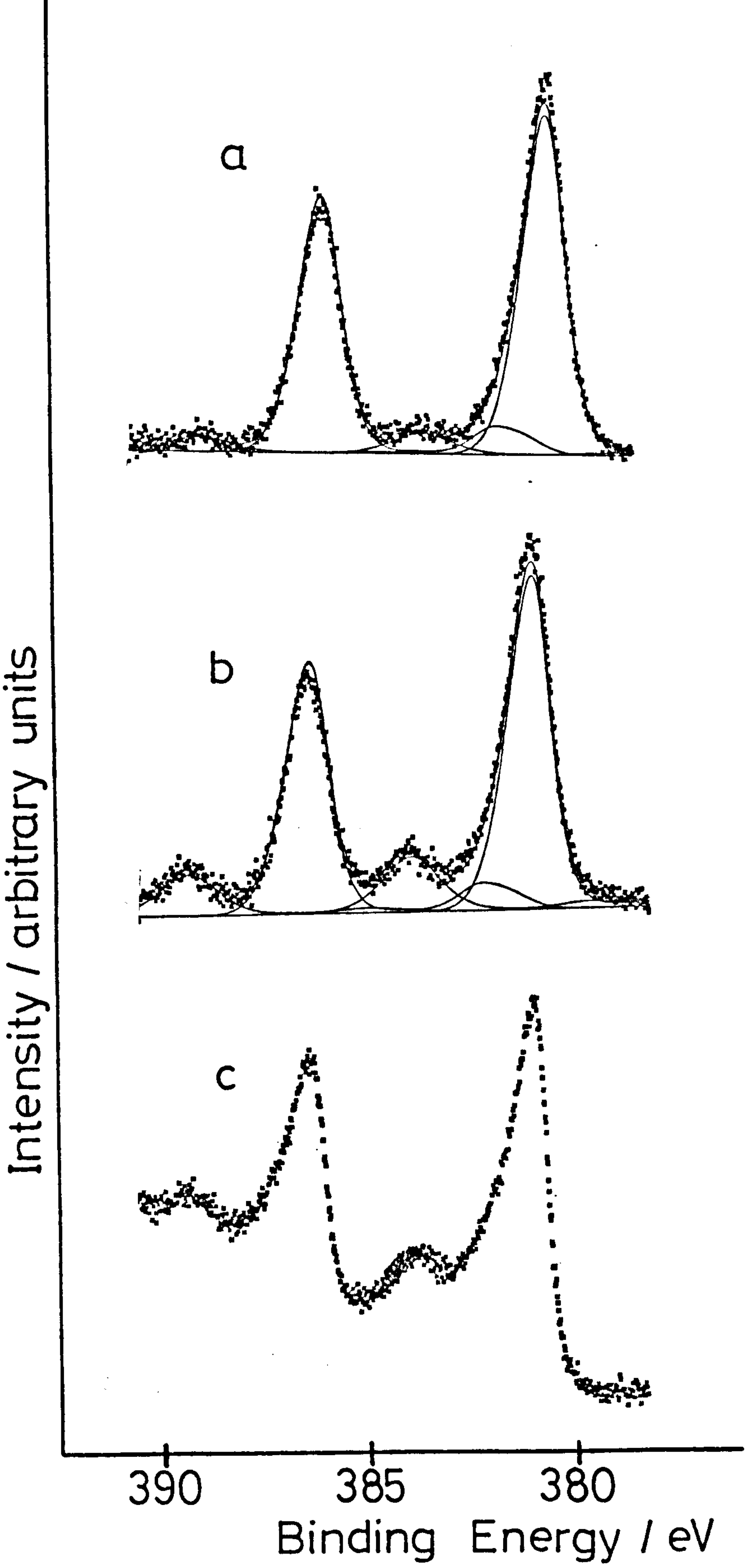

Fig 5.11:- U4f spectra recorded for

a) Uranyl Formate*,
b) Uranyl Oxalate*
c) Uranyl sulphate

* = background subtracted

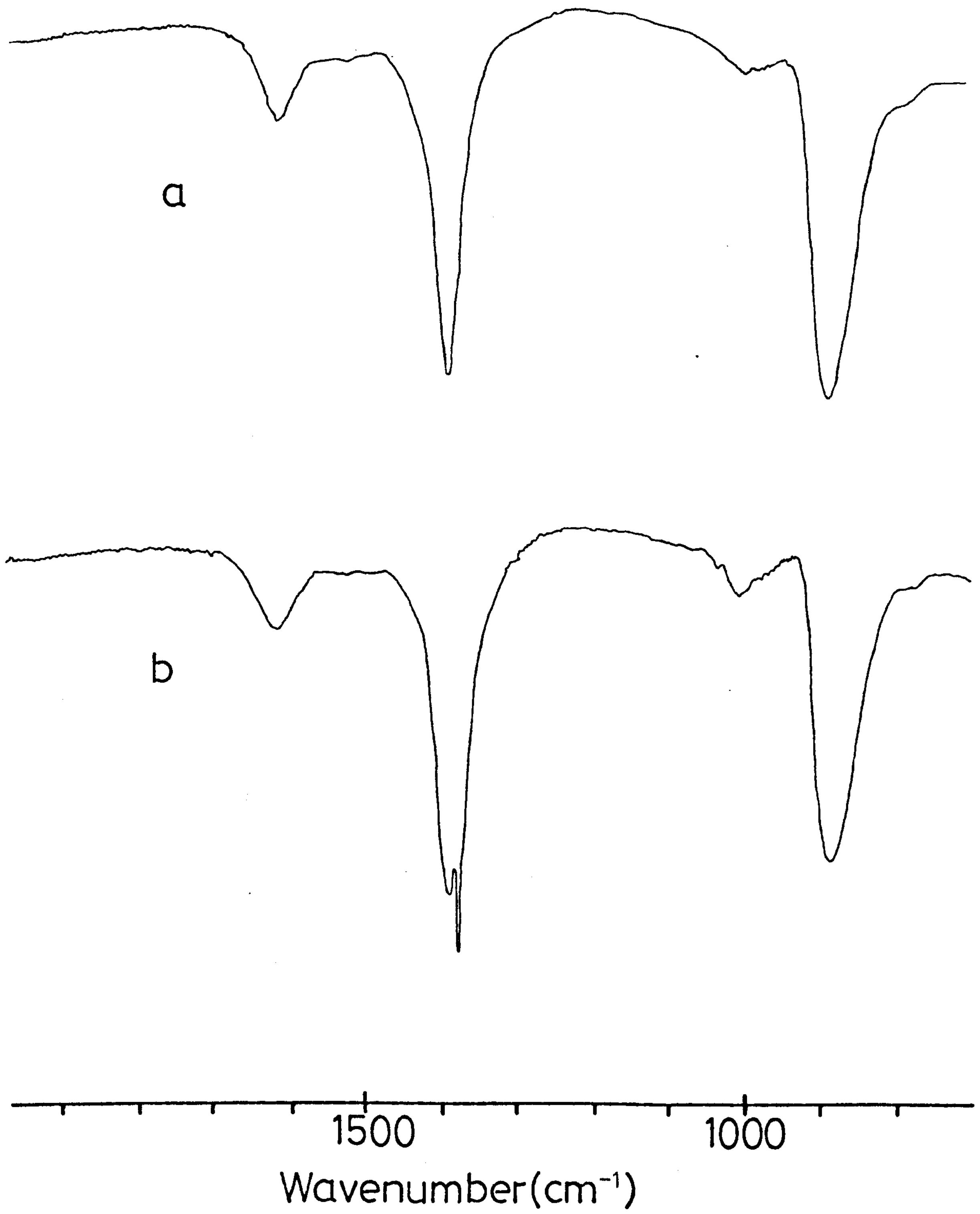

Fig 5.12:- Infrared Spectra recorded for pH 10.3 sample

a) Washed, b) Unwashed.

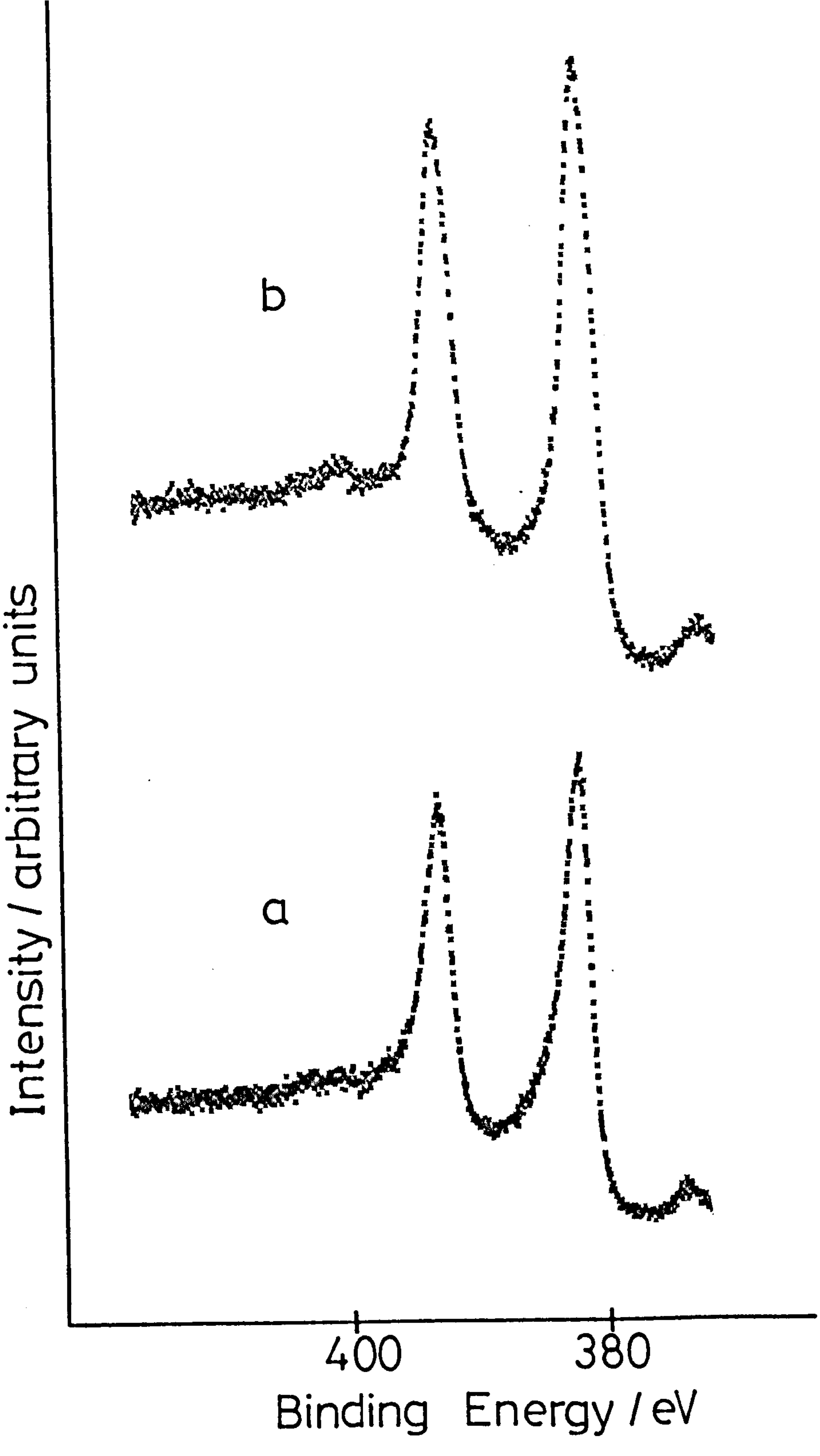

Fig 5.13:- U4f/N1s spectra recorded at 77K for a) pH 10.3 sample, b) ADU2.

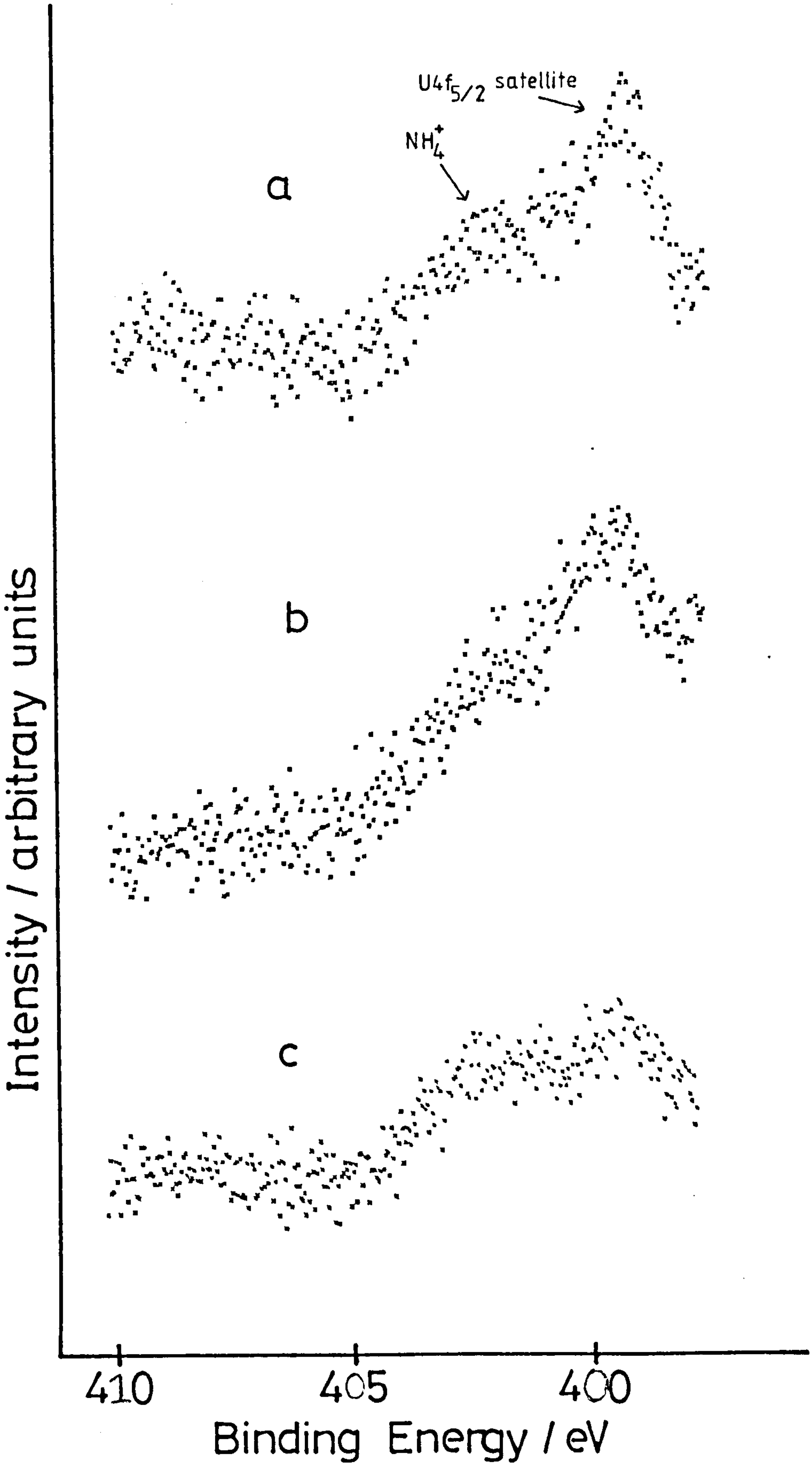

Fig 5.14:- N1s region recorded at 77K for

a) pH 5.6, b) pH 10.3, c)ADU2.

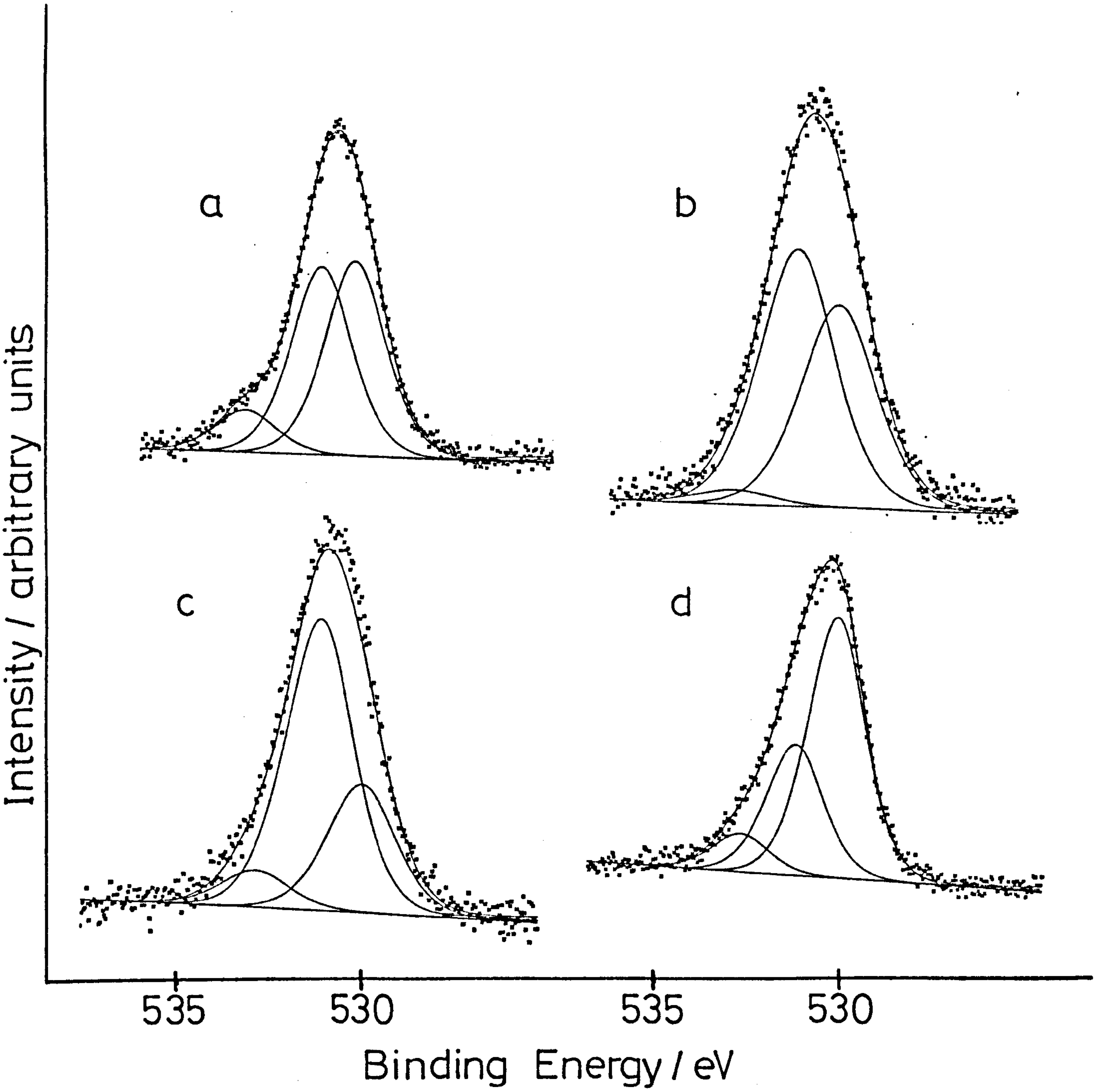

Fig 5.15:- O1s spectra recorded (at 77K) for some of the Ammonium Uranates

a) pH 5.6, b) pH 10.5, c) pH 11.2, c) ADU2

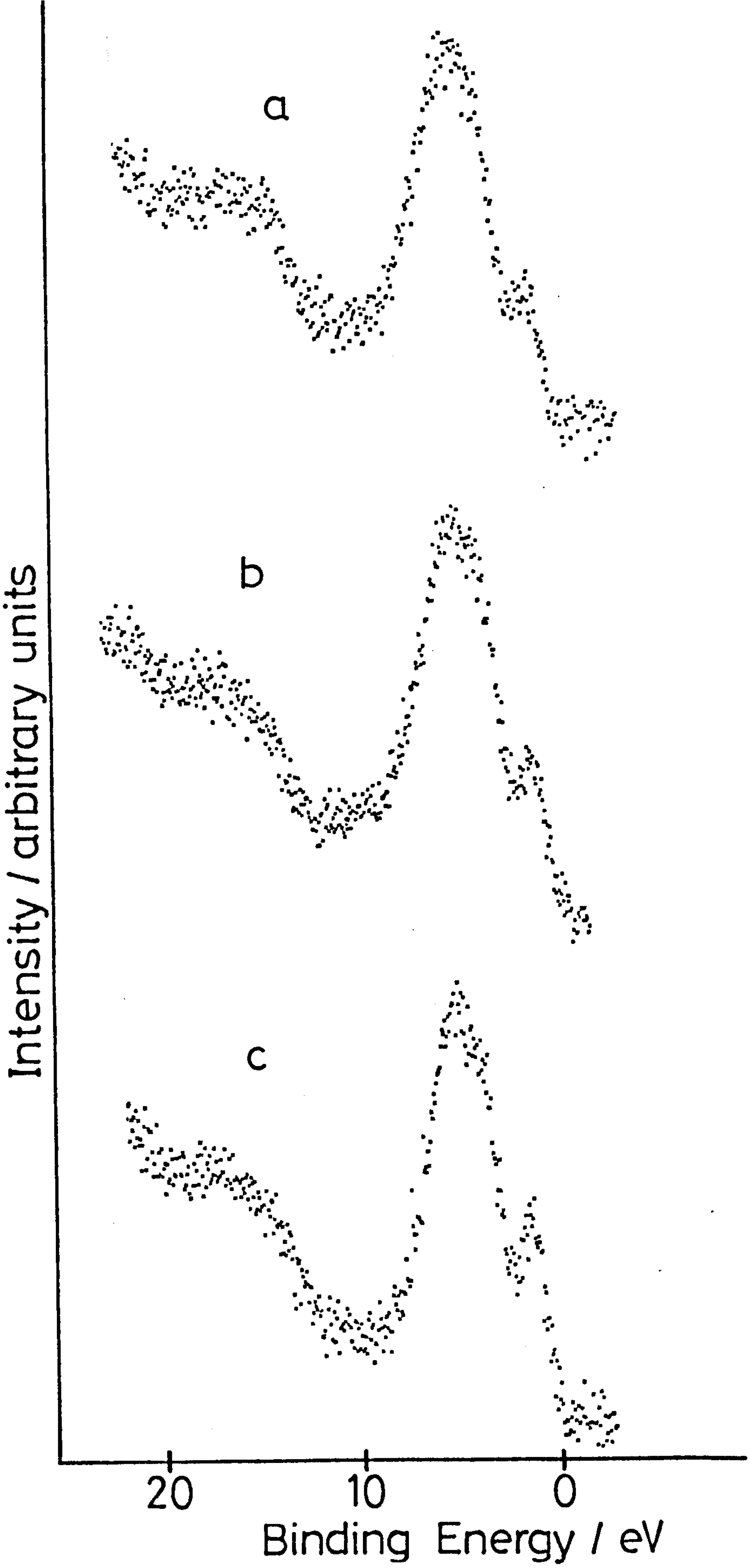

Fig 5.16 :- Selection of valence band spectra recorded for some ammonium uranates. Spectra recorded at ambient temperauture unless stated.

a) ADU(2), b) pH 5.6 sample (recorded at 77K),

c) pH 10.3 sample.

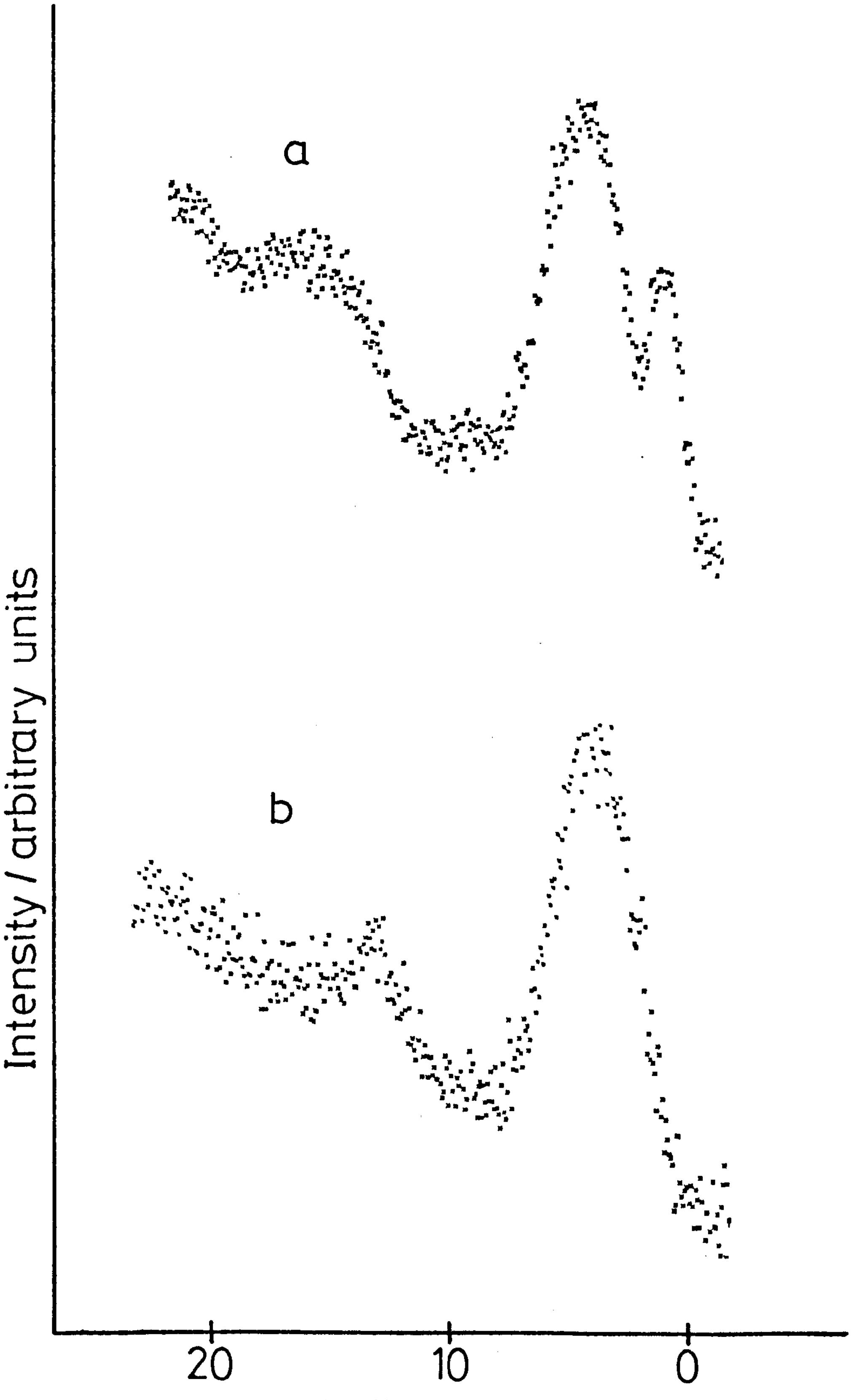

Fig 5.17:- Valence Band Spectra recorded for a) UO_3, b) Uranyl Nitrate.

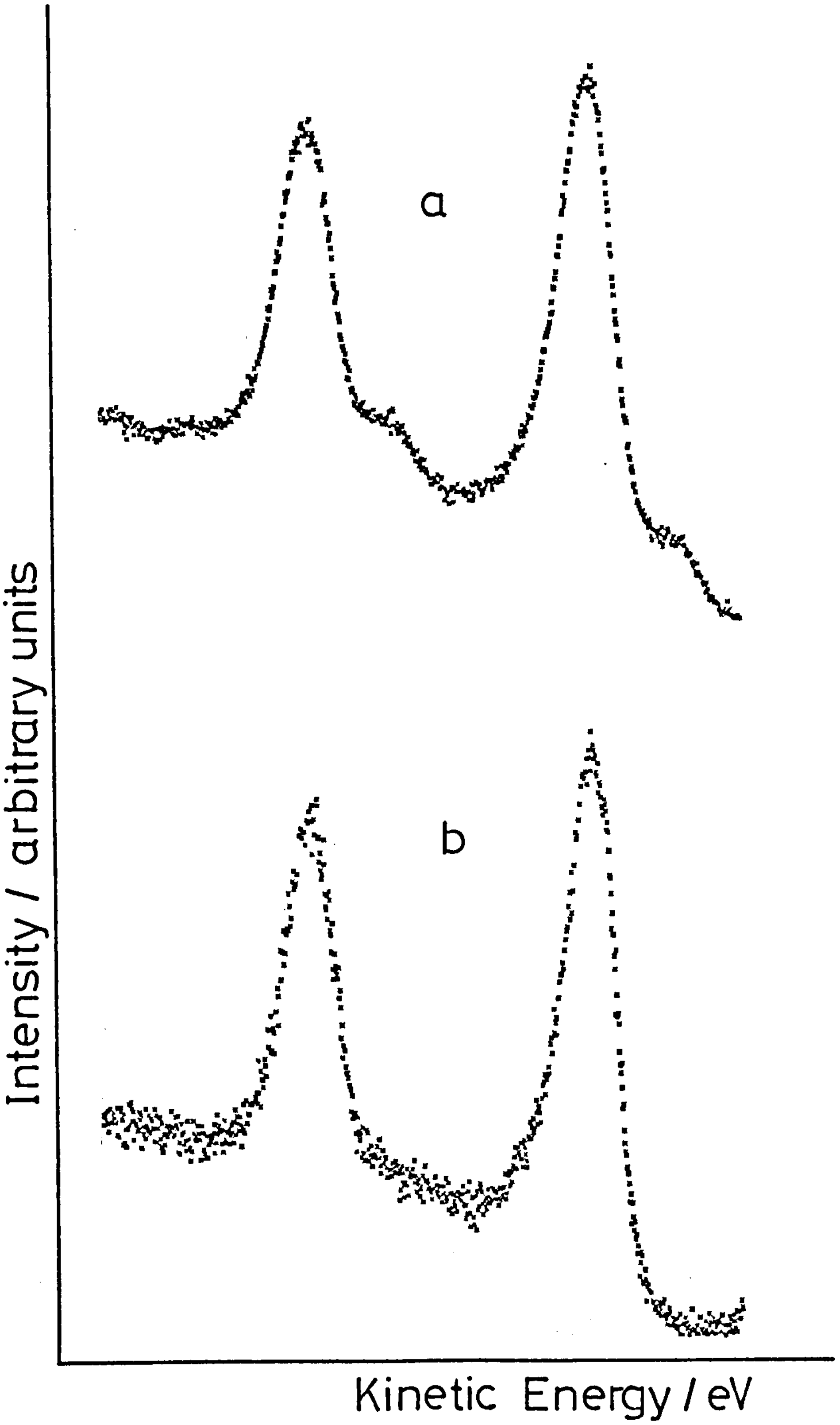

Fig 5.18:- U4f spectra for pH 5.6 sample used in the thermal decomposition work. Recorded at a) ambient temperature, b) 275°C.

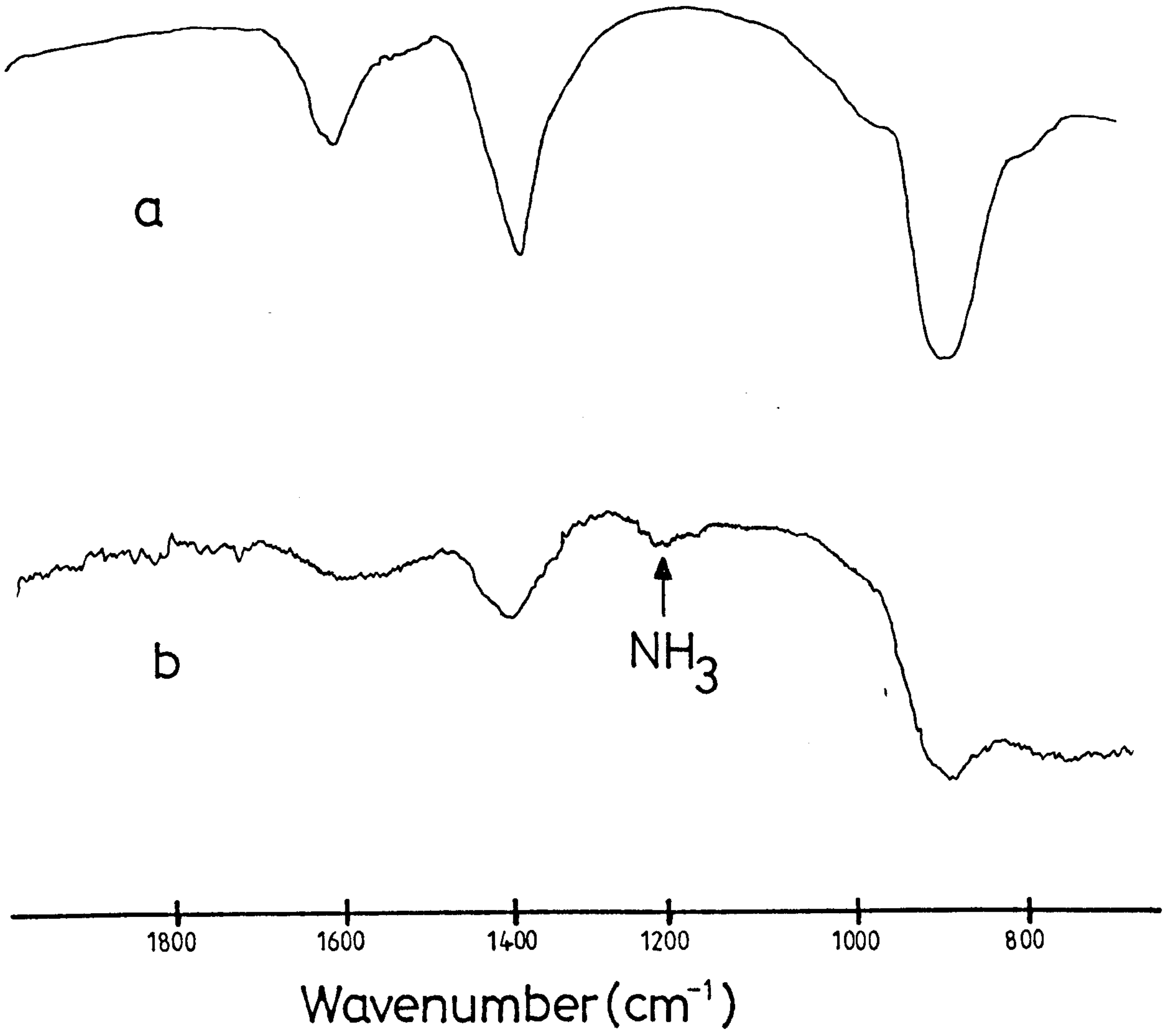

Fig 5.19:- Infrared spectra recorded for

a) pH 5.6 sample before thermal decomposition experiment,

b) pH 5.6 sample after thermal decomposition experiment.

CHAPTER SIX

SURFACE SEGREGATION OF IMPURITIES IN PLATINUM AND PALLADIUM

6.1 Introduction

The chemical composition of a solid surface plays a critical role in determining the type of process which will occur at this interface. This relates to surface phenomena in general, including a diversity of technologically important fields such as catalysis, metallurgy and corrosion science. It is normally true, in any multicomponent system, that the chemical composition of the surface or surfaces is different to that of the bulk. This situation arises from surface adsorption and/or surface segregation and it is the latter phenomenon which is the subject of the work presented in this chapter.

For a bulk condensed-phase system, the redistribution of the constituent species near a two dimensional discontinuity is termed surface or interfacial segregation. The thermodynamic description of surface segregation originates from the work of Gibbs (230,231) and it was concluded that the process exists in order to minimise the total free energy of the system. The Gibbs surface tension equation arose out of this early work and, for an n component solution, has the form:-

$$d\gamma = -\sum_{i=1}^{n} \Gamma_i . d\mu_i \qquad (6.1)$$

where γ = surface tension of the solution. A surface tension of γ Nm^{-1} corresponds to a surface energy of γ Jm^{-2},

Γ_i = surface excess of the i^{th} component,

μ_i = chemical potential of the i^{th} component.

There has been a great deal of work, both experimental and theoretical, on binary solid solutions (232) in which a solute species B is dissolved in a solvent matrix A. In this case, equation (6.1) may be rewritten as:-

$$\Gamma_B = \frac{-d\gamma}{d\mu_B} = \frac{-a_B . d\gamma}{RT\ da_B} \qquad (6.2)$$

where Γ_B = surface excess of solute B relative to Γ_A .

a_B= activity of solute B.

R = universal gas constant.

T = temperature.

It is clear (230-232) that, in order to minimise the surface energy of the system, the surface will be enriched in that species, either solute or solvent, which lowers the surface tension of the solution.

For both binary and multicomponent alloys, thermodynamic models have attempted to predict and rationalise segregation phenomena in terms of experimentally accessible quantities (232,233). Equations have been developed using properties of the pure component materials which constitute an alloy (232-234). For a binary system, it has been shown that the segregation characteristics can be related to the surface tension of the pure components, and the surface is enriched in the component with the smaller surface tension. However, surface tension data are not readily available for many metallic solids at temperatures below the melting point. Overbury (235) has correlated the surface tensions of pure solid metals with their heats of sublimation (ΔHsub) and theoretical predictions based on this latter quantity have been particularly successful in a wide range of binary alloys.

6.1.1 Studies of Binary Alloys

A large number of binary alloy systems have been investigated using a variety of techniques, leading to the discovery of two generally applicable rules.

(a) When heated in a vacuum, the surface of a binary alloy becomes enriched in the component which has the lowest heat of sublimation (ΔHsub).

(b) The interaction of an active gas with a binary alloy results in the surface segregation of the component which forms the strongest chemical bond with the gas.

Before considering some examples, it should be stated that most studies have observed surface segregation at elevated temperatures. This is due to enhanced atom diffusion and reaction rates in addition to the temperature dependence of the equilibrium surface composition. In several cases, however, surface enrichment can be observed at relatively low temperatures.

Surface analysis techniques have greatly aided the understanding of surface segregation in alloys. Auger electron (AES) and X-ray photoelectron (XPS) spectroscopy have been, by far, the most widely applied methods. Low energy electron diffraction (LEED) and scanning electron microscopy (SEM) have been used to a much lesser extent.

Surface enrichment, due to annealing in a vacuum, has been observed for binary alloys such as Cu-Ni (473°C, ref 236), Pt-Sn (500°C, ref 237), Ni-Au (100-1000°C, ref 233), Pd-Au (600°C, ref 238) and Cu-Al (200-700°C, ref 239); the surface segregating species is underlined. A number of alloy systems have exhibited both type (a) and (b) segregation behaviour under the appropriate conditions (234,237,240-243). For example, Sedlacek (242) has used AES, XPS and UPS to study a number of Pt-Ni alloys. On annealing *in vacuo*, these samples undergo surface enrichment in platinum whereas oxidation treatments result in the surface segregation of nickel.

6.1.2 Multicomponent Systems

There have been several studies of ternary, quaternary and more complex alloy systems. Holm and Storp (244) have used XPS to investigate the alloys Ag-Sn-Cu and Ag-Sn-Cu-Zn under a variety of conditions, and demonstrated that the surface segregation behaviour of the components is well described by the simple rules which apply to binary systems.

Many multicomponent alloys do not however, behave in such a well defined manner. For a ternary system consisting of two solute species dissolved in a solvent, the segregation characteristics of one solute can be strongly dependent on the behaviour of the other (245,246). Thus, very small quantities of a strongly segregating solute can suppress the segregation of another which is present in much larger quantities because of the competition for available surface sites. It has been shown (245) that the segregation behaviour of a binary alloy can be dramatically altered by the presence of a trace amount of impurity. Lea and Seah (246) have used AES to observe the direct site competition between tin and sulphur co-segregating to the surface of Fe-Sn-S ternary alloys. Annealing *in vacuo* at 650°C resulted in strong surface segregation of tin. This process was, in turn, suppressed by heating to 750°C due to the replacement of tin with sulphur at the surface. Several studies have shown that favourable interactions between different solutes can enhance or suppress the surface segregation of such species. For example, Dumoulin (247) has studied an Fe-Mo-P alloy and observed that the degree of phosphorus segregation is reduced relative to the Fe-P system. This behaviour is associated with strong preferential Mo-P interactions in the bulk matrix. Finally, in this work, the presence and segregation of trace impurities (C,N,S) severely interfered with the behaviour of the principal alloy constituents.

6.1.3 Surface Segregation of Impurities

Surface analysis techniques have been widely used to study the segregation of impurities to free surfaces and grain boundary interfaces in steels (248-250). For example, Stulen (248) has used XPS and AES to observe the surface segregation of boron and nitrogen in Cr-Ni-Mn steels during *in vacuo* annealing at temperatures up to 800°C. In steels, the invariably large number of impurities in addition to any alloying elements normally results in complex segregation behaviour (250,251) as discussed above. Although considerable segregation effects are expected in such low purity systems, it is perhaps surprising that there have been several observations of significant impurity segregation in high purity metals.

Such studies have shown that sulphur in its elemental form is, by far, the most common surface segregation species (252-254). Using AES, Haas (252) has investigated the transition metals Sc, Ti, V, Cr, Fe, Co, Ni, Y, Zr, Nb, Mo, Ru, Rh, La, Hf, Ta, W, Re, Ir, Pt and Au. All samples, except La, exhibited sulphur segregation after heating to 500°C *in vacuo*. Swartz and Holloway (255) have used AES to study the diffusion of sulphur and carbon in α-iron. Carbon was found to preferentially migrate to the surface in the temperature range 25-500°C whereas heating to 400-700°C resulted in the surface segregation of sulphur. Powell (256) has detected small amounts of sodium segregating on to a >99.97% pure lithium metal surface at room temperature *in vacuo*. This behaviour was successfully explained, at least on a qualitative basis, using the simple thermodynamic model for binary solutions. Sodium segregates to the surface due to its lower surface tension. A particularly important AES study concerns the segregation of a calcium impurity on to the surface of a 99.999% pure gold sample which was heated, in vacuo, to 600°C and then exposed to molecular oxygen at 5×10^{-7} torr (257). It was concluded that gas-phase oxygen induced this process and that, in turn, the calcium impurity enhanced the rate of chemisorption of oxygen on to the gold. Furthermore, it was noted that oxygen previously chemisorbed on to the gold surface promoted the surface segregation of calcium even in the absence of gas-phase oxygen. Proctor and Sherwood (258), using XPS, have reported the segregation of antimony, in its metallic form, on to the surface of gold upon heating in vacuo to 600°C. The segregation characteristics of this impurity were not as dependent as calcium upon the presence of previously adsorbed or gas-phase oxygen. A few studies of impurity segregation in platinum and palladium have been carried out and these will be discussed in the relevant sections.

6.1.4 Concluding Remarks

Interfacial segregation is clearly a very important phenomena in the field of surface science. It has been concluded that such processes are responsible for a number of technological problems such as the partial inhibition or deactivation of catalysts (259-261), variation in material properties (250,262) and metallurgical failures (250,263). A great deal of attention, both experimental and theoretical, has been focused on surface segregation in alloys. The study of such effects in steels and other important materials is now a rapidly growing area of research. It is hardly surprising that there have been relatively few reports of surface segregation in high purity metals. A number of studies (*vide supra*) have clearly demonstrated that small amounts of surface segregating impurities can have a significant effect on the surface properties of high purity metals. The remainder of this chapter discusses the observation of impurity surface segregation in high purity samples of platinum and palladium.

6.2 Experimental

Four platinum samples (99.99% purity, Johnson Matthey Ltd.) and 2 palladium samples (99.99% purity, Alfa products) were investigated in this work. Both palladium samples were from the same batch, but the four platinum samples were taken from three different batches. To simplify the following text these will be denoted as B1, B2 and B3. Two samples from batch one were investigated and these will be identified by the notation B1(1) and B1(2). Samples were mounted on to the HTP probe and heated to a maximum temperature of 600°C, with most of the work concentrating on the effect(s) of *in vacuo* heating. The effect(s) of exposure of samples to oxygen was briefly studied. All sample surfaces were cleaned via argon ion bombardment before heat treatment .

Samples were mounted on to the HTP probe in such a way that no signal could be attributed to the probe tip. Heating experiments were carried out on the probe itself to determine whether the probe tip material was the source of the segregating impurities (Ag, Au, S, C) observed on the platinum and palladium samples. The results clearly showed that the probe tip material did not contain Ag, Au or S. Carbon was, of course, detected but it is quite unreasonable to assume that the tip is therefore responsible for the observation of carbon segregation in one of the platinum samples. Such a situation would only arise if a) the carbon migrates from the probe surface to the platinum and, b) surface → bulk → surface diffusion occurs. The results show that all segregating impurities are directly associated with the Pt and Pd samples used in this work.

A large number of analogue spectra were recorded throughout this work. They proved to be useful to monitor any possible spectral changes with time, which may have been occurring during the collection of the digital data. They were also suitable for scanning the specific spectral regions of the most likely impurities in addition to wide scan and overall spectra. Binding energy and FWHM errors (±2 x standard deviation), obtained from the curve fitting analysis, are quoted in parentheses where necessary using the same format as described in section 3.4.1.

6.3 Impurity Segregation in Platinum

6.3.1 Previous Studies

There have been a few observations of impurity segregation in platinum samples. One example has already been mentioned, namely the segregation of sulphur in high purity platinum after heating *in vacuo* to 500°C (252). Impurities such as S,C,P,Ca,Si and O have been observed to segregate from the bulk to the surface of a Pt(110) crystal after annealing *in vacuo* at temperatures up to 1340°C (264).

Recently, there has been considerable interest concerning the role of segregating impurities on the interaction of oxygen with platinum. Several years ago, a number of papers (265,266) appeared suggesting that the reaction of platinum with oxygen (at low pressures, 900-1400K) produced a "platinum oxide" species even though this was in complete disagreement with thermodynamic data. Such studies did not, however, consider the possibility of surface segregating impurities acting as oxygen getters. Bonzel (267) has used AES to detect the segregation of silicon on to the surface of a Pt(111) crystal as a result of *in vacuo* heating (770-1170K) and exposure to oxygen (7 x 10^{-7} mbar, 873K). The latter process was associated with the formation of SiO_2 clusters on the platinum surface. Similarily, in an AES investigation of a Pt(111) crystal, Jupille (268) observed the surface segregation of aluminium under certain conditions (10^{-4} - 10^{-6} torr of O_2, 1200-1400K). It was concluded that this particularly strong oxygen getter may be responsible for certain observations of "platinum oxide" formation in cases where samples are known to be free of impurities such as Si and Ca (269).

6.3.2 Results and Discussion

6.3.2.1 Binding Energy Calibration

All spectra reported in this section are referenced against the $Pt4f_{7/2}$ peak (71.01eV) corresponding to a clean metal surface which was obtained via argon ion bombardment. This reference binding energy was obtained by using the $Au4f_{7/2}$ level (83.92eV) for pure gold metal to measure the spectrometer workfunction at the time these experiments were carried out. Thus, the metal $Pt4f_{7/2}$ level is effectively referenced against the spectrometer Fermi edge. As previously stated, the alternative use of adventitious carbon for calibration purposes is somewhat dubious in the case of metallic substrates due to the often considerable EARE effects (chapter 3). Indeed, for a heavily etched Pt metal surface, a minimum adventitious C1s binding energy of 283.93 was obtained (i.e. relative to $Pt4f_{7/2}$ = 71.01eV). This core level was, therefore, not used for binding energy calibration.

6.3.2.2 Surface Segregation of Silver

Heating to 600°C *in vacuo* promoted significant surface segregation of silver in three out of the four samples (B1(1), B1(2) and B3). The fourth sample (B2) did show evidence of a slight trace of Ag impurity on initial heating to 600°C, but this signal was not observable on subsequent runs.

The segregation process is illustrated by fig 6.1 which shows the Ag3d region for the B3 sample. A single Ag3d doublet is clearly observed in this region on heating the sample, *in vacuo*, to 600°C (fig 6.1b). This spectrum compares with that obtained for an argon ion etched surface (fig 6.1a). Fig 6.1a is plotted on an expanded intensity scale and clearly shows that no Ag impurity signal is detectable.

For all samples, the equilibrium surface concentration of silver was achieved almost immediately at 600°C. The amount of silver segregant on each sample was unchanged after cooling to ambient. The silver impurity was easily removed via argon ion etching, in all cases, and subsequent heating again resulted in the surface segregation of silver. In fact all Ag3d spectra, exhibiting a measurable Ag3d signal, were composed of a single Ag3d doublet.

Before going on to consider the chemical nature of the silver segregant, it is important to consider the amount of silver segregated in each case. A measure of this quantity is given by the $Ag3d_{5/2}/Pt4f_{7/2}$ peak area ratio (Rs) which is expressed as a percentage. The maximum Rs values for each sample were 5.9% (B1(1)), 5.4% (B1(2)) and 3.1% (B3). It should be mentioned that use of a linear background in the curve fitting of the Pt4f spectra resulted in an overestimation of the true peak area. The exponential tail used in the Gaussian-Lorentzian fitting function is, of course, included in the peak area calculation. Inelastic background effects, associated with the Ag3d levels themselves, were insignificant. The use of the cyclic scheme of etch-heat-etch etc. resulted in the gradual reduction in the Rs values for the B1(1) and B3 samples. Thus for the B1(1) sample, Rs was reduced from 5.9% to 0.7% in four cycles. The Rs value for the B3 sample was reduced from 3.1% to 0.5% in three cycles. This behaviour is due to the gradual depletion of the total bulk silver impurity from each of these samples. In contrast to the above well defined behaviour, the amount of Ag impurity segregated to the surface of the B1(2) sample was somewhat variable within the range 5.4% to 0.4%. This is quite unexpected since this sample was taken from the same batch as the B1(1) sample. Although the maximum Rs values are in good agreement, the behaviour of the Ag impurity is markedly different for the B1(2) sample. The poorly defined behaviour in the latter case may well be due to a complex co-segregation process (section 6.1.2) due to the presence of some other impurity (section 6.2.3).

For all samples, the binding energy obtained for the $Ag3d_{5/2}$ peak showed no correlation with the Rs value. Thus, the average value obtained from 9 different measurements was 367.49 (±0.04, ±0.30*) eV with a FWHM of 0.87 (±0.09, ±0.09*) eV. This corresponds to a negative chemical shift of -0.41eV with respect to pure silver metal (see chapter 3). The observed chemical shift is due to the fact that silver atoms located on the platinum surface are situated in a chemical environment which is quite different to that which exists in the pure silver metal state (270). Kim and Winograd (271) have observed a negative chemical shift (-0.6eV) for a small amount of Ag implanted into, or alloyed with, platinum.

An angular variation study was carried out on the B1(2) sample in order to determine the approximate location of the silver segregant. The results clearly showed an increase in the Rs value for spectra recorded at a surface sensitive angle. Furthermore, most of the silver segregant was removed after a very light etch (2 minutes). It is therefore concluded that the Ag impurity is located in the immediate surface layers of the sample.

The effect of heating a platinum sample (B3) to 600°C in 5×10^{-4} torr of oxygen (10 minutes) was briefly investigated. The silver impurity again segregated in its metallic form (fig 6.1c) in an amount close to that which was observed *in vacuo* (600 °C). There was no oxidation of the segregated silver species. The actual level of silver observed in this experiment was low since the bulk silver content of the B3 sample had been severely depleted during the preceeding experiments. No other impurities were observed to segregate with this treatment.

The results reported in this section are well explained using simple thermodynamic arguments. The heat of sublimation of silver (ΔHsub = 69.12 Kcal mole^{-1}, ref 272) is considerably lower than the corresponding value for platinum (121.6 Kcal mol^{-1}, ref 272). Thus, the segregation of silver to the surface of each platinum sample results in a reduction in the surface free energy of the system (type (a) behaviour, see sections 6.1 and 6.1.1). The implication in theory, therefore, is that the silver segregant detected in this work is located in the immediate surface layers of each platinum sample.

6.3.2.3 Surface Segregation of Gold

A small amount of gold co-segregated with silver in the case of the B1(1) and B1(2) samples after heating *in vacuo* to 600 °C. The process is illustrated by fig 6.2 (B1(2) sample) which shows the change in the Pt4f/Au4f region for the sample which is argon ion etched (fig 6.2a) and then heated to 600°C *in vacuo* (fig 6.2b). The equilibrium surface concentration of the gold segregant was achieved very quickly upon reaching 600°C. The amount of segregant did not alter with time at this temperature. Furthermore, the amount of gold did not appear to change after cooling the sample to ambient temperature. The gold segregant was easily removed via argon ion etching and replaced by subsequent re-heating to 600°C. The gold signal (fig 6.2b) appeared to be composed of a single doublet. This was confirmed by collectng a Pt4f/Au4f spectrum (different cycle) over an extended time period in order to produce very high quality data (fig 6.3).

As previously stated, the amount of gold segregated in each B1 sample was small with Rg values (i.e. % $Au4f_{7/2}/Pt4f_{7/2}$ peak area ratios) ranging from 0.6-0.8% (B1(1) sample) and 0.4-1.4% (B1(2) sample). The Rg values for the B1(1) sample were consistently low throughout the series of experiments. The Rg values for the B1(2) sample were, however, quite variable within the Rg range. The latter behaviour is similar to that which was observed for the silver impurity in the same sample. The difference in the segregation behaviour between both B1 samples is quite surprising since both samples came from the same batch. In the case of the B1(2) sample, it is possible that the gold and silver species are co-segregating in a complex manner (section 6.1.2) due to the apparently greater amount of gold in this sample. Alternatively, some other impurity may be present in small amounts which is enhancing or suppressing the segregation characteristics of the silver and gold impurities. The results suggest that the distribution of impurities in the original platinum sheet (B1) is not uniform.

For both B1 samples, the binding energy of the $Au4f_{7/2}$ level showed no correlation with the Rg values. The average value obtained from 7 different measurements was 83.57 (±0.12, ±0.21*) eV with a FWHM of 0.85eV (fixed). This value is shifted -0.35eV with respect to the $Au4f_{7/2}$ level measured for pure gold metal.

The small amount of gold segregated in each sample meant that a surface sensitive study was rather difficult to carry out due to the very low signal to noise ratio for the Au peaks. Although the corresponding Pt4f/Au4f spectrum was fairly poor in terms of its statistical quality, the Rg value did increase slightly at a highly surface sensitive angle. Furthermore, most of the gold segregant was removed via a light argon ion etch (2 minutes). The results are similar to those obtained for the Ag impurity and suggest that the gold segregant is located close to, or at, the immediate surface of the sample.

The segregation of gold in platinum due to *in vacuo* heating is predicted by using simple thermodynamic rules (sections 6.1 and 6.1.1). The lower ΔHsub for gold (82.29 Kcal mole^{-1}, ref 272) compared to platinum (121.6 Kcal mol^{-1}) means that surface enrichment in gold is thermodynamically favourable. The gold segregant is expected, at least in theory, to be located in the immediate surface layers of each platinum sample.

6.3.2.4 The Platinum 4f Region

The clean metal Pt4f spectrum (fig 6.4a) was accurately curve fitted since this would allow the detection of any small chemical changes which may have been occuring with the heat treatment. This is, of course, in addition to the accurate measurement of peak positions and areas etc. All Pt4f spectra recorded in this work were well fitted by using the etched metal peak parameters. Thus, there is no indication of platinum oxide formation for samples heated *in vacuo* (fig 6.4b) or oxygen (fig 6.4c). Possible Pt4f chemical shifts, associated with platinum atoms no longer in a completely platinum-like chemical environment (i.e those near the Ag/Au layer), appear to be insignificant.

6.2.3.5 The Carbon 1s Region

The effect of heat treatment on the C1s region for the B2 sample was markedly different to that which was observed for the other samples. In the latter cases, the amount of carbon remaining on the sample surface, after argon ion bombardment, was little affected by heating to 600°C *in vacuo*. This contrasts with the results obtained for the B2 sample where a significant increase in the principal C1s signal was observed. The results are illustrated by fig 6.5 which shows the C1s region (intensities are normalised) for the etched sample (fig 6.5a) and the change induced by heating to 600°C (fig 6.5b). Furthermore, the C1s signal intensity maximised almost immediately upon reaching 600°C, implying that an equilibrium surface concentration of carbon was achieved very quickly. The cyclic scheme of etch-heat-etch gave reasonably reproducible results with similar amounts of carbon on the surface at 600°C for each cycle. The observations are consistent with the process of carbon segregating from the bulk of the B2 sample to the surface at high temperature. The Rca value s (i.e. $C1s/Pt4f_{7/2}$ peak area ratio s) ranged from 4.0-5.8% for the sample at 600°C. As previously stated, the surface segregation of carbon in platinum has already been reported (264).

The 1s binding energy of the principal carbon situated on the sample surface at 600°C was obtained from four measurements to give a value of 284.00 (±0.02, ±0.17) eV with a FWHM of 1.37 (±0.04, ±0.09) eV. This probably corresponds to carbon in its elemental state.

6.3.2.6 The Oxygen 1s Region

For each sample, heated *in vacuo* to 600°C, the total O1s peak intensity decreased slightly relative to that which was observed for the corresponding etched surface. Ro values (i.e. % O1s/Pt4f$_{7/2}$ peak area ratio s), for both surface treatments, were normally in the range 1-4%. The exposure of the B3 sample to O_2 (600°C,5 x 10^{-4} torr,10mins) induced a small but significant increase in the Ro value (4.3 $\longrightarrow$ 7.3%).

There has been much interest in the range of O1s species which exist on noble metal surfaces. Hall and Sherwood (157) have observed three species on both an etched and heated (*in vacuo*, 600°C) iridium metal surface. These peaks were thought to correspond to a mixture of chemisorbed and subsurface oxygen. The same workers also observed three oxygen species on the surface of etched rhodium metal (91), with similar conclusions (vide supra) as to their origin. Proctor and Sherwood (258), in a study of the surface segregation of antimony in gold, concluded that at least two, and possibly three, oxygen species were associated with the surface after various treatments i.e. etched, heated *in vacuo* to 600°C, and heated at 600°C in 10^{-6} torr of O_2.

From visual inspection in this work, often aided by the spectral smoothing technique, it was concluded that all O1s spectra were composed of at least two closely overlapping peaks. Curve fitting was used in an attempt to determine the number of O1s peaks present, in addition to their binding energies.

As previously indicated (chapter 2), the choice of the best fit must not only consider the statistical significance of the fit. The use of a large number of peaks will normally give a good statistical fit (low χ^2), but this is often chemically meaningless. Thus, the change in χ^2 ($\Delta\chi^2$) is a better criterion for trying to determine the best fit than χ^2 alone.

The process is demonstrated by fig 6.6 which shows the Ols spectrum obtained for an argon ion etched platinum surface(B3 sample) and the spectrum obtained by subsequent heating in O_2 (600°C,5 x 10^{-4} torr,10 mins). The spectral details are given in table 6.1.

For the etched surface (fig 6.6a-c), the change in χ^2 is small in going from one to two, and two to three, peaks (see table 6.1). These results are typical to those obtained for other 'etched' Ols spectra and, therefore, conclusions based on the $\Delta\chi^2$ value are uncertain. As stated earlier, visual inspection suggested at least two peaks present in all cases. Quite similar results were obtained for the Ols spectra recorded for sample surfaces at 600°C *in vacuo*. However, for the B3 sample heated in O_2 (vide supra, fig 6.6d-f), conclusions based on the $\Delta\chi^2$ value are much more certain. There would appear to be at least two and possibly three oxygen species associated with the metal surface.

For most Ols spectra recorded for samples heated *in vacuo*, the oxygen envelope peak maximum shifted by a small amount to lower binding energy (normally -0.1 to -0.3eV) relative to that observed for the etched state. A larger shift (-0.83eV), relative to the etched case, is observed for the sample heated in O_2. These observations are consistent with an increase in the relative intensity of the lower binding energy component in addition to any absolute change in individual component binding energies due to the surface treatment. It is clear from fig 6.6, using either two or three peak fits, that the relative intensity of the lowest Ols binding energy component increases considerably for the 'heated in O_2' case compared to the etched state. Indeed, this is confirmed by the individual component Ro values. Furthermore, the corresponding shift in the individual component binding energy, using two or three peaks, is quite apparent (see table 6.1). The latter observation is similar to that made by Proctor and Sherwood (258) in their study of the surface segregation of antimony in gold. This lowest binding energy species probably corresponds to chemisorbed oxygen. The shift in binding energy with heating may correspond to the loss of water adsorbed on chemisorbed oxygen (273) which is replaced largely by chemisorbed oxygen alone, i.e. corresponds to the replacement of O_{ads}..H-O-H by O_{ads}. The middle component may correspond to subsurface oxygen species.

6.4Impurity segregation in Palladium

6.4.1Previous Studies

There have been very few studies of impurity segregation in samples of palladium. Bader (274), using AES, reported the segregation of silicon to the surface of a Pd(100) crystal after heating to 800-1000°C in ~10^{-6} torr of O_2. This resulted in the formation of an oxide species closely related to SiO_2. The surface segregation of sulphur has been detected for a number of palladium samples (275-277). AES has been used to observe sulphur segregation in a >99.9% pure palladium foil after heating *in vacuo* to 773K (275). In another AES study (276), the exposure of a 99.99% pure Pd(100) crystal to hydrogen (~2×10^{-3} - 2×10^{-2} Pa) induced the migration of sulphur from the bulk to the surface of the sample. For a fixed H_2 pressure, the degree of sulphur segregation increased with increasing temperature.

6.4.2 Results and Discussion

6.4.2.1 Calibration and the Palladium 3d Region

All spectra, discussed in this section, are referenced against the $Pd3d_{5/2}$ level (335.18eV) corresponding to a clean metal surface which was obtained via argon ion bombardment. This binding energy was obtained by directly referencing against the palladium metal Fermi edge (see chapter 3).

The curve fitting of the Pd3d region was complicated by a number of factors. Although highly accurate peak binding energies could be obtained in all cases, the measurement of peak area was less certain. The principal difficulty with the analysis of these spectra is due to the presence of easily observable satellites lying approximately 6eV from the main lines (fig 6.7a). The problem is further complicated by a small Coster-Kronig broadening of the $3d_{3/2}$ component of the spin-orbit doublet (48-50), in addition to the effect of the inelastic background.

Inclusion of the satellites, in any attempted curve fit, was quite unsuccessful since suitable peak parameters could not be established. It was therefore decided to use the empirical peak profile approach (91) in order to allow a reasonably accurate measurement of the Pd3$d_{5/2}$ peak. In this approach, the metal Pd3d spectrum is fitted to two peaks whose intensity ratios are not fixed. Thus, satellite intensity is incorporated into the Pd3$d_{5/2}$ peak. As can be seen from fig 6.7b, the fit to the data is quite good. The loss in peak area for the 3$d_{5/2}$ component due to the neglect of its satellite is counteracted to some degree by the use of a linear background. Thus, the Pd3$d_{5/2}$ peak area measurement using this approach is reasonably accurate for the purposes of intensity ratios. Unacceptable inaccuracies (see fig 6.7b) were often introduced into the determination of the Pd3$d_{5/2}$ peak centre. This problem was overcome by fitting the Pd3$d_{5/2}$ component on its own.

All palladium 3d spectra recorded in this work were fitted by the use of etched metal peak parameters. In many cases the curve fits were comparable in quality to that shown in fig. 6.7b. In some cases, for samples heated *in vacuo*, several spectra were best fitted with the use of greater asymmetric tails on both spin-orbit components. This might suggest the presence of small amounts of chemically shifted species, however surface sensitization showed no change in the spectrum. It thus seems that there is only one species, and the differences in the curve fits may be due to the difficulties in fitting such a complex spectral envelope.

6.4.2.2 Surface Segregation of Silver

As previously stated, two samples of palladium, from the same batch, were investigated in this work. These will be identified by the notation S1 and S2 in the following text.

Heating to 600°C *in vacuo* promoted the surface segregation of silver in both samples. However, the amount of silver segregated in each case was quite different (*vide infra*). This observation is similar to the behaviour observed for the platinum B1 samples. The process is best illustrated by fig 6.8 which shows the Ag3d region for the S2 sample. A silver 3d signal, seemingly composed of a single doublet, is observed on heating tha sample *in vacuo* to 600°C (fig 6.8b). This spectrum compares with that observed for an argon ion etched surface (fig 6.8a, same intensity scales). The use of digital spectra confirmed that a single Ag3d spin-orbit doublet was present for both palladium samples heated to 600°C *in vacuo*. Thus, fig 6.9 shows the change in the Ag3d region for the S2 sample which is etched (fig 6.9a) and then heated to 600°C *in vacuo*. It is important to note that a slight signal is detectable in the 'etched' Ag3d spectrum (see also fig 6.9c). Digital spectra, collected over considerably longer time periods, confirmed the presence of an Ag3d signal for both etched S1 and S2 samples. However, much of this signal is probably due to the slow segregation of silver in palladium at ambient temperature (80°C, measured directly) in the time taken to collect the digital spectra.

The behaviour of the silver segregant was quite similar to that observed for the platinum samples. Thus, the equilibrium surface concentration of silver was achieved almost immediately on reaching 600°C. The silver impurity was easily removed via argon ion etching and subsequent re-heating to 600°C again induced the surface segregation of silver.

As stated earlier, the amount of silver segregated in each palladium sample was quite different. The maximum Rsi value (i.e. % $Ag3d_{5/2}/Pd3d_{5/2}$ peak area ratio) for the S1 sample was 6.1%. This compares with the value of only 2.8% for the S2 sample. The use of the cyclic scheme of etch-heat-etch etc. resulted in the gradual reduction of the Rsi value for the S1 sample (6.1% to 1.8% in four cycles). The Rsi value of the S2 sample remained unchanged, within experimental error, after 3 cycles.

For both samples, the binding energy obtained for the $Ag3d_{5/2}$ peak showed no correlation with Rsi value. It is generally true of this value (Rsi) and the other values of this type (Rs, Rg - *vide supra*), that they might be expected to show a correlation with binding energy. The binding energy of the surface segregant might be expected to vary with the amount and distribution on the substrate surface (271). The lack of correlation in all cases studied is notable, and may be due to the surface segregant being distributed over the whole surface and not in the form of 'islands' (271). Indeed, the measured value of Rsi, obtained from the range of experiments, was very consistent. Thus, the average value obtained from 12 different measurements was 367.42 (±0.05, ±0.06*) eV with a FWHM of 0.88 (±0.08, ±0.06*) eV. This corresponds to a chemical shift of -0.48eV with respect to pure silver metal (see chapter 3). Steiner (270) has observed a binding energy shift of -0.95eV for a dilute alloy of silver with palladium (less than 10% Ag).

An angular variation study was carried out on the S2 sample in order to determine the approximate location of the silver segregant. As expected, the Rsi value increased as the sample was turned to a more surface sensitive angle. Furthermore, a light argon ion etch (1-3 mins) removed most of the silver segregant. The conclusion, as expected in theory (*vide supra*), is that the silver impurity is located in the immediate surface layers of the sample.

The effect of heating a palladium sample (S2) to 600°C in 5 x 10^{-4} torr of oxygen (40 minutes) was briefly studied. The silver impurity again segregated in its metallic form (fig 6.9d) in an amount close to that which was observed *in vacuo*. No other impurities were observed to segregate with this treatment.

Finally, it is important to note that a short temperature dependent study was carried out on the S2 sample by heating *in vacuo* (fig 6.10). In this experiment, the S2 sample was argon ion etched to generate a clean palladium surface. The temperature was raised to 200°C and analogue spectra were recorded immediately and after one hour (approx). A similar procedure was used for the subsequent temperatures of 300°C and 450°C. These results compare with the Ag3d spectrum recorded at 600°C (fig 6.8b). For each temperature, the spectrum recorded immediately was essentially identical to that which was recorded approximately 1 hour later. Thus, the attainment of an equilibrium surface concentration of silver is very fast. It is clear that, within the timescale of the experiment, significant segregation is occurring between 200 and 300°C.

The results reported in this section are well predicted by simple thermodynamic rules. The lower ΔHsub for silver (69.12 kcal mol^{-1}, ref 272) compared to palladium (93.0 kcal mol^{-1}, ref 272) means that surface enrichment in silver is thermodynamically favourable. Indeed, previous experimental surface studies on Pd-Ag alloys have clearly observed surface enrichment in silver due to *in vacuo* heating (241).

Finally, in this work, it should be noted that a very weak sulphur 2p signal was detected on the palladium samples after heating to 600°C *in vacuo*. The $S2p_{3/2}$ peak binding energy was 162.24(±0.24), which probably corresponds to sulphur in its elemental state. This species is thought to have co-segregated with the silver species on sample heating.

6.4.2.3 The Oxygen 1s Region

The analysis of the oxygen 1s region for palladium samples is extremely complex due to its overlap with the palladium $3p_{3/2}$ peak. For the S1 palladium sample, spectra were recorded over the normal kinetic energy range. Thus any change in the total oxygen 1s intensity was monitored by a change in the total ($O1s+Pd3p_{3/2}$) intensity. The result of heating the S1 sample *in vacuo* (600°C) was to dramatically increase this quantity relative to the corresponding etched surface.

The increased oxygen 1s intensity is more clearly observed in the experiments carried out on the S2 sample. In this case, a wide scan kinetic energy range was used to include the palladium $3p_{1/2}$ (fig. 6.11) since the Pd $3d_{5/2}$ component could easily be removed from the combined O1s/Pd$3p_{3/2}$ signal. From fig. 6.11, the increase in the oxygen 1s signal is quite substantial. The Rox values (% O1s/Pd$3p_{3/2}$ peak area ratio) increased from 4.2% to 20.1% in going from the etched to the heated *in vacuo* sample. Heating in oxygen (*vide supra*) resulted in an Rox value of 22·3%.

The substantial increase in the amount of surface oxygen in going from the etched to the heated (*in vacuo*) case may be due to the diffusion of dissolved oxygen from the bulk to within the experimental sampling depth (258,278). The additional effect of chemisorbing gaseous oxygen in addition to any possible oxygen surface segregation process accounts for the increased Rox value for the sample heated in oxygen.

6.5 Conclusions

This work has demonstrated that significant amounts of impurities may segregate to the surface of high purity metals at elevated temperatures. Although, the actual amount of surface segregating impurities is small, as expected in principle, it is their location on the sample surface which is of prime importance. Surface sensitisation measurements have indicated that the segregating impurities are located in the immediate surface layers. This location is expected in theory since the driving force behind the segregation processes, observed in this work, is a reduction in the surface free energy of the system.

For metals, in general, small amounts of surface segregating impurities are expected to have a significant effect on immediate surface chemical processes. This may be particularly important in the case of platinum and palladium in view of their extensive catalytic applications (279).

In all cases, the surface segregated metals have a binding energy that is less than that of the pure bulk metal. These results suggest that the metal atoms are in a significantly different chemical environment to that of the bulk metal. The difference in binding energy is possibly due to the different extra-atomic relaxation energies in the two situations.

This work has also demonstrated the need for care when using XPS, and spectroscopic techniques in general, to study metal surfaces at elevated temperatures. Assignment of peaks, based on the expected chemical composition of the material under study, may be incorrect.

Finally, it is important to note that the surface segregation of silver and gold may be significant in a wide range of noble metal samples. This stems from the fact that the noble metals Rh,Pd,Ag,Ir,Pt and Au are usually found alloyed together in the natural state. The ΔHsub value of silver is the lowest of all these metals (272). Gold has the second lowest value. Thus, traces of silver and gold in other noble metals are predicted to segregate (type (a) behaviour), *in vacuo*, at elevated temperatures in the absence of any inhibiting processes (e.g. see sections 6.1.1 and 6.1.2).

Table 6.1

Spectral details for Oxygen 1s spectra recorded for the Platinum B3 sample.

Surface Treatment	Fig No's	No of Peaks	Binding Energies (eV)	FWHM(eV)	x^2
Argon ion Etched.	6.6a	1	532.07(0.02)	2.48(0.06)	402.4
	6.6b	2	532.41(0.13),531.34(0.18)	2.12(0.15)	382.4
	6.6c	3	533.29(0.17),532.20(0.09),530.99(0.10)	1.63(0.16)	361.2
Heated to 600°C in 5×10^{-4} torr of O_2 for 10 mins.	6.6d	1	531.24(0.03)	3.01(0.06)	508.4
	6.6e	2	532.08(0.06),530.62(0.06)	2.23(0.08)	364.1
	6.6f	3	532.72(0.16),531.59(0.14),530.34(0.10)	1.89(0.12)	339.1

Note:- The errors (+2 x standard deviation) associated with the binding energy and FWHM measurements are quoted in parentheses. These refer to the fitting of each single spectrum.

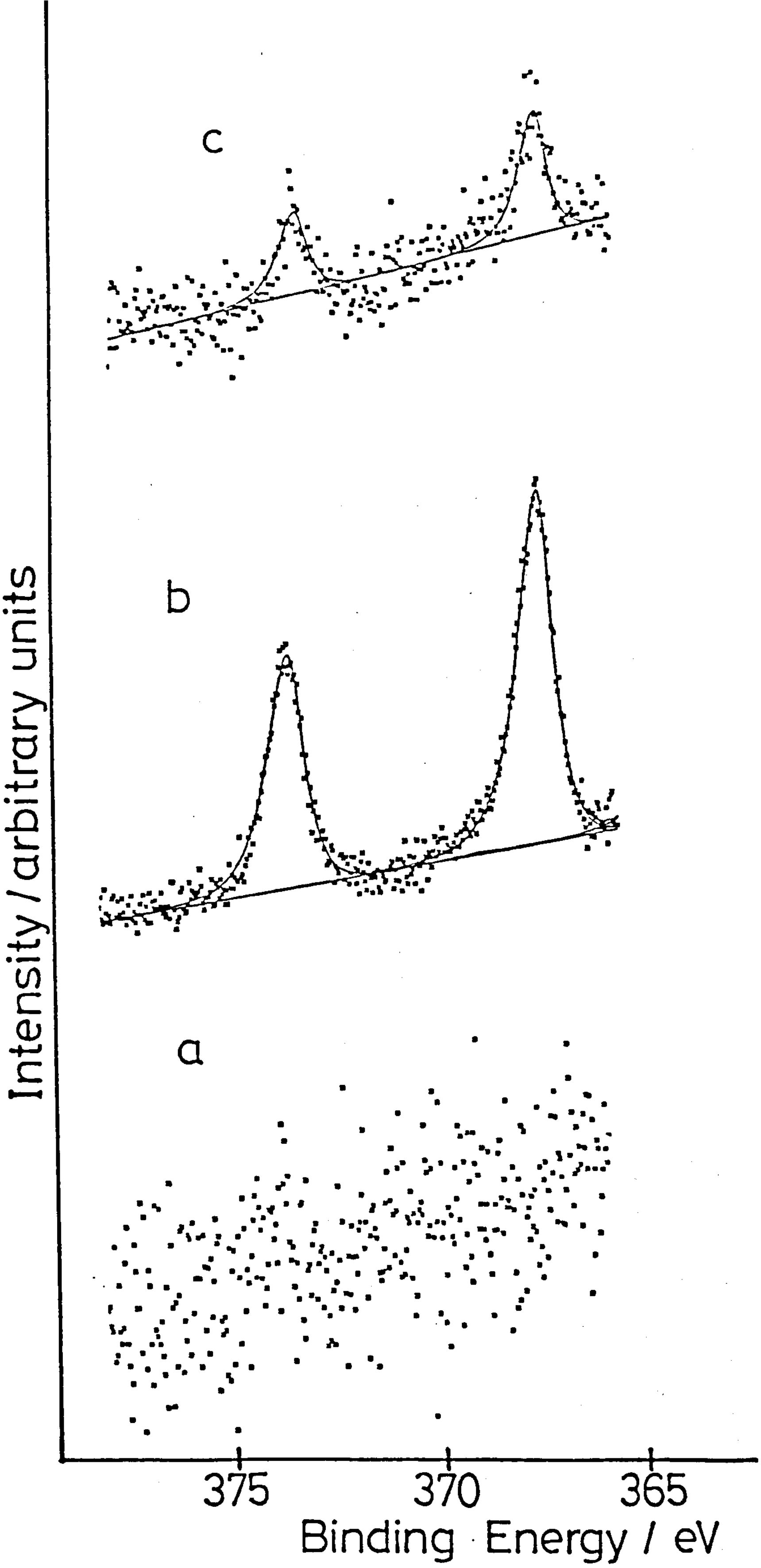

Fig 6.1:- Ag3d spectra for the B3 platinum sample.

a) Argon ion etched surface.
b) Heated in vacuo to 600°C.
c) Heated in O_2.

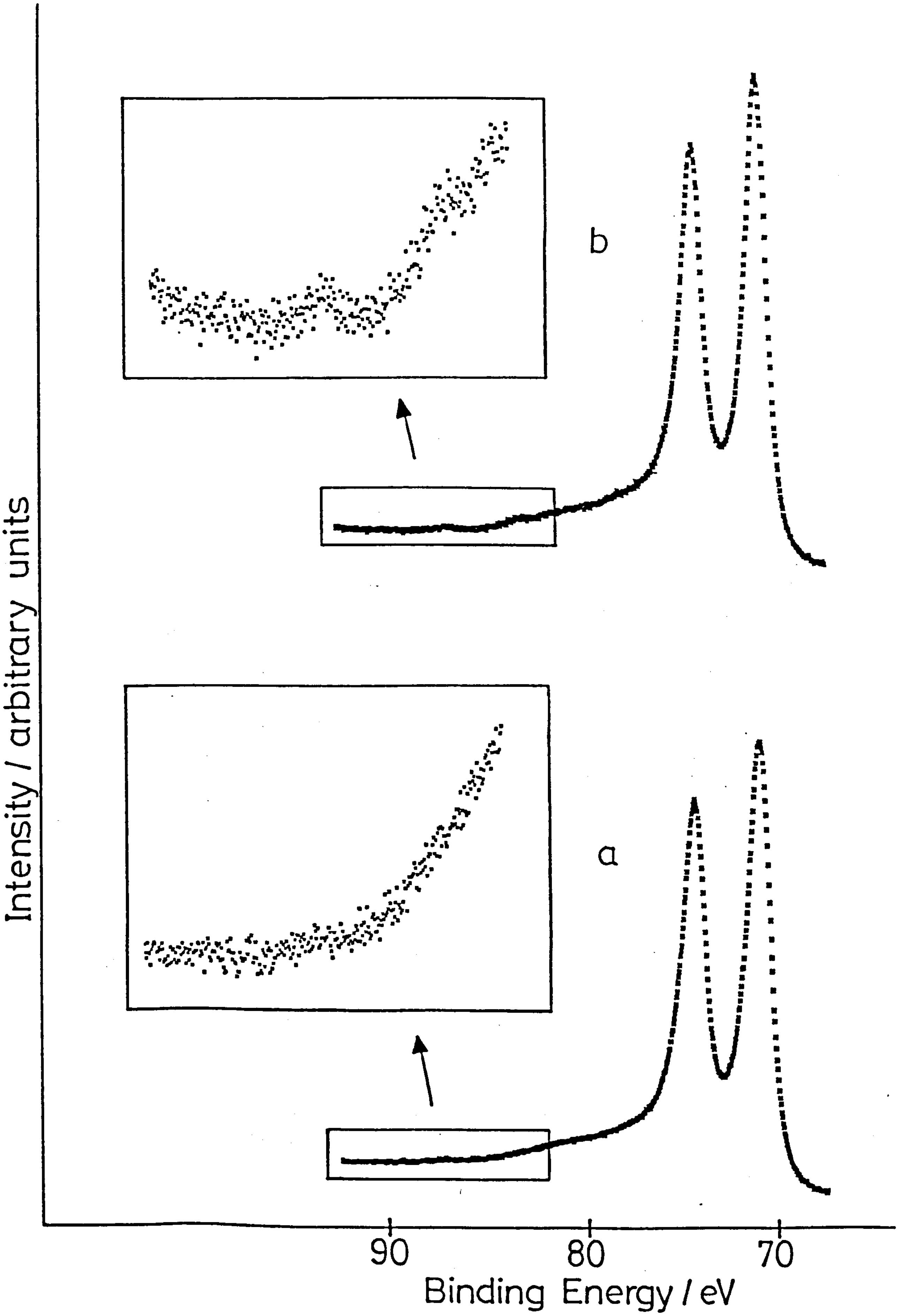

Fig 6.2:- Pt4f/Au4f spectra for B1(2) platinum sample.
a) Argon ion etched , b) Heated to 600°C in vacuo.

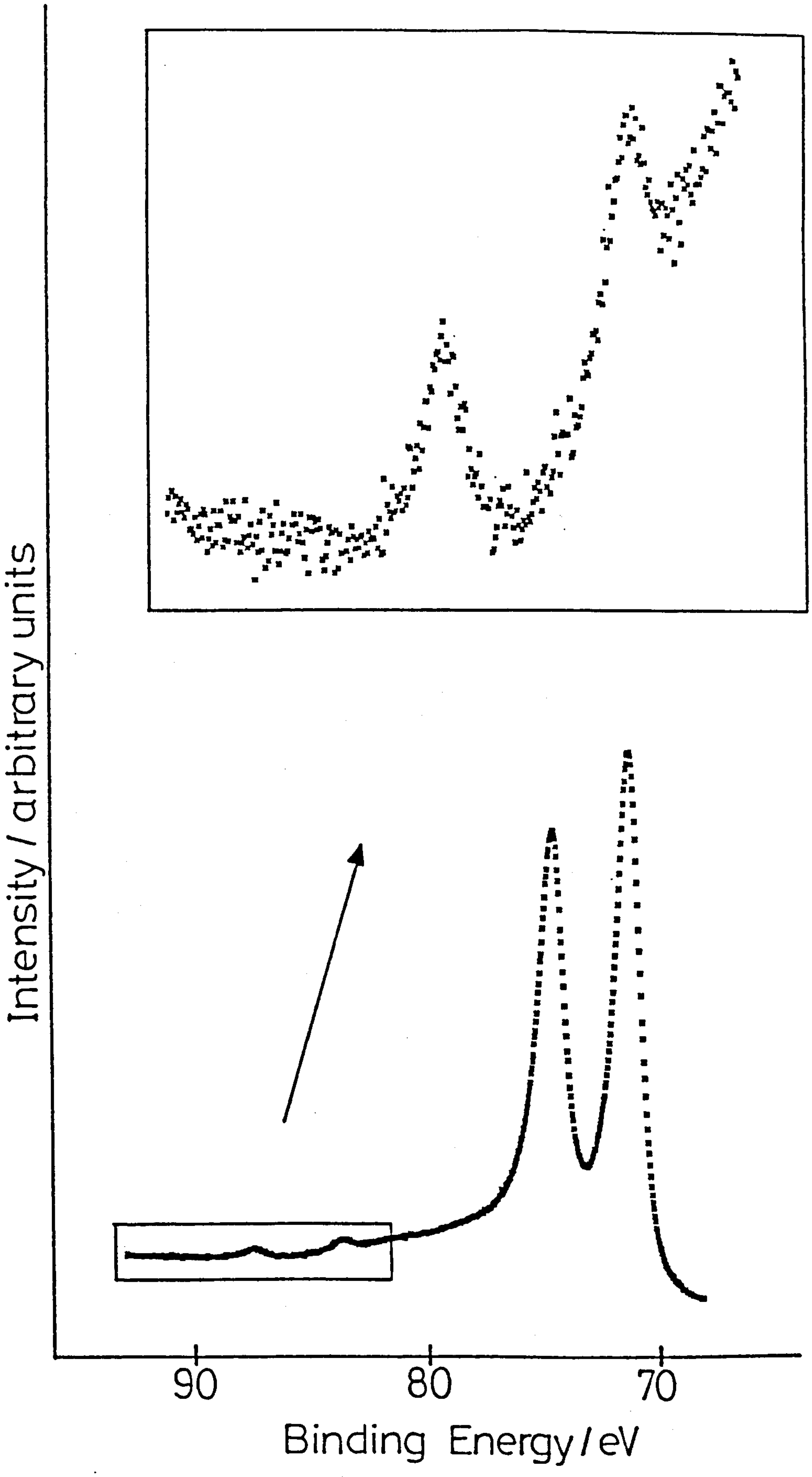

Fig 6.3:- High quality Pt4f/Au4f spectrum obtained for B1(2) platinum sample heated to 600°C in vacuo.

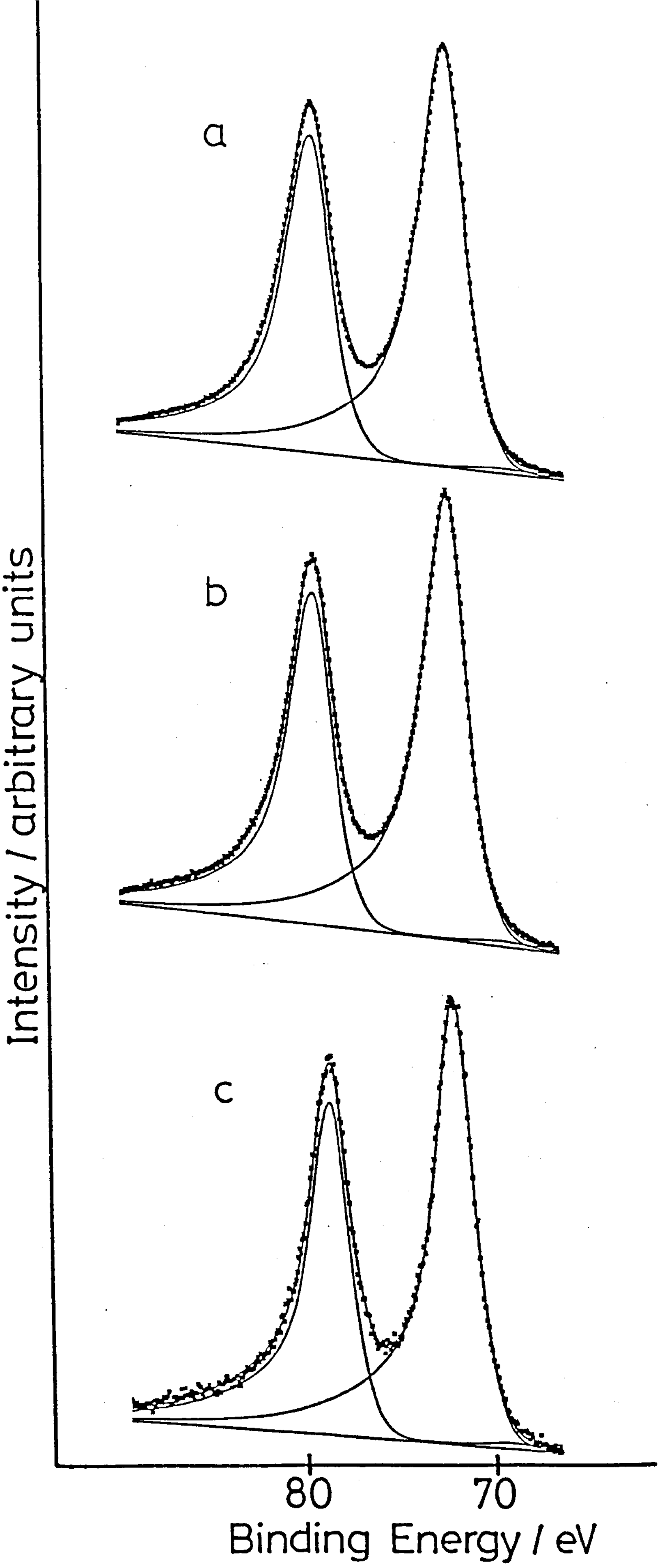

Fig 6.4:- Selection of Pt4f spectra.

a) Argon ion etched surface.
b) Sample heated in vacuo to 600°C.
c) Sample heated in O_2 (600°C, 5×10^{-4} torr, 10 mins).

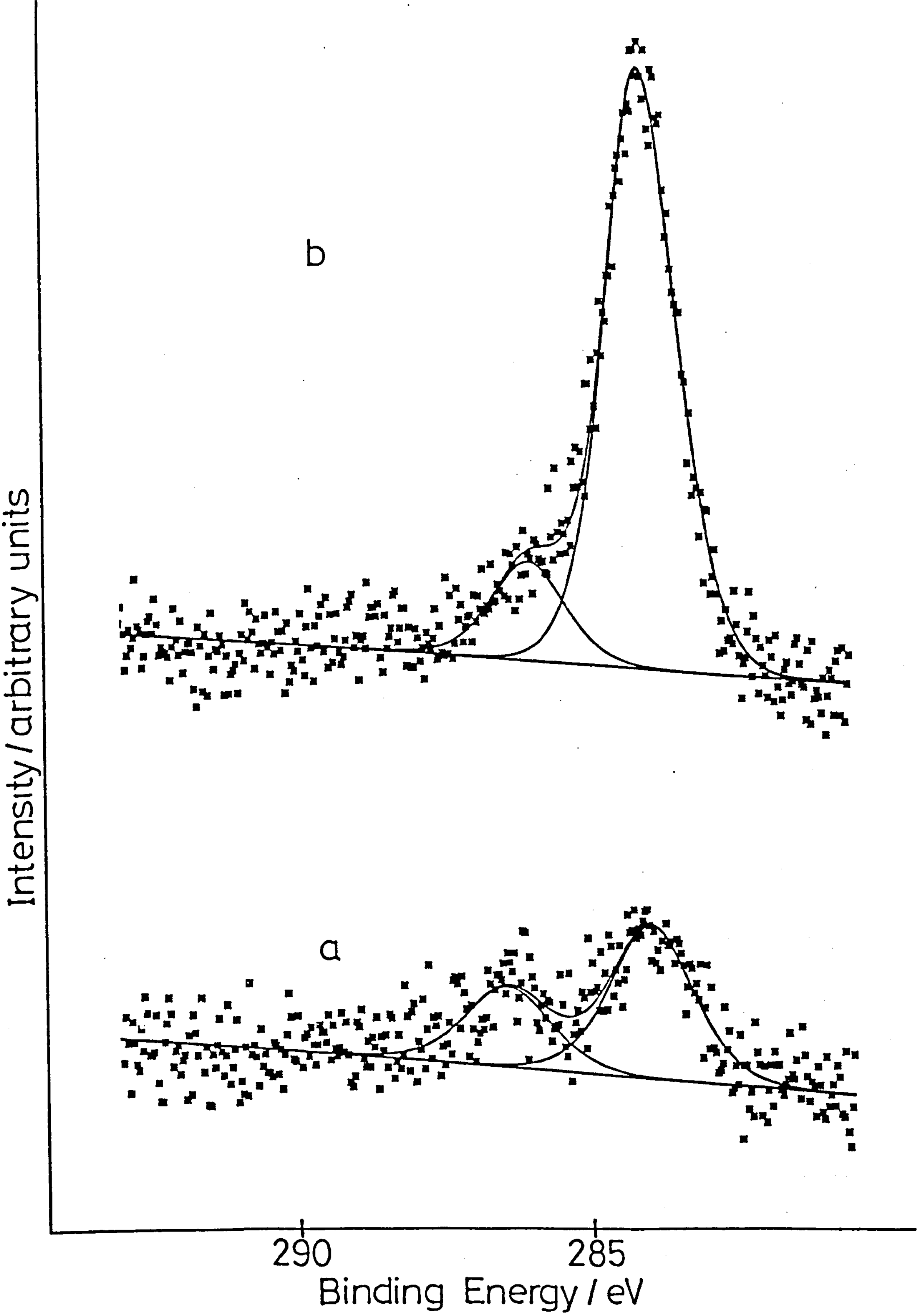

Fig 6.5:- C1s region for B2 platinum sample.

a) Argon ion etched surface (prior to spectrum (b)).
b) Heated to 600°C in vacuo.

Intensities scales are the same.

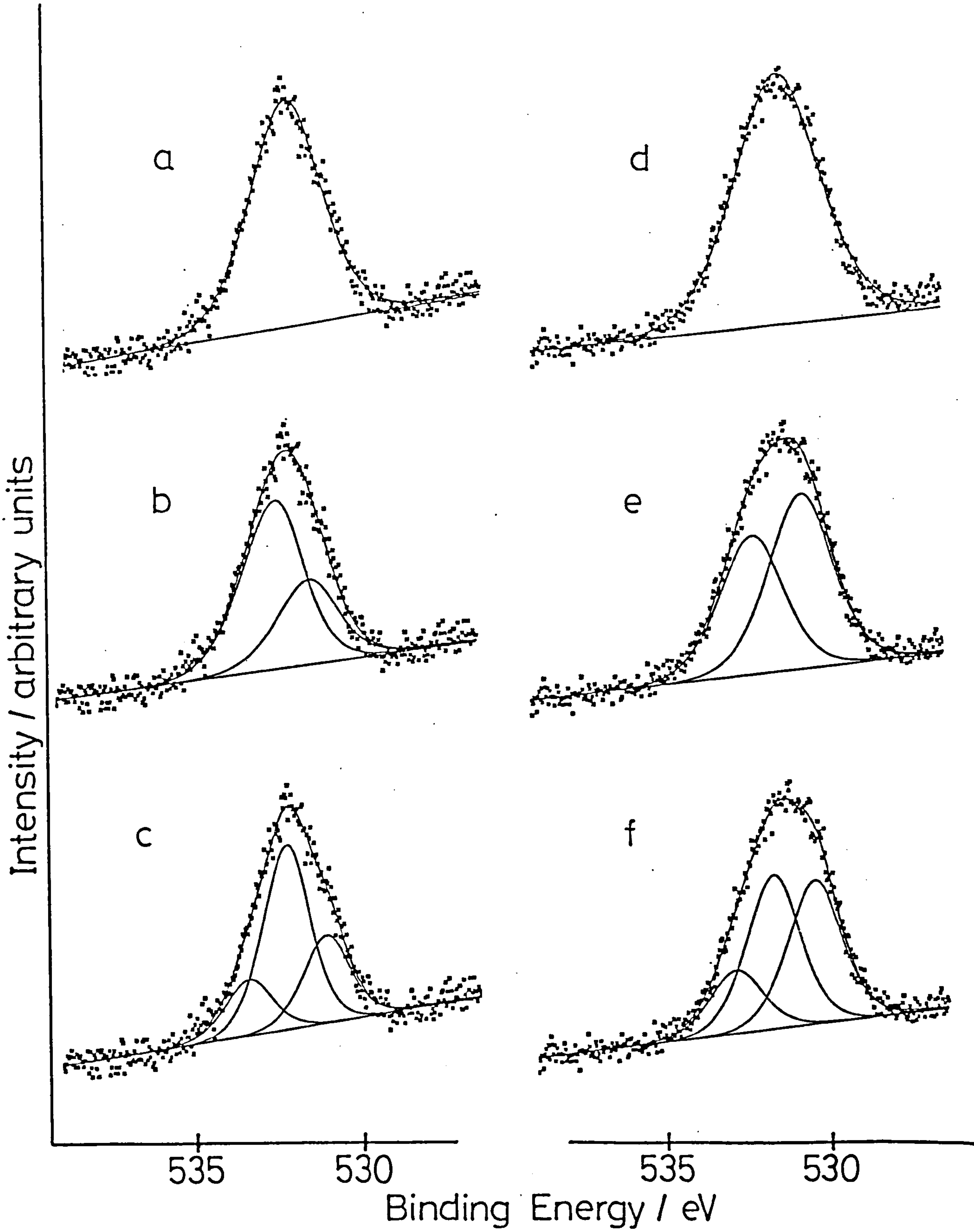

Fig 6.6:- O1s spectra recorded for platinum B3 sample.

Spectra a-c; O1s spectrum for argon ion etched surface fitted to a) 1 peak, b) 2 peaks, c) 3 peaks.

Spectra d-f; O1s spectrum for sample heated in O_2 (see text) fitted to d) 1 peak, e) 2 peaks, f) 3 peaks.

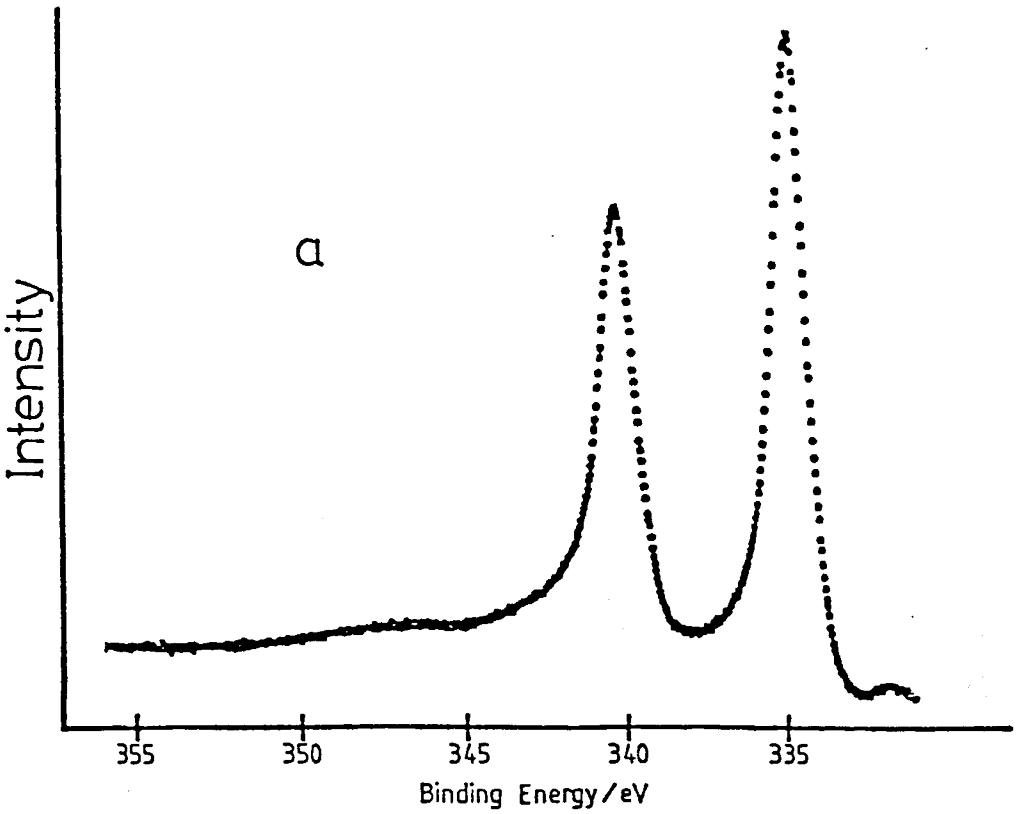

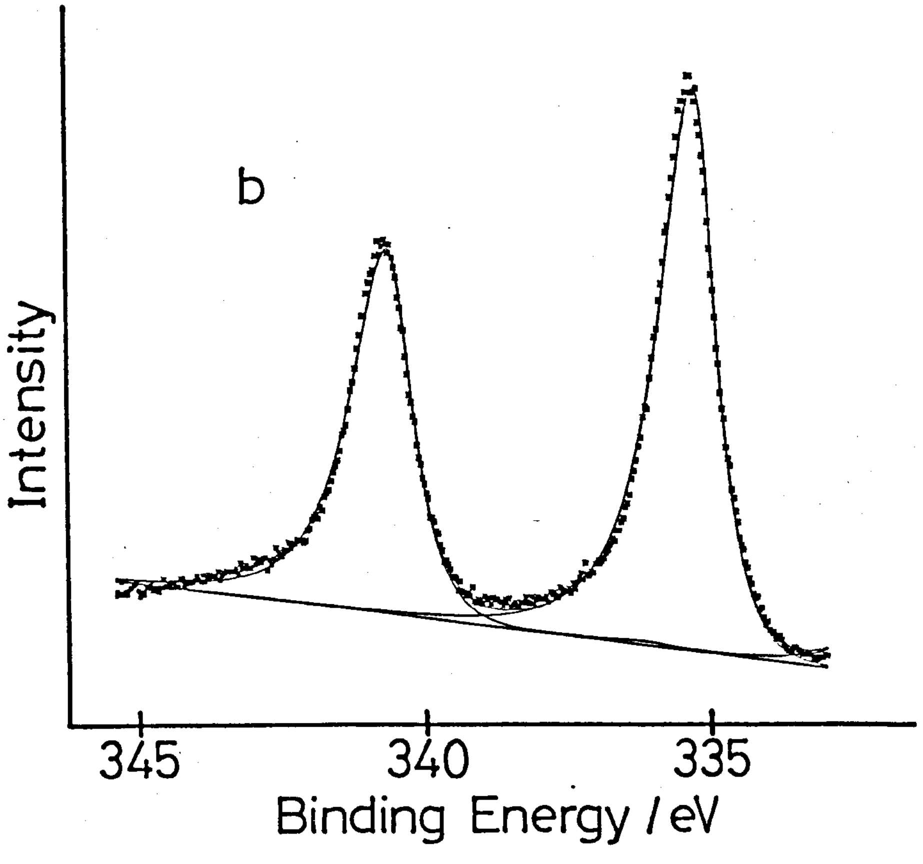

Fig 6.7:- Pd3d region for argon ion etched palladium metal.

a) Wide scan spectrum (25 eV).
b) Fitted spectrum using empirical peak parameters.

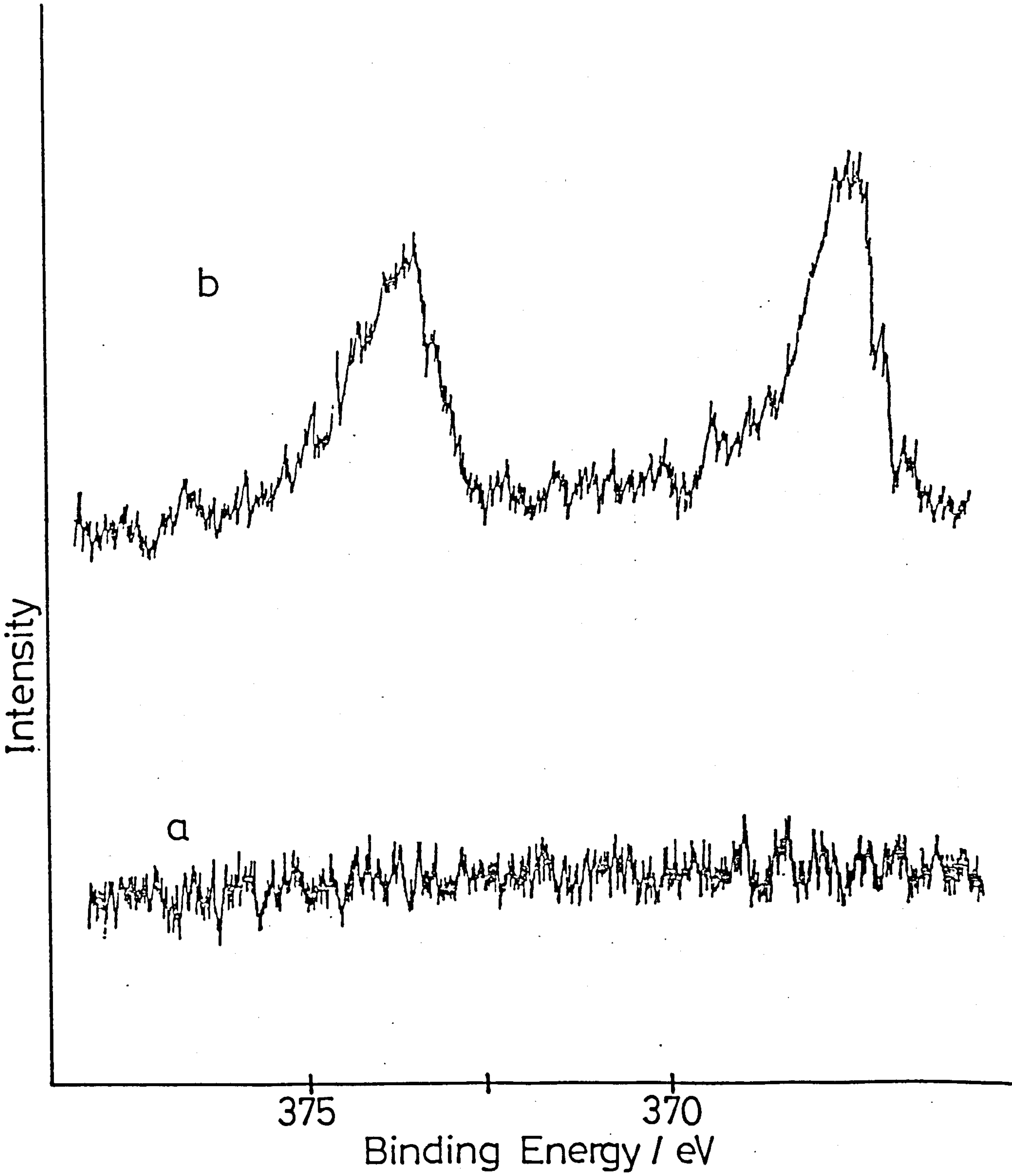

Fig 6.8:- Ag3d region for palladium (S2) sample.

a) Argon ion etched surface.
b) Sample heated to 600°C in vacuo.

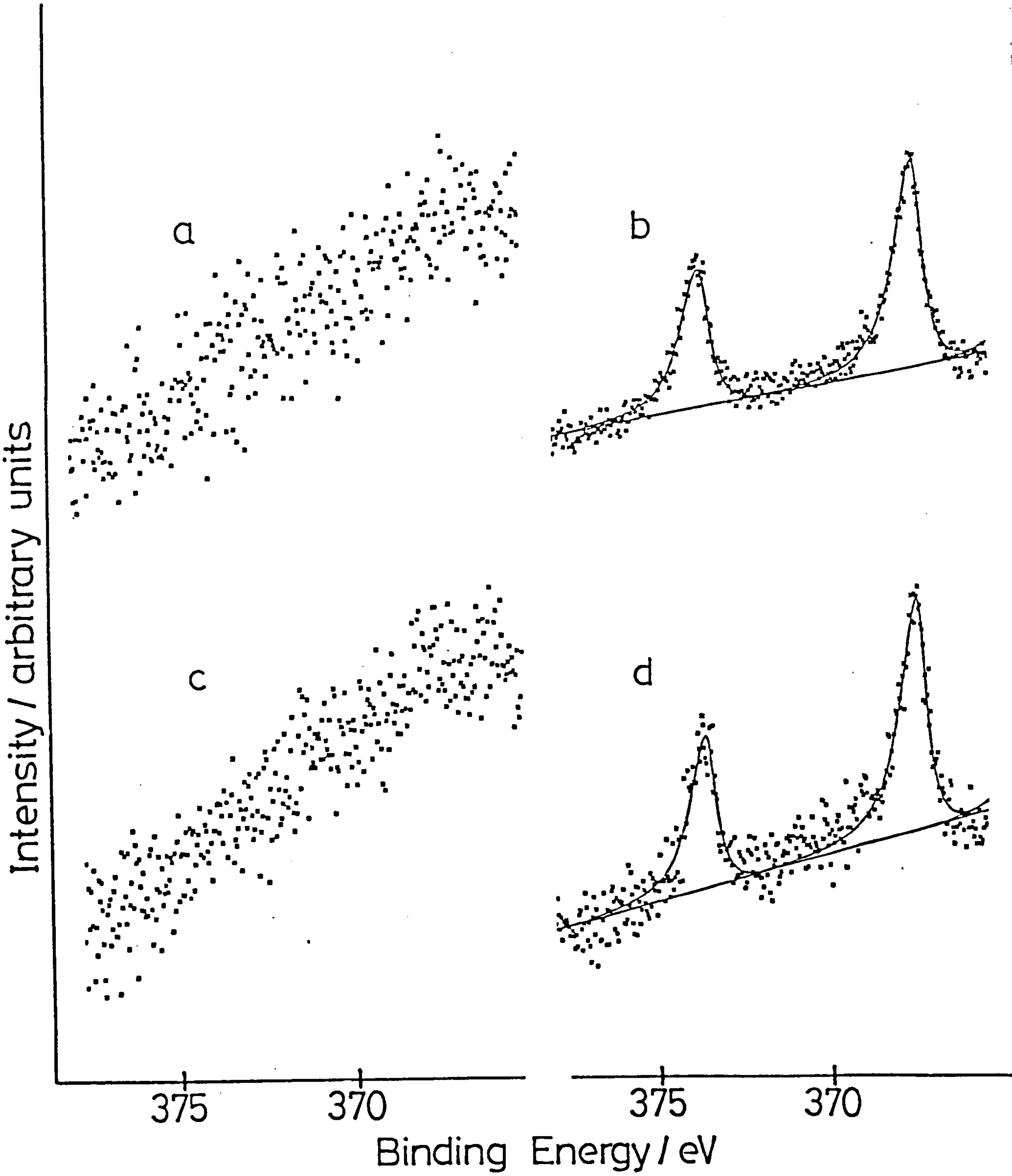

Fig 6.9:- Ag3d region for palladium (S2) sample.

a) Argon ion etched surface (before (b)).
b) Heated to 600°C in vacuo.
c) Argon ion etched surface (before (d)).
d) After heating in O_2 (600°C, 5×10^{-4} torr, 40 minutes).

'Etched' spectral intensities are expanded.

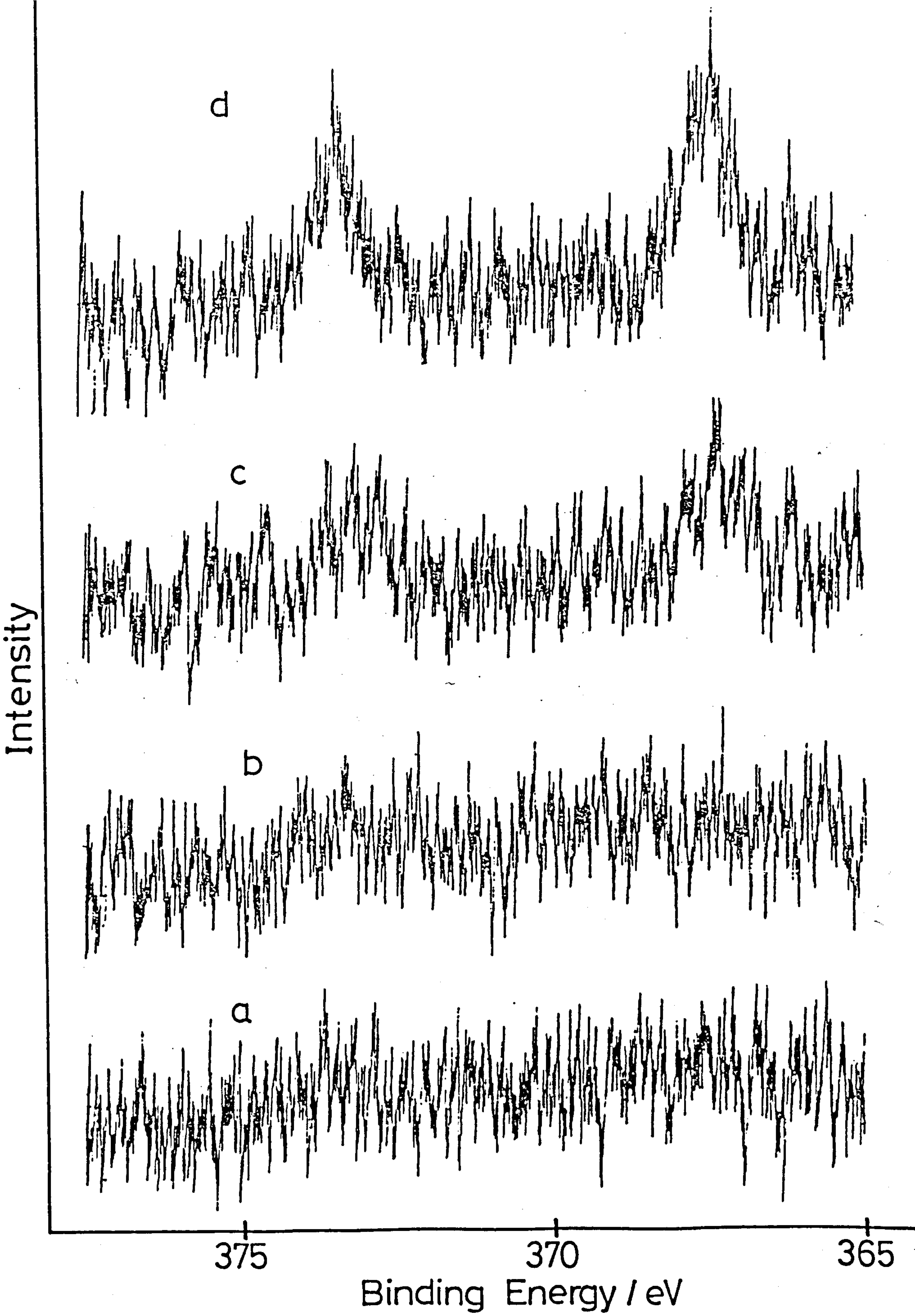

Fig 6.10:- Change in the Ag3d region with sample heating in vacuo. Spectra were recorded one hour (approx) after reaching the required temperature.

a) Ambient, b) 200°C, c) 300°C, d) 450°C.

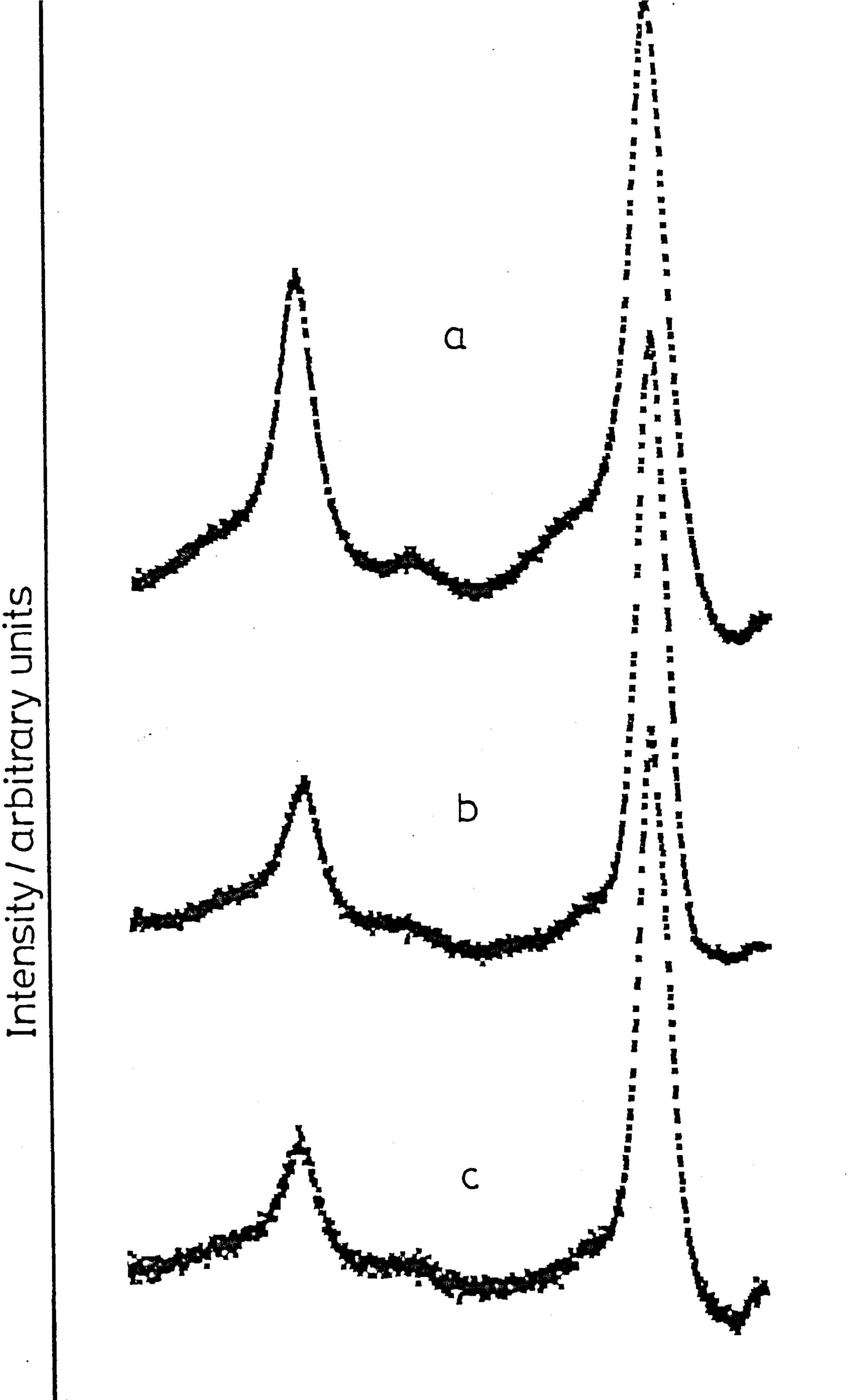

Fig 6.11:- O1s/Pd3p spectra for S2 sample.

a) Argon ion etched surface.
b) Heated to 600°C in vacuo.
c) Heated in O_2 (see text).

REFERENCES

1. H.Hertz, **Ann.Physik.**, 31, 983, (1887).

2. J.J.Thompson, **Phil.Mag.**, 48, 547, (1899).

3. P.Lenard, **Wien Ber.**, 108, 649, (1899); **Ann.Physik.**, 2, 359, (1900); ibid., 8, 149, (1902).

4. A.Einstein, **Ann.Physik.**, 17, 132, (1905).

5. D.W.Turner, A.D.Baker, C.Baker, C.R.Brundle, "Molecular Photoelectron Spectroscopy:- A Handbook of He 584Å Spectra", Interscience, London-New York, (1970).

6. N.Shevchik, J.Tejeda, M.Cardona, **Phys.Rev.B**, 9, 2627, (1974).

7. K.Siegbahn, C.Nordling, A.Fahlman, R.Nordberg, K.Hamrin, J.Hedman, C.Johansson, T.Bergmark, S.Karlsson, I.Lindgren , B.Lindberg, "ESCA- Atomic, Molecular and Solid State Structure studied by means of Electron Spectroscopy", WNova.Acta.Regiae. WSoc.Sci.Upsaliensis&, ESer IVR, Vol 20, (1967).

8. K.Siegbahn, C.Nordling, G.Johansson, J.Hedman, P.F.Heden, K.Hamrin, U.Gelius, T.Bergmark, L.O.Werme, R.Manne, Y.Baer, " ESCA Applied to Free Molecules", North-Holland Amsterdam, (1969).

9. U.Gelius, **J.Electron Spec.Relat.Phenom.**, 5, 985, (1974).

10. H.Fellner-Feldegg, H.Siegbahn, L.Asplund, P.Kelfve, K.Siegbahn, **J.Electron Spec.Relat.Phenom.**, 7, 421, (1975).

11. H.Siegbahn, S.Svennson, M.Lundholm, **J.Electron Spec.Relat. Phenom.**, 24(2), 205, (1981).

12. P.Auger, **Surf.Sci.**, 48, 1, (1975).

13. "Handbook of X-ray and UV Photoelectron Spectroscopy" edited by D.Briggs, Chapters 4,8 and 9, Heyden, (1977).

14. "Practical Surface Analysis by Auger and X-ray Photoelectron Spectroscopy" edited by D.Briggs and M.P.Seah, Wiley and Sons Ltd, (1983).

15. R.Kammerer, J.Barth, J.Gerken, A.Flodstroem, L.I.Johansson, **Solid State Commun.**, 41(5), 435, (1982).

16. D.R.Lloyd, C.M.Quinn, N.V.Richardson, **J.Chem.Soc.Farad. Trans.2**, 72, 1036, (1976).

17. P.H.Citrin, G.K.Wertheim, Y.Baer, **Phys.Rev.Lett.**, 41, 1425, (1978).

18. "Handbook of X-ray and UV Photoelectron Spectroscopy" edited by D.Briggs, Chapter 3 by S.Evans, Heyden, (1977).

19. J.C.Carver, R.C.Gray, D.M.Hercules, **J.Am.Chem.Soc.**, 96, 6851, (1974).

20. A.F.Povey, P.M.A.Sherwood, **J.Chem.Soc.Farad.Trans.2**, 70, 1240, (1974).

21. K.S.Kim, R.E.Davis, **J.Electron Spec.Relat.Phenom.**, 1, 251, (1973).

22. C.A.Tolman, W.M.Riggs, W.J.Linn, C.M.King, R.C.Wendt, **Inorg.Chem.**, 12, 2770, (1973).

23. T.C.Koopmans, **Physica**, 1, 104, (1933).

24. L.Hedin, A.Johansson, **J.Phys.B**, 2, 1336, (1969).

25. R.L.Martin, D.A.Shirley in "Electron Spectroscopy: Theory, Techniques and Applications" edited by C.R.Brundle and A.D.Baker, Academic Press London, Vol 1, 1977.

26. D.A.Shirley, **Adv.Chem.Phys.**, 23, 85, (1973).

27. H.Basch, **Chem.Phys.Lett.**, 5, 337, (1970).

28. W.L.Jolly, D.N.Hendrickson, **J.Am.Chem.Soc.**, 92, 1836, (1970).

29. D.W.Davis, M.S.Banna, D.A.Shirley, **J.Chem.Phys.**, 60, 237, (1974).

30. D.A.Shirley, **Chem.Phys.Lett.**, 15, 325, (1972).

31. P.M.A.Sherwood, **J.Chem.Soc.Farad.Trans.2**, 72, 1791, (1976).

32. C.S.Fadley in "Electron Spectroscopy: Theory, Techniques and Applications" edited by C.R.Brundle and A.D.Baker, Academic Press London, Vol 2, 1978.

33. T.A.Carlson, G.E.McGuire, **J.Electron Spec.Relat.Phenom.**, 1, 161, (1972/3).

34. C.J.Powell, **Surf.Sci.**, 44, 29, (1974).

35. I.Lindau, W.E.Spicer, **J.Electron Spec.Relat.Phenom.**, 3, 409, (1974).

36. M.P.Seah, W.A.Dench, Natl.Phys.Lab(UK)., Div.Chem.Stand. Report, 82, (1978).

37. W.A.Fraser, J.V.Florio, W.N.Delgass, W.D.Robertson, **Surf.Sci.**, 36, 661, (1973).

38. C.S.Fadley, **J.Electron Spec.Relat.Phenom.**, 5, 725, (1974).

39. J.P.Coad, J.G.Cunningham, **J.Electron Spec.Relat.Phenom.**, 3, 435, (1974).

40. R.O.Ansell, T.Dickinson, A.F.Povey, P.M.A.Sherwood, **J.Electron Spec.Relat.Phenom.**, 11, 301, (1977).

41. P.H.Middleton, A.J.Paul, P.M.A.Sherwood, **J.Chem.Soc.Farad. Trans.1**, 80, 2549, (1984).

42. C.S.Fadley, **Faraday Discuss.**, 60, 18, (1975).

43. M.Mehta, C.S.Fadley, **Phys.Lett.**, 55A, 59, (1975).

44. M.O.Krause, **Chem.Phys.Lett.**, 10, 65, (1971).

45. M.S.Banna, D.A.Shirley, **J.Electron Spec.Relat.Phenom.**, 8, 23, (1976).; and 8, 225, (1976).

46. R.Nilsson, R.Nyholm, A.Berndtsson, J.Hedman, C.Nordling, **J.Electron Spec.Relat.Phenom.**, 9, 337, (1976).

47. K.Siegbahn, **J.Electron Spec.Relat.Phenom.**, 5, 3, (1974).

48. R.Nyholm, N.Martensson, **Chem.Phys.Lett.**, 74, 337, (1980).

49. N.Martensson, R.Nyholm, **Phys.Rev.B**, 24, 7121, (1981).

50. R.Nyholm, N.Martensson, A.Lebugle, U.Axelsson, **J.Phys.F. Metal.Phys.**, 11, 1727, (1981).

51. R.W.Shaw, T.D.Thomas, **Phys.Rev.Lett.**, 29, 689, (1972).

52. P.H.Citrin, P.Eisenberger, D.R.Hamann, **Phys.Rev.Lett.**, 33, 965, (1974).

53. U.Gelius, E.Basilier, S.Svennson, T.Bergmark, K.Siegbahn, **J.Electron Spec.Relat.Phenom.**, 2, 405, (1973).

54. T.Dickinson, A.F.Povey, P.M.A.Sherwood, **J.Electron Spec. Relat.Phenom.**, 2, 441, (1973).

55. S.P.Kowalczyk, L.Ley, R.A.Pollak, F.R.McFeely, D.A.Shirley, **Phys.Rev.B**, 7, 4009, (1973).

56. G.K.Wertheim in "Electron Spectroscopy: Theory, Techniques and Applications" edited by C.R.Brundle and A.D.Baker, Academic Press London, Vol 2, 1978.

57. U.Gelius, **J.Electron Spec.Relat.Phenom.**, 5, 985, (1974).

58. D.T.Clark, A.Dilks, **J.Polym.Sci.Polym.Chem.Ed.**, 15, 15, (1977).

59. D.C.Frost, C.A.McDowell, A.Ishitani, **Molec.Phys.**, 24, 861, (1972).

60. K.S.Kim, R.E.Davies, **J.Electron Spec.Relat.Phenom.**, 1, 251, (1972/3).

61. S.Larsson, **Chem.Phys.Lett.**, 32, 401, (1975).; ibid., 40, 362, (1976).

62. S.Asada, S.Sugano, **J.Phys.Soc.Jap.**, 41, 1291, (1976).

63. P.Burroughs, A.Hamnett, A.F.Orchard, G.Thornton, **J.Chem.Soc. Dalton Trans.**, 1686, (1976).

64. D.Briggs, V.A.Gibson, **Chem.Phys.Lett.**, 25, 493, (1974).

65. L.J.Matienzo, W.E.Schwarz, S.O.Grim, **Inorg.Nucl.Chem.Lett.**, 8, 1085, (1972).

66. S.T.Manson, **J.Electron Spec.Relat.Phenom.**, 9, 21, (1976).

67. R.L.Martin, D.A.Shirley, **J.Chem.Phys.**, 64, 3685, (1976).

68. R.L.Martin, D.A.Shirley, **Phys.Rev.A**, 13, No 4, 1475, (1976).

69. R.L.Martin, B.E.Mills, D.A.Shirley, **J.Chem.Phys.**, 64, 3690, (1976).

70. D.A.Shirley in "Electron Spectroscopy: Theory, Techniques and Applications" edited by C.R.Brundle and A.D.Baker, Academic Press London, Vol 1, 1977.

71. A.Kasdan, W.C.Lineberger, **Phys.Rev.A**, 10, 1658, (1974).

72. S.Hufner, G.K.Wertheim, D.N.E.Buchanan, K.W.West, **Phys.Lett.**, 46A, No 6, 420, (1974).

73. G.K.Wertheim, S.Hufner, **J.Inorg.Nucl.Chem.**, 38, 1701, (1976).

74. S.Doniach, M.Sunjic, **J.Phys.C**, 3, 285, (1970).

75. S.Hufner, G.K.Wertheim, **Phys.Rev.B**, 11, 5197, (1975).

76. A.Barrie, **Chem.Phys.Lett.**, 19, 109, (1973).

77. L.Ley, F.R.McFeely, S.P.Kowalczyk, J.G.Jenkin, D.A.Shirley, **Phys.Rev.B**, 11, 600, (1975).

78. D.R.Penn, **Phys.Rev.Lett.**, 38, 1429, (1977).

79. S.Evans, E.Raftery, **J.Electron Spec.Relat.Phenom.**, 17, 137, (1979).

80. "Handbook of X-ray and UV Photoelectron Spectroscopy" edited by D.Briggs, Chapter 2 by A.Barrie, Heyden, (1977).

81. P.A.Breeze, H.L.Hartnagel, P.M.A.Sherwood, **J.Electrochem. Soc.**, 127, 454, (1980).

82. J.P.Coad, J.G.Cunningham, **J.Electron Spec.Relat.Phenom.**, 3, 435, (1974).

83. K.S.Kim, W.E.Baitinger, J.W.Amy, N.Winograd, **J.Electron Spec. Relat.Phenom.**, 5, 351, (1974).

84. R.Holm, S.Storp, **Appl.Phys.**, 12, 101, (1977).

85. A.Proctor, P.M.A.Sherwood, **Anal.Chem.**, 54, 13, (1982).

86. R.O.Ansell, T.Dickinson, A.F.Povey, P.M.A.Sherwood, **J.Electroanal.Chem.**, 98, 79, (1979).

87. P.M.A.Sherwood in "Practical Surface Analysis by Auger and Photoelectron Spectroscopy" edited by D.Briggs and M.P.Seah (J.Wiley, London, 1983), Appendix 3.

88. D.A.Shirley, **Phys.Rev.**, B5, 4709, (1972).

89. A.Proctor, P.M.A.Sherwood, **Anal.Chem.**, 52, 2315, (1980).

90. P.M.Th.M. Van Attekum, J.M.Trooster, **J.Electron Spec. Relat.Phenom.**, 11, 363, (1977).

91. H.Y.Hall, Ph.D Thesis, University of Newcastle-upon-Tyne, 1983.

92. A.F.Povey, Ph.D Thesis, University of Newcastle-upon-Tyne, 1975.

93. J.S.Brinen, **J.Electron Spec.Relat.Phenom.**, 5, 377, (1974).

94. T.Dickinson, A.F.Povey, P.M.A.Sherwood, **J.Electron Spec. Relat.Phenom.**, 2, 441, (1973).

95. R.S.Swingle, W.M.Riggs, Critical Reviews in Analytical Chemistry, Vol 5, Issue 3, p267-321, (1975).

96. G.Grimvall, **Phys.Script.**, 9, 43, (1974).

97. C.D.Cook, K.Y.Wan, U.Gelius, K.Hamrin, G.Johansson, E.Olsson, H.Siegbahn, C.Nordling, K.Siegbahn, **J.Am.Chem.Soc.**, 93, 1904, (1971).

98. D.T.Clark, H.R.Thomas, **J.Polym.Sci.Polym.Chem.Ed.**, 14, 1671, (1976).

99. J.L.Ogilvie, A.Wolberg, **Appl.Spectrosc.**, 26(3), 401, (1972).

100. R.Nordling, H.Brecht, R.G.Albridge, A.Fahlman, J.R.Van Wazer, **Inorg.Chem.**, 9, 2469, (1970).

101. G.Johannsson, J.Hedman, A.Berndtsson, M.Klasson, R.Nilsson, **J.Electron Spec.Relat.Phenom.**, 2, 295, (1973).

102. W.E.Schwartz, P.H.Watts, J.P.Watts, J.W.Brasch, E.R.Lippincott, **Anal.Chem.**, 44, 2001, (1972).

103. W.J.Stec, W.E.Mirgan, R.G.Albridge, J.R.Van Wazer, **Inorg.Chem.**, 11, 219, (1972).

104. W.P.Dianis, J.E.Lester, **Anal.Chem.**, 45, 1416, (1973).

105. C.D.Wagner, **J.Electron Spec.Relat.Phenom.**, 18, 345, (1980).

106. J.A.Connor, in "Handbook of X-ray and Ultraviolet Photoelectron Spectroscopy" (Edited by D.Briggs), Chap 5, p183, Heyden, London (1977).

107. D.J.Hnatowich, J.Hudis, M.L.Perlman, R.C.Ragaini, **J.Appl.Phys.**, 42(12), 4883, (1971).

108. C.R.Ginnard, W.M.Riggs, **Anal.Chem.**, 46(9), 1306, (1974).

109. Y.Uwamino, T.Ishizuka, H.Yamatera, **J.Electron Spec.Relat. Phenom.**, 23, 55, (1981).

110. D.S.Urch, M.Webber, **J.Electron Spec.Relat.Phenom.**, 5, 791, (1974).

111. D.Betteridge, J.C.Carver, D.M.Hercules, **J.Electron Spec. Relat.Phenom.**, 2, 327, (1973).

112. L.I.Matienzo, S.O.Grim, **Anal.Chem.**, 46(13), 2052, (1974).

113. S.Kohiki, T.Ohmura, K.Kusao, **J.Electron Spec.Relat.Phenom.**, 28, 229, (1983).

114. B.Carriere, J.P.Deville, D.Brion, J.Escard, **J.Electron Spec. Relat.Phenom.**, 10, 85, (1977).

115. J.P.Contour, G.Mouvier, **J.Electron Spec.Relat.Phenom.**, 7, 85, (1975).

116. V.I.Nefedov, **J.Electron Spec.Relat.Phenom.**, 25, 29, (1982).

117. P.Swift, **Surf.Interface.Anal.**, 4(2), 47, (1982).

118. S.Kinoshita, T.Ohita, H.Kuroda, **Bull.Chem.Soc.Jpn.**, 49(4), 1149, (1976).

119. S.Kohiki, K.Oki, **J.Electron Spec.Relat.Phenom.**, 33, 375, (1984).

120. A.Jaegle, A.Kait, G.Nanse, J.C.Peruchetti, **Analusis**, 9, 252, (1981).

121. D.T.Clark, D.B.Adams, **Chem.Phys.Lett.**, 10, 121, (1971).

122. D.A.Huchital, R.T.McKeon, **Appl.Phys.Lett.**, 20, 158, (1972).

123. R.T.Lewis, M.A.Kelly, **J.Electron Spec.Relat.Phenom.**, 20, 105, (1980).

124. C.P.Hunt, C.T.H.Stoddart, M.P.Seah, **Surf.Interface.Anal.**, 3, 157, (1981).

125. P.Swift, D.Shuttleworth, M.P.Seah, in "Practical Surface Analysis by Auger and X-ray Photoelectron Spectroscopy" edited by D.Briggs and M.P.Seah, (J.Wiley, London, 1983), Appendix 2.

126. T.E.Madey, C.D.Wagner, A.Joshi, **J.Electron Spec.Relat. Phenom.**, 10, 359, (1977).

127. V.I.Nefedov, Ya.V.Salyn, G Leonhardt, R.Scheibe, **J.Electron Spec.Relat.Phenom.**, 10, 121, (1977).

128. R.J.Bird, P.Swift, **J.Electron Spec.Relat.Phenom.**, 21, 227, (1980).

129. C.J.Powell, N.E.Erickson, T.E.Madey, **J.Electron Spec.Relat. Phenom.**, 17, 361, (1979).

130. G.Schon, **J.Electron Spec.Relat.Phenom.**, 1, 377, (1972).

131. K.Asami, **J.Electron Spec.Relat.Phenom.**, 9, 469, (1976).

132. K.Richter, B.Peplinski, **J.Electron Spec.Relat.Phenom.**, 13, 69, (1978).

133. C.D.Wagner, L.H.Gale, R.H.Raymond, **Anal.Chem.**,51, 466, (1979).

134. J.C.Fuggle, N.Martensson, **J.Electron Spec.Relat.Phenom.**, 21, 275, (1980).

135. A.Lebugle, U.Axelsson, R.Nyholm, N.Martensson, **Phys.Scrip.**, 23, 825, (1981).

136. A.Proctor, P.M.A.Sherwood, **Surf.Inter.Anal.**, 2, No 5, 191, (1980).

137. R.Thompson in "Progress in Boron Chemistry", edited by R.J.Brotherton and H.Steinberg, (Pergamon Press, Oxford, 1970), Vol.2 Chapter 5.

138. Y.Okamoto, Y.Nitta, T.Imanaka, S.Teranishi, **J.Chem.Soc., Faraday Trans.I**, 75, 2027, (1979).

139. J.M.Lafferty, **J.Appl.Phys.**, 22, 299, (1951).

140. W.Hodge, R.M.Evans, A.F.Haskins, **J.Metals**, 7, 824, (1955).

141. C.E.Ransley, **J.Metals**, 14, 129, (1962).

142. "Handbook of Chemistry and Physics", The Chemical Rubber Co., Cleveland, Ohio. page E-72, 1982-83.

143. G.Mavel, J.Escard, P.Costa, J.Castaing, **Surf.Sci.**, 35, 109, (1973).

144. H.Ihara, M.Hirabayashi, H.Nakagawa, **Phys.Rev.B.**, 16, 726, (1977).

145. T.Tanaka, Y.Ishizawa, E.Bannai, S.Kamai, **Solid State Comm.**, 26, 879, (1978).

146. D.L.Johnson, B.N.Harman, S.H.Liu, **J.Chem.Phys.**, 73, 1898, (1980).

147. D.J.Joyner, O.Johnson, D.M.Hercules, **J.Amer.Chem.Soc.**, 102, 1910, (1980).

148. A.Berrada, J.P.Mercurio, J.Etourneau, P.Hagenmuller, **Rev.Int. Htes.Temp.et Refract.**, 15, 115, (1978).

149. J.N.Chazalviel, M.Campagna, G.K.Wertheim, P.H.Schmidt, **Phys. Rev.B.**, 14, 4586, (1976).

150. A.Lebugle, G.Montel, **Rev.Int.Htes.Temp.et Refract.**, 11, 231, (1974).

151. R.J.Cotton, J.W.Rabalais, **Inorg.Chem.**, 15, 236, (1976).

152. V.G.Alyoshin, A.I.Kharkmov, V.M.Prokopenko, **J.Solid State Chem.**, 38, 105, (1981).

153. P.H.Middleton, Ph.D.Thesis, University of Newcastle-upon-Tyne, (1983).

154. R.Thompson in "Borides: Their Chemistry and Applications", R.I.C.Lecture Series, No.5, (1965).

155. B.W.Veal, D.J.Lam, D.G.Westlake, **Phys.Rev.B.**, 19, 2856, (1979).

156. N.N.Berezina, D.P.Valyukhov, E.S.Vorontsov, **Russian J.Phys. Chem.**, 55, 1650, (1981).

157. H.Y.Hall, P.M.A.Sherwood, **J.Chem.Soc.Faraday I**, 80, 135, (1984).

158. A.Proctor, P.M.A.Sherwood, **Surface and Interface Analysis**, 2, 191, (1980).

159. S.Evans, J.M.Thomas, **J.Chem.Soc.Faraday II**, 71, 313, (1975).

160. M.W.Roberts, **Pure Appl.Chem.**, 53, 2269, (1981).

161. P.R.Norton, **J.Catal.**, 36, 211, (1975).

162. P.Nozieres, C.T.De Dominicis, **Phys.Rev.**, 178, 1097, (1969).

163. G.K.Wertheim, S.Hufner, **Phys.Rev.Lett.**, 35, 53, (1975).

164. S.Hufner, G.K.Wertheim, **Phys.Rev.B**, 11, 678, (1975).

165. E.Antonangeli, A.Balzarotti, A.Bianconi, P.Perfett, P.Ascarelli, N.Nistico, **Solid State Comm.**, 21, 201, (1977).

166. M.O.Krause, T.A.Carlson, R.D.Dismukes, **Phys.Rev.**, 170, 37, (1968).

167. D.W.Fischer, **Adv.X-Ray Anal.**, 13, 159, (1969).

168. A.Barrie, F.J.Street, **J.Electron Spec.Relat.Phenom.**, 7, 1, (1975).

169. N.S.McIntyre, D.G.Zetaruk, **Anal.Chem.**, 49, 1521, (1975).

170. D.J.Joyner. D.M.Hercules, **J.Chem.Phys.**, 72, 1095, (1980).

171. D.R.Wheeler, **J.Vac.Sci.Technol.**, 15, 24, (1978).

172. D.N.Hendrickson, **Inorg.Chem.**, 9, 612, (1970).

173. D.T.Clark, A.Dilks, **J.Polymer Sci.Polymer Chem.Ed.**, 16, 791, (1978).

174. D.D.Sarma, C.N.R.Rao, **J.Electron Spec.Relat.Phenom.**, 20, 25, (1980).

175. E.Zintl, W.Morawietz, E.Z.Gastenger, **Z.anorg.Chem.**, 245, 8, (1940).

176. D.Nicolls in "Mellor's Comprehensive Treatise on Inorganic and

Theoretical Chemistry", Volume V, Part A, Section A5, (Macmillan, London, 1962).

177. A.W.Searcy, C.E.Myers, **J.Phys.Chem.**, 61, 957, (1957).

178. A.W.Searcy, University of California, Radiation Laboratory Report, UCRL-1404, (1951).

179. L.M.Kovba, E.M.Kenina, I.I.Kornilov, V.V.Glazova, **Dokl.Akad. Nauk.SSSR.**, 180, 360, (1968).

180. R.F.Domagala, D.J.McPherson, **J.Metals**, 6, 238, (1954).

181. G.N.Krishnan, B.J.Wood, D.Cubicciotti, **J.Electrochem.Soc.**, 128, 191, (1981).

182. T.A.Carlson, G.E.McGuire, **J.Electron Spec.Relat.Phenom.**, 1, 182, (1972-73).

183. J.H.Scofeld, **J.Electron Spec.Relat.Phenom.**, 8, 129, (1976).

184. P.M.A.Sherwood, **J.Chem.Soc.Farad.Trans.2**, 72, 1791, (1976).

185. C.S.Fadley, D.A.Shirley, **Phys.Rev.A**, 2, 1109, (1970).

186. R.J.Baird, C.S.Fadley, S.M.Goldberg, P.J.Feibleman, M.Sunjic, **Surf.Sci.**, 72, 495, (1978).

187. K.S.Robinson, P.M.A.Sherwood, **Surf.Inter.Anal.**, in press.

188. W.J.M.Tegart in "The Electrolytic and Chemical Polishing of Metals", Pergamon Press, (1959).

189. P.T.Dawson, S.A.J.Stazyk, **J.Vac.Sci.Technol.**, 21, 36, (1982).

190. J.G.Helliwell, Ph.D Thesis, Newcastle-upon-Tyne, (1984).

191. E.H.P.Cordefunke, 'The Chemistry of Uranium', Elsevier (Amsterdam), (1969).

192. C.A.Colmenares in 'Progress in Solid State Chemistry', edited by J.O.McCaldin and G.Somorjai, Vol.9, Chap.5, 139 (1974).

193. J.Verbist, J.Riga, J.J.Pireaux, R.Caudano, **J.Electron Spec. Relat.Phenom.**, 5, 193, (1974) and references therin.

194. D.Chadwick, **Chem.Phys.Lett.**, 21, 291, (1973).

195. G.C.Allen, J.A Crofts, M.T.Curtis, P.M.Tucker, D.Chadwick, P.J.Hampson, **J.Chem.Soc.Dalton.Trans.**, 1296, (1974).

196. J.J.Verbist, J.Riga, C.Tenret-Noel, J.J.Pireaux, G.d'ursel, R.Caudona, E.G.Derouane, in 'Plutonium and Other Actinides', ed by H.Blanck and R.Lindner, (North Holland, Amsterdam), p409, (1976).

197. G.C.Allen, P.M.Tucker, J.W.Wyler, **Vacuum**, 32, No 8, 481, (1982).

198. R.Delobel, H.Baussart, J-M.Leroy, J.Grimblot, L.Gengembre,

J.Chem.Soc.Farad.Trans.1, 79, 879, (1983).

199. L.E.Cox, **J.Electron Spec.Relat.Phenom.**, 26, 167, (1982).

200. S.Evans, **J.Chem.Soc.Farad.Trans.2**, 73, 1341, (1977).

201. J.G.Dillard, H.Moers, H.Klewe-Nebenius, G.Kirch, G.Pfennig, H.J.Ache, **J. Phys. Chem.**,, 88, 4104, (1984).

202. B.W.Veal, D.J.Lam, **Phys.Lett.**, 49A, No 6, 466, (1974).

203. B.W.Veal, D.J.Lam, W.T.Carnall, H.R.Hockstra, **Phys.Rev.B**, 12, 5651, (1975).

204. G.C.Allen, P.M.Tucker, J.W.Tyler, **J.Phys.Chem.**, 86, 224, (1982).

205. G.C.Allen, P.M.Tucker , **J.Chem.Soc.Dalton.Trans.**, 470 , (1973).

206. N.Beatham, A.F.Orchard, G.Thornton, **J.Electron Spec. Relat.Phenom.**, 19, 205, (1980).

207. J.Weber, V.A.Gubanov, **J.Inorg.Nucl.Chem.**, 41, 693, (1979).

208. J.Bloch, U.Atzmony, M.P.Dariel, M.H.Mintz, N.Shamir, **J.Nucl.Mater.**, 105, 196, (1982).

209. S.B.Nornes, R.G.Meisenheimer, **Surf.Sci.**, 88, 191, (1979).

210. C.Benndorf, C.Nobl, F.Theime, **Surf.Sci.**, 121, 249, (1982).

211. L.Ramqvist, K.Hamrin, G.Johannson, A.Fahlman, C.Nordling, **J.Phys.Chem.Solids**, 30, 1835, (1969).

212. L.Ramqvist, K.Hamrin, G.Johansson, U.Gelius, C.Nordling, **J.Phys.Chem.Solids**, 31, 2669, (1970).

213. P.Chiotti, W.C.Robinson, M.Konno, **J. Less-Common Metals**, 10, 273 (1966).

214. W.P.Ellis, **Surf.Sci.**, 61, 37, (1976).

215. D.T.Larson, J.M.Haschke, **Inorg.Chem.**, 20, no 7, 1945, (1981).

216. E.H.P.Cordefunke, **J.Inorg.Nucl.Chem.**, 24, 303, (1962).

217. M.E.A.Hermans, T.Markestein, **J.Inorg.Nucl.Chem.**, 25, 461, (1963).

218. W.I.Stuart, T.L.Whateley, **J.Inorg.Nucl.Chem.**, 31, 1639, (1969).

219. N.Quy-Dao, **Bull.Chem.Soc.Franc.**, 12, 4751, (1968).

220. J.L.Woolfrey, Report AAEC/E397 (Research Establishment, Lucas Heights), Nov 1976.

221. H.Brusset, N.Quy-Dao, **C.R.Acad.Sc.Paris**, C265, 1141, (1967).

222. J.Janov, P.G.Alfredson, V.K.Vilkaitis, Report AAEC/E220 (Research Establishment, Lucas Heights), 1971.

223. V.Urbanek, V.Sara, J.Moravec, **J.Inorg.Nucl.Chem.**, 41, 537, (1979).

224. J.L.Woolfrey, Report AAEC/TM476 (Research Establishment, Lucas Heights), 1968.

225. A.Deptula, **Nukleonika**, 7, 265, (1962).

226. A.M.Deane, **J.Inorg.Nucl.Chem.**, 21, 238, (1961).

227. P.C.Debets, B.O.Loopstra, **J.Inorg.Nucl.Chem.**, 25, 945, (1963).

228. W.I.Stuart, **J.Inorg.Nucl.Chem.**, 38, 1378, (1976).

229. A.I.Vogel in 'Macro and Semimicro Qualitative Inorganic Analysis', Fourth Edition (Longman's), 1954.

230. J.W.Gibbs, **Trans.Conn.Acad.Sci.**, 3, 108, (1875/6); ibid 343, (1877/8).

231. A.W.Adamson, "Physical Chemistry of Surfaces", Wiley, New York, (1967).

232. F.F.Abrahams, C.R.Brundle, **J.Vac.Sci.Technol.**, 18(2), 506, (1981).

233. J.J.Burton, C.R.Helms, R.S.Polizotti, **J.Chem.Phys.**, 65(3), 1089, (1976).

234. C.Berry, D.Majumdar, Y.W.Chung, **Surf.Sci.**, 94, 293, (1980).

235. S.H.Overbury, P.A.Bertrand, G.A.Somorjai, **Chem.Rev.**, 75, 547, (1975).

236. F.J.Kuijers, V.Ponec, **Surf.Sci.**, 68, 296, (1977).

237. R.Bouwman, L.H.Toneman, A.A.Holsher, **Surf.Sci.**, 35, 8, (1973).

238. A.Jablonski, S.H.Overbury, G.A.Somorjai, **Surf.Sci.**, 65, 578, (1977).

239. J.Ferrante, **Acta.Metall.**, 19, 743, (1971).

240. G.Maire, L.Hilaire, P.Legare, F.G.Gault, A.O Cinneide, **J.Catal.**, 44, 293, (1976).

241. R.Bouwman, G.J.M.Lippits, W.M.H.Sachtler, **J.Catal.**, 25, 350, (1972).

242. J.Sedlacek, L.Hilaire, P.Legare, G.Maire, **Surf.Sci.**, 115, 541, (1982).

243. R.Holm, S.Storp, **J.Electron Spec.Relat.Phenom.**, 8, 139, (1976).

244. R.Holm, S.Storp, **J.Electron Spec. Relat.Phenom.**, 8, 459, (1976).

245. R.P.Gupta, B.Perraillon, **Surf.Sci.**, 103, 397, (1981).

246. C.Lea, M.P.Seah, **Surf.Sci.**, 53, 272, (1975).

247. P.H.Dumoulin, M.Guttman, **Mat.Sci.Eng.**, 42, 249, (1980).

248. R.H.Stulen, R.Bastasz, **J.Vac.Sci.Technol.**, 16(3), 940, (1979).

249. L.A.Harris, **J.Appl.Phys.**, 39(3), 1428, (1968).

250. "Practical Surface Analysis by Auger and X-ray Photoelectron Spectroscopy" edited by D.Briggs and M.P.Seah, Chap 7, P273-9, Wiley and Sons Ltd, (1983).

251. H.Erhart, H.J.Grabke, **Metal.Sci.**, 15, 401, (1981).

252. T.W.Haas, J.T.Grant, G.J.Dooley III, **J.Vac.Sci.Technol.**, 7(1), 43, (1970).

253. I.H.Khan, **Surf.Sci.**, 40, 723, (1973).

254. E.N.Sickafus, **Surf.Sci.**, 19, 181, (1970).

255. W.E.Swartz, D.M.Holloway, **Appl.Spectrosc.**, 31(3), 210, (1977).

256. G.L.Powell, R.E.Clausing, G.E.McGuire, **Surf.Sci.**, 49, 310, (1975).

257. M.E.Schrader, **Surf.Sci.**, 78, L227, (1978).

258. A.Proctor,P.M.A.Sherwood, **Surf.Interface.Anal.**, 2(5), 191, (1980).

259. M.H.Basin, **J.Catal.**, 38, 218, (1975).

260. T.Imanaka, T.Hashimoto, K.Sakurai, Y.Okamoto, S.Teranishi, **Bull.Chem.Soc.Jpn.**, 53, 1206, (1980).

261. Y.Okamoto, T.Shimokawa, T.Imanaka, S.Teranishi, **J.Chem.Soc.Chem.Commun.**, 47, (1978).

262. M.A.Smith, D.E.Day, L.L.Levenson, **Ceram.Bull.**, 62(6), 638, (1982).

263. E.D.Hondros, M.P.Seah, C.Lea, **Met.Mater.**, Jan 1976, 26, (1976).

264. H.P.Bonzel, R.Ku, **J.Vac.Sci.Technol.**, 9, 663, (1972).

265. R.W.McCabe, L.D.Schmidt, **Surf.Sci.**, 60, 85, (1976); ibid, 65, 189, (1977).

266. C.E.Smith, J.P.Biberian, G.A.Somorjai, **J.Catal.**, 57, 426, (1979).

267. H.P.Bonzel, A.M.Franklin, G.Pirug, **Surf.Sci.**, 104, 625, (1981).

268. J.Jupille, **Surf.Sci.**, 123, L674, (1982).

269. M.Salmeron, L.Brewer, G.A.Somorjai, **Surf.Sci.**, 112, 207, (1981).

270. P.Steiner, S.Hufner, N.Martensson, B.Johansson, **Solid. Stat.Commun.**, 37, 73, (1981).

271. K.S.Kim, N.Winograd, **Chem.Phys.Lett.**, 30, 91, (1975).

272. F.D.Rossini (Ed.), 'Selected Values of Chemical Thermodynamic Properties', Circular 500, issued by the National Bureau of Standards, 1952.

273. C.Benndorf, C.Nobl, F.Theime, **Surf.Sci.**, 121, 249, (1982).

274. S.D.Bader, L.Richter, T.W.Orent, **Surf.Sci.**, 115, 501, (1982).

275. M.Yoshio, S.Mitsuyuki, O.Takaharu, T.Kenzi, **J.Chem.Soc.Farad. Trans.I**, 76(5), 1122, (1980).

276. P.Legare, L.Hilaire, G.Maire, G.Krill, A.Amamou, **Surf.Sci.**, 107, 533, (1981).

277. I.Szymersksa, M.Lipski, **J.Catal.**, 41, 197, (1976).

278. P.Legare, L.Hilaire, M.Sotto, G.Maire, Surf.Sci. , 91 ., 1757, (1980).

279. 'Comprehensive Inorganic Chemistry' ed by J.C.Bailar, H.J.Emeleus, Sir Ronald Nyholm and A.F Trotman-Dickinson, Vol 3, p1163-1370, (1973).